
This item was submitted to [Loughborough's Research Repository](#) by the author.
Items in Figshare are protected by copyright, with all rights reserved, unless otherwise indicated.

Sensor technology for in situ monitoring of the surface temperature distribution of SOFC

PLEASE CITE THE PUBLISHED VERSION

PUBLISHER

© Manoj Prasanna Ranaweera

PUBLISHER STATEMENT

This work is made available according to the conditions of the Creative Commons Attribution-NonCommercial-NoDerivatives 4.0 International (CC BY-NC-ND 4.0) licence. Full details of this licence are available at: <https://creativecommons.org/licenses/by-nc-nd/4.0/>

LICENCE

CC BY-NC-ND 4.0

REPOSITORY RECORD

Ranaweera, Manoj Prasanna. 2016. "Sensor Technology for in Situ Monitoring of the Surface Temperature Distribution of SOFC". figshare. <https://hdl.handle.net/2134/21995>.

Sensor Technology for *in situ* Monitoring of the Surface Temperature Distribution of SOFC

By

Manoj Prasanna Ranaweera

Doctoral Thesis

Submitted in partial fulfilment of the requirements for the award of Doctor
of Philosophy of Loughborough University

Department of Aeronautical and Automotive Engineering

July 2016

© By Manoj Prasanna Ranaweera, 2016

Dedicated to
my beloved mother, farther (late)
and
my loving wife Nilmini

Acknowledgement

The journey towards this doctoral thesis would not have been possible without the kind help and support from many.

First and foremost, I wish to convey my utmost gratitude to my supervisor Dr. Jung-Sik Kim for his invaluable advices, guidance, and support throughout. His generous allocation of time and effort for his students is commendable.

The advices and encouragements received from my co-supervisor, Prof. Rob Thring, were invaluable in this journey; thank you very much.

I wish to convey my sincere gratitude to Prof. Michael Walls for his wonderful advices, and Dr. Keith Yendall for giving me training, advices and support on sputter deposition.

To Mr Martin Coleman, thank you very much for your wonderful support given to me in my experiments. I am indeed thankful to all the other staff members from the Mechanical Service Workshop for their generous support. Mr. Pradip Karia and Mr. Harshad Purohit from Electronic Services Workshop extended a wonderful support for my research; thank you very much.

To Mrs. Chris Spencer from the Student Union; your support to maintain my student life in the UK was commendable – thank you very much.

To all the staff members of the AAE, especially, Dr. Anoma Malalasekara, Prof. Victor Krylov, Dr. Andrew Watson, Dr. Gang Zhou; thank you very much for your direct and indirect support for my research.

I must be thankful to the Vice Chancellor, HoD of DoME and all my colleagues at University of Moratuwa for their patience and support during this extended journey.

It's my research colleagues, Indae, Vijay, Erdogan, and Yunus who deserve a big thank for their support, friendship and care.

To all my Sri Lankan friends living in Loughborough, it was an amazing period full of fun and joy; thank you very much for your friendship, love, and care.

To my family, you all have my heartfelt thanks for your support and unconditional love.

Finally, to my loving wife for making my home the sweetest and the most relaxed place in this planet for me.

Abstract

Solid oxide fuel cell (SOFC) is the most efficient energy conversion technology of all-time in producing electricity from fuels. However, temperature-driven premature degradation is one of the biggest problems that impedes the widespread use of this technology. Understanding the temperature distribution of an operating SOFC is central to mitigate such degradations as well as to further enhance the performance.

The published efforts on SOFC temperature sensing, except small button cells, are mainly confined to measure temperature only from the gas channels (fuel/ air) with relatively low spatial resolution. However, the electrodes' temperature distribution measured with an adequate spatial resolution is more desirable than the gas temperature to investigate a cells' behaviour and its correlation to a stack's performance. The insufficiency of technology to *in situ* monitor the cell surface temperature distribution with an adequate spatial resolution was identified as a crucial research gap in the SOFC development cycle. Therefore, this research is aimed at developing a sensing technology to monitor *in situ* the cell surface temperature distribution of an operating SOFC with an adequately high spatial resolution and applying that technology to get a better insight into SOFC operation.

After having reviewed the strengths and weaknesses of presently available temperature sensing technologies concerning the application of SOFC, this thesis proposes multi-junction thermocouples, which share thermoelements between different sensing points of a thermocouple network to reduce the number of thermoelement required in multi-point temperature sensing. The law of intermediate conductors in thermocouples is the fundamental science that governs the thermoelectric performance of multi-junction thermocouples. A set of multi-junction thermocouples were fabricated by spot-welding of Ø 0.5 mm K-type thermocouple wires. The accuracy of these in-house constructed multi-junction thermocouples was compared with calibrated K-type thermocouples. The ability of multi-junction thermocouples to measure temperatures independently from each sensing points, despite sharing thermoelements, is theoretically established and experimentally demonstrated. Practical limitations of the proposed concept are discussed.

Multi-junction thermocouple grids having nine sensing points (with approximately 10 mm pitch) were employed to measure the cathode temperature distribution of operating SOFCs (5 cm × 5 cm, *NextCell-5*) under different operating conditions. The measurements were validated with conventional thermocouples on both working and non-working (open-circuit) cells.

Agreeing with theoretical explanations on the OCV-temperature relationship, a decrease of OCV could be observed with the increase of cell temperature. However, under a constant current of 60 mA, an increase of cell voltage could be observed with the increase of operating temperature from 700 °C to 850 °C with 50 °C intervals. This confirmed the decrease of ohmic polarisation with the increase of temperature. Polarisation curves at different operating temperatures revealed a relatively linear increase of the cell temperature with increasing the load. This positive correlation between cell temperature and current demonstrated the potential cell temperature fluctuations due to load changes. A slight out-of-phase response of cell temperature to current could be observed, where the

cell temperature change lags the current change. Although no activation polarisation could be observed, slight concentration polarisation could be noticed at higher current densities. Consequently, a noticeable, yet small, increase of the cell temperature could be observed under concentration polarisation. Flowrate dependent cell surface temperature fluctuations could be observed due to the presence of gas leakages; this inadvertently helped diagnose a gas leakage in the test rig using cell temperature measurements. Near-surface temperature measurements made approximately 7 mm above the cathode were found to be ineffective in discovering the cell surface temperature variations.

Further advancement of the proposed methodology was attempted by fabricating thin-film multi-junction thermocouple array integral to SOFC. A cell integrated multi-junction thermocouple array was used to measure the temperature distribution of a non-working SOFC (open-circuit). The multi-junction array could adequately measure the cell temperature distribution under different fuel flow rates.

Publications

- **Manoj Ranaweera**, Jung-Sik Kim, In-Situ Temperature Sensing of SOFC during Anode Reduction and Cell Operations using a Multi-Junction Thermocouple Network, *ECS Transactions*, 2015, 68(1), pp. 2637-2644
- **Manoj Ranaweera**, Jung-Sik Kim, A cell integrated multi-junction thermocouple array for SOFC temperature sensing: N+1 architecture, *Journal of Power Sources*, 2016, vol.351, pp. 70-78
- **Manoj Ranaweera**, Jung-Sik Kim, Cell integrated thin-film multi-junction thermocouple array for in-situ temperature monitoring of Solid Oxide Fuel Cells, *Proceedings of the IEEE Sensors 2015*, November 2015. South Korea, pp. 5-8
- Indae Choi, **Manoj Ranaweera**, Jung-Sik Kim, Fabrication of three-dimensional wavy type single chamber solid oxide fuel cell by in situ observation of curvature evolution, *Journal of the American Ceramic Society*, vol.99(4), pp. 1174-1183
- **Manoj Ranaweera**, Vijay Venkatesan, Erdogan Guk, Jung-Sik Kim, High spatial resolution monitoring of the temperature distribution from an operating SOFC, *12th European SOFC & SOE Forum*, Switzerland, 2016 (conference proceedings pending)
- **Manoj Ranaweera**, Indae Choi, Jung-Sik Kim, Multi-junction thermocouple array for in-situ temperature monitoring of SOFC: Simulation, *Intl. Journal of Research in Engineering and Technology*, 2015 Vol.4(2), pp. 330-338
- **Manoj Ranaweera**, Indae Choi, Jung-Sik Kim, Thin-film multi-junction thermocouple array for in-situ temperature monitoring of SOFC, *International Conference on Nanotechnology, Nanomaterials & Thin Films for Energy Applications*, UK, 2015 (Oral presentation - abstract only)
- **Manoj Ranaweera**, Jung-Sik Kim, SOFC temperature sensing during anode reductions and cell operations, *Supergen Researcher Conference*, UK, 2014 (Oral presentation -abstract only)
- **Manoj Ranaweera**, Jung-Sik Kim, THERMONO: Cell integrated thin-film sensor array for in-situ monitoring of SOFC temperature, *10th International Hydrogen Fuel Cell conference*, UK, 2014 (Oral presentation - abstract only)
- Indae Choi, **Manoj Ranaweera**, Jung-Sik Kim, Fabrication of wavy type porous triple-layer SC-SOFCs via experimental observation of curvature evolution during co-sintering, *20th World Hydrogen Energy Conference*, South Korea, 2014, pp. 515-521

Patent:

- GB1509690.2.1 – multi-junction thermocouple for electrochemical energy conversion devices (in progress)

Contents

Acknowledgement	iv
Abstract	v
Publications	vii
List of Figures	xii
Nomenclature	xvii
Chapter 1 : Introduction	1
1.1 Problem Statement	6
1.2 Thesis Plan	7
1.3 References	9
Chapter 2 : Literature Review of SOFC	10
Chapter Summary:	11
2.1 State of the Art Technology	12
2.1.1 Introduction	12
2.1.2 Fuel Flexibility	13
2.1.3 Cell / Stack Configurations	14
2.1.4 Major Components of a Cell	19
2.2 Fundamental Sciences	29
2.2.1 Reversible Cell Voltage	30
2.2.2 Losses in Cell Voltage	32
2.2.3 Practical Cell Voltage	36
2.2.4 Degradation	37
2.3 Thermal Requirement and Management	38
2.3.1 The Thermodynamic Efficiency	38
2.3.2 Efficiency Improvement with a Bottoming Cycle: The Thermodynamic Perspective	39
2.3.3 Heat Sources and Sinks in SOFC	41
2.3.4 The Effects of Temperature on Power Output	45
2.3.5 Temperature Distribution and Thermal Stresses	48
2.4 Conclusions	52
2.5 References	54
2.6 Bibliography	57
Chapter 3 : Literature Review of SOFC Temperature Sensing	58
Chapter Summary	59
3.1 Literature Review: Temperature Sensing	60

3.1.1	Introduction.....	60
3.1.2	Thermistors	61
3.1.3	Thermocouples.....	63
3.1.4	Resistance Temperature Detectors (RTD)	71
3.2	State of the Art SOFC Temperature Sensing	77
3.3	Aim and Objectives.....	84
3.3.1	Aim	84
3.3.2	Objectives	84
3.4	Conclusions	85
3.5	References	87
Chapter 4 : Design and Numerical Calculations of Multi-Junction Thermocouples.....		91
Chapter Summary		92
4.1	Introduction	93
4.1.1	Seebeck Effect	93
4.1.2	The Law of Intermediate Conductors	94
4.1.3	Array Architecture	97
4.1.4	Grid Architecture	100
4.2	Numerical Calculation of Performance.....	102
4.2.1	Method of Seebeck Coefficient Calculation	102
4.2.2	Method of Temperature Calculation	103
4.2.3	Material Selection for Calculations.....	106
4.3	Calculations 1: Array Architecture $\sim \{N+I\}$	107
4.3.1	Performance without Dissimilar Zones	110
4.3.2	Influence of Dissimilar Zones.....	110
4.3.3	Results and Discussion	112
4.4	Calculations 2: Grid Architecture $\sim \{N^2 \text{ to } 2N\}$	116
4.4.1	Performance without Dissimilar Zones	118
4.4.2	Influence of Dissimilar Zones.....	118
4.4.3	Results and Discussion	119
4.5	Conclusions	122
4.6	References	124
Chapter 5 : Experimental Investigation of Performance of Multi-Junction Thermocouples.....		125
Chapter Summary		126
5.1	Introduction	127

5.2	External Wire Selection	129
5.3	Effects of Multiple Junctions on Measurement Accuracy	133
5.3.1	Results and Discussion	134
5.4	Multi-Junction Thermocouples: Concept Validation	138
5.4.1	Results and Discussion	139
5.5	Surface Temperature Measurements	142
5.5.1	Results and Discussion	146
5.6	Conclusions	148
5.7	References	149
Chapter 6 : SOFC Temperature Sensing		150
Chapter Summary		151
6.1	Introduction	152
6.2	Effects of Thermocouple Grid on SOFC Performance	153
6.2.1	Method Selection	154
6.2.2	Methodology	154
6.2.3	Results and Discussion	156
6.3	Temperature of a Non-Working Cell: Case I – Grid Only	157
6.3.1	Results and Discussion	160
6.4	Temperature of a Non-Working: Case II – Grid with Thermocouples	168
6.4.1	Results and Discussion	170
6.5	Temperature Measurements from a Working Cell	178
6.5.1	Results and Discussion	181
6.6	Conclusions	196
6.7	References	198
Chapter 7 : Feasibility Investigation on Cell Integration of Multi-Junction Thermocouples		199
Chapter Summary		200
7.1	Introduction	201
7.2	Fabrication and Testing of Array Architecture	204
7.2.1	Results and Discussion	206
7.3	Failure Mode Investigation and Hypothesis Testing	210
7.3.1	Results and Discussion	211
7.4	Failure Mode Analysis of External Wire Connection	216
7.4.1	Results and Discussion	218
7.4.2	Failure Mechanism Investigation	219

7.5	Application into SOFC Temperature Sensing: Case I.....	223
7.5.1	Results and Discussion	225
7.6	Application into SOFC Temperature Sensing: Case II	228
7.6.1	Results & Discussion	231
7.7	Conclusions	235
7.8	References	236
Chapter 8 :	Conclusions and Future Works.....	237
8.1	Conclusions	238
8.2	Limitations and Implications.....	241
8.3	Recommendations for Future Research	242
Appendix I	244
Appendix II	245
Appendix III	246
Appendix IV	247
Appendix V	248

List of Figures

<i>Figure 1:1 Global energy history and projection^[1]</i>	3
<i>Figure 1:2 the energy sector CO₂ emission^[3]</i>	3
<i>Figure 1:3 Power rating and efficiency of energy conversion devices^[5]</i>	4
<i>Figure 2.1 A schematic diagram of an SOFC</i>	12
<i>Figure 2.2 Self-support structures</i>	15
<i>Figure 2.3 External-support structures</i>	15
<i>Figure 2.4 Cutaway of a flat tubular design^[13]</i>	15
<i>Figure 2.5 Monolithic SOFC design^[14]</i>	16
<i>Figure 2.6 Segmented in series design^[15]</i>	17
<i>Figure 2.7 Tubular SOFC stack^[16]</i>	18
<i>Figure 2.8 A schematic diagram of a planar SOFC stack</i>	19
<i>Figure 2.9 Ionic conductivity of yttria stabilised zirconia with varying dopant composition^[21]</i>	20
<i>Figure 2.10 The change of ionic conductivity with respect to sintering temperature^[18]</i>	21
<i>Figure 2.11 Triple Phase Boundary (TPB) and TPB enhancement</i>	23
<i>Figure 2.12 Change of conductivity with Ni content in Ni/YSZ^[39]</i>	25
<i>Figure 2.13 Enhancement of electrical conductivity with increase of coarse YSZ content^[39]</i>	25
<i>Figure 2.14 Optical micrograph images taken before and after firing a cermet containing 30% Ni by volume^[41]</i>	26
<i>Figure 2.15 A typical polarization curve^[44]</i>	33
<i>Figure 2.16 Temperature distribution with fuel reforming (+Jh ~ with Joule heating and – Jh ~ without Joule heating)^[57]</i>	44
<i>Figure 2.17 Performance of a single cell at different temperatures^[59]</i>	45
<i>Figure 2.18 Temperature distribution in the electrolyte and the current density along the length of the cell^[57]</i>	46
<i>Figure 2.19 Temperature and current density distribution of a planar SOFC under cross-flow configuration (a) the temperature distribution (b) the current density distribution^[60]</i>	47
<i>Figure 2.20 In-plane temperature profiles on the cell and interconnect of a 3-cell SOFC stack model after: (a) 30 s, (b) 1 min, (c) 2 min, (d) 6 min, (e) 14 min from start-up, and (f) steady-state condition^[65]</i>	49
<i>Figure 2.21 Temperature distribution at the steady-state condition in three-cell SOFC model^[65]</i>	50

Figure 2.22 Simulated temperature and corresponding stress distribution on a model electrolyte (a) the temperature distribution, (b) the stress distribution ^[59]	51
Figure 3.1 Resistivity Vs Temperature curve of a PTC thermistor ^[5]	62
Figure 3.2 A schematic diagram of a thermoelectric loop	67
Figure 3.3 Schematic diagram showing the thermal diffusion of charge carriers under a temperature gradient	68
Figure 3.4 Schematic diagram of a thermocouple with a voltmeter connected across it.....	69
Figure 3.5 RTD two-wire configuration	74
Figure 3.6 RTD three-wire configuration.....	75
Figure 3.7 RTD four-wire configuration	75
Figure 3.8 Simulated temperature distribution under different flow configurations (a) Counter-flow (b) co-flow (c) cross-flow ^[60]	78
Figure 3.9 Simulated temperature distribution under cross-flow configuration ^[59]	78
Figure 3.10 The schematic diagram of the experimental setup used to measure the anode temperature using IR thermometry ^[61]	79
Figure 3.11 Special anode arrangement for IR temperature sensing ^[62]	80
Figure 3.12 The oven with front window panel removed to provide optical access to the anode ^[62]	80
Figure 3.13 SOFC stack with thermocouples ^[63]	82
Figure 3.14 Temperature probe locations ^[63]	82
Figure 3.15 Different temperature probe locations ^[65]	83
Figure 4.1 A schematic representation of the Seebeck voltage	94
Figure 4.2 Schematic diagram of a thermocouple with an intermediate conductor	95
Figure 4.3 Recursive unit of the array architecture	97
Figure 4.4 Three iterations of the array architecture.....	99
Figure 4.5 The recursive unit of the grid architecture	100
Figure 4.6 A grid architecture with nine temperature sensing points.....	101
Figure 4.7 The estimation errors resulted by K, S, R, and N type thermocouples at different temperatures during temperature calculations	106
Figure 4.8 N+1 Architecture of multi-junction thermocouple array.....	107
Figure 4.9 A schematic diagram of a 9-point thermocouple grid	116
Figure 4.10 Change of error with the increase of boundary temperature range	121
Figure 5.1 Schematic diagram of a thermocouple attached to a data logger	129
Figure 5.2 Variation of EMF at different connection point temperatures when the external wires are made of nicrosil.....	132

Figure 5.3 Schematic diagram of the architecture (the array).....	133
Figure 5.4 Multi-junction thermocouple with four commercial thermocouples (S1-S4: four sensing points of array; TC-S1 to TC-S4: four thermocouples at S1 to S4)	134
Figure 5.5 A schematic diagram of the three-point multi-junction thermocouple	138
Figure 5.6 Spatial temperatures measured by the multi-junction thermocouple and conventional thermocouples. (a) to (d) are four random instances of time.....	139
Figure 5.7 (a) nine-point thermocouple grid; (b) SOFC test cell fitted onto the cell holder having its 4 cm × 4 cm cathode facing up	144
Figure 5.8 SOFC test rig with the cell in place. The dead weight was used to force the grid onto the cathode	145
Figure 5.9 Temperature from the grid and the thermocouple (Heating rate 400 °C/hour—set value) S1to S9: nine sensing points of the grid, TC: commercial thermocouple.....	146
Figure 5.10 Change of average cell temperature and the cathode air temperature (T_{avg} represents average cell temperature and TC represents thermocouple temperature)	147
Figure 6.1 A schematic diagram of the nine-point K-type thermocouple grid (each wire is 0.5 mm in diameter)	155
Figure 6.2 A schematic diagram of the locations of the grid and the current collector on the 4 cm × 4 cm cathode of NextCell-5.....	155
Figure 6.3 Change of the cell current over time with and without the thermocouple grid operating on the cell. (P_{avg} : the average power output).....	156
Figure 6.4 The nine-point thermocouple grid.....	157
Figure 6.5 The cell with the grid and the current collector in place.....	158
Figure 6.6 Approximate locations of sensing points on the cathode	158
Figure 6.7 SOFC test setup used for OCV measurements.....	159
Figure 6.8 Temperature distribution during the anode reduction and the average temperatures over 45 th and 70 th minute (TC: commercial thermocouple S1-S9: nine sensing points of the grid. Temperature values are in degree Celsius).....	161
Figure 6.9 Temperature and OCV over cell operation (TC: thermocouple, S1-S9: sensing points of the grid, OCV: open circuit voltage of the cell).....	162
Figure 6.10 Variation of average cell temperature with hydrogen flow rate.....	163
Figure 6.11 Variation of OCV with hydrogen flow rate.....	165
Figure 6.12 Change of OCV with cell temperature	166
Figure 6.13 SOFC test cell with the thermocouple grid in place	168
Figure 6.14 Location of the anode's thermocouple	169

Figure 6.15 Temperature during the anode reduction (S1 to S9: temperatures from the grid, TC-S1, TC-S5, TC-S7: thermocouples near S1, S5, and S5, respectively. TC-Cathode: Cathode thermocouple).....	171
Figure 6.16 OCV and temperature response during cell operation.....	173
Figure 6.17 Average cell temperature sketch at each flow rate (T_x = average temperature at x ml /min flow rate).....	174
Figure 6.18 Anode chamber exhaust gas temperature	175
Figure 6.19 Temperature from the grid and adjuecent thermocouples (a) S1 and TC-S1 (b) S5 and TC-S5 (c) S7 and TC-S7 (d) difference between grid points and their corresponding thermocouples.....	176
Figure 6.20 Dimensions of the grid and the positioning of thermocouples.....	179
Figure 6.21 A schematic diagram of the location of the grid, thermocouples, and the current collector on the 4 cm × 4 cm cathode	179
Figure 6.22 Polarisation curve at 850 °C operations along with cell temperature.....	183
Figure 6.23 Change of average cell temperature with current (Cell operation at 850 °C).	186
Figure 6.24 Polarisation curve at 700 °C operations along with cell temperature.....	187
Figure 6.25 Polarisation curve at 800 °C operations along with cell temperature.....	188
Figure 6.26 Polarisation curve at 750 °C operations along with cell temperature.....	188
Figure 6.27 Temperature and voltage response to different flow compositions / rates at 70.8 mA and 850 °C.....	189
Figure 6.28 Schematic diagram of the SOFC in operation	191
Figure 6.29 Temperature measured by the grid and thermocouples at 800 °C nominal temperature operation under a constant current of 30 mA. (a) Temperature from S1 and TC-S1, (b) temperature from S5 and TC-S5, (c) temperature from S9 and TC-S9, and (d) difference of measurements; where S1, S5, and S9 are three sensing point of the grid and TC-S1, TC-S5, and TC-S9 are the corresponding thermocouples, respectively.....	193
Figure 7.1 Variation of EMF with temperature for 100 nm thick chromel film ^[6]	202
Figure 7.2 NIST standard EMF of a K-type thermocouple (Graph plotted based on NIST thermocouple data)	203
Figure 7.3 The sensor fabricated on the cathode of Ø52 mm SOFC	204
Figure 7.4 External wires connected with Silver paste	205
Figure 7.5 Sensor pattern protected by alumina	206
Figure 7.6 Temperature measurements from the array and the thermocouple (S1 –S4: four sensing points of the array, TC – commercial thermocouple)	207
Figure 7.7 Enlarged view of the first temperature interruption	207

<i>Figure 7.8 Actual temperature difference (raw data)</i>	209
<i>Figure 7.9 Polynomial fitted temperature difference (5th order)</i>	209
<i>Figure 7.10 dual-array fabricated on cathode</i>	211
<i>Figure 7.11 Temperature from the dual array and thermocouple (TC: thermocouple, S1-S7: seven sensing points from the dual array)</i>	212
<i>Figure 7.12 (a) momentary diversion during first heating (b), an enlarged view of the encircled section in (a)</i>	213
<i>Figure 7.13 Input circuitry for one channel of NI9213^[11]</i>	213
<i>Figure 7.14 (a) first failure of dual-array during cooling (b) enlarged view of diversion encircled in (a)</i>	214
<i>Figure 7.15 First heating and cooling cycle of grid architecture</i>	215
<i>Figure 7.16 wire thermocouple arrangement</i>	216
<i>Figure 7.17 thermocouples with alumina protected connection points</i>	217
<i>Figure 7.18 thermocouple setup in the box furnace</i>	217
<i>Figure 7.19 Temperature measurements (TC – commercial thermocouple, TC-A: thermocouple A, TC-B: thermocouple B)</i>	218
<i>Figure 7.20 External wire connection to thermocouples</i>	219
<i>Figure 7.21 Thermocouples as alumina and silver hardened</i>	220
<i>Figure 7.22 Temperature profile during first cycle</i>	221
<i>Figure 7.23 Temperature profile during second cycle</i>	221
<i>Figure 7.24 appearance of the silver (a) after experiment (b) before experiment</i>	222
<i>Figure 7.25 thermocouple array fabricated on cathode and covered with alumina</i>	223
<i>Figure 7.26 Test rig with sensor attached cell in place</i>	224
<i>Figure 7.27 Temperature distribution during anode reduction</i>	225
<i>Figure 7.28 Temperature and OCV during cell operation (TC: commercial thermocouple, S1-S4: four sensing points, OCV – Cell's OCV)</i>	226
<i>Figure 7.29 Correlation between average cell temperature and OCV</i>	227
<i>Figure 7.30 Wire connected cell (a) connecting external wires to the cell (b) the SOFC test cell (NextCell-5) with the cathode facing up before connecting wires</i>	229
<i>Figure 7.31 The cell fixed to the cathode with sensing locations shown</i>	230
<i>Figure 7.32 Temperature response to varying flow rates</i>	232
<i>Figure 7.33 Change of OCV with hydrogen composition</i>	233
<i>Figure 7.34 Change of OCV with cell temperature</i>	234

Nomenclature

SOFC – Solid oxide fuel cell

PEM – Polymer exchange membrane fuel cell

RMS – Root mean square

EMF – Electromotive force

OCV – Open circuit voltage

NIST – National institute of standards and technology

RTD – Resistance temperature detector

YSZ – Yttria stabilised zirconia

LSM – Lanthanum strontium manganite

LSCF – Lanthanum strontium cobalt ferrite

S_t – Seebeck coefficient at temperature t °C

\varnothing – Diameter

T – Absolute temperature

A – Ampere or the symbol of ammeter

V – Volt or the symbol of voltmeter

DC – Direct current

G – Gibbs free energy

\bar{g} – Molar Gibbs free energy

H – Enthalpy

S – Entropy

F – Faraday constant

R – Universal gas constant

E – Reversible cell voltage

E^0	– Reversible cell voltage at standard pressure and temperature
i	– Current density
i_0	– Exchange current density
η_{act} / v_{act}	– Activation polarisation
v_{con}	– Concentration polarisation
v_{ohmic}	– Ohmic polarisation
β	– Transfer coefficient
η_{th}	– Thermodynamic efficiency
λ	– Electrical conductivity

Chapter 1 : Introduction

In this thesis, the author investigates to developing a temperature sensing technology to monitor *in situ* the cell surface temperature distribution of an SOFC with an adequate spatial resolution to gain a better insight into the relationship between the cell temperature and performance of SOFC. With the proven capabilities of thermocouple thermometry in measuring temperature from SOFCs, the author has attempted to advance the thermocouple thermometry for multi-point temperature sensing from SOFC with a reduced number of thermoelements. The chosen approach is to share thermoelements between different sensing points of a thermocouple network to make multi-junction thermocouples. The approach is scientifically supported by the law of intermediate conductors for thermocouples. Based on the concept of sharing thermoelements between sensing points, two multi-junction thermocouple architectures namely, the array and the grid were proposed for the task of SOFC temperature sensing. The array is the fundamental building block of the multi-junction concept while the grid is a derivative of the array architecture. Upon adequate scientific and experimental investigations into the plausibility of the concept, multi-junction thermocouples were used to explore the cell temperature response to different operating conditions. The limitations of the research methodology and possible implications of the results are provided. Some recommendations for further research to advance the proposed sensing technology are also provided in the thesis. The following sections of this chapter first establish the locale of the broad research theme in the global energy landscape, and the specific research problem is subsequently defined. The chapter concludes with a detailed overview of the thesis structure.

An unprecedented growth in the global energy demand is predicted for the coming decades, particularly because of the rapid industrialisation of highly populated countries like China and India. The US Energy Information Administration (EIA) estimates a 56% increase in energy demand between the years 2010 and 2040, from 524 quadrillion Btu in 2010 to 820 quadrillion Btu in the year 2040^[1], as shown in Figure 1.1. A more specific growth pattern predicted by the International Energy Agency (IEA) shows that the global energy demand will continue to increase by 2% each year, until the year 2025, and then its annual increase is expected to drop to 1% due to price and policy effects^[2]. Acknowledging the growth of the renewable energy sector, both organisations estimate that fossil fuels will hold a share of approximately three-quarters of the global energy mix by the year 2040. Therefore, unless significant advancements in technology could be made realistic to reduce the greenhouse gas emissions from combustion of fossil fuels, a detrimental change in climate is inevitable.

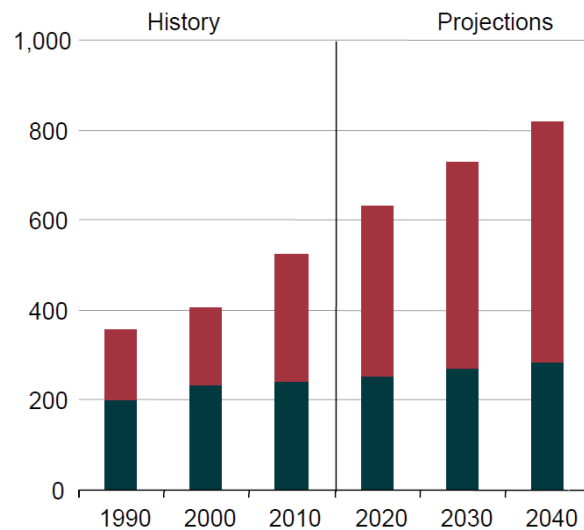
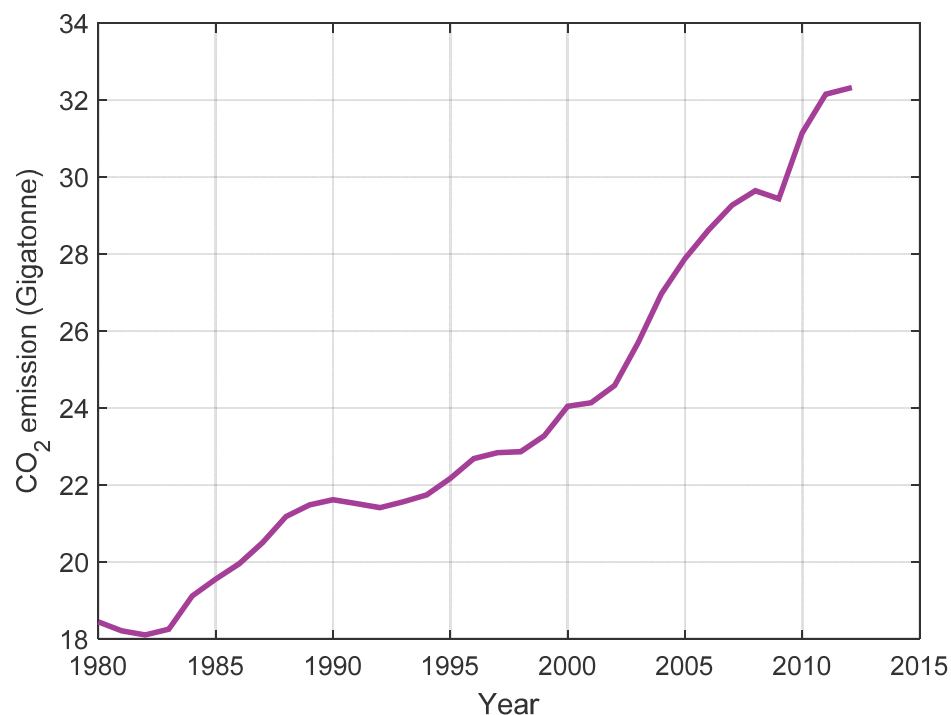
Figure 1.1 Global energy history and projection^[1]

Figure 1.2 shows the annual carbon dioxide emissions by energy consumption from the year 1980 to 2012 (the graph is plotted based on EIA statistics^[3]). The increased dependency on fossil fuels to meet the growing energy demand will continue to increase the carbon dioxide emissions, likely in more aggressive manner. However, in order to limit the global warming to 2 °C (relative to the pre-industrialised era) to curtail the risks, impacts, and damages of climate change, the cumulative total of CO₂ emission between the years 2000 and 2049 must be limited to 886 Gt or below^[4]: this is approximately 18 Gt per year. However, the current annual CO₂ emission in the energy sector is already almost twice this threshold. Thus, expeditious measures must be taken to cut down carbon

Figure 1.2 the energy sector CO₂ emission^[3]

dioxide emissions. Technologies to more efficiently convert the chemical energy of fossil fuels into other usable forms, such as electricity, are an effective avenue to cater to the growing energy demand with less environmental impact.

Since SOFCs can operate on hydrocarbon fuels and they are the most efficient energy conversion devices available today, SOFC technology is in a unique position to better utilise existing fossil fuel sources with less emission. Figure 1.3 shows the electrical efficiencies of power generation systems versus system size. The hybrid fuel cell systems, which use a steam turbine (perhaps, and a gas turbine) to produce further electricity from high-temperature steam produced by SOFC, have an exceptionally high overall efficiency range.

In addition to the high-capacity power generation discussed before, SOFC systems can be used for on-site medium- or low-capacity power generation. This distributed power generation is very important, particularly in applications where the reliability and

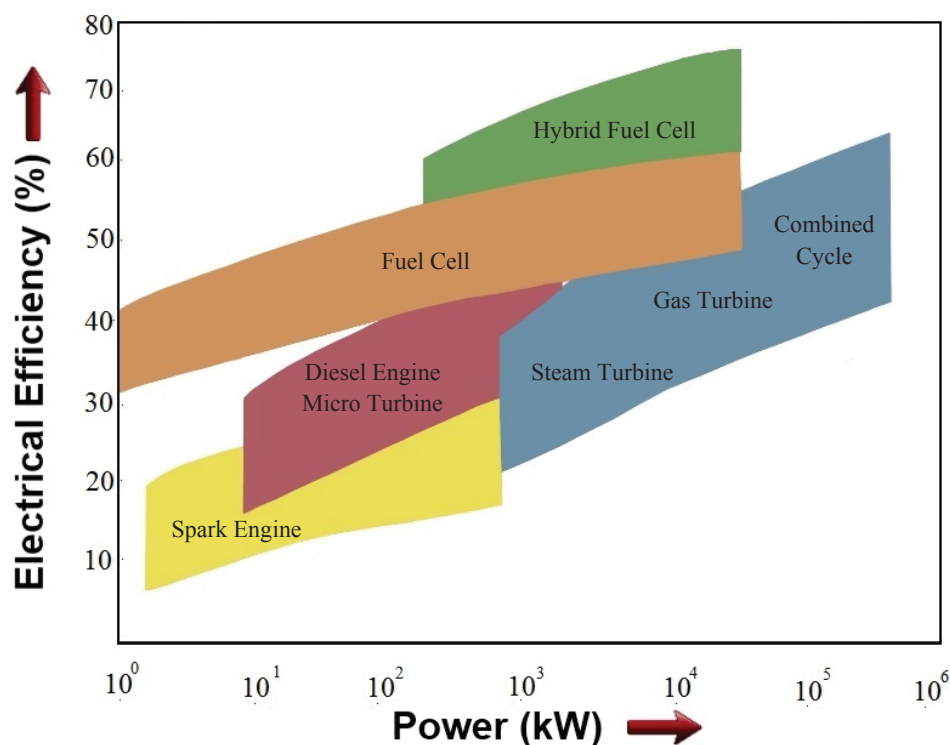


Figure 1.3 Power rating and efficiency of energy conversion devices^[5]

the quality of electricity are critical. For instance, modern chip manufacturing industries and internet-based businesses, such as data centres, transaction servers, etc. require high quality and high reliability in their electricity supply. While it is less economical or practical for the grid to produce such a high reliability and quality, SOFC is an ideal solution to cater to such needs.

However, in spite of the unique advantages of SOFC technology in better serving the global energy sector, premature degradation of cells and stacks significantly hinders the successful commercialisation and widespread use of this technology. Among a number of factors aggravating the degradation, thermal fluctuations at elevated temperatures (usually, between 600 °C to 900 °C) have a dominant role in a number of degradation mechanisms. However, on the other hand, the high operating temperature is directly coupled with the fuel flexibility and high efficiency of SOFC systems. Therefore, any correlations between the cell temperature, degradation, and performance must be comprehensively investigated to optimise the performance while mitigating the degradations. Understanding the cell-level temperature distribution of an operating SOFC is central to the success of such investigations.

A number of attempts have been made to understand the operating temperature of SOFC. In the majority of such efforts, computational techniques have been used to predict the cell-level temperature distribution, while only a limited number of efforts are found in the literature on experimental measurements. The present experimental approaches to measure SOFC temperature are also confined to measuring temperature only from a few points of a chosen cell. No literature evidence was found, to the best of author's knowledge, demonstrating the cell-level temperature measurements with adequately high spatial resolution, except small button cells. Since simulations predict some significant temperature gradients across a fuel cell under different operating conditions^[6], temperature measurements made from a distance away from a cell and with limited spatial resolution are likely to be of less support to formulate any correlations between the cell temperature, performance, and degradation. Therefore, the absence of a sensing technology to monitor *in situ* the cell-level temperature distribution of an operating SOFC is a significant research gap in the SOFC research domain.

1.1 Problem Statement

The use of state of the art simulation techniques with advanced computing power to investigate the cell-level temperature distribution of an operating SOFC stack is a good approach, but it cannot revoke the need of experimental measurements. Despite the advancements in modelling techniques, the yet-to-be-fully-known electrochemical behaviour within a fuel cell stack aggravates the need for experimental validation of such models prior to accepting the authenticity of their predicted temperatures. Further, although computational models may be sufficiently comprehensive to respond to a set of predetermined variations of operating characteristics, whether such models can effectively respond to all or most operational conditions is highly uncertain. Further, *in situ* temperature sensing can serve in a number of sub-disciplines in the broad spectrum of SOFC research, where it may be nearly impossible to customise simulations. The development of new materials, testing of different fuel types and internal reforming, new stack architectures, testing different operating parameters, different reactant flow configurations, etc. are only a few options where *in situ* monitored temperature can provide important information to understand the performance and degradation. Therefore, cell surface temperature distribution of an operating SOFC is a new form of knowledge, and a technology to enable *in situ* cell surface temperature monitoring is a significant contribution to the advancement of the SOFC technology.

1.2 Thesis Plan

This thesis consists of eight chapters; a brief contextual introduction to each chapter and the interrelationships between chapters are outlined below.

Chapter 2: Literature Review of SOFC

A technological overview of SOFC technology is first presented, and then, the fundamental sciences behind SOFC operation are discussed.

The influence of temperature on the SOFC performance is theoretically explained. The primary sources of heat generation, as well as heat absorption in SOFC, are discussed. The effects of temperature gradient on performance as well as on thermal stresses are discussed.

Chapter 3: Literature Review of SOFC temperature Sensing

A review of the literature on SOFC temperature sensing is presented along with a detailed discussion on temperature sensing technologies that can be adapted for SOFC temperature sensing to better reveal the cell-level temperature distribution than the present technologies. The chapter concludes by presenting the objective selection of thermometry for this research.

Chapter 4: Design and numerical calculations of multi-junction thermocouples

Once the thermometry was objectively selected and its limitations and merits were identified, the focus was to overcome the limitations it has in SOFC temperature sensing. Two multi-junction thermocouple architectures are proposed namely, the array architecture and the grid architecture. The theoretical performance of multi-junction thermocouple is numerically assessed. The influence of potential error sources is investigated, considering hypothetical yet close-to-practical situations.

Chapter 5: Experimental investigation of the performance of multi-junction thermocouples

This chapter presents and discusses the experimental investigation of the multi-junction thermocouple architectures proposed and mathematically assessed in Chapter 4. The choice of materials for thermoelements and external wires is presented. Limitations and potential implications of the said choices are discussed. The accuracy of the proposed sensor architectures is assessed with standard thermocouples, and their performance is discussed. The suitability of the proposed grid architecture in measuring the temperature

distribution of a surface is discussed. The chapter concludes by stating the major conclusions drawn from the experimental results and potential implications.

Chapter 6: SOFC temperature sensing

The multi-junction thermocouple grid was applied to monitor the cell surface temperature distribution from SOFCs. The temperature during anode reduction, open-circuit, and under different operating conditions was measured. The measurements were compared and validated with commercial thermocouples. The effectiveness of the cell surface temperature measurement is qualitatively compared with near-cell temperature sensing. Conclusions drawn from the findings are presented at the end of the chapter.

Chapter 7: Feasibility investigation on cell integration of multi-junction thermocouples

After the thermocouple grid made of wires adequately demonstrated its ability to effectively measure the cell surface temperature distribution of an operating SOFC, the feasibility of further advancing the proposed sensing technology by cell integration is investigated. Sputter deposition was assessed as a potential fabrication technique. The temperature measurement from an SOFC using thin-film thermocouple array is presented and discussed.

Chapter 8: Conclusions and future work

The thesis is brought to a conclusion by discussing the findings with respect to the aim and objectives. The contribution of this research to the field of SOFC is discussed. The limitations of the research are discussed, and some recommendations for further research are also provided.

1.3 References

- [1] U.S. Energy Information Administration, *International Energy Outlook 2013*, USA, 2013
- [2] International Energy Agency, *World Energy Outlook 2014 – Executive Summary*, France, 2014
- [3] U.S. Energy Information Administration, *International Energy Statistics*, [viewed: 30/10/2015] Available at:
<http://www.eia.gov/cfapps/ipdbproject/iedindex3.cfm?tid=90&pid=51&aid=8&cid=ww&syid=1980&eyid=2011&unit=MTCDPP>
- [4] Meinshausen M., Meinshausen, N., Hare, W., Raper, S.C.B., Frieler, K., Jnutti, R., Frame, D.J., and Allen, M.R., Greenhouse-gas emission targets for limiting global warming to 2 °C, *Nature Letters*, 2009, vol. 458, pp. 1158-1163
- [5] Singhal, S.C. and Kendal, K. *High temperature Solid Oxide Fuel Cells: Fundamentals, Design and Applications*, UK:Elsevier, 2003.
- [6] Achenbach, E., Three-dimensional and time-dependent simulation of a planar solid oxide fuel cell stack, *Journal of Power Sources*, 1994, 49(1-3), pp. 333-348.

Chapter 2 : Literature Review of SOFC

Chapter Summary:

This chapter begins with presenting the state of art SOFC technology in Section 2.1 where Section 2.1.1 introduces SOFC technology, and Section 2.1.2 discusses fuel flexibility which is a unique advantage of SOFC over other fuel cells. Section 2.1.3 introduces major cell/ stack configurations, and Section 2.1.4 presents some detailed information about main cell components.

Fundamental sciences of SOFC operation is presented and discussed in Section 2.2. The reversible cell voltage, the sources of voltage losses, and the practical cell voltage are discussed in Sections 2.2.1, 2.2.2, and 2.2.3, respectively. Degradation of SOFC is briefly mentioned in Section 2.2.4.

Section 2.3 is dedicated to theoretically bridge the SOFC performance and the operating temperature. The section begins with introducing the thermodynamic efficiency in Section 2.3.1. A theoretical explanation on how the overall plant efficiency can be increased using waste heat is presented in Section 2.3.2. The primary heat sources and sinks in SOFC are given in Section 2.3.3, while the effects of temperature on performance are presented in Section 2.3.4. Section 0 presents a case study on how the temperature gradients across a cell and stack generate thermal stresses.

The chapter concludes by presenting the conclusions in Section 2.4.

2.1 State of the Art Technology

2.1.1 Introduction

A solid oxide fuel cell (SOFC) is, essentially, an electrochemical energy conversion device that converts the chemical energy of fuel into electricity by electrochemical oxidation of fuel with the absence of combustion. Figure 2.1 shows a schematic, operational diagram of a cell that uses hydrogen as the fuel. The anode and the cathode are where the fuel oxidation and oxygen reduction take place, respectively. The electrolyte transports oxygen ions from the cathode to the anode. The external circuit passes the electrons from the anode to the cathode thus, producing current. Although SOFC can operate on a number of fuels, the following explanation of the cell operation considers hydrogen as the fuel.

Hydrogen enters the porous anode and gets oxidised releasing two electrons per each hydrogen molecule according to the half reaction in Equation (2.1)**Error! Reference source not found..** The released electrons then pass through the external circuitry to the cathode creating a current flow through the load. The transferred electrons then combine with oxygen molecules in the cathode and produce oxygen ions as per the half reaction in Equation (2.2). The oxygen ions then travel through the electrolyte to reach the anode. At the anode, the transferred oxygen ions combine with hydrogen ions producing water, according to Equation (2.3). The electrolyte is essentially an electron transfer inhibitor while being an excellent oxygen ion conductor. Thus, electrons are forced through the external circuitry to reach the cathode – no short circuiting through the electrolyte. Further, the electrolyte is designed to be a highly dense layer, and thus, it can

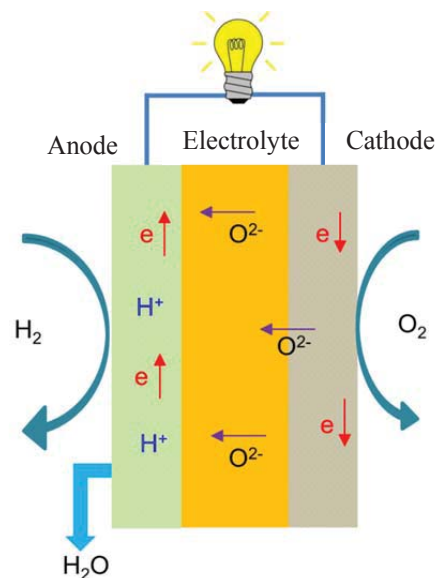
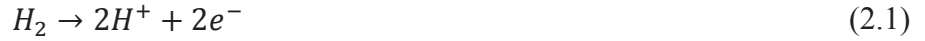


Figure 2.1 A schematic diagram of an SOFC

prevent fuel crossover to the cathode or oxygen crossover to the anode – no combustion of fuel. This process continues to produce electricity as long as the reactant gasses are available.



The typical operating temperature range of an SOFC is from 600 °C to 900 °C. The heat liberated from exothermic reactions maintains this temperature enabling SOFCs to be thermally self-sustained^[1]. Further, as a result of high operating temperature, the water produced at the anode comes out as heated steam. The use of this steam for district heating or to generate further electricity with suitable bottoming cycles, such as steam turbines or gas turbines, enables the overall efficiency of a stack to reach as high as 80%^{[2][3]}.

The underlying chemical reactions involved in SOFC operation appear very simple. However, some stringent operational and material characteristic requirements arise for individual component when building fuel cells for commercial applications. Researchers have been striving over decades to make SOFC an economically viable and technically feasible green energy conversion technology to cater to the ever-growing energy demands. Although such efforts have yielded a great success, many challenges still remain to be addressed.

2.1.2 Fuel Flexibility

Fuel flexibility refers to the ability of an SOFC to operate on fuels other than pure hydrogen. This is a distinct feature granted from the high operating temperature. Because of high operating temperature, hydrocarbons can be directly reformed on the anode making SOFC flexible on fuels. Further, while low-temperature fuel cells are highly sensitive to carbon monoxide, SOFC can use carbon monoxide itself as a fuel^[4]. Some research evidences, briefly discussed below, show the excellent fuel flexibility that SOFC can offer.

Numerous evidences in the literature reveal the ability of SOFC in operating on light and heavy hydrocarbons. While the interest on biodiesel is being sparked out in recent decades, SOFC also has shown promising performances running on biodiesel.

Nahar and Kendall^[5] have demonstrated biodiesel on an SOFC that operated at 800 °C. The SOFC has produced an open circuit voltage of 0.95-1 V and peak power density of 0.1564 W/cm². Meanwhile, Liu and Barnett^[6] claim to have recorded a power density as high as 0.96 W/cm² when using methane in a conventional SOFC at 800 °C. Gorte *et al*^[7] also claim to have developed a novel anode that can directly use hydrocarbons as fuels. Other efforts on using synthetic diesel^[8] and waste cooking oil^[9] as fuels are also recorded in literature. Moreover, Zhou *et al*^[10] claim to have demonstrated Copper-Ceria based SOFC with a power density of approximately 0.1 W/cm² that utilised Pennsylvania crude oil and jet fuel, which contained sulphur up to 910 ppm. However, the use of sulphur containing fuels could damage the cells and may cause degradation.

The arrangement of widespread hydrogen infrastructure network and efficient production of hydrogen through an environmentally friendly process, such as water splitting from renewable electricity, is a long term futuristic mission. Until such facilities are properly arranged, the efficient use of existing fossil fuel resources is an essential requirement for which SOFC can cater with its fuel flexibility.

2.1.3 Cell / Stack Configurations

The solid state of cell components gives designers abandon choices in determining the cell and stack geometry. However, because the other practical aspects, such as fabrication constraints, sealing, etc. limit the degree of freedom; currently, there are only five basic cell configurations in use: tubular, planar (or flat plate), bell & spigot, corrugated, and banded cells^[11]. The tubular and planar designs have been the basis for most of the research and development activities available in the literature. Complexity and the resulting excessive fabrication costs of stacks might have made the other designs relatively unpopular despite their some key advantages. For example, the corrugated design has relatively higher power density due to its compact shape, but it is difficult to fabricate.

Cell arrangements are broadly categorised based on the supporting mechanism as self-supporting and external supporting. Self-supporting structures, schematically shown in Figure 2.2, have one cell component made larger to provide sufficient mechanical strength, and it supports the other two components. The Electrolyte support structure is relatively robust. However, due to increased ohmic resistance with increased electrolyte thickness, this design is less attractive. The anode or the cathode support arrangements give the flexibility to make electrolyte as thin as possible. The external supporting

configuration, on the other hand, provides the flexibility to make all three cell components as thin as required. In this configuration, all cell components are externally supported on the interconnect or a porous substrate as schematically shown in Figure 2.3.

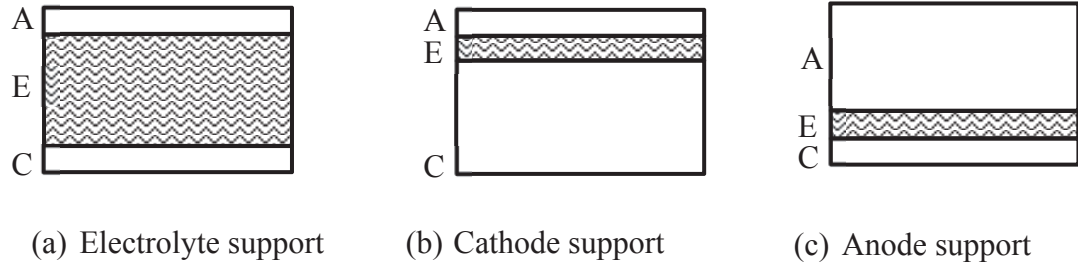


Figure 2.2 Self-support structures

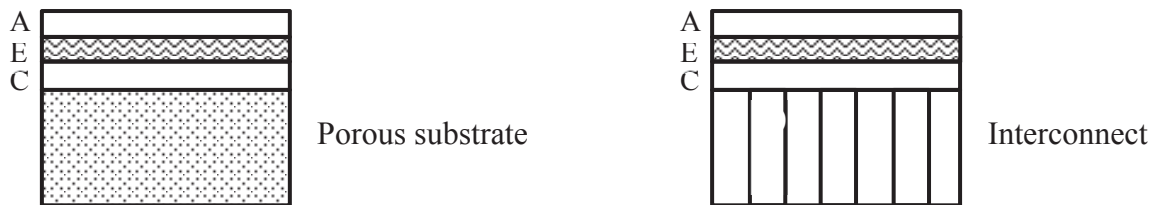


Figure 2.3 External-support structures

2.1.3.1 Stack Configurations

A stack is an arrangement that is formed by bundling cells together in electrical series or parallel to cumulate the power produced from cells. There can be as small as a couple of cells or as large as a few hundreds of cells in a stack. Four major stack configurations could be found from literature: tubular, planar (or flat plate), segmented in series, and monolithic design^[12]. Figure 2.4 shows a different cell design called flat tubular. This is an exclusive design that Siemens Westinghouse Power Corporation has

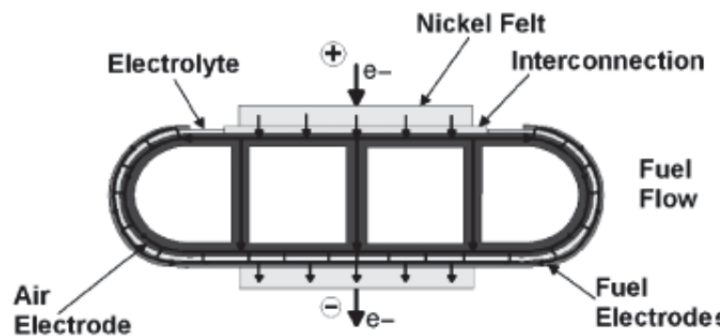


Figure 2.4 Cutaway of a flat tubular design^[13]

developed^[13]. This design merges the advantages of tubular and planar designs into a single cell (Reducing the sealing problem associated with planer designs is a key benefit of tubular design over planar design). Among these stack configurations, tubular design appears to be the most advanced technology while planar type design has gained significant attention due to its higher power density, compact design, and relatively lower operating temperature than the tubular designs.

Monolithic stack design, shown in Figure 2.5, is based on corrugated cell shapes where the electrolyte is most commonly the supporting structure. These are fabricated using tape casting and hot roll calendaring. Matching the shrinkage behaviour of electrodes, electrolyte, and interconnect is considered as the primary challenge in fabrication^[14]. This design can have power density as high as 2.5 W/cm^2 and it is a unique advantage over other designs. Further, short ionic paths through the electrolyte, electrodes, and interconnect reduces the ohmic polarisation loss. However, complexity in the structure has confined the development of monolithic fuel cells to laboratory scales, and no commercial applications have been reported to the author's best knowledge.

Segmented-in-series stacks consist of cells arranged in electrical series or gas flow series. Bell & Spigot cells and banded cells are the primary building blocks for this

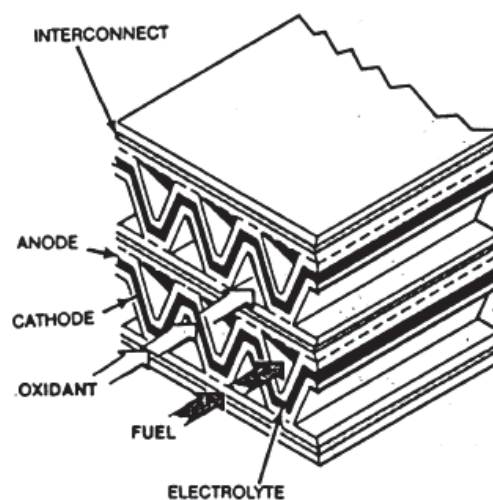


Figure 2.5 Monolithic SOFC design^[14]

architecture as shown in Figure 2.6. Cells are arranged in thin banded structures supported on a porous substrate (external supporting) or fitted one into the other forming tubular self-supporting structure; usually, electrolyte supported. A significant advantage of segmented in series design is its high efficiency compared with large area single cell configurations in other designs. However, factors such as relatively high ohmic losses,

requirements of high-temperature gas-tight seals, and complexity in fabrication have limited the widespread use of this design.

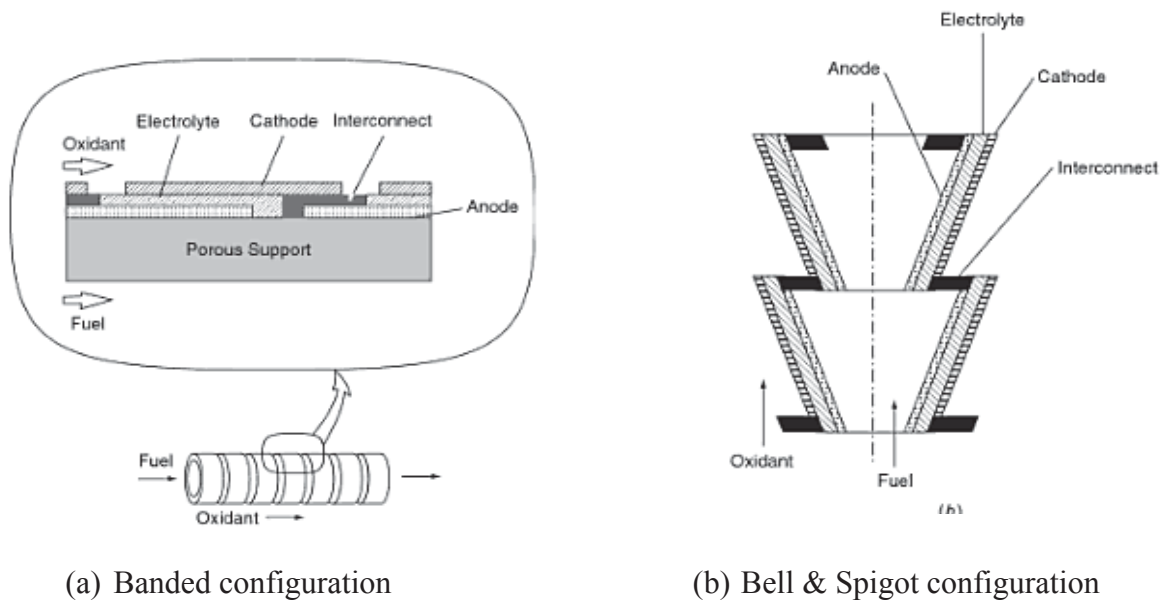


Figure 2.6 Segmented in series design^[15]

In a tubular stack, the tubular cells are bundled together as shown in Figure 2.7. Individual cells are usually cathode supported and closed at one end; like a test tube. Thus, this arrangement eliminates the need of high-temperature sealing, which is one of the major advantages of tubular cell/ stack design. However, the formation of large voids between cells in forming stacks reduces the power density of these stacks. Further, much longer current carrying paths result in higher ohmic polarisation. Fabrication of tubular cells is also more complicated than the planar cells. The innermost layer, usually the cathode, is first fabricated by extrusion and then sintered. The cathode has a porosity of approximately 30%-40% to allow reactants (air) to reach electrolyte efficiently. Electrolyte (usually made of YSZ¹) is applied on the cathode using electrochemical vapour deposition (EVD) techniques. Finally, the anode is electrochemically deposited over the electrolyte. Although, the high cost of fabrication and low power density are key problems, tubular SOFC are much closer to commercialisation with thousands of hours of successful demonstrations.

¹ Yttrium stabilised zirconia

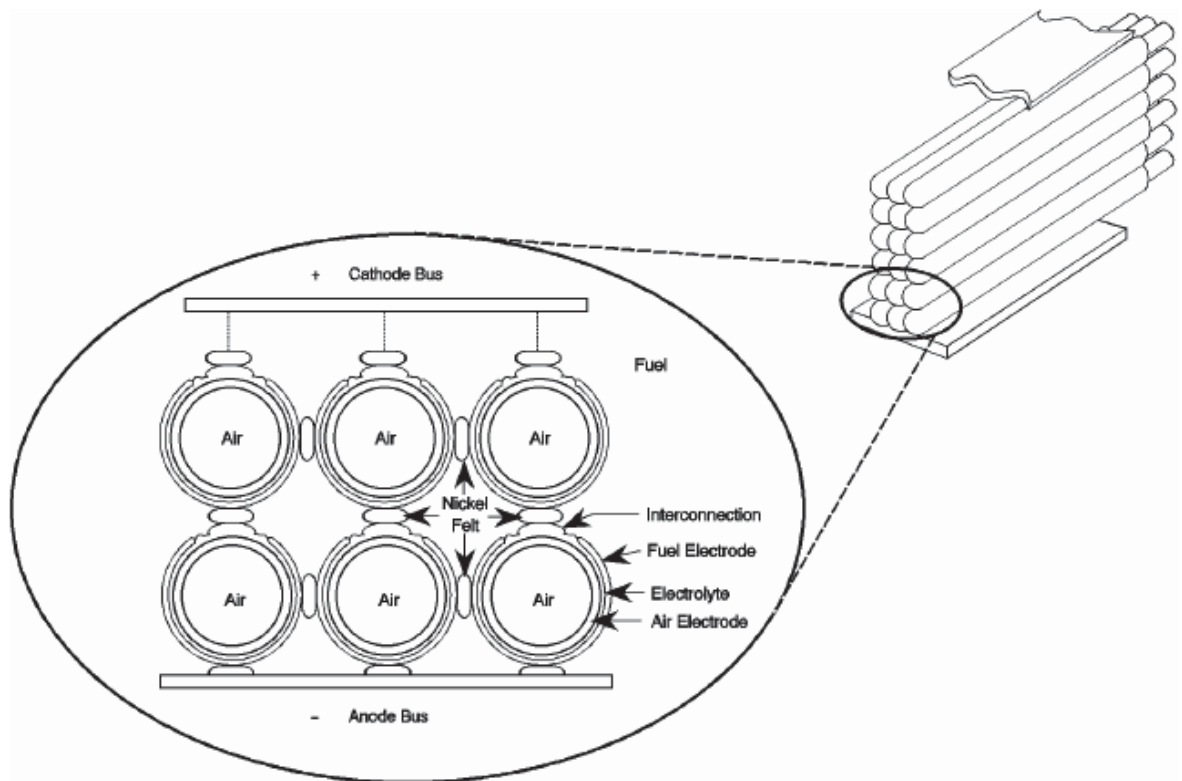


Figure 2.7 Tubular SOFC stack^[16]

The planar SOFC design has gained a growing interest in the research community. The promises it gives to reduce the operating temperature, highly compact design with increased power density, and the simplicity of fabrication can be considered as primary motives behind its growing popularity. These cells can easily be made from tape casting followed by sintering. Planar designs are mainly made as interconnect support or anode support structures giving the flexibility to make the electrolyte as thin as possible to help decrease the operating temperature. Figure 2.8 shows a schematic diagram of the recurring unit of a planar SOFC stack. Despite all its advantages, factors such as obtaining high-temperature gas tight sealing and cell degradation are the key challenges that need extensive investigations and improvements.

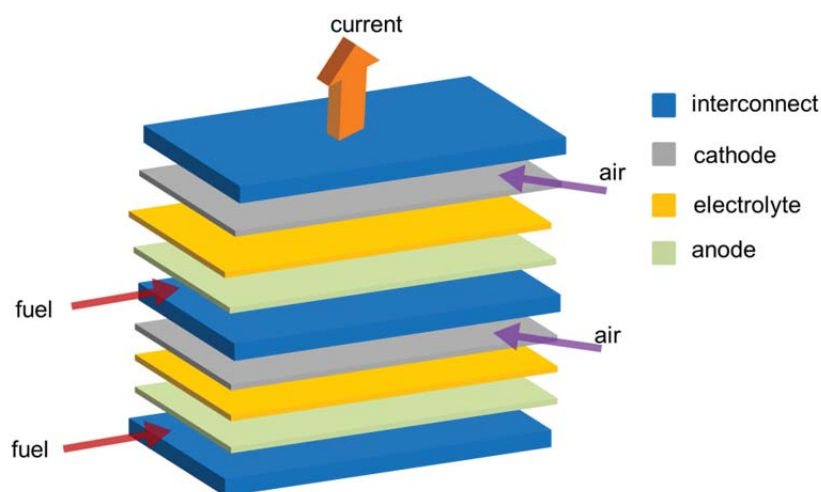


Figure 2.8 A schematic diagram of a planar SOFC stack

2.1.4 Major Components of a Cell

Each cell consists of three essential components for its electrochemical operation: anode, cathode, and electrolyte. The other critical component, though not a part of a cell, is the interconnect. The interconnect connects cells together when forming a stack. Each cell component possesses a particular set of unique characteristics that enables them to perform its intended operation. All components must be chemically and mechanically stable under the highly reducing and oxidising environment inside an SOFC at its operating temperatures. Further, all cell components must demonstrate matching thermal expansion with each other to prevent thermal cracking and delamination of layers. The cost of materials and fabrication are also, undoubtedly, essential factors. Following section briefly describes the key features of cell components and interconnects.

2.1.4.1 Electrolyte

The electrolyte must facilitate efficient transport of ions between the electrodes (usually, oxygen ions from the cathode to the anode). It must also resist the electron transfer to prevent the two electrodes being short-circuited through the electrolyte. Thus, the electrolyte material must demonstrate excellent ionic conductivity while showing extremely poor electronic conductivity. Further, it must be able to fabricate as a thin layer to reduce ohmic resistance to ionic conduction. However, despite how thin it is, the layer must be dense enough to prevent any gas cross-overs between the anode and the cathode. Although there are a number of electrolyte materials being researched, yttria stabilised zirconia (YSZ) has been the most favoured electrolyte material. It has a good oxygen ion conductivity and high resistance to electron transfer.

Chemical composition determines the conduction characteristics and mechanical strength of YSZ. While yttria (Y_2O_3) stabilises the cubic fluorite phase of zirconia, it enhances the ionic conductivity through the introduction of oxygen vacancies to the lattice structure. Further, it helps to decrease the electronic conduction. Dixon *et al*^[17] have evaluated the electrical resistivity of hot pressed and sintered YSZ samples with yttria contents (mole) 10%, 15%, 20%, and 30%. Their results show an increase in resistivity with the increase of yttria content within the temperature from 600 °C – 1,000 °C. However, the ionic conductivity peaks around 8% Y_2O_3 as shown in Figure 2.9. In addition to yttria content, the conductivity of YSZ also depends on the microstructure^{[18]-[20]}. Since microstructure is affected by the sintering temperature, the ionic conductivity varies with sintering temperature as shown in Figure 2.10

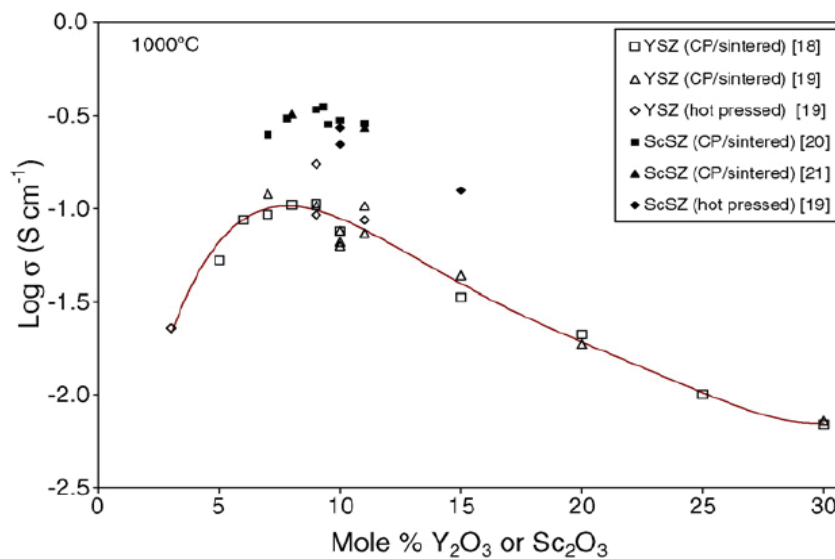


Figure 2.9 Ionic conductivity of yttria stabilised zirconia with varying dopant composition^[21]

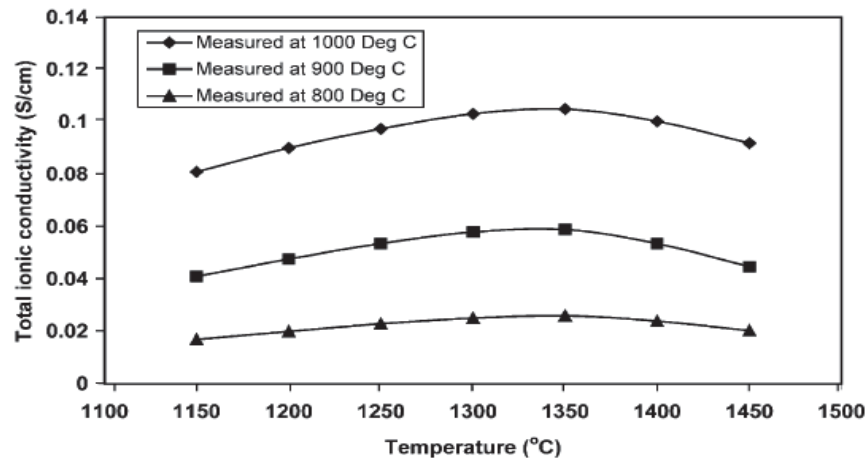


Figure 2.10 The change of ionic conductivity with respect to sintering temperature^[18]

The mechanical strength is also a crucial parameter, particularly, for electrolyte-supported cells. Table 2.1 shows the variation of ionic conductivity and mechanical strength of YSZ with varying yttria content. Two types of YSZ electrolytes are commonly used: one with 8% by mole yttria content (8YSZ) and the other with 3% by mole yttria content (3YSZ). Among them, 8YSZ has the greatest ionic conductivity while 3YSZ is the mechanically strongest.

Table 2.1 Properties of yttria stabilised zirconia^[5]

Electrolyte	Conductivity at 1,000 °C (S/cm)		Bending strength (MPa)	Thermal exp. coefficient (1/K × 10 ⁻⁶)
	As sintered	After annealing		
ZrO ₂ – 3mol% Y ₂ O ₃	0.059	0.050	1200	10.8
ZrO ₂ – 3mol% Yb ₂ O ₃	0.063	0.09		
ZrO ₂ – 2.9mol% Sc ₂ O ₃	0.09	0.063		
ZrO ₂ – 8mol% Y ₂ O ₃	0.13	0.09	230	10.5
ZrO ₂ – 9mol% Y ₂ O ₃	0.13	0.12		
ZrO ₂ – 8mol% Yb ₂ O ₃	0.20	0.15		
ZrO ₂ – 10mol% Yb ₂ O ₃	0.15	0.15		
ZrO ₂ – 8mol% Sc ₂ O ₃	0.30	0.12	270	10.7
ZrO ₂ – 11mol% Sc ₂ O ₃	0.30	0.30	255	10.0

YSZ possess a number of advantages to qualifying as an electrolyte material. The abundance of zirconia on Earth's crust makes YSZ very economical material to use. Its chemical stability and non-toxicity are two more advantages. However, the high thermal expansion coefficient and requiring high temperatures to demonstrate sufficiently higher ionic conductivity with low electronic conductivity are two significant drawbacks. This

prevents SOFCs being operated at low temperatures. Thus, a number of research efforts have been made to develop alternative electrolyte materials to enable low-temperature operation of SOFCs.

Among different types of alternative electrolyte materials, scandia stabilised zirconia (ScSZ) is one of the key materials being investigated for electrolyte^{[23]-[26]}. ScSZ has a better ionic conductivity than 8YSZ^[27]. Cerium gadolinium oxide (CGO) (ceria is the based material, and gadolinium is the dopant) also appears to be a promising material. CGO with 10 mole% gadolinium has shown better ionic conductivity and lower polarisation loss than YSZ at temperatures below 600 °C^[28]. Further, power density with CGO is higher than YSZ based fuel cell. Hence, Ceria appears to be a competitive choice for electrolytes, particularly, when lower operating temperature and higher power density are the primary concerns. However, higher electronic conductivity at lower oxygen partial pressures remains as a significant disadvantage and a challenge with CGO. Lanthanum strontium gallate magnesium (LSGM) is also another material being investigated for the electrolyte, particularly, for low and intermediate temperature SOFC with high performance^{[29][30]}. Table 2.2 summarises the advantages and disadvantages of 4 electrolyte materials discussed. However, despite all developments on alternative electrolyte materials, YSZ remains as the preferable choice for wide range of SOFC development works.

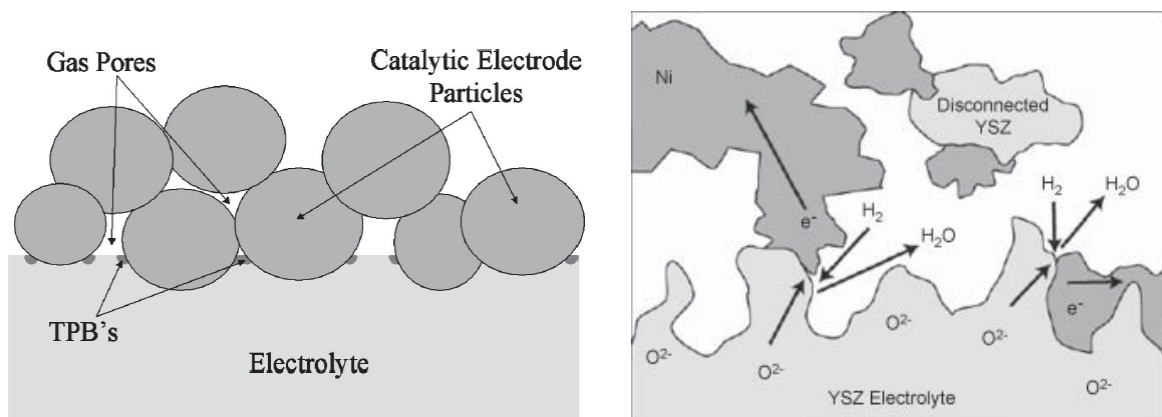
Table 2.2 Advantages and disadvantages of different electrolyte materials^[31]

YSZ	CGO	LSGM	ScSZ
Excellent stability in oxidising and reducing environments Excellent mechanical stability High quality raw materials available Low ionic conductivity Incompatibility with some cathode materials	Good compatibility with cathode materials Mechanical stability Electronic conductivity at low oxygen partial pressures	Good compatibility with cathode materials. Mechanical stability Ga evaporation at low oxygen partial pressures Incompatible with NiO	Excellent stability in oxidising and reducing environments Better long term stability than 8YSZ Less availability and high price

Since no alternative material is yet able to replace YSZ entirely, an alternative approach to reducing operating temperature is reducing the electrolyte thickness. Conventional electrolyte thickness is in the range 100 -200 μm while thin film electrolyte technology is targeting to reduce this thickness to few micrometres or even to nanometre scale^{[32]-[35]}. Tsuchiya *et al* claim to have developed the first fully functional and scalable nano-scale SOFC having 10 nm thick YSZ electrolyte^[36]. This cell is said to be capable of producing 155 mW cm^{-2} of power density at 510 $^{\circ}\text{C}$ and total power output of 20 mW. This is a remarkable achievement and might be a key milestone in fuel cell technology. However, it might need further extensive research to bring this technology to the commercial stage.

2.1.4.2 Electrodes

Electrodes (anode and cathode) are the chemically most active components of a fuel cell. Unlike the electrolyte, which must be highly dense to prevent reactant crossover, the electrodes must be porous to enable gas diffusion (oxygen and fuel gases). Redox reactions occur in areas called as Triple Phase Boundary (TPB). TPB is an area where the electrolyte material, electrode material, and gasses meet hence, forming three phases. Thus, these are essentially located in pores. Figure 2.11 (a) shows a simplified schematic diagram of a TPB. In this diagram, the TPB is confined to the electrode-electrolyte interface; thus, reaction sites are confined to a very small area. The introduction of electrolyte material into the electrodes can significantly increase the reaction sites by extending TPBs. Figure 2.11 (b) shows such an arrangement where the electrolyte



(a) Triple phase boundary TPB^[37]

(b) Enhanced TPB area by introducing electrolyte into anode^[38]

Figure 2.11 Triple Phase Boundary (TPB) and TPB enhancement

material (YSZ) is introduced into the anode. The enhancement of reaction sites by this method generates more room for reactions to take place.

In general, an electrode must demonstrate mixed ionic and electronic conductivity. An excellent electronic conductivity permits the passage of electrons from the anode to the cathode with low ohmic losses. A good ionic conductivity facilitates efficient transport of ions into the reaction sites reducing the polarisation losses. The following sections describe the anode and the cathode specific characteristics.

Anode

The primary function of the anode is fuel oxidation; hence, it must have a higher electro-catalytic activity to facilitate rapid fuel oxidation with minimum overpotential. Catalytic activity towards hydrocarbon reforming is a preferable supplementary characteristic that enables direct internal reforming of hydrocarbons on the anode.

A cermet of Ni and YSZ (usually written as Ni/YSZ) is the most commonly used SOFC anode material for high-temperature SOFC. Nickel facilitates efficient transport of electrons from reaction sites to the current collector (the device that collects current from electrodes). YSZ incorporates the necessary ionic conductivity into the anode and inhibit Ni sintering, and helps to match the thermal expansion coefficient of the anode to the electrolyte. Ni/YSZ possesses several key advantages: higher chemical stability, compatible thermal expansion coefficient with electrolyte, excellent hydrogen oxidation capacity, and low cost.

Nickel has a vital role in the anode's performance and economy. Apart from being the electrical conduction agent, it is an excellent reforming catalyst and electrocatalyst for electrochemical oxidation of hydrogen. Therefore, the need of expensive platinum catalyst is eliminated making anodes more economically viable. Figure 2.12 shows the variation of electrical conductivity as a function of the volumetric composition of Ni. A dramatic increase in electrical conductivity is evident when the volumetric Ni composition changes from 20% to 40%. Although the increase of Ni content increases the electrical conductivity, it reduces the thermal expansion compatibility with the electrolyte. Further, Ni agglomeration may occur at higher Ni content, reducing the TPB. Thus, usually, Ni content is maintained around 30% by volume.

Apart from nickel content, the electrical conductivity of the anode also depends on the YSZ particle size where larger particles promote better conductivity as shown in Figure 2.13. Coarse YSZ particles promote better Ni to Ni particle contact and thereby increase electron transfer paths. However, larger YSZ particles have detrimental effects on the porosity.

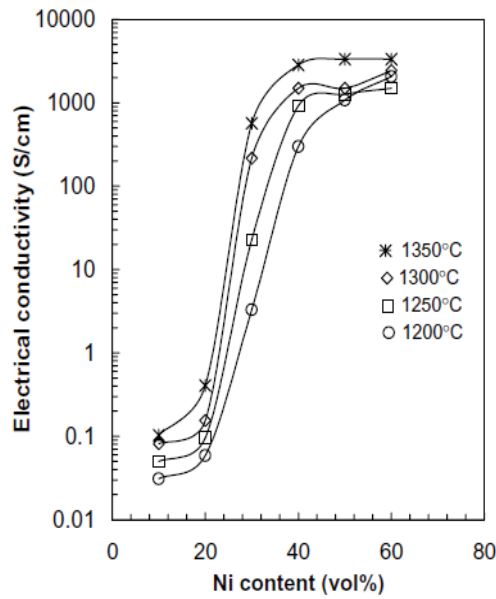


Figure 2.12 Change of conductivity with Ni content in Ni/YSZ^[39]

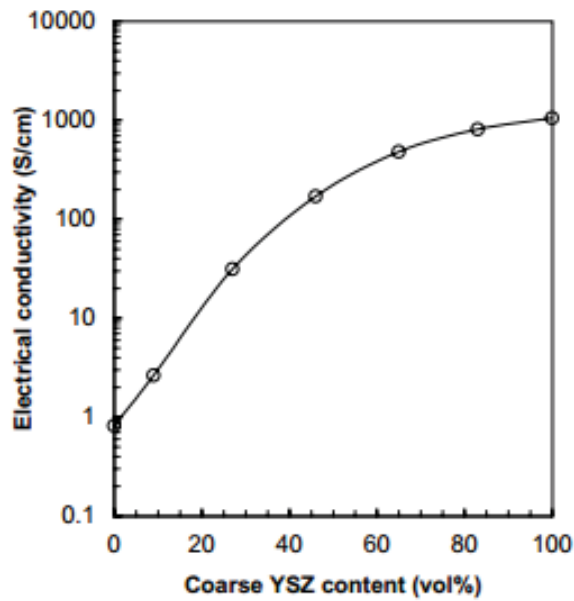


Figure 2.13 Enhancement of electrical conductivity with increase of coarse YSZ content^[39]

The anode must maintain sufficient porosity to enable fuel to reach reaction sites; usually, 20% - 40% porosity is maintained^[40]. The porosity is obtained by reducing NiO to Ni by firing in a hydrogen atmosphere. Once the anode is sintered, it is exposed to H₂ at 800 °C or above to reduce NiO into Ni^[41]. Formation of porosity can be clearly seen from Figure 2.14, which shows optical micrograph images before and after firing a cermet containing 30% Ni by volume. The dark areas show the porous regions.

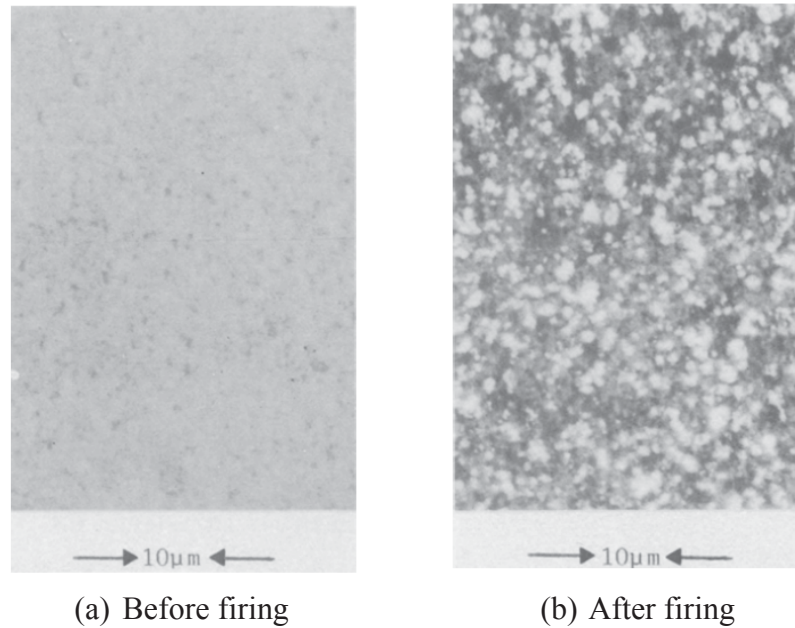


Figure 2.14 Optical micrograph images taken before and after firing a cermet containing 30% Ni by volume^[41]

Amidst a number of advantages of Ni/YSZ as an anode material, sulphur poisoning, particularly at low temperatures, is a major problem^[42]. Carbon coking is also an issue when hydrocarbons are reformed internally on the anode. However, despite attempts on developing various other anode materials, Ni/YSZ remains as the strongest candidate material for the anode in high-temperature SOFCs, which this research is based on.

Cathode

The cathode is where oxygen reduction process takes place, and it is known to be the predominant source of activation polarisation loss in SOFCs due to its lower reaction kinetics. In fact, it is considered as the reaction rate determining component of SOFC. Thus, the performance of cathode is very critical to the overall operation/ efficiency of an SOFC.

Among the many different cathode materials developed, lanthanum strontium manganite (LSM) has been the most widely employed material with YSZ electrolytes. LSM has very low chemical reactivity with YSZ making it chemically stable with YSZ electrolytes. However, the poor ionic conductivity of LSM confines the electrochemically active regions into TPB. Therefore, composites of LSM and YSZ are being used to enhance the ionic conductivity and thereby increasing the TPB. In addition to YSZ, substitution of some manganese with cobalt found to improve the ionic conductivity significantly^[43]. However, cobalt composition needs to be carefully controlled; otherwise, the thermal expansion mismatch between the cathode and the electrolyte will introduce a significant level of stresses across themselves, and may lead to a mechanical failure.

Although choices of the cathode materials for high-temperature SOFC are limited, there is a range of alternative materials for intermediate temperature SOFCs. Lanthanum strontium ferrite (LSF), lanthanum strontium cobalt ferrite (LSCF), lanthanum strontium manganese ferrite (LSMF), praseodymium strontium manganite (PSM), and praseodymium strontium manganese ferrite (PSMF) are some examples.

Chromium poisoning of the cathode is a significant problem when the interconnect materials contain chromium. Chromium evaporates from the interconnect and reacts with Sr forming SrCrO_4 (strontium chromate). The deposition of SrCrO_4 covers reaction sites and significantly hinders the oxygen reduction process. Further, the high thermal expansion coefficient of SrCrO_4 leads thermal incompatibilities between the electrolyte and the cathode generating significant interfacial stresses.

2.1.4.3 Interconnects

Interconnect is not a component of a cell, but an essential component in a stack. It plays the vital role of connecting individual cells to form a stack. Interconnect should meet certain requirements in order to fulfil its role:

- Excellent electrical conductivity
- Chemical and mechanical stability (including dimensional stability) throughout the entire operating temperature range
- Matching thermal expansion coefficients with the other cell components
- No reaction or diffusion with the adjacent cell components
- Low cost, durability, and easily manufacturability

The most common interconnect material for high-temperature SOFC is lanthanum chromite (LaCrO_3), which is a conductive ceramic. This demonstrates a remarkable electronic conductivity around 1,000 °C. Its matching thermal expansion coefficient with the rest of the cell component is an added advantage. However, chromium vapour emitted at higher operating temperatures is a significant drawback.

2.2 Fundamental Sciences

Electrochemistry and thermodynamics are the key fundamental sciences that help better understanding of the performance of an SOFC. Therefore, an overview of the electrochemical and thermodynamics aspects associated with the operation of SOFCs is presented in this section. Since hydrogen is the primary fuel for SOFC though, carbon monoxide also can serve as a fuel; the following discussion considers hydrogen as the fuel.

When the fuel cell is in operation, hydrogen and oxygen react with each other producing water following the stoichiometric reaction given in Equation (2.4). The enthalpy of formation of water is released from this reaction and, this energy is converted into electricity and heat. However, the more useful quantity of energy with respect to SOFC is the Gibbs free energy because not all the enthalpy is converted to electricity. Gibbs free energy is the maximum amount of energy available to get a useful work output from a fuel cell under constant pressure and temperature; thus, this is the reversible work output from a fuel cell under constant pressure and constant temperature. Although temperature varies within an SOFC, the assumption of constant temperature is a sufficiently accurate assumption to analyse the performance theoretically. The change of Gibbs free energy of a thermodynamic system can be expressed as Equation (2.5) where, ΔG , ΔH , and ΔS are the changes in Gibbs free energy, enthalpy, and entropy, respectively; T is the absolute temperature. The change of Gibbs free energy associated with the reaction in Equation (2.4) can be calculated from Equation (2.6) where, ΔG_{fH_2O} , ΔG_{fH_2} , and ΔG_{fO_2} are the Gibbs free energy of formation of water, hydrogen, and oxygen, respectively. A more useful form of expressing the change of Gibbs free energy is showing it in molar basis as given in Equation (2.7). Since only half mole of oxygen is involved in the stoichiometric reaction, only half of the Gibbs free energy of formation of oxygen is counted. In general, when any other fuel is used, the respective Gibbs free energy can be calculated by subtracting the Gibbs free energy of formation of reactants from that of product(s). It is important to notice that the Gibbs free energy is theoretically the maximum amount of work that can be extracted from a fuel cell. However, in practice, due to various losses and thermodynamic irreversibilities associated with fuel cell operation, the practical work output from a fuel cell is lower than the Gibbs free energy.



$$\Delta G = \Delta H - T\Delta S \quad (2.5)$$

$$\Delta G = \Delta G_{fH_2O} - (\Delta G_{fH_2} + \Delta G_{fO_2}) \quad (2.6)$$

$$\Delta \bar{g} = \Delta \bar{g}_{fH_2O} - \left(\Delta \bar{g}_{fH_2} + \frac{1}{2} \Delta \bar{g}_{fO_2} \right) \quad (2.7)$$

Where,

$\Delta \bar{g}$ – Change of molar Gibbs free energy of the reaction

$\Delta \bar{g}_{fH_2O}$ – Change of molar Gibbs free energy of formation of water

$\Delta \bar{g}_{fH_2}$ – Change of molar Gibbs free energy in formation of hydrogen

$\Delta \bar{g}_{fO_2}$ – Change of molar Gibbs free energy of formation of oxygen

In general, the Gibbs free energy determines the spontaneity of a chemical reaction where, a negative change implies a spontaneous reaction, zero change implies equilibrium and a positive change means a non-spontaneous reaction.

2.2.1 Reversible Cell Voltage

The reversible cell voltage is the maximum voltage a cell can produce. As the name implies, this voltage is generated only when the cell is operating in a reversible manner, which is impossible to expect in reality due to unavoidable irreversibilities, such as ohmic losses, activation losses, concentration losses, and heat transfer associated with a fuel cell. A fuel cell produces its reversible cell voltage only when the entire Gibbs free energy is converted to electrical energy. Each molecule of hydrogen gas releases two electrons as per the anodic half-cell reaction given in Equation (2.8). Thus, each mole of hydrogen produces $-2Ne$ coulombs charge where N is the Avogadro number and e is the magnitude of the charge of an electron. Alternatively, the amount of charge transfer through the external circuit per mole of hydrogen can be expressed as $-2F$ where F is the Faraday constant.



Since the amount of work done when a charge flows across a potential gradient is the product of charge and the potential difference (charge \times potential difference); if the reversible cell voltage is E , the electrical work done when a mole of hydrogen is reacted in a fuel cell can be expressed as:

$$\text{Electrical work done} = -2FE$$

When the fuel cell operates reversibility (thus, with no loss), the total amount of Gibbs free energy is converted to electricity. Thus, the electrical work done is equal to the Gibbs free energy. Thus,

$$\Delta \bar{g} = -2FE$$

$$\text{reversible cell voltage, } E = -\frac{\Delta \bar{g}}{2F} \quad (2.9)$$

It is important that Equation (2.9) was derived considering hydrogen as the fuel; thus, releasing two electrons per each molecule of hydrogen. Hence, the equation is valid in this form only for hydrogen. However, replacing the number two in Equation (2.9) with the actual number of electrons released per mole of fuel, the same equation can be used to calculate the reversible cell voltage with any other fuel type.

Equation (2.9) shows that the reversible cell voltage is directly proportional to the Gibbs free energy of the chemical reaction concerned. Gibbs free energy depends on factors such as temperature, pressure, and the reactant concentration. Thus, to calculate the reversible cell voltage using this equation the values of the Gibbs free energy under all operating conditions of a fuel cell must be known. This is not practically convenient or perhaps, impossible. The Nernst potential defined in Equation (2.10) solves this problem and enables calculating the reversible cell voltage under different operating conditions while having to know only the Gibbs free energy at the standard pressure and temperature.

$$E = E^0 + \frac{RT}{2F} \ln \left(\frac{P_{H_2} \cdot P_{O_2}^{\frac{1}{2}}}{P_{H_2O}} \right) \quad (2.10)$$

E – Reversible cell voltage at a given temperature and pressures

E^0 - Reversible cell voltage at standard pressure and temperature

P_x - Partial pressure of the constituent x where, x stands for H_2O , O_2 , and H_2

T – Absolute temperature of the system

R – Universal gas constant

F – Faraday constant

All the partial pressures must be substituted in the unit of bar to this equation (this constraint comes from the simplification of the equation into this form). The reversible cell voltage under standard and pressure and temperature can be calculated by substituting the Gibbs free energy at standard pressure and temperature to Equation (2.9). In order to apply Equation (2.10) for fuels other than hydrogen, the number two in the denominator

must be replaced by the number of electrons released per molecule of the fuel. The Nernst equation assumes ideal gas behaviour for both the products and the reactants.

Although the Nernst equation may appear to suggest increasing the reversible cell voltage with the increase of temperature (because of the positive proportionality of E with T in Equation (2.10)), in fact, the reversible cell voltage decreases with an increase of the temperature. This is because the Gibbs free energy decreases (positively increase), more aggressively with the increase of temperature than the positive linear proportionality of temperature with the reversible cell voltage as depicted in the Nernst equation. In other words, the decrease of E^0 is more prominent than the increase of the remaining term with temperature. The temperature effect on the Gibbs free energy is expressed by the Gibbs-Helmholtz equation given in Equation (2.11). Thus, although Nernst equation comprehensively demonstrates the effects of concentration and pressure on the cell voltage, it is less comprehensive in showing the effect of temperature on the cell voltage.

$$\left(\frac{\partial(\frac{G}{T})}{\partial T} \right)_P = -\frac{H}{T^2} \quad (2.11)$$

The Nernst potential decreases with the increase of temperature suggesting that lower operating temperatures are preferable to higher temperatures. However, there are temperature-dependent losses in practical SOFCs, which are more prominent at low temperatures (discussed next). These losses contribute to reducing the practical cell voltage at low operating temperatures unless suitable measures are taken to mitigate these losses at low temperatures, such as new material developments. Therefore, despite the theoretical suggestion to operate at lower temperatures, SOFCs operate at higher temperatures to reduce losses. Further, SOFCs operating at higher temperatures produce high-temperature steam, which can be further utilised in suitable bottoming cycles to produce more electricity. Thus, enabling the overall plant efficiency to reach higher values than the other fuel cell types cannot achieve.

2.2.2 Losses in Cell Voltage

The Nernst potential calculated in the previous section considered a reversible operation of the SOFC. However, in practice, SOFCs, like any other systems, are associated with irreversibilities that cause a drop of practical cell voltage below the ideal Nernst potential. There are three primary sources of voltage loss in SOFC, known as polarisations: activation polarisation, ohmic polarisation, and concentration polarisation.

Figure 2.15 shows a typical polarisation curve indicating the dominance of different polarisation mechanisms at various current densities.

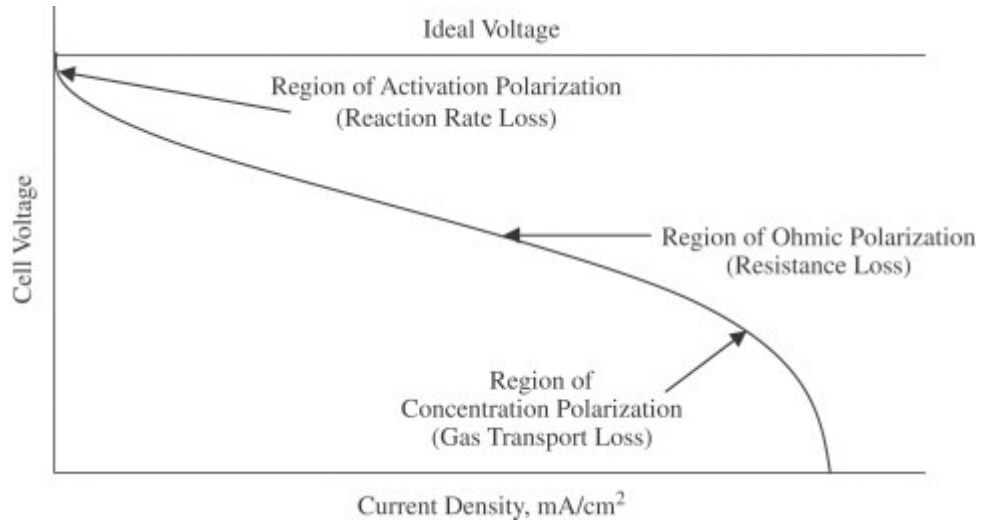


Figure 2.15 A typical polarization curve^[44]

2.2.2.1 Ohmic Polarisation

This is a prominent loss in SOFC caused by the resistance to electron and ion transfer within a fuel cell. The resistance to ionic conduction lies mainly within the electrolyte, and the resistance to electronic conduction lies primarily within the electrodes and interconnects. The electrodes and interconnect materials are relatively good current conductors whereas; the electrolyte has relatively higher resistance to ionic conduction. Thus, the ohmic polarisation is more dominant in the electrolyte. This is, in fact, why the attempts are made, whenever possible, to make the electrolyte as thin as possible. Further, the ionic conductivity of electrolyte (usually, made of YSZ) is low at low temperatures thus, requiring SOFCs to operate at higher temperatures to minimize the ohmic polarisation. As the name implies, ohmic polarization obeys the Ohms law and, the voltage drop can be expressed as Equation (2.12), where, Δv_{Ohmic} , i , and R are the voltage drop, current density, and the electrical resistance, respectively. The losses in the middle region of the polarization curve (Figure 2.15), where the cell operates with moderate current densities, is the area in which the ohmic polarisation is dominant.

$$\Delta v_{Ohmic} = iR \quad (2.12)$$

2.2.2.2 Activation Polarisation

The activation polarization is due to the inherent energy barrier in chemical reactions, which must be overcome by reaction species. Thus, the activation polarization occurs at the electrodes and, its severity depends on the degree of chemical reactivity of the electrode. Hence, catalytically highly active electrodes have less activation polarisation, and catalytically less active electrodes have higher activation polarisation. The activation polarization depends on various factors such as the nature of electrode material, ion-ion interaction, and electric double layer. This loss can be minimized by using more efficient catalysts, increasing the temperature, increasing the active area of the electrode, increasing reactant concentration, and increasing the pressure. In SOFC, due to the high reactivity of the anode, the activation polarisation at the anode is much lower than that at the cathode. In general, activation polarisation is low in SOFC due to high operating temperature because the reduction and oxidation reactions at the cathode and the anode, respectively, are more favoured at higher temperatures than at lower temperatures. A very comprehensive correlation between the activation polarisation and the current density is predicted by Butler-Volmer equation given in Equation (2.13).

$$i = i_0 \left\{ e^{\beta \frac{n_e F \eta_{act}}{RT}} - e^{-(1-\beta) \frac{n_e F \eta_{act}}{RT}} \right\} \quad (2.13)$$

Where;

i – Current density

i_0 – Exchange current density

η_{act} – Activation polarisation

R – Universal gas constant

T – Absolute temperature

β – Transfer coefficient (usually, ranges from about 0.2 to 0.5 for most electrochemical reactions)

n_e – Number of electrons involved per mole of fuel

Tafel equation given in Equation (2.14) is a simplified version of Butler-Volmer equation for higher current densities. Although the activation polarisation, as per the Tafel equation, appears to be directly proportional to the temperature and causing to increase with the increase of temperature, in reality, it decreases with the increase in the

temperature. This is because the exchange current density more aggressively increases with the increase of temperature outweighing the increases resulted by the proportionality with the temperature.

$$\Delta v_{act} = \frac{RT}{\beta nF} \ln \left(\frac{i}{i_0} \right) \quad (2.14)$$

Δv_{act} – Activation polarisation

R – Universal gas constant

T – Absolute temperature

n – Number of electrons (with hydrogen, $n = 2$)

F – Faraday constant

β – Charge transfer coefficient

i – Current density

i_0 – Exchange current density

2.2.2.3 Concentration Polarisation

For the chemical reactions to take place at electrodes, the gaseous reactants (oxygen and hydrogen) need to diffuse through their respective electrodes into the reaction sites – the triple phase boundaries. Thus, the diffusion characteristics of reactants determine how fast those can reach the reaction sites. If the reactants cannot reach the reaction sites as quickly as they are consumed, the partial pressure of reactants drops near reaction sites. This, in turn, causes the cell voltage to drop as suggested by the Nernst equation. This voltage drop is known as the concentration polarisation. Although this phenomenon can happen at all current densities, because the fuel is consumed, concentration polarisation is more pronounced at higher current densities where the reactants are more rapidly consumed. The sharp voltage drop at higher current densities, as shown in Figure 2.15, is caused by the concentration polarisation. The concentration polarisation can be calculated from Equation (2.15). Apart from the ideal gas behaviour assumed in the Nernst equation, the derivation of this equation assumes that the pressure linearly drops with the increase of current density.

$$\Delta v_{con} = \frac{RT}{nF} \ln \left(1 - \frac{i}{i_l} \right) \quad (2.15)$$

Δv_{con} – Concentration polarisation

R – Universal gas constant

T – Absolute temperature

F – Faraday constant

n – Number of electrons per mole of reactant ($n=2$ for hydrogen and $n=4$ for oxygen)

i – Current density

i_l – Limiting current density

2.2.3 Practical Cell Voltage

Apart from the losses mentioned above, the voltage drop due to fuel crossover across the electrolyte is another critical loss in fuel cells. However, due to the solid phase of the electrolyte in SOFC, the probability of fuel crossover is low unless the electrolyte is defective. Thus, in general, fuel crossover loss is not considered significant in SOFC.

Considering the three losses, the practical cell voltage can be expressed as Equation (2.16) where, E and V are the reversible cell voltage (Nernst voltage) and the practical cell voltage, respectively. Δv_{ohmic} , Δv_{act} , Δv_{con} are the ohmic, activation, and concentration polarisation, respectively. It is evident from this equation that the practical cell voltage is lower than the Nernst voltage due to losses. Increasing the operating temperature is a way to reduce the ohmic losses by increasing the ionic conductivity of the electrolyte, and to reduce the activation polarisation. Thus, the practical cell voltage is higher at higher temperatures than at lower temperatures. However, this should not be confused with the Nernst potential, which decreases with increase in the temperature.

$$V = E - \Delta v_{ohmic} - \Delta v_{act} - \Delta v_{con} \quad (2.16)$$

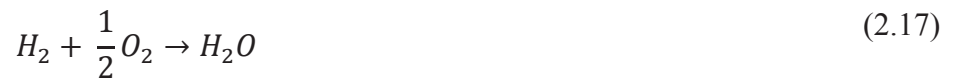
2.2.4 Degradation

Premature degradation of cells and stack is a significant problem in SOFC developments. Degradation is usually defined as the performance deterioration over time and mechanical failures such as crack formation and propagation. Mechanical failures commonly occur on cells and stack sealing. Degradation originates from a number of sources at cell and stack level. Cell level sources include, but not limited to: increase of electron transfer across YSZ electrolyte over time^[45], anode degradation such as nickel coarsening, the increase of ohmic resistance due to redox cycling, carbon coking^{[46]-[48]}, cathode degradation^{[49][50]}. Meanwhile, chromium poisoning of the cathode is a major stack level degradation mechanism^{[51][52]}. In addition to these various degradation mechanisms, the unavoidably high operating temperature itself is a primary source of degradation. However, the operating temperature is directly linked to the performance as well. This complicated nature the temperature is linked to the performance as well as with the degradation requires careful investigations into the role of the operating temperature on an SOFC's performance and durability.

2.3 Thermal Requirement and Management

2.3.1 The Thermodynamic Efficiency

The thermodynamic efficiency of a fuel cell is the ratio of the useful work output of the fuel cell to the energy input to the fuel cell. Thermal energy released by the electrochemical reaction of hydrogen and oxygen, given in Equation (2.17), is the enthalpy change associated with the reaction. However, not all this energy is converted into electricity because part of the energy is released as heat. Therefore, as discussed previously, the maximum work output (the reversible work output) from a fuel cell is the Gibbs free energy associated with this reaction at its operating temperature and pressure. Therefore, the maximum thermodynamic efficiency can be expressed as Equation (2.18).



$$\eta_{th} = \frac{\Delta G}{\Delta H} \quad (2.18)$$

Where;

η_{th} - thermodynamic efficiency

ΔG – change of Gibbs free energy

ΔH – change of enthalpy

Since Gibbs free energy decreases with the increase of temperature (as described by Gibbs-Helmholtz equation), the theoretical efficiency decreases with the increase of temperature. Table 2.3 shows the maximum thermodynamic efficiency of an SOFC at different temperatures; $\Delta \bar{g}_f$ is the molar basis Gibbs free energy of formation of water. It can be seen from these expressions that the maximum thermodynamic efficiency decreases with the increase in operating temperature. Although the theoretical efficiency of the conversion of chemical energy into electrical energy decreases with increasing temperature, the waste heat from high-temperature SOFC can be used with a suitable bottoming cycle² to produce more electricity. Thus, the overall plant efficiency can be improved despite the direct-conversion efficiency of the fuel cell being decreased. Under ideal operating conditions and with some additional assumptions, it can be shown that an SOFC operating at an elevated temperature can achieve the same theoretical efficiency as

² A gas turbine or steam turbine that partially converts the waste heat from SOFC into electricity

an SOFC operating at room temperature by utilising waste heat in a suitable bottoming cycle.

Table 2.3 Theoretical efficiency of SOFC at different temperatures^[53]

Phase of water product	Temperature (°C)	$\overline{\Delta g_f}$ (kJ / mole)	Maximum Theoretical Efficiency (%)
Liquid	25	-237.2	83
	80	-228.2	80
Steam	100	-225.2	79
	200	-220.4	77
	400	-210.3	74
	600	-199.6	70
	800	-188.6	66
	1000	-177.4	62

2.3.2 Efficiency Improvement with a Bottoming Cycle: The Thermodynamic Perspective

Although lowering operating temperature increases the theoretical efficiency of a fuel cell, running a fuel cell below room temperature consumes energy for cooling and it is less practical. Thus, room temperature can be considered as the ideal operating temperature for a fuel cell to deliver the highest theoretical efficiency.

To theoretically assess the effects of operating an SOFC at an elevated temperature (circa 750 °C) with a bottoming cycle on the ideal performance, we may consider two SOFCs, of which one operates at room temperature (T_R) and the other operates at an elevated temperature of T_H . A bottoming cycle is employed with the SOFC operating at T_H to produce electricity from waste heat of that SOFC. All three components (two SOFCs and the bottoming cycle) are assumed to be in reversible operation.

In reversible operation, the electrical work outputs from the two SOFCs are the Gibbs free energy at their operating temperatures as given in Equations (2.19) and (2.20) for the room-temperature SOFC and the high-temperature SOFC, respectively.

$$\Delta G_{T_R} = (\Delta H)_{T_R} - T_R(\Delta S)_{T_R} \quad (2.19)$$

$$\Delta G_{T_H} = (\Delta H)_{T_H} - T_H(\Delta S)_{T_H} \quad (2.20)$$

Where;

ΔG_{T_R} – Gibbs free energy released at temperature T_R

ΔG_{T_H} – Gibbs free energy released at temperature T_H

$(\Delta H)_{T_R} / (\Delta H)_{T_H}$ – Enthalpy change at T_R / T_H

$(\Delta S)_{T_R} / (\Delta S)_{T_H}$ – Entropy change at T_R / T_H

If the difference between the enthalpy at T_R and T_H and the difference between the entropy at the same two temperatures is assumed to be negligible (this assumption is neither very accurate nor very erroneous), Equations (2.19) and (2.20) can be rewritten as Equations (2.21) and (2.22), respectively.

$$\Delta G_{T_R} = \Delta H - T_R \Delta S \quad (2.21)$$

$$\Delta G_{T_H} = \Delta H - T_H \Delta S \quad (2.22)$$

Where;

ΔH – Enthalpy change

ΔS – Entropy change

Since the two SOFCs are operating reversibly, $T\Delta S$ terms represent the reversible heat rejection from SOFCs. The released heat from the high-temperature SOFC is used in the heat engine (bottoming cycle) to produce further electricity. However, due to thermodynamic limitations (dictated by the Kelvin-Planck statement of the second law of thermodynamics), this heat cannot be completely converted to electricity; part of that must be rejected to the surroundings. Since the surrounding space is at room-temperature (T_R), the amount of heat that is converted into electricity within the bottoming cycle can be expressed as Equation (2.23). Thus, the total amount of electricity produced by the high-temperature SOFC and its combined bottoming cycle can be expressed as Equation (2.24).

$$Q_{elect} = (T_H - T_R) \Delta S \quad (2.23)$$

$$E_{total} = \Delta G_{T_H} + Q_{elect} \quad (2.24)$$

Where;

Q_{elect} – The amount of heat converted into electricity in the bottoming cycle

E_{total} – Total electricity produced by elevated-temperature SOFC and its bottoming cycle

Substituting of Q_{elect} into Equation (2.24) and eliminating entropy terms by substituting from Equations (2.21) and (2.22) yields:

$$\begin{aligned} E_{total} &= \Delta G_{T_H} + (\Delta H - \Delta G_{T_H}) - (\Delta H - \Delta G_{T_R}) \\ E_{total} &= \Delta G_{T_R} \end{aligned} \quad (2.25)$$

Since ΔG_{T_R} is the electricity produced by the room-temperature SOFC under ideal operation; Equation (2.25) shows that the amount of electricity generated by the high-temperature SOFC along with its bottoming cycle is equal to the electricity generated by the room-temperature SOFC. However, since this equality was achieved under hypothetical conditions, stated as assumptions in the proceeding text, this equality does not hold in practice. However, the overall plant efficiency of high-temperature SOFCs can still be improved with bottoming cycles despite the fact that the thermodynamic efficiency of the fuel cell decreases with the increase of temperature.

2.3.3 Heat Sources and Sinks in SOFC

There are different heat sources and sinks in SOFC, which contribute to changes in cell/stack temperature. A primary source of heat generation is the entropy change associated with the electrochemical reactions. The entropy generation due to irreversibilities is also a source of heat generation. Joule heating is the major irreversibility that generates heat in SOFC. Although other irreversibilities such as activation polarisation and concentration polarisation also contribute to entropy generation (thus, generating heat), they are less prominent in SOFCs compared to joule heating. Apart from these heat sources, the heat-absorbing endothermic reforming reactions act as a heat sink in SOFCs, causing cooling effects when fuels are directly reformed on SOFC anodes. In this section, the underlying science of the aforementioned phenomena is discussed. (In these fundamental scientific explanations, the effects from stack heating by external heat sources, the cooling effects of chilled gases, etc. are not considered)

2.3.3.1 Entropy Effects on SOFC

Fuel oxidation and oxygen reductions take place at the triple phase boundaries of the anode and the cathode, respectively. These redox reactions are associated with entropy change. This entropy change generates heat, and this heat contributes to increasing the temperature of reactants and products as well as the fuel cell components. In order to calculate the heat at each electrode, the corresponding enthalpy and entropy

change at respective electrode due to their half-cell reactions must be considered. Numerical investigations considering the entropy change of half-cell reactions at anode and cathode can be found in the literature^{[54][55]}.

In addition to the heat transfer due to entropy changes associated with the electrochemical reactions, fuel cell irreversibilities also generate heat. The entropy and the heat can be related to any process (reversible or irreversible) as per Equation (2.26), where δq and T are the heat transfer and the absolute temperature at which the heat transfer takes place, respectively. The equality of the equation holds for reversible processes, and the inequality holds for irreversible processes. The inequality can be mathematically expressed as an equality as given in Equation (2.27) where, $(\delta q)_{rev}$ and $(\delta q)_{irr}$ are the reversible and irreversible heat transfer associated with the entropy change respectively. This equation shows that irreversibilities generate more heat (by reducing the work output of the cell) and consequently, contributing to increasing the temperature. Therefore, in addition to the entropy change due to chemical reactions, the entropy generation due to irreversibilities contribute to raising the temperature of SOFC by generating more heat.

$$\Delta S \geq \frac{\delta q}{T} \quad (2.26)$$

$$\Delta S = \frac{(\delta q)_{rev}}{T} + \frac{(\delta q)_{irr}}{T} \quad (2.27)$$

2.3.3.2 Joule Heating (Ohmic Heating)

The resistance to the flow of electrons and ions in all the conducting components of SOFC contributes to Joule heating. Joule heating is the energy loss due to collisions of charge (electrons / ions) with other molecules in the system. For metals, the Joule heating increases with the increase of temperature because of the amount and the severity of collisions become higher at higher temperatures due to rapid molecular vibrations. However, for the SOFC electrolyte, where the flow of oxygen ions is made easier at elevated temperatures than at low temperatures (thus incurring less resistance), Joule heating (also known as the Ohmic polarisation), decreases with the increase in temperature.

Since the electrodes and other electron transfer components (such as interconnect) are good electrical conductors, Joule heating in those components is relatively small and hence can be neglected. Therefore, the primary source of Joule heating in SOFC is due to the resistance to oxygen ion transfer in the electrolyte.

Joule heating can be expressed as Equation (2.28). A more useful form of this expression for fuel cells is found in the literature^[54] as given in Equation (2.29). Joule heating in planar SOFCs is comparatively lower than that of tubular SOFCs due to shorter current paths in planar cells compared to tubular cells (this is one advantage of planar over tubular SOFCs). Zhang *et al*^[56] claim that Joule heating for planar SOFC as a percentage of the total heat produced is in the range from 2.37% to 4.1% while that for tubular cells is 8%. Furthermore, the same study reveals that the flow configuration and internal reforming changes the magnitude of Joule heating. In contradiction to the above findings, Ho *et al*^[57] found that Joule heat contribution in planar SOFC is as high as 14.1% of the total heat production.

$$Q_{Joule} = i^2 R t \quad (2.28)$$

Where;

Q_{Joule} – Joule heat generated

i – Current

R – Resistance

t – Time

$$q_{Joule} = \frac{i^2}{\lambda} \quad (2.29)$$

Where;

q_{Joule} – rate of oule heat per unit volume

i – local current density

λ – conductivity of the material

2.3.3.3 Effects of Fuel Reforming on Temperature

When a hydrocarbon is used instead of pure hydrogen as the fuel for SOFC, the fuel undergoes reforming reactions first to produce hydrogen from the fuel. Methane is a common hydrocarbon being used for SOFC. The stoichiometric steam reforming reactions for methane are given in Equations (2.30) and (2.31), where Equation (2.30) is the reforming reaction, and Equation (2.31) is the gas shift reaction that takes place in the presence of excess steam. Since carbon monoxide is also a fuel for SOFC, the shift

reaction is not essential all the time. In fact, Ho *et al.*^[58] claim that the presence of CO up to 25% with 75% H₂ in a fuel mixture has negligible effects on the temperature compared to having pure hydrogen as the fuel.



Hydrocarbon reforming reaction is an endothermic reaction where approximately 44% of the heat generated due to entropy effect in electrochemical reactions, and the Joule heating is consumed^[57]. In SOFCs, due to high operating temperature, these reforming reactions can take place on the anode. Therefore, a significant level of cooling can be expected near the fuel inlet where reforming reactions are likely to occur more extensively. Thus a significant temperature gradient across the cell, from the fuel inlet to outlet, can exist.

Some computational analysis on the cooling effect due to fuel reforming can be found in the literature. The analytical temperature distribution along the cell length (measured from the fuel inlet) in the fuel and air channels and electrolyte of a planar SOFC are given in Figure 2.16. The analysis shows the temperature profile with and without the influence of Joule heating. The temperature profiles with the consideration of Joule heating are denoted by “+Jh” and those without joule heating are denoted by “-Jh”. The high cooling effect near the fuel inlet is due to heat absorbed by the endothermic fuel reforming reaction. The gradual gain of the temperature along the length of the fuel cell is due to the heat generated by electrochemical oxidation of the fuel as the reformed fuel

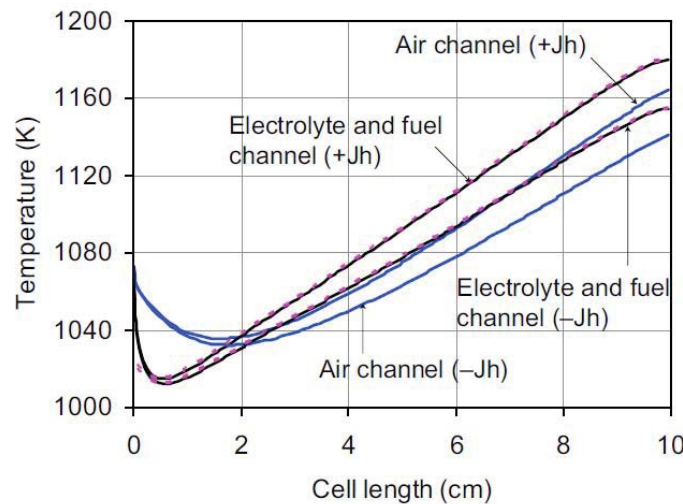


Figure 2.16 Temperature distribution with fuel reforming (+Jh ~ with Joule heating and -Jh ~ without Joule heating)^[57]

progressed along fuel channels. It can be noted from the graphs that the effect of the Joule heating has also contributed to the overall temperature of a magnitude of approximately 20 K. This computational analysis shows that the internal reforming has induced temperature gradients across a cell, and Joule heating has aggravated this temperature gradient.

2.3.4 The Effects of Temperature on Power Output

In the preceding sections, discussion centred on how the entropy effect, joule heating, and fuel reforming induce uneven temperature distributions in a cell. This section is dedicated to investigating the consequences of those temperature distributions on the power output of an SOFC.

Figure 2.17 show the simulated performance of an SOFC at three different temperatures. If the current density of 0.5 A/cm^2 is considered under all three operating temperatures, the voltage at which this current delivered is approximately 0.81 V, 0.66V, and 0.45V for operating temperatures of 1000 °C, 900 °C, and 800 °C respectively. Thus, an apparent drop in the operating voltage (and the power output) is demonstrated for a given current density with the decrease in operating temperature. Although this effect cannot be explained with Nernst effect, voltage drop with the decrease of operating temperature is due to the increase of losses in the fuel cell, particularly the ohmic losses. The ohmic losses are high due to high resistance to ionic conduction through the electrolyte at low operating temperatures. Thus, although the Nernst potential is high at

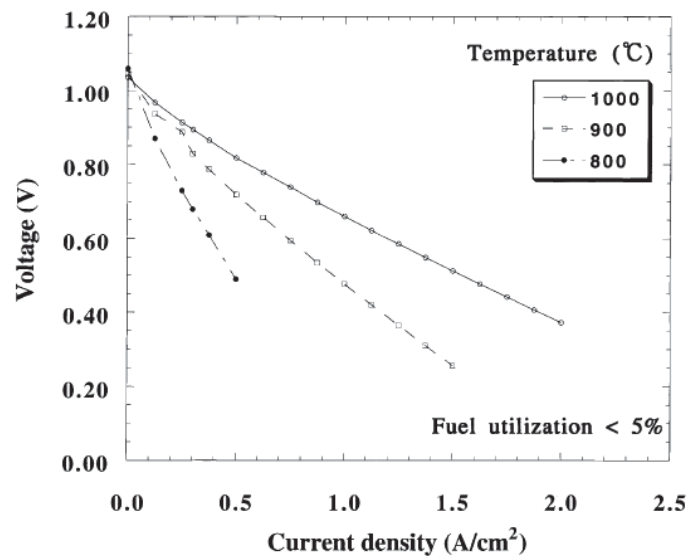


Figure 2.17 Performance of a single cell at different temperatures^[59]

low temperatures, the actual voltage output is lower at low temperatures than that at high temperatures. Therefore, when a cell operates with non-uniform temperature distribution across the cell, it delivers non-uniform power densities across the cell.

Figure 2.18 shows a simulated result of the temperature distribution of the electrolyte and the current density along the length, measured from the gas inlet. The graph reveals that the temperature drops at the gas inlet due to the cooling effect from fuel reforming as discussed previously. As a result of this temperature drop, the current density has also dropped due to increase of resistance in the electrolyte at low temperatures. As the fuel proceeds along fuel channels after reforming, the electrochemical reaction takes place, causing the temperature to rise. Thus, the current density has increased along the length of the cell as the temperature increases. This is because the ionic resistance decreases with the increase of the temperature. The drop of the current density at a length beyond 8 cm has been ascribed to the decline of the fuel strength along the flow channel due to fuel consumption^[57]. This simulation results also clearly evidences that the temperature distribution in a cell leads to non-uniform performance across the cell.

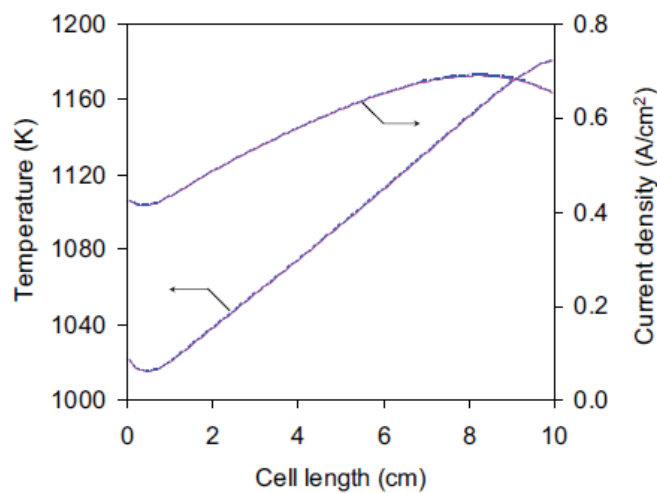


Figure 2.18 Temperature distribution in the electrolyte and the current density along the length of the cell^[57]

Iwata *et al*^[60] have developed a two-dimensional model of a planar SOFC, which use hydrogen and air, to predict the temperature and current density profile under varying operating conditions and flow configurations. Figure 2.19 (a) shows the temperature distribution under cross-flow of fuel and air, both at 800 °C at their respective inlets. No air or fuel circulation has been applied to flatten the temperature gradients. The low temperature at the air inlet has been ascribed to the cooling effect from the air. Figure 2.19 (b) shows the corresponding current density distribution. The higher current density at the fuel inlet region, where fuel pressure is high, is due to the higher Nernst effect. The lower current density at the fuel outlet region, where fuel pressure is low, is once again due to the Nernst effect. The temperature effect on the current density can be seen from the current density distribution graph. Consider the vertical line drawn on Figure 2.19 (b). Since this line is parallel to the fuel inlet, the fuel supply can be considered uniform along the line. However, since the temperature increases from the air inlet to the air outlet, the current density has also increased in response to this temperature increase. These simulation results also show the cell performance non-uniformity caused by non-uniform temperature across a cell.

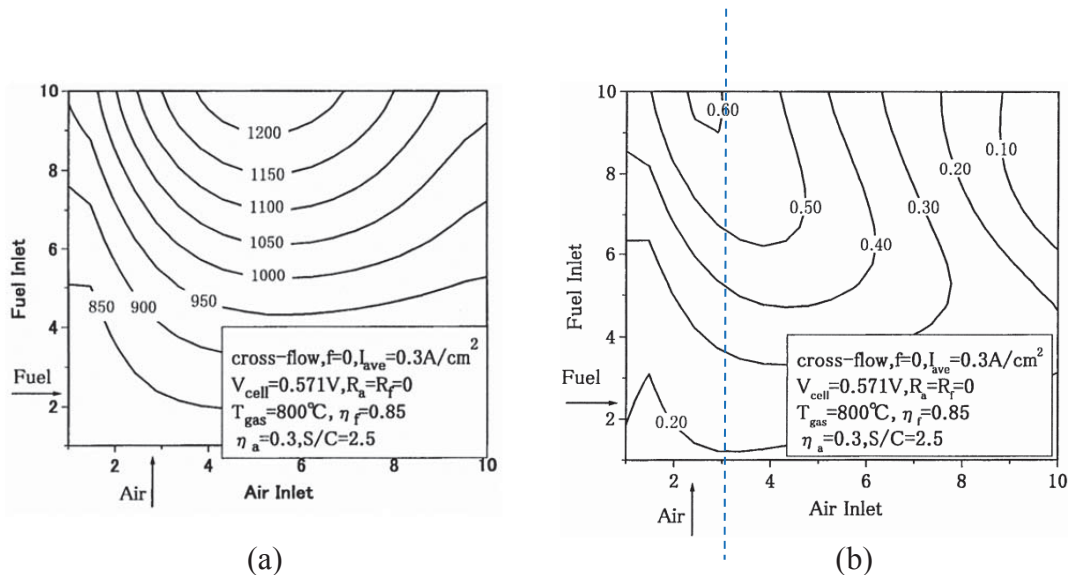


Figure 2.19 Temperature and current density distribution of a planar SOFC under cross-flow configuration (a) the temperature distribution (b) the current density distribution^[60]

2.3.5 Temperature Distribution and Thermal Stresses

Besides to the resulting nonhomogeneous performance, the presence of a nonhomogeneous temperature distribution on a cell can potentially be very harmful to the durability of the cell due to thermal stress generation. A number of studies have been carried out to investigate the thermal stress generation due to uneven temperature distribution and the thermal expansion mismatch between cell components. The high operating temperature is itself sufficient to trigger thermal expansion mismatch-driven stresses. Such stresses can be mitigated by matching the thermal expansion coefficient of materials. However, even without having mismatches in thermal expansion coefficient, uneven temperature distributions can generate thermal stresses on the same material due to uneven thermal expansion. Thus, such problems can only be mitigated through eliminating the evolution of detrimental temperature distributions over the cell.

In addition to the previously discussed factors that evolve uneven temperature distribution on a cell, formation of hot-spots on cells can also lead to the formation of thermal cracks or delamination of the cell components due to uneven thermal expansion^[61]. Hot-spots are generally created due to localised current concentrations. The current-concentrated sites become chemically overactive and hence, liberate more heat creating hot-spots^[62]. Non-uniform reactant distribution over a cell can generate hot spots / hot regions. The areas which readily get reactants becomes chemically active and consequently, generates more heat while areas starved of reactants generate less heat due to less chemical activity. Thus, uniform distribution of reactants is also an important aspect in preventing thermal stresses. Furthermore, power demand fluctuations and start-up/ shut-down cycles can also generate thermal cycles which promote mechanical failures^{[63][64]}.

Lin *et al.*^[65] have computationally simulated the temperature distribution of three-cell SOFC stack in different stages of operation. They have considered an 80 mm × 80 mm cell supported by 100 mm × 150 mm interconnect. A cross-flow configuration of gasses (fuel from the bottom and air from the top) and a current density of 640 mAcm⁻² have been assumed for their simulation. Figure 2.20 shows the temperature distribution at different durations from the start-up as well as after reaching steady state operation. (Note: due to the symmetry, only half of the assembly had been simulated). These simulated results show that an in-plane temperature distribution over the cell is evolved during the start-up. Further, even in the steady-state operation, a high-temperature region can be observed near the fuel inlet while a low-temperature zone can be observed near the air-

inlet. High-fuel concentration near fuel inlet has made that region electrochemically highly active, thus; generating more heat. Meanwhile, the air inlet area has less fuel concentration and high-level of cooling due to chilling effect from air. Thus, a relatively low temperature is recorded near the air inlet. The situation could have been different if internal reforming was involved, where the fuel inlet will be a lot cooler. These uneven temperature profiles on a cell, present during start-up as well as in steady-state operation, leads to thermal stresses and potentially damaging the cell depending on the severity of the stress. The three-dimensional temperature distribution of the three-cell stack in the steady-state operation, generated by the same study, is shown in Figure 2.21. This result shows that the cross-plane temperature distribution is less prominent than the in-plane temperature distribution despite minor changes in the sizes of different temperature zones in each plane. This indicates that temperature measurement from each cell of a stack may not be necessary, though the temperature of a cell needs to be measured with high-spatial resolution. Apart from the temperature distributions evolved due to start-ups and fuel concentration sites, changes in operating conditions such as load, flow rates, etc. also generate detrimental evolutions of temperature profiles across cells^[66]. Whatever may be

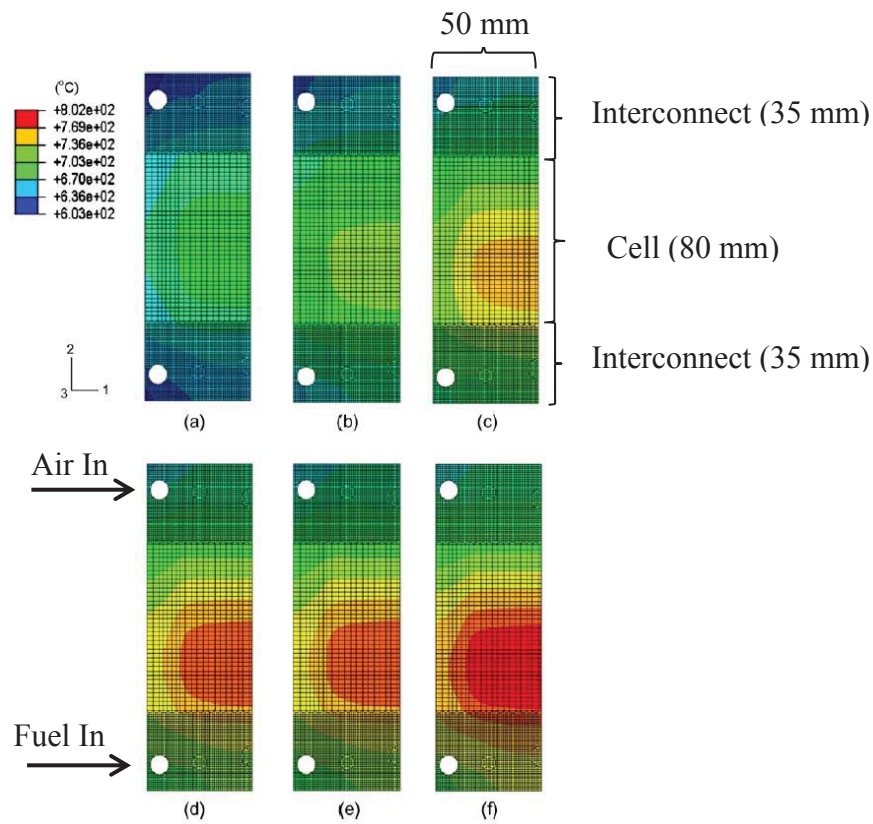


Figure 2.20 In-plane temperature profiles on the cell and interconnect of a 3-cell SOFC stack model after: (a) 30 s, (b) 1 min, (c) 2 min, (d) 6 min, (e) 14 min from start-up, and (f) steady-state condition^[65]

the cause of the temperature distribution evolved on a cell, large temperature gradients can generate thermal stresses causing damage to both cells and stacks.

The exact values and the locations of stress concentration depend on the temperature profile evolved on a cell, which in turn depends on aforementioned factors such as flow-configurations, fuel reforming, current load, fuel concentration, etc. However, for the comprehensiveness of the discussion in this chapter, a simulation result of stresses from a work of literature is presented.

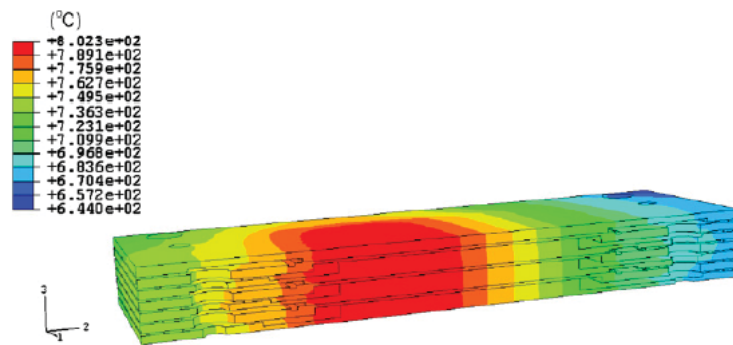
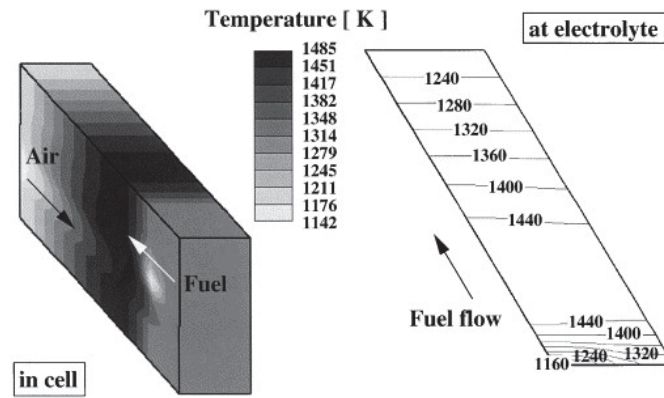
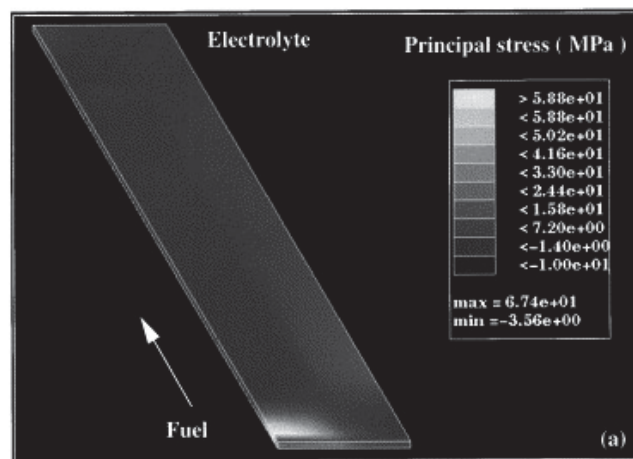


Figure 2.21 Temperature distribution at the steady-state condition in three-cell SOFC model^[65]

Yakabe *et al*^[59] investigated the temperature and stress profile of a planar SOFC under different operating conditions and considering internal reforming as well. The flow configuration was set as cross-flow. The temperature profile evolved, shown in Figure 2.22 (a), shows that the temperature near fuel inlet is the lowest while that in the middle is the greatest. Lower temperature at the fuel inlet is due to the cooling effects of the endothermic reforming reactions. Temperature near air inlet is also relatively low because of the cooling effect from the air as well as less heat generation due to less fuel concentration. The middle region is free from cooling due to fuel reforming and has good fuel concentration as well. Thus, the temperature is the highest due to high electrochemical activity in that region. The stress distribution shown in Figure 2.22 (b) shows that there is a significant stress concentration near fuel inlet due to the steep temperature gradient present in that region. Since it has already been established that various detrimental temperature profiles can evolve on a cell due to different operating conditions, consequently, detrimental stress levels may also be generated depending on the temperature distribution. Therefore, the formation of cracks in cell and stack components as well as delamination of the cell component is possible, depending on the severity of the stress level.



(a)



(b)

Figure 2.22 Simulated temperature and corresponding stress distribution on a model electrolyte (a) the temperature distribution, (b) the stress distribution^[59]

2.4 Conclusions

The state of art the technology of SOFC is presented and the fundamental sciences behind SOFC operation are discussed. The three key losses in SOFC; activation polarisation, ohmic polarisation, and concentration polarisation along with their impacts on the operational cell voltage are discussed.

The effects of temperature on SOFC, concerning the cell performance and durability, were presented and discussed. The theoretical maximum efficiency of SOFC was defined, and its change with temperature was presented. A theoretical investigation on how to improve the efficiency of high-temperature SOFC by employing a bottoming cycle was presented and discussed. It was shown that waste heat utilisation in high-temperature SOFCs could increase the overall plant efficiency despite the decrease in the ideal thermodynamic cell efficiency.

Entropy change associated with electrochemical reactions as well as irreversibilities are two primary sources of heat generation within SOFC. Among the irreversibilities, the effect of joule heating is substantial. The cooling effects due to reforming reactions, as well as that due to the heat transfer to air supply are found to induce significant temperature variations across a cell. The fuel inlet region becomes the coolest region of a cell when reforming is employed. Consequently, relatively larger stress concentrations can be noticed near such low-temperature regions. In contrary, when internal reforming is not used, the fuel inlet region becomes the hottest part of a cell due to high chemical activity in that area.

Cell performance (the current density and voltage) is directly influenced by the local temperature, where high-temperature regions demonstrate higher current density while low-temperature regions demonstrate low current density. Thus, in parallel with non-uniform temperature distribution, non-uniform power density across a cell can be observed.

The temperature gradient across a stack (between cells) is less prominent than the temperature gradient on a cell; however, this depends on the stack architecture and many other parameters. This may suggest that it may not be necessary to measure temperature from each cell of a stack though temperature from a cell needs to be measured with high spatial resolution to detect accurately and reflect the temperature distribution. However, the exact temperature distribution across a stack may need to be further investigated as it

is likely to be affected by other factors such as the stack size, balance of plant equipment, air/fuel ratio, etc.

2.5 References

- [1] Shao, Z., Haile, S.M., Ahn, J., Ronney, P.D., Zhan, Z., and Barnett, S.A., A thermally self-sustained micro solid oxide fuel cell stack with high power density, *Nature*, 2005, 435, pp.795-798.
- [2] Ellis, M.W., Von Spakovsky, M.R., and Nelson, D.J., Fuel cell systems: efficient, flexible energy conversion for the 21st century, *Proceedings of the IEEE*, 2001, 89(12), pp.1808-1818.
- [3] Williams, M.C., Strakey, J.P., and Surdoval, W. A., The U.S. Department of Energy, Office of Fossil Energy Stationary Fuel Cell Program, *Journal of Power Sources*, 2005 , 143(1-2), pp.191-196.
- [4] Homel, M., Gur, T.M., Hoh, J.H., and Vikar, A.V., Carbon monoxide-fueled solid oxide fuel cell, *Journal of Power Sources*, 2010, vol.195(19), pp.6367-6372
- [5] Nahar, G. and Kendall, K., Biodiesel formulations as fuel for internally reforming solid oxide fuel cell, *Fuel Processing Technology*, 2011, 92(7), pp.1345-1354.
- [6] Liu, J. and Barnett, S.A., Operation of anode-supported solid oxide fuel cells on methane and natural gas, *Solid State Ionics*, 2003, 158, pp.11-16.
- [7] Gorte, R.J., Kim, H., and Vohs, J.M., Novel SOFC anodes for the direct electrochemical oxidation of hydrocarbon, *Journal of Power Sources*, 2002, 106(1-2), pp.10-15.
- [8] Kim, H., Park, S., Vohs, J.M., and Gorte, R.J, Direct Oxidation of Liquid Fuels in a Solid Oxide Fuel Cell, *Journal of The Electrochemical Society*, 2001, 148(7), pp. A693.
- [9] Zhou, Z.F., Kumar, R., Thakur, S.T., Rudnick, L.R., Schobert, H., and Lvov, S.N., Direct oxidation of waste vegetable oil in solid-oxide fuel cells, *Journal of Power Sources*, 2007, 171(2), pp.856-860.
- [10] Zhou, Z., Gallo, C., Pague, M.B., Shobert, H., and Lvov, S.N, Direct oxidation of jet fuels and Pennsylvania crude oil in a solid oxide fuel cell, *Journal of Power Sources*, 2004 133(2), pp.181-187.
- [11] Minh, N., Solid oxide fuel cell technology-features and applications, *Solid State Ionics*, 2004, 174(1-4), pp.271-277.
- [12] Minh, N.Q., Ceramic Fuel Cells, *Journal of American Ceramic Society*, 1993, 76(3), pp.563-588.
- [13] Blum, L., Meulenberg, W.A., Nabielek, H., and Steinberger-Wilckens, R., Worldwide SOFC Technology Overview and Benchmark, *International Journal of Applied Ceramic Technology*, 2005, 2(6), pp.482-492.
- [14] Myles, K.M. and Mcpheeters, C.C., Monolithic solid oxide fuel cell development. *Journal of Power Sources*, 1990, 29, pp.311-319.
- [15] Yamamoto, O., Solid oxide fuel cells: fundamental aspects and prospects, *Electrochimica Acta*, 2000, 45(15-16), pp.2423-2435.
- [16] US Department of Energy, *Fuel Cell Handbook* ,6th Edition, 2002
- [17] Dixon, J.M., LaGrange, L.D., Merten, U., Miller, C.F, and Porter, J.T., Electrical Resistivity of Stabilized Zirconia at Elevated Temperatures, *Journal of The Electrochemical Society*, 1963, 110(4), pp.276.
- [18] Chen, X.J., Khor, K.A., Chan, S.H., and Yu, L.G., Influence of microstructure on the ionic conductivity of yttria-stabilized zirconia electrolyte, *Materials Science and Engineering: A*, 2002, 335(1-2), pp.246-252.

- [19] Xing, Y-Z., Li, C-J., Zhang, Q., Li, C-X., and Yang, G-J, Influence of microstructure on the ionic conductivity of plasma-sprayed yttria stabilised zirconia deposits, *Journal of American Ceramic Society*, 2008, 91(12), pp. 3931-3936.
- [20] Petot-Ervas, G., Petot, C., Zientara, D., and Kusinski, J., Microstructure and transport properties of Y-doped zirconia and Gd-doped ceria. *Materials Chemistry and Physics*, 2003, 81(2-3), pp.305-307.
- [21] Fergus, J.W., Electrolytes for Solid Oxide Fuel Cells, *Journal of Power Sources*, 2006, 162, pp.30-40.
- [22] Singhal, S.C. and Kendal, K. *High temperature Solid Oxide Fuel Cells: Fundamentals, Design and Applications*, UK:Elsevier, 2003.
- [23] Haeringa, C., Roosena, A., Schichlb, H., and Schnollerc, M., Degradation of the electrical conductivity in stabilised zirconia system: Part II: Scandia-stabilised zirconia, *Solid State Ionics*, 2005, 176(3-4), pp. 261-268.
- [24] Sumi, H., Ukai, K., Mizutani, Y., Mori, H., Wen, C-J., Takahashi, H., and Yamamoto, O., Performance of nickel–scandia-stabilized zirconia cermet anodes for SOFCs in 3% H₂O–CH₄, *Solid State Ionics*, 2004, 174(1-4), pp.151-156.
- [25] Leea, D., Leea, I., Jeona, Y., and Songb, R., Characterization of scandia stabilized zirconia prepared by glycine nitrate process and its performance as the electrolyte for IT-SOFC, *Solid State Ionics*, 2005, 176(11-12), pp.1021-1025
- [26] Yamamotoa, O., Aratia, Y., Takedaa, Y., Imanishia, N., Mizutanib, Y., Kawaib, M., and Nakamurab, Y., Electrical conductivity of stabilized zirconia with ytterbia and Scandia, In: *Proceedings of the 20th Commemorative Symposium on Solid State Ionics*, Japan, 1995, 79, pp.137-142.
- [27] Nomura, K., Mizutani, Y., Kawai, M., and Nakamura, Y., Aging and Raman scattering study of scandia and yttria doped zirconia, *Solid State Ionics*, 2000, 132(3-4), pp.235-239.
- [28] Dalslet, B., Blennow, P., Hendriksen, P.V., Bonanos, N., Lybye, D., and Mogensen, M., Assessment of doped ceria as electrolyte, *Journal of Solid State Electrochemistry*, 2006, 10(8), pp.547-561.
- [29] Leea, D., Hana, J-H., Chuna, Y., Songb, R-H., and Shinb,D.R., Preparation and characterization of strontium and magnesium doped lanthanum gallates as the electrolyte for IT-SOFC, *Journal of Power Sources*, 2007, 166(1), pp.35-40.
- [30] Bi, Z., Yi, B., Wang, Z., Dong, Y., Wu, H., She, Y., and Chengz, M., A High-Performance Anode-Supported SOFC with LDC-LSGM Bilayer Electrolytes, *Electrochemical and Solid-State letters*, 2004, 7(5), pp.A105-A107.
- [31] Ivers-Tiffe'e. E., Weber, A., and Herbristrit, D., Materials and technologies for SOFC-components , *Journal of the European ceramic society*, 2001, 21, pp. 1805-1811.
- [32] Gestel, V.T., Sebold, D., Meulenber, W.A., and Buchkremeret, H-P., Development of thin-film nano-structured electrolyte layers for application in anode-supported solid oxide fuel cells, *Solid State Ionics*, 2008, 179(11-12), pp.428-437.
- [33] Kim, J.C., Lee, D.Y., Kim, H-R., Lee, H-W., Lee, J-H., Son, J-W., Surface modification of anode substrate via nano-powder slurry spin coating for the thin film electrolyte of solid oxide fuel cell, *Thin Solid Films*, 2011, 519(8), pp.2534-2539.
- [34] Li,J., Zhang, N., Sun, S., Sun, W., and Li W., A facile and environment-friendly method to fabricate thin electrolyte films for solid oxide fuel cells, *Journal of Alloys and Compounds*, 2011, 509(17), pp.5388-5393.

-
- [35] Souza, S.D., Visco, S.J., and Jonghe, L.C.D., Thin-film solid oxide fuel cell with high performance at low- temperature, *Solid State Ionics*, 1997, 98, pp.57-61.
- [36] Tsuchiya, M., Lai, B-K., and Ramanathan, S., Scalable nanostructured membranes for solid-oxide fuel cells, *Nature Nanotechnology*, 2011, 6, pp.282-286.
- [37] O'Hayre, R., Barnett, D.M., and Prinz, F.B., The Triple Phase Boundary: A mathematical model and experimental investigation for fuel cells, *Journal of The Electrochemical Society*, 2005, 152(2), p.A439-A444.
- [38] Sun, C. and Stimming, U., Recent anode advances in solid oxide fuel cells, *Journal of Power Sources*, 2007, 171(2), pp.247-260.
- [39] Zhu, W. and Deevi, S., A review on the status of anode materials for solid oxide fuel cells, *Materials Science and Engineering: A*, 2003, 362(1-2), pp.228-239.
- [40] Larminie, J. & Dicks, A., 2003. *Fuel Cell Systems Explained*, John Willy & Sons Ltd.
- [41] Dees, D.W., Claar, T.D., Easler, T.E., Fee, D.C., and Mrazek, F.C., Conductivity of Porous Ni/ZrO₂-Y₂O₃ Cermets, *Journal of The Electrochemical Society*, 1987, 134(9), p.2141.
- [42] Matsuzaki, Y. & Yasuda, I., 2000. The poisoning effect of sulfur-containing impurity gas on a SOFC anode : Part I . Dependence on temperature, time, and impurity concentration. *Solid State Ionics*, 132, pp.261-269.
- [43] Ivers-tiffe, E., Weber, A., and Herbsttritt, D., Materials and technologies for SOFC-components, 2001, *Journal of the European Ceramic Society*, 21, pp.1805-1811.
- [44] Pramuanjaroenkij, A., Kakac, S., and Zhou, X.Y., Mathematical analysis of planar solid oxide fuel cells, *International Journal of Hydrogen Energy*, 2008, vol.33(10), pp. 2547-2565
- [45] Muller, A.C., Weber, A., Herbsttritt, D., and Ivers-Tiffée, E., Long term stability of yttria and Scandia doped zirconia electrolytes, *Proceedings of the 8th international symposium on Solid Oxide Fuel Cells*, 2003, 7, pp.196-199
- [46] Lussier, A., Sofie, S., Dvorak, J., Idzerda, Y.U., Mechanism for SOFC anode degradation from hydrogen sulphide exposure, *International Journal of Hydrogen Energy*, 2008, 33(14), pp.3945-3951.
- [47] Simwonis, D., Tietz, F., and Stöver, D., Nickel coarsening in annealed Ni/8YSZ anode substrates for solid oxide fuel cells, *Solid State Ionics*, 2000, 132(3-4), pp.241-251.
- [48] Iwanschitz, B., Sfeir, J., Mai, A., and Schütze, M., Degradation of SOFC Anodes upon Redox Cycling: A Comparison Between Ni/YSZ and Ni/CGO, *Journal of the electrochemical society*, 2010, 157(2), pp.B269-B278.
- [49] Simnerz, S. P., Anderson, M. D. , Engelhard, M. H., and Stevenson, J. W., Degradation Mechanisms of La – Sr – Co – Fe – O₃ SOFC Cathodes, *Electrochemical and Solid-State Letters*, 2006, 9(10), pp.A478-481.
- [50] Hjalmarsson, P., Søgaaard, M., Mogensen, M., Electrochemical performance and degradation of (La_{0.6}Sr_{0.4})_{0.99}CoO₃ – δ as porous SOFC-cathode, *Solid State Ionics*, 2008, 179(27-30), pp.1422-1426.
- [51] Matsuzaki, Y. and Yasuda, I., Dependence of SOFC Cathode Degradation by Chromium-Containing Alloy on Compositions of Electrodes and Electrolytes, *Journal of the electrochemical society*, 2001, 148(2), pp.A126-A131.
-

-
- [52] Jianga, S.P. and Chen, X., Chromium deposition and poisoning of cathodes of solid oxide fuel cells – A review, *International Journal of Hydrogen Energy*, 2014, 39(1), pp.505-531
 - [53] Larminie, J. and Dicks, A., 2003, *Fuel Cell Systems Explained* Second Edition, John Wiley & Sons Ltd.
 - [54] Andreassi, L., Rubeo, G., Ubertini, S., Lunghi, P., and Bove, R., Experimental and numerical analysis of a radial flow solid oxide fuel cell, *Int. Journal of Hydrogen Energy*, 2007, vol.32(17), pp. 4559-4574
 - [55] Chaisantikuwat, A., Diaz-Goano, C., and Meadows, E.S, Dynamic modelling and control of planar anode-supported solid oxide fuel cell, *Computers and Chemical Engineering*, 2008, vol. 32(10), pp.2365-2381
 - [56] Zhang, X., Li, G., Li, J., and Feng, Z., Numerical study on electric characteristics of solid oxide fuel cells, *Energy conversion and management*, 2007, vol. 48(3), pp.977-989
 - [57] Ho, T.X., Kosinski, P., Hoffmann, A.C., and Vik, A., Effects of heat sources on the performance of a planar solid oxide fuel cell, *Int. Journal of Hydrogen Energy*, 2010, vol.35, pp.4276-4284
 - [58] Ho, T.X., Kosinski, P., Hoffmann, A.C., and Vik, A., Numerical analysis of a planar anode-supported SOFC with composite electrode, *Int. Journal of Hydrogen Energy*, 2009, vol.34(8), pp.3488-3499
 - [59] Yakabe, H., Ogiwara, T., Hishinuma, M., and Yasuda, I., 3-D model calculation for planar SOFC, *Journal of Power Sources*, 2001, vol.102(1-2), pp.144-154
 - [60] Iwata, M., Hikosaka, T., Morita, M., Iwanari, T., Ito, K., Onda, K., Esaki, Y., Sakaki, Y., and Nagata, S., Performance analysis of planar-type unit SOFC considering current and temperature distribution, *Solid State Ionics*, 2000, vol.132(3-4), pp.297-308
 - [61] Vikar, A.V., A model for solid oxide fuel cell stack degradation, *Journal of Power Sources*, 2007, 172(2), pp.713-724.
 - [62] Kawada, T., Horita, T., Sakai, N., Yokokawa, H., Dokiya, M., and Mizusaki, J., A novel technique for imaging electrochemical reaction sites on a solid oxide electrolyte, *Solid State Ionics*, 2000, vol.131(1-2), pp.199-210
 - [63] Hagen, A., Hendriksen, P.V., Frandsen, H.L., Thuden, K., and Barfod, R., Durability study of SOFCs under cycling current load conditions, *Fuel Cells*, 2009, 9(6), pp.814-822.
 - [64] Dikwal, C., Bujalski, W., and Kendall, K., The effect of temperature gradients on thermal cycling and isothermal aging of micro tubular solid oxide fuel cells, *Journal of Power Sources*, 2009, 193(1), pp.241-248.
 - [65] Lin, C-K., Chen, T-T, Chyou, Y-P., and Chiang, L-K., Thermal stress analysis of a planar SOFC stack, *Journal of Power Sources*, 2007, vol.164, pp.238-251.
 - [66] Nakajo, A., Mueller, F., Brouwer, J., Van herle, J., and Favrat, D., “Mechanical reliability and durability of SOFC stacks. Part II: Modelling of mechanical failure during ageing and cycling”, *International Journal of Hydrogen Energy*, 2012 vol. 37, pp.9269-9286.

2.6 Bibliography

- [1] O’hayre, R., Cha, S-W., Colella, W., and Prinz, F.B., 2009, *Fuel cell fundamentals*, John Wiley & Sons Ltd.

**Chapter 3 : Literature Review of SOFC
Temperature Sensing**

Chapter Summary

This chapter presents the state of art SOFC temperature sensing technologies and the potential temperature sensing technologies that can be adapted for SOFC temperature sensing to better reveal the temperature distribution at cell level.

The chapter begins with presenting the applicable temperature sensing technologies for SOFC in Section 3.1 where; thermistor, thermocouple, and RTD technologies are presented in detail in Sections 3.1.2, 3.1.3, and 3.1.4, respectively. Section 3.2 presents the state of art SOFC temperature sensing technologies. The key problems associated with these technologies are also discussed. The aim and objectives of this research are outlined in Section 3.3

Finally, the thermometry selection for this research is presented in Section 3.4 along with the conclusions to the overall chapter.

3.1 Literature Review: Temperature Sensing

3.1.1 Introduction

Temperature sensing technology is a well-matured area in the broad domain of instrumentation technology. Therefore, investigating the potential adaptability of existing sensing technologies as *in situ* sensors for SOFC was considered as the best approach to start with. The key characteristic requirements sought were:

- 1) Operating temperature, at least, up to approximately 950 °C
- 2) Temperature measurability from a surface
- 3) Compatibility with cell components
- 4) Adaptability with minimum system modifications
- 5) Stability in redox environments
- 6) Less disturbance to cell/ stack operation during sensing

IR imaging reveals surface temperature details with excellent spatial resolution. However, the lack of visibility into inner cells does not enable IR imaging to be employed unless significant stack alterations are adapted (attempts on using IR imaging to measure temperature distribution of SOFC are presented later in this chapter). However, a significant level of design modification diverts an SOFC from its normal operation hence; the measurements cannot be claimed as *in situ*. The *in situ* measurement is essential to get an accurate understanding of the temperature distribution during normal cell / stack operation. Therefore, all non-contact thermometry were opt-out from the investigation.

The choice needs to be made from contact temperature sensors. Thermocouple, Resistance Temperature Detector (RTD), thermistor, and IC temperature sensor are the currently available contact temperature sensors. Integrated circuit (IC) sensor is applied only for low-temperature measurements, particularly, in consumer electronics industry. It's not adaptable to SOFC operating conditions. Thus, IC sensors were also eliminated from the investigation at the initial stage. Since the existing methods of SOFC temperature sensing do not measure temperature with sufficiently high spatial resolution, the technological feasibility of thermistors, thermocouples, and RTDs were assessed with the aim of adapting them for high-spatial resolution temperature measurements from SOFCs as described in following sections. The choice of thermometry is presented in Section 3.4

3.1.2 Thermistors

Thermistors are generally made from mixtures of oxides of manganese, nickel, cobalt, iron, and titanium. They are the most sensitive temperature sensors presently used in practice; the typical value of sensitivity is in the order of 50 mV/°C^[1]. However, their extreme non-linearity, fast aging, cracking, and batch-to-batch tolerance^[2] are some drawbacks. Although thermistors generally measure temperatures below 300 °C, there were some research-stage thermistor developments that operate at high temperature and use materials well compatible with SOFC. Following brief discussion starts with an overview to technology and then, focusses more on high-temperature thermistor developments.

3.1.2.1 The Principle of Operation

Temperature dependent resistivity of semiconductor materials is the basis of thermistor operation. A simplified linear temperature-resistance relationship is given in Equation (3.1) where this linearity is valid only for small temperature ranges. Depending on the value of k , thermistors are classified into two categories: positive temperature coefficient (PTC) thermistors for positive k values and negative temperature coefficient (NTC) thermistors for negative k values. A more accurate temperature-resistance relationship is presented by the Steinhart-Hart equation given in Equation (3.2). Values of the device-specific constants must be provided with the corresponding thermistor device.

$$\Delta R = k\Delta T \quad (3.1)$$

Where,

ΔR – the change of resistance

ΔT – the change of temperature

k – the temperature coefficient of resistance

$$\frac{1}{T} = a + b \ln(R) + c(\ln(R))^3 \quad (3.2)$$

Where,

T – absolute temperature

R – resistance

a, b, c – device specific constants

A PTC thermistor's resistance proportionally increases with the temperature to a certain threshold (known as the transition temperature) and then, it abruptly increases making a significant barrier to current flow beyond the transition temperature. Figure 3.1 illustrates this behaviour. (Note: this figure is for illustration purposes only; the actual threshold temperature may vary from material to material.) This feature of PTC has made it quite popular as overcurrent protectors. For instance, Tucker and Cheng^[3] used a layer of PTC material between the cathode and the interconnect of an SOFC to prevent excessive increase of temperature when current is drawn from the cell. NTC type thermistors, on the other hand, have an inverse correlation between temperature and the resistance: resistance decreases with the increase of temperature. They are being used as temperature sensors, and find broad applications: domestic appliances, bio-medical instruments, manufacturing industries, transportation, and security are to name a few. PEMFC³ is a common research domain where thermistors are applied^[4].

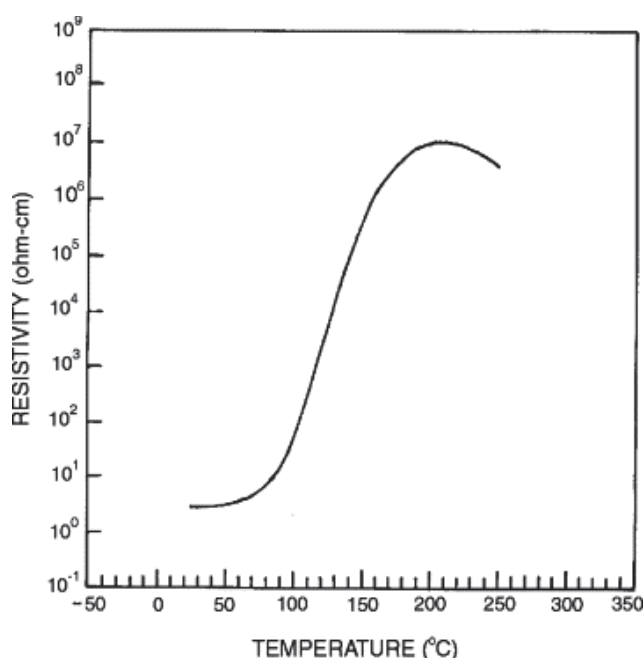


Figure 3.1 Resistivity Vs Temperature curve of a PTC thermistor^[5]

3.1.2.2 High-Temperature Thermistors

High-temperature thermistor development is relatively a new research area. Yttria appears to be the most widely used material for applications around or beyond 1,000 °C. Maintaining the stability at high temperature (above 1,000 °C) due to fast aging, reproducibility, lead wire material selection, and techniques for lead wire attachment

³ Polymer Exchange Membrane Fuel Cell

remain as the key challenges to commercialise high-temperature thermistors^[6]. Banerjee and Akbar^[7] developed a new method to fabricate thermistors from high purity (99.99%) yttria, and they claim to have eliminated the aging problem and lead wire connection problem. However, they failed at showing good reproducibility. Wang *et al*^[8] studied the suitability of yttria and calcium zirconate as raw materials for high-temperature (above 1,000 °C) thermistors. There were six samples of yttria used with varying amount of zirconia doping: un-doped yttria, 0.15, 0.5, 1.0, 5.0, 15, 20 mole% of zirconia. A slight decrease in the sensitivity was observed with increase in zirconia content. Since the electrical properties are very sensitive to composition and impurity (dopant)^[9], reproducibility becomes an obvious challenge when the composite ceramic is used. The influence of wetness to electrical properties of yttria is another problem that needs further investigation^[10]. Despite the exciting promises of thermistors for high-temperature applications, they are still in highly research stage.

3.1.3 Thermocouples

The thermocouple is the most widely applied thermometry in industrial applications, particularly, in high-temperature applications and harsh environments. The wide operating temperature range (usually from -200 °C to about 1,800 °C), rugged yet simple construction, and low cost are a few attractive characteristics behind its popularity. An S-type thermocouple was used in establishing the international temperature scale (ITS-1968)^[11]. However, instability caused by oxidation, evaporation, and migration of rhodium^[12] eliminated thermocouple thermometry in ITS-90 international standards since 1st of January 1990. Nevertheless, their widespread application in the industry remains intact. Table 3.1 briefly summarises the temperature range and the accuracy of commonly used thermocouple types.

Table 3.1 Popular thermocouple types^[13]

Thermocouple type	Overall temperature range (°C)	Typical accuracy °C (at 0 °C, unless otherwise stated)	Remarks
Type E (Chromel/ Constantan)	-200 to 900	1.7	Has high sensitivity (68 $\mu\text{V/K}$)
Type J (Iron/ Constantan)	-40 to 760	2.2	Permanent de-calibration occurs if used above the range.
Type K (Chromel/ Alumel)	-200 to 1,300	2.2	Sensitivity is approximately 48 $\mu\text{V/K}$.
Type N (Nicrosil/ Nisil)	-200 to 1,300	2.2	High stability and high-temperature oxidation resistance.
Type T (Copper/ Constantan)	-200 to 400	1	Best accuracy. Often used for food monitoring and environmental observations.
Type B (Pt:Rh 30:70 by wt/ Pt:Rh 6:94 by wt.)	100 to 1,800	5 (at 1,000 °C)	Suitable for high-temperature measurements. Not suitable for below 50 °C, because it gives the same reading for 42 °C and 0 °C .
Type R (Pt:Rh 87:13 by wt./ Pt)	-50 to 1,760	1.5	
Type S (Pt:Rh 90:10 by wt. / Pt)	-50 to 1,760	1.5	Low sensitivity 10 $\mu\text{V/K}$. Expensive

In addition to market available bulk material thermocouples, custom built thin-film thermocouples have gained a significant attention during the recent past in a broad spectrum of research. For example, Chu *et al*^[14] developed a thin film gold/ nickel nano-thermocouple with junction size of 100 nm \times 100 nm for applications in laser and electron beam irradiation. Other applications include, but not limited to, time-resolved surface temperature mapping^{[15][16]}, temperature measurements in machining^{[17]-[20]}, ultrasonic welding^{[21][22]}, medical applications^[23], engines^[24], gas turbines^[25], batteries^[26], and high-temperature PEM fuel cells^[27]. Thin-film thermocouple made from conductive

ceramics is an exciting research area with potential applicability into SOFC. Table 3.2 summarises some ceramic materials and their characteristics demonstrated as thermoelement materials. Unlike bulk-material thermocouples, thin-film thermocouples are fast responsive to temperature changes. Response times as short as 10 nS have been recorded in the literature^[28]. However, an important factor to consider in using thin-film thermocouples is their dimensional influence on the performance. Table 3.3 summarises some literature evidences on how the dimensions affect the performance.

Table 3.2 Ceramic thermocouple materials and characteristics

Material	Characteristics	Reference
In ₂ O ₃	Linear temperature-emf relationship from room temperature to about 1,700 °C	[29]
ZnO	Very complex relationship between temperature and Seebeck coefficient	
Nano composite comprised of NiCoCrAlY and aluminium oxide	Very high Seebeck coefficient of 375 μ V/K (relative to platinum) Enhanced high temperature stability	[30]
TiO ₂	Demonstrated operation up to 1,500 °C in gas turbine operating environments. Very linear temperature-emf relationship was demonstrated. Difference in Seebeck coefficient has been obtained by changing the sputtering conditions.	[31][32]

Table 3.3: Dimensional and fabrication influence on thermocouple performance

Parameter	Influence	Reference
Influence of film thickness on sensitivity	Sensitivity of Cu/ Cu-Ni thermocouples was observed to be decreasing with increase in film thickness.	[33]
	A study on thickness-emf relationship of thin film copper-constantan thermocouples reveals that the induced emf was independent of thickness above 1200 Å for copper and 1000 Å for constantan.	[34]
Influence of deposition rate on sensitivity	The dependence of Seebeck coefficient (hence, sensitivity) on film thickness varies with the deposition rate. Experiments were carried out on iron films with depositions rates of 12 Ås^{-1} , 2 Ås^{-1} , and 8 Ås^{-1} . Sensitivity was found to be almost independent of film thickness for films deposited at a rate of 8 Ås^{-1} .	[35]
Influence of surface roughness on sensitivity	Seebeck coefficient is independent of film surface roughness when film thickness is more than 400 Å for iron films.	[35]
Influence of junction size on sensitivity	Induced emf has no obvious dependence on junction size up to $3 \times 3 \text{ μm}^2$ for Ni-Cr thin film thermocouples.	[15]

3.1.3.1 The Principle of Operation

The operation of a thermocouple is based on the principle of thermoelectricity, which is the direct conversion of heat energy into electricity in a conductor. The amount of electricity produced (the electromotive force) is used as a measure of the temperature in thermocouples. When two dissimilar metals are joined to form a loop, and the two junctions are at two different temperatures, an electric current can be observed to flow through the closed circuit. This effect is known as the Seebeck effect. Figure 3.2 illustrates the Seebeck current flows (denoted by the two arrows) when the two dissimilar metals (A and B), which form a loop, has two temperatures at their junctions (T_1 and T_2). When current flows from thermoelement A to B at the cold junction, the thermoelement A is considered to be positive with respect to thermoelement B . The Seebeck effect is independent of any temperature distributions along the conductor as long as the conductors are homogenous^[36]; it relies on the temperature gradient between the two junctions.

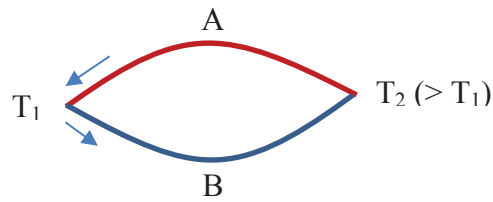


Figure 3.2 A schematic diagram of a thermoelectric loop

The Seebeck coefficient is used to calculate the magnitude of the voltage induced across a conductor when it is subjected to a given temperature gradient. Equation (3.3) defines the Seebeck coefficient where, S , ΔV , and ΔT are the Seebeck coefficient, the induced voltage, and the temperature gradient across the conductor, respectively. The Seebeck coefficient is a temperature dependant, materials specific (microstructure, impurities, etc.) function. The Seebeck coefficient of a few standard thermocouple materials at different temperatures are listed in Table 3.4. It can be noted that the Seebeck coefficient of some materials are positive while that of some others are negative. This can be understood by investigating the fundamental mechanisms behind the Seebeck effect, as briefly discussed next.

$$S = \frac{\Delta V}{\Delta T} \quad (3.3)$$

Table 3.4 Seebeck coefficients of some commercial thermocouple materials^[37]

Temperature (°C)	Seebeck Coefficient ($\mu V/^{\circ}C$)						
	<i>Alumel</i>	<i>Chromel</i>	<i>Pt</i>	<i>Pt/Rh</i>	<i>Pt/Rh</i>	<i>Nicrosil</i>	<i>Nisil</i>
0	-17.7	21.8	-4.0	1.3	1.4	11.4	-14.5
200	-16.2	23.7	-9.0	-0.2	-0.6	14.0	-19.0
400	-20.0	22.2	-12.3	-2.0	-2.8	14.0	-23.1
600	-24.0	18.5	-15.2	-3.9	-5.1	12.8	-26.2
800	-27.2	13.8	-18.3	-6.0	-7.5	10.9	-28.4
1000	-29.6	9.4	-21.4	-8.2	-9.9	8.8	-29.8

Although the Seebeck current was discovered in the early 1820s by the great scientist Sir Thomas Seebeck, the underline mechanism behind the Seebeck effect (named after him for his discovery) could be explained only with emerge of quantum mechanics. The reason for a conductor to induce a voltage across its ends, when they are under a temperature gradient is ascribed to the thermal diffusion of the majority charge carriers (electrons or holes) of the conductor. Even for metals, the thermally activated majority carries can be holes instead of electrons. This is why the Seebeck coefficients of different materials have different signs though all are metals. The positive and negative Seebeck coefficients of materials is described in terms of the curvature of Fermi surface of materials^[38]. Those metals have holes as majority thermally driven charge carries have positive Seebeck coefficients and those having electrons as the majority charge carriers have negative Seebeck coefficients. The phenomena of Seebeck voltage is depicted in Figure 3.3 in terms of charge carriers (either holes or electrons). When the conductor is heated at its one end, the charge carriers diffuse into the clod end. Therefore, an electric field is generated in the conductor due to the imbalance of charge. The generated electric field opposes further movement of charge carriers. For example, when electrons move from the hot end to the cold end making the hot end electrically positive with respect to the cold end, the direction of the built electric field is from the hot end to the cold end. This electric field opposes the movement of electrons from the hot end to the cold end



Figure 3.3 Schematic diagram showing the thermal diffusion of charge carriers under a temperature gradient

and the movements are sufficiently restricted as the field strength is built beyond a certain threshold value. The potential difference between the hot and the cold end at this threshold is the Seebeck voltage for that particular temperature gradient for that particular material.

Although the induced voltage across a single conductor is a measure of the temperature gradient that the conductor experience; this voltage cannot be measured directly. When a voltmeter probe is connected to the conductor, the probe itself is subjected to the same temperature gradient and a voltage is induced along the voltmeter probe due to this temperature gradient. Therefore, the measured voltage is the algebraic sum of the two voltages. This is why a thermocouple needs two thermoelements in order to measure the temperature at a point. Figure 3.4 shows a schematic diagram of a thermocouple and a voltmeter connected across its free ends. The free ends are at a temperature of T_0 while the junction is at a temperature of T_J . Two thermoelements are made of two different materials, namely A and B , whose Seebeck coefficients are S_A and S_B , respectively. Since there is no temperature gradient across the voltmeter, no voltage is induced across it as per Equation (3.3). Based on the definition of the Seebeck coefficient, the voltage induced across the two open ends of the thermocouple can be expressed as Equation (3.4). This equation shows that if the two thermoelements have the same Seebeck coefficient, no voltage will be induced across the open ends of the thermocouple. This is why a thermocouple must be made by joining two dissimilar materials. Further, it shows that the greater the difference in the Seebeck coefficients between the two thermoelements, the greater the induced voltage, thus better the resolution of temperature measurements. This is why thermocouples are formed by using materials having Seebeck coefficients of opposite signs.

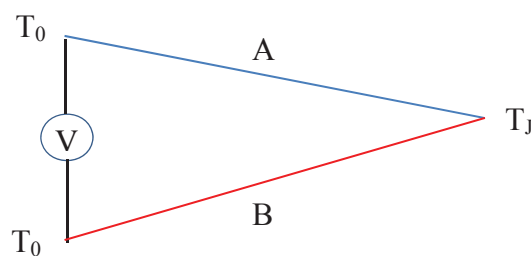


Figure 3.4 Schematic diagram of a thermocouple with a voltmeter connected across it

$$V = \int_{T_0}^{T_J} S_A dT + \int_{T_J}^{T_0} S_B dT = \int_{T_0}^{T_J} (S_A - S_B) dT \quad (3.4)$$

Where;

V – thermally induced voltage (electromotive force)

S_A, S_B – Seebeck coefficient of A and B, respectively

T_J, T_0 – temperature at the junction and at open ends, respectively

3.1.3.2 Cold Junction Compensation

It is evident from Equation (3.4) that the voltage induced across the open ends of the thermoelements is not a measure of the temperature at the junction. Instead, it is a measure of the temperature gradient between the free ends and the junction. Thus, only if the temperature at the free ends is known, the temperature at the junction can be calculated based on the measured voltage. If the free ends are kept at 0 °C (ice point), the measured voltage across the open ends is a measure of the temperature at the junction. However, in general, the open ends are at the room temperature, which is not 0 °C in most cases. In order to compensate this and to directly measure the actual temperature at the junction, thermocouple data logging systems use a feature called *Cold Junction Compensation*, which enables thermocouples to measure the true temperature at its junction without having to maintain its open ends at 0 °C.

There are two types of cold junction compensation mechanism: hardware compensation and software compensation. In both methods, the temperature at the open ends (known as the cold junction or reference junction) is measured separately using integrated circuit temperature sensor. In the hardware compensation, a voltage equivalent to the temperature at the open ends is externally applied across the open ends. Therefore, what the data logger records is the sum of the two voltages (the induced voltage described in Equation (3.4) and the externally applied voltage). Thus, the recorded voltage is equivalent to the voltage that the logger would record if the open ends were at ice point. In the software compensation, instead of applying an external voltage across the open ends, the equivalent voltage is computed within the software by taking the temperature at the open end as a reference. This voltage is added to the measured voltage every time a temperature is read. Since the software compensation involves extra computing steps at each temperature measurement, it has slower response than the hardware compensation.

3.1.4 Resistance Temperature Detectors (RTD)

RTD is, perhaps, the most stable and accurate temperature sensor in industrial scale. Platinum is the most expensive, most reliable, and the most linear RTD material with an excellent stability at elevated temperatures. Other common RTD materials include Ni, Cu, Au, W, and Ag. A standard platinum resistance temperature detector (SPRTD) is used in ITS-90 as the standard instrument to interpolate temperatures from 13.8033 K (triple point of hydrogen) to 1,234.93 K (freezing point of silver)^[39]. However, the upper-temperature limit of most industrial scale RTD sensors is approximately 750 °C. The standardised performance for platinum RTDs under BS1904:1984 and IEC 751:1983 is also limited to a maximum 850 °C. RTDs are very sensitive to strains and it must ensure strain free at all times of operation^[40]. Although platinum group materials are generally considered as oxidation resistant materials, at higher temperatures, volatile oxides are formed. PtO₂ is formed above 630 °C, and evaporation of these volatile oxides results in material loss at higher operating temperatures^[41] causing measurement instability of RTD. Characteristics of thin-film RTD have been assessed in research, but they were not successful beyond 400 °C^{[42][43]}. A research-level development of ceramic RTD that operates up to 1,400 °C was available in the literature^[44].

3.1.4.1 Principle of Operation

The positive correlation between the electrical resistivity and the temperature of metals is the fundamental physics behind the development of resistance temperature detectors. The physical meaning of the electrical resistance is the difficulty the material imposes on the free flow of electrons under the force of an electric field. This is a result of electrons' collision with atoms in the lattice structure; the higher the number of collisions the higher the resistivity. As the temperature increases, the internal energy of a substance increases (in this case, metal). Therefore, the atoms / molecules have higher vibrational kinetic energy. Because of these increased vibrations, the collisions between electrons and the molecules increases imposing more difficulties for the electrons to flow under a given electric field; thus, the electrical resistivity increases. The electrical resistivity is defined in Equation (3.5). According to this equation, the resistivity of a conductor can be defined as the resistance of a conductor across 1 m length of it, whose cross-sectional area is 1 m².

$$\rho = R \frac{A}{l} \quad (3.5)$$

Where,

ρ – Resistivity

R – Resistance

A – Cross-sectional area

l – Length of the conductor

Platinum is the most widely used material for RTDs. The change of the electrical resistance of platinum with temperature, known as the temperature coefficient of resistance, is defined as Equation (3.6) in the British Standards BS:1904:1984. The same standards define the resistance at temperature t for platinum RTDs as given in Equation (3.7) for temperatures from -200 °C to 0 °C and as Equation (3.8) for temperatures between 0 °C and 850 °C. The standard resistance values at operating temperatures are tabulated in BS:1904:1984. Therefore, measuring the resistance and comparing the measured value against the standardised resistance values reveals the temperature the RTD is subjected to.

$$\alpha = \frac{R_{100} - R_0}{100 \times R_0} \quad (3.6)$$

Where,

α - Temperature coefficient of resistance

R_{100} – Resistance at 100 °C

R_0 – Resistance at 0 °C

$$R_t = R_0(1 + At + Bt^2 + C(t - 100^\circ\text{C})t^3) \quad (3.7)$$

$$R_t = R_0(1 + At + Bt^2) \quad (3.8)$$

Where,

R_t – Resistance at temperature t

R_0 – Resistance at 0 °C

t – Temperature in degree Celsius

A – A constant of value $3.90802 \times 10^{-3} \text{ }^{\circ}\text{C}^{-1}$

B – A constant of value $-5.802 \times 10^{-7} \text{ }^{\circ}\text{C}^{-2}$

C – A constant of value $-4.27350 \times 10^{-12} \text{ }^{\circ}\text{C}^{-4}$

3.1.4.2 Resistance Measurements

Unlike thermocouples, which measure the temperature difference between the hot and the cold junctions, RTDs give the absolute temperature at the measuring point. Therefore, a RDT's measurement is a direct temperature measurement. However, unlike voltage measurements, resistance measurement is not a straightforward process. A known current is passed through the resistor, and the resulting voltage drop across the resistor is measured. Then, from the Ohms law, given in Equation (3.9), the resistance is calculated. Therefore, in order to measure the resistance (thus, temperature using RTD), a current source is needed. Based on the way the resistor element in the RTD is powered, there are three configurations of RTD namely, two-wire, three-wire, and four-wire configuration.

$$V = IR \quad (3.9)$$

Where,

V – Potential difference across the resistor

I – current through the resistor

R – Resistance of the resistor

Two-wire configuration

In this arrangement, schematically shown in Figure 3.5, the two lead wires of the resistance element are shared by the current source and the voltmeter. Since the current passes along the lead wires, the resistance in the lead wires causes voltage drop along the wires. In the way the voltmeter is connected, it records the voltage drop along the wires as well as that across the resistance element. Therefore, the measurements are associated with a significant level of errors. If the resistance of the lead wires is known, this error can be reduced to some extent through computation. However, the temperature effects on the wire resistance are difficult to assess during operation. Therefore, the measurement can still have significant errors.

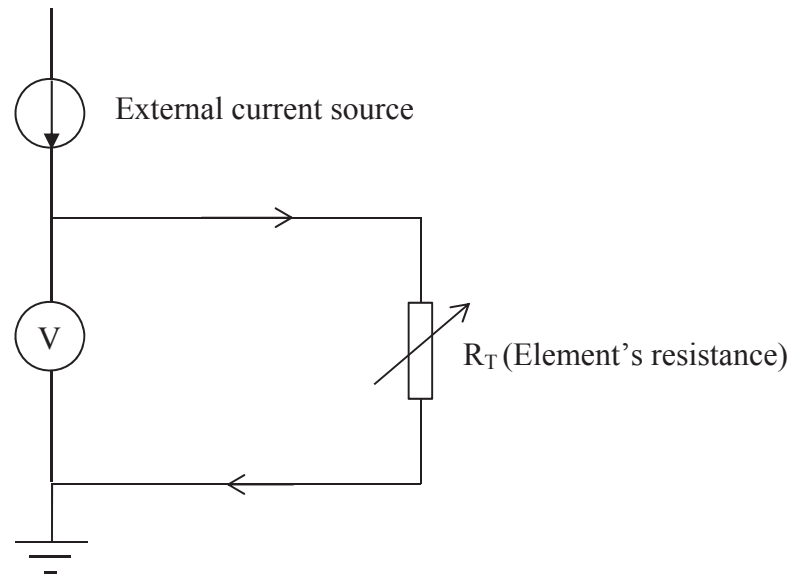


Figure 3.5 RTD two-wire configuration

Three-wire configuration

Figure 3.6 shows a schematic diagram of the three-wire configuration. As the diagram shows, differently to the two-wire configuration, only one lead wire of the resistance element is shared by the current source and the voltmeter. There is no voltage drop along the lead wire of the voltmeter as its high internal impedance does not permit current to flow through the voltmeter. Therefore, only the voltage drop along the shared lead wire of the resistance element will introduce errors in measurements. Hence, the three-wire configuration is more accurate than the two-wire configuration. However, each temperature sensing point requires three external wires for temperature measurements. This is not a favourable condition for multi-point temperature sensing in space constraint applications, such as fuel cells.

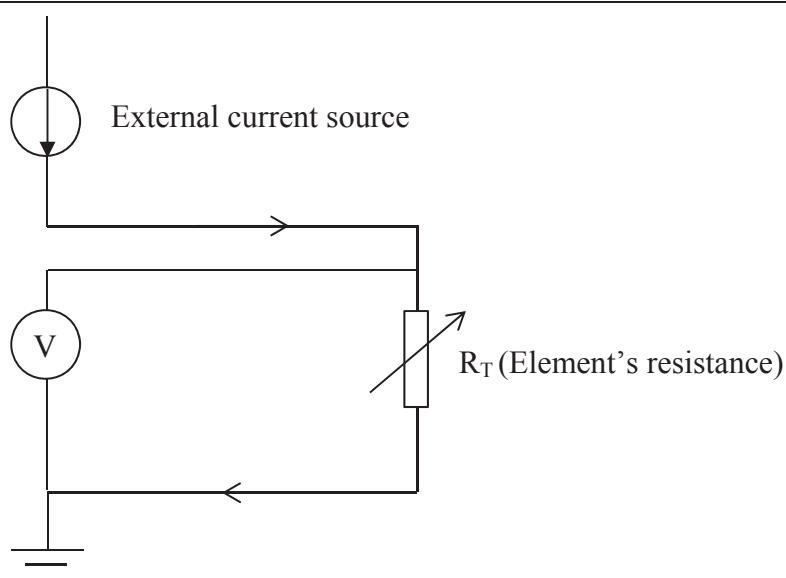


Figure 3.6 RTD three-wire configuration

Four-wire configuration

The four-wire configuration is schematically shown in Figure 3.7. As the diagram depicts, two separate lead wires are used to connect the voltmeter. Since no current is permitted to flow along these wires due to the high internal impedance of the voltmeter, there is no voltage drop along the voltmeter's lead wires. Although there is a voltage drop on the resistance element's lead wires because of the current source, since those wires are not shared with the voltmeter the voltmeter does not record those voltage drops. Thus, the voltmeter reading is a more accurate measure of the voltage drop across the resistance element compared to the other two configurations. Therefore, this arrangement gives the

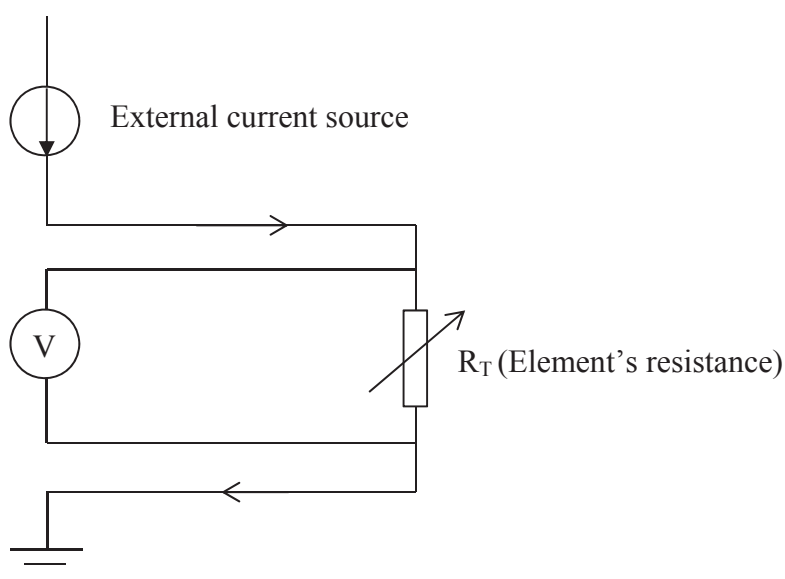


Figure 3.7 RTD four-wire configuration

greatest accuracy among all three configurations. However, on the other hand, this arrangement requires the largest number of wires per single temperature sensing points – four wires per sensing point. This is again not a favourable condition for space constrained applications when high spatial resolution is required in temperature measurements.

3.2 State of the Art SOFC Temperature Sensing

Present efforts on understanding the temperature distribution over cells and stack are predominantly based on simulations. In which, application of physical modelling^{[45]-[51]} as well as data-driven modelling, such as Artificial Neural Networks (ANN)^{[52]-[55]}, are noticeable. Physical models rely on a variety of assumptions and simplifications of operating conditions, which may not realistically exist in an operating stack. Therefore, these models need to be experimentally validated under different operating conditions prior to use for temperature predictions. In contrast, data-driven models eliminate the necessity of having an accurate knowledge of the cell operation. Data-driven models map input data onto output data without paying any insight into the cell operation. Hence, ANN models are free from simplifications assumptions that physical models require. However, the accuracy of an ANN model is governed by the accuracy of the training data set. Thus, it also requires an accurate experimental data set representing some different operating conditions. Further, although the chemical reactions within fuel cells are relatively straightforward, there are a number of reaction mechanisms that depend on the material and microstructure^{[56]-[58]}. Thus, the exact reaction mechanism is impossible to determine with any degree of certainty. Therefore, the experimental temperature measurement from operating SOFC stacks is a task with a significant importance.

Despite the aforementioned limitations, the simulations pave an excellent way to get a theoretical overview of the temperature distribution on a cell under various operating conditions. These results can be used as a guideline in experimental measurements, particularly, to determine the locations of importance in temperature sensing and the spatial resolution of measurements. For example, Figure 3.8 shows the simulated temperature distribution on 130 mm × 130 mm cell having electrochemically active cell area of 100 mm × 100 mm under three flow configurations. The cell is simulated to perform reforming reactions as well. The temperature distribution under counter-flow, co-flow, and cross-flow patterns are shown in Figure 3.8 (a), (b), and (c), respectively. Having investigated these temperature profiles on the cell, it can be estimated that a spatial resolution of approximate 10 mm × 10 mm would be necessary for experimental temperature measurements to better understand the temperature distribution. Another study by Iwata *et al.*^[59] also reveals the presence of a similar temperature distribution for cross-flow configuration as shown in Figure 3.9 for 100 mm × 100 mm cell with pure hydrogen. This result also suggests the need of approximately 10 mm × 10 mm resolution for experimental temperature measurements.

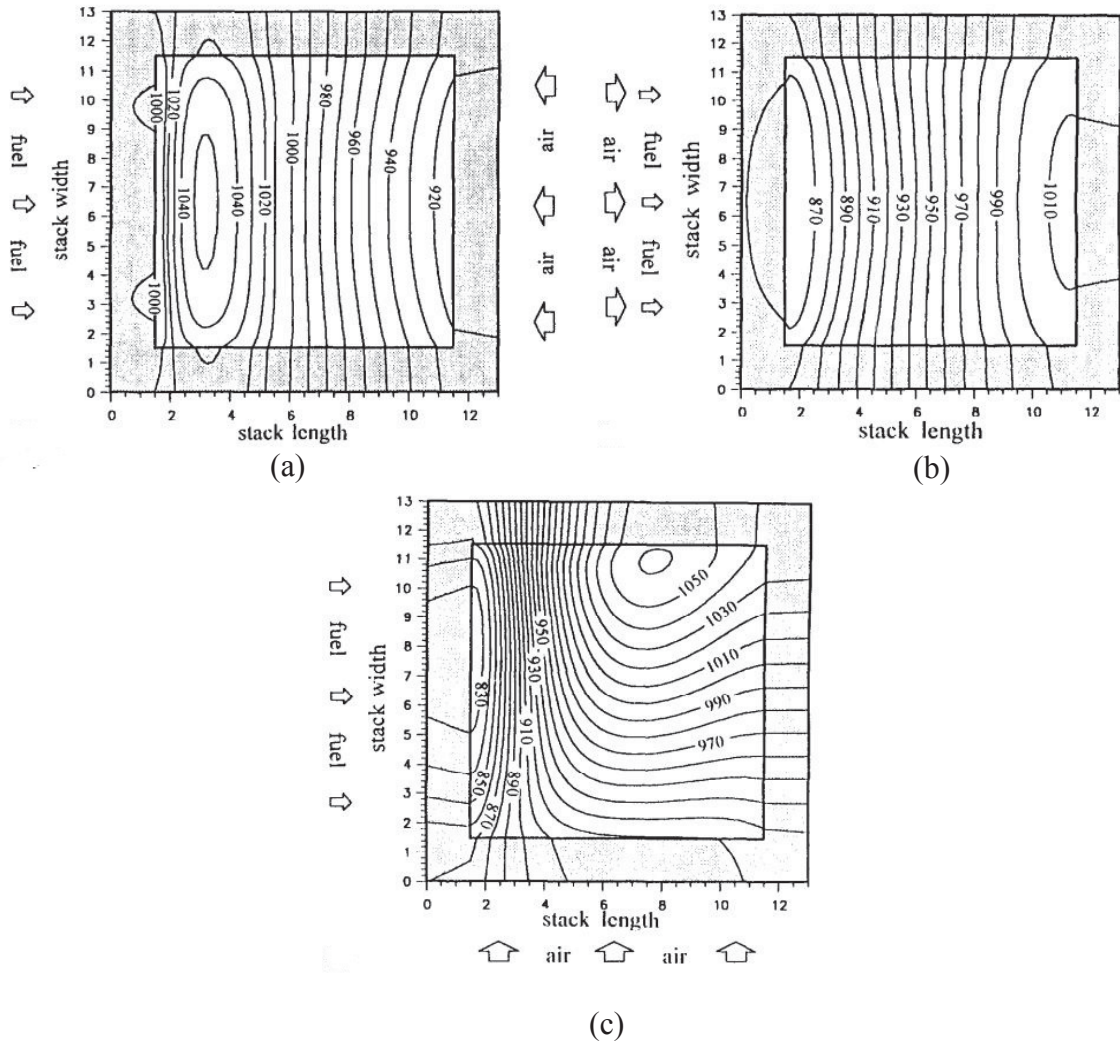


Figure 3.8 Simulated temperature distribution under different flow configurations (a) Counter-flow (b) co-flow (c) cross-flow^[60]

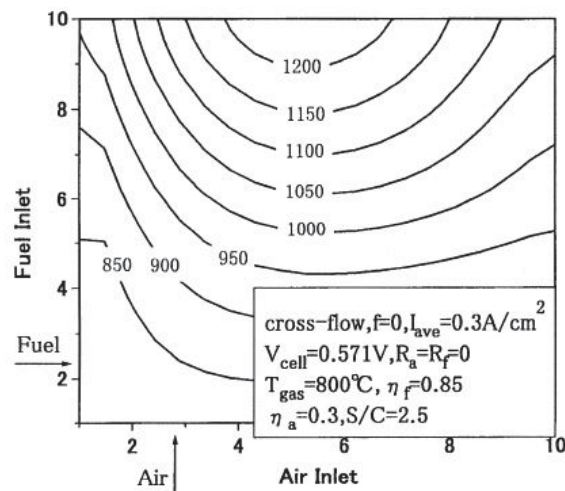


Figure 3.9 Simulated temperature distribution under cross-flow configuration^[59]

The number of experimental approaches to measure the cell/ stack temperature is very limited in the literature compared to simulations. In fact, only one of such was found when the literature survey was carried out, except the attempts made to measure the temperature of small pallet cells. However, a few such efforts were later published, though they have not met the specific research gap this thesis addresses. All those literature were critically evaluated, analysed, and synthesised to continuously refine the direction of the author's research.

In a study to investigate the steam-methane reforming process within a direct internal reforming SOFC, Saunders and Davy^[61] employed infrared thermometry to measure the surface temperature of a reformer anode (100 mm × 50 mm). A schematic diagram of the setup is given in Figure 3.10. Temperature measurements were made normal to the anode surface at 10 mm intervals along the centre line of the anode by focusing the thermometer (Omega Vanzetti Model No. 1562, 203.1 mm focal length, 0.91 mm spot size) through the sapphire window above the anode. The exact experimental setup is published elsewhere^[62]. Figure 3.11 shows the anode arrangement with sapphire window above it and Figure 3.12 shows the oven where the test setup was placed in.

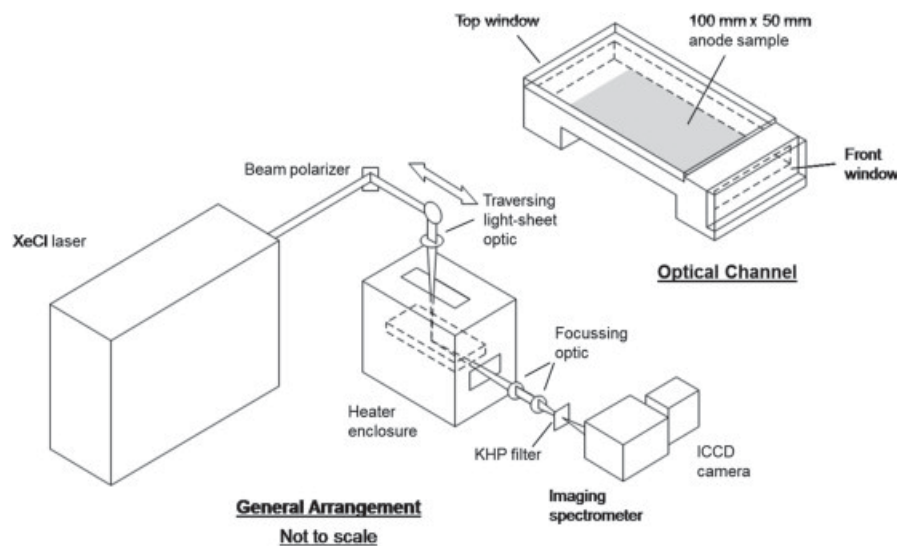


Figure 3.10 The schematic diagram of the experimental setup used to measure the anode temperature using IR thermometry^[61]

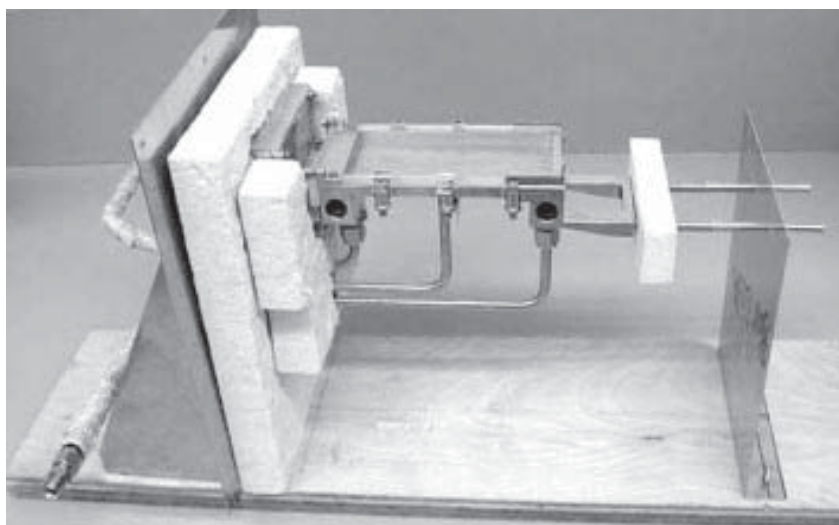


Figure 3.11 Special anode arrangement for IR temperature sensing^[62]

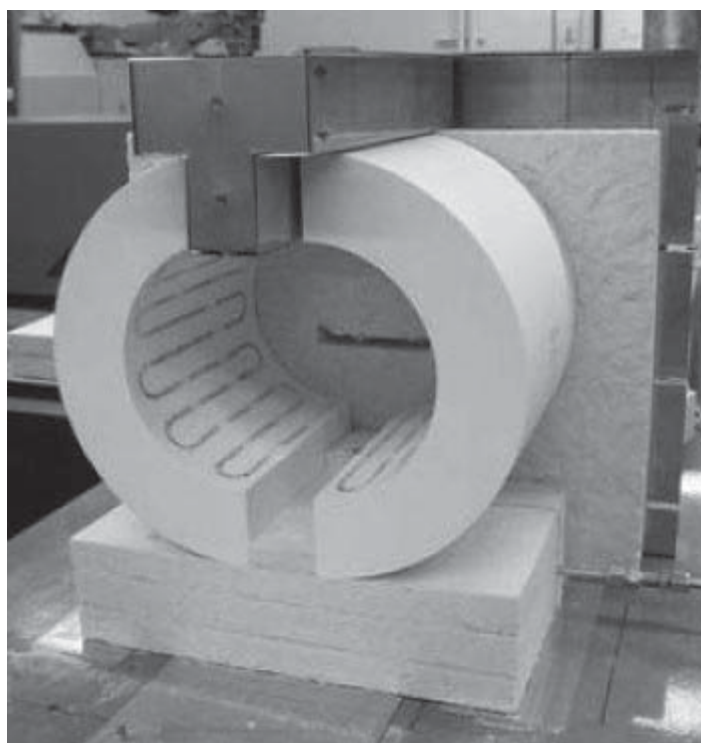


Figure 3.12 The oven with front window panel removed to provide optical access to the anode^[62]

This experimental setup had not been published by the time the literature survey was carried out. However, although non-contact thermometry was eliminated from the candidate methods; this experimental setup was still carefully investigated as IR thermometry is a good technique to get surface temperature profile with an excellent spatial resolution.

The use of IR thermometry in this setup is limited for point measurements. However, replacing the IR thermometer with a suitable IR imaging camera (ex: FLIR GF309 Infrared Camera), may facilitate obtaining proper surface temperature profiles. However, this kind of a special test rig arrangement cannot be adapted for commercial level stacks or even laboratory scale multi-cell stacks. On the other hand, the significant level of modifications done to the system disqualifies this being called as *in situ* measurements. Since this thesis is focused on *in situ* temperature measurements, this test rig arrangement does not provide tangible benefits. Instead, it re-confirmed that non-contact thermometry is not a candidate method. Although there are other approaches of using IR thermometry for SOFC temperature sensing from small cells, the focus of this thesis is laid on relatively larger cells (approx. 10 cm^2 or above active cell area) where, a larger temperature gradient can be expected. Thus, such works are not discussed here.

Razbani *et al*^{[63][64]} have made a more direct approach to measuring the operating temperature of a 6-cell SOFC stack by using commercial thermocouples (K-type, $\Phi 0.5\text{ mm}$). Five thermocouples were inserted into the stack through air channels between third and fourth cells. It was assumed that the difference between gas temperature and the electrode surface temperature is negligible. However, no evidence to justify this assumption is given. Because of the flow field of gas and the heat transfer characteristics of the electrode and gas, there may be a discrepancy between the gas temperature and the electrode temperature. Figure 3.14 shows the approximate locations of temperature sensing points in a cell ($86\text{ mm} \times 110\text{ mm}$) and Figure 3.13 shows the stack with thermocouples inserted. Celik *et al*^[65] also claim to have used 5 K-type thermocouples to measure temperature from two sets of SOFC short stacks of active cell area 16 cm^2 and 81 cm^2 . Figure 3.15 shows the locations of temperature probes in their experimental setup. These research findings confirm that thermocouple thermometry is applicable for SOFC temperature sensing. However, there remain two significant problems to address: 1) the measured temperature may not reflect the cell surface temperature where reactions take place 2) spatial resolution of measurements may not be sufficient to get a clear understanding of the role of temperature on the performance and the degradation.



Figure 3.13 SOFC stack with thermocouples^[63]

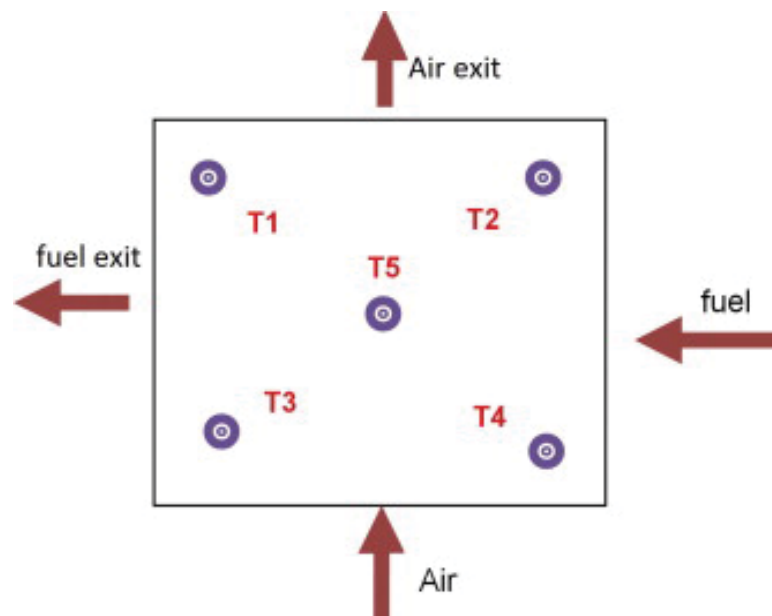


Figure 3.14 Temperature probe locations^[63]

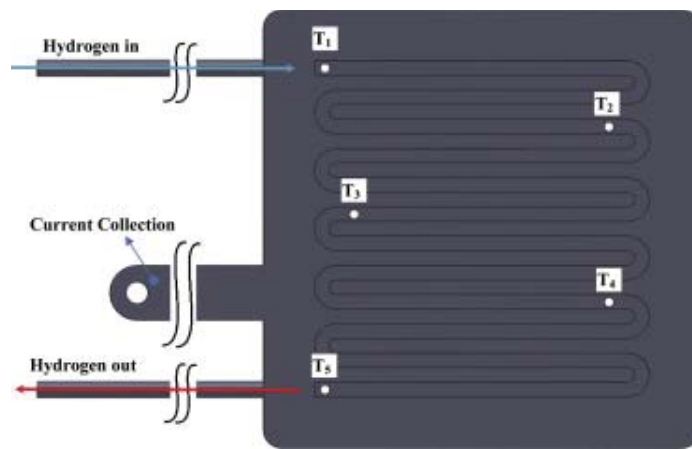


Figure 3.15 Different temperature probe locations^[65]

3.3 Aim and Objectives

3.3.1 Aim

The aim of this research is to develop a sensing technology to monitor *in situ* the cell surface temperature distribution of an operating SOFC.

3.3.2 Objectives

The objectives established to streamline the accomplishment of the aim are:

- 1) To critically evaluate the present methods of SOFC temperature sensing.
- 2) To understand the merits and limitations of presently available temperature sensing technologies with respect to SOFC temperature sensing.
- 3) To develop a sensing technology that can appreciably overcome the limitations associated with the present sensing technologies identified in objective 3.
- 4) To understand the cell temperature response under arbitrary operating conditions.
- 5) To qualitatively assess the significance of the surface temperature measurements compared with near-surface temperature measurements and to provide suggestions where appropriate.

3.4 Conclusions

The knowledge on temperature distribution at the cell level, where reactions take place, is vital to get a thorough understanding of different degradation mechanisms as well as performance characteristics of SOFC. Simulations provide a good foundation to understand temperature distribution under different operating conditions. However, *in situ* temperature measurements can provide very accurate information on the temperature distribution under a number of different operating conditions than the simulations could predict. Further, *in situ* temperature monitoring can be used as a performance measuring technique when testing new cell materials. This cannot be done with simulations unless the electrochemistry of such new materials is fully known. Therefore, the importance of *in situ* temperature sensing is well evident.

The literature on simulated temperature distributions presented in this chapter showed very dramatic temperature variations on a small cell under varying operating conditions. These results suggest the need of approximately 10 mm × 10 mm spatial resolution for experimental temperature measurements in order to get a better view of the thermal behaviour of a cell. However, the existing methods of temperature sensing from SOFC, except small button cells, does not either measure the cell level temperature distribution or measure it with sufficient spatial resolution. Therefore, the knowledge on the cell level temperature distribution with sufficiently higher spatial resolution can be identified as a significant research gap in the SOFC development cycle.

The thermometry selection is vital for an *in situ* sensing from SOFC. Among three sensing technologies investigated, thermocouple thermometry appears as the strongest candidate. Its prior applications in a number of other harsh environments build the confidence on its capability to meet the required operational characteristics within the SOFC environment. Although thermistors made from yttria also appear as a good choice, the technology is still at a highly research stage with many problems yet to be solved. On the other hand, the presently available temperature range of RTDs is not adequate to cover the operating temperature range of a typical SOFC. Although high-temperature RTD has been researched, the performance of such sensors is not yet standardised. Therefore, employing such non-standard technologies in already a complicated task of SOFC temperature sensing may lead to complex questions, which are difficult to investigate without extensively broadening the research scope. Therefore, thermistors and RTDs were eliminated from this research. In fact, when thermocouple thermometry provides a promising direction, there is no need to take an aerial route unless

thermocouples are found to be inappropriate. Therefore, thermocouple thermometry is chosen as the basis to *in situ* monitor the temperature from SOFC.

Although thermocouple thermometry has already been used for SOFC temperature sensing, enhancing the spatial resolution of measurement with thermocouples is a significant challenge. Since each sensing point of a thermocouple is composed of two unique thermoelements, use of thermocouples for multi-point temperature sensing requires $\{2N\}$ number of thermoelements for $\{N\}$ number of sensing points. Even if the two thermoelements of a thermocouple are bundled together forming a single wire, it still requires $\{N\}$ number of wires passing into a stack. Although there shouldn't be a much problem in sending a couple of tens of wires into a stack, as the number of sensing points increases to increase the spatial resolution of measurements, the problem becomes very acute causing disturbance to the normal operation of the stack. Thus, the present architecture of thermocouples is a significant barrier in employing thermocouple thermometry for *in situ* temperature sensing from SOFC with higher spatial resolutions.

Therefore, to address the fundamental knowledge gap of knowing the cell temperature distribution of operating SOFCs with higher spatial resolutions, the aforementioned technical barrier of thermocouple thermometry in measuring multi-point temperature sensing needs to be overcome first. Thus, this research project needs to first focus on utilising thermocouple thermometry for multi-point temperature sensing while preserving the meritorious characteristics of the thermometry.

3.5 References

- [1] Childs, P.R.N., *Practical Temperature Measurement*, Butterworth-Heinemann, 2001.
- [2] Kamat, R.K. and Naik, G.M., Thermistors – in search of new applications, manufacturers cultivate advanced NTC techniques, *Sensor Review*, 2002, 22(4), pp.334-340.
- [3] Tucker, M.C. and Cheng, L., Integrated thermal management strategy and materials for solid oxide fuel cells, *Journal of Power Sources*, 2011, 196(23), pp.10074-10078.
- [4] He, S., Mench, M.M., and Tadigadapa, S., Thin film temperature sensor for real-time measurement of electrolyte temperature in a polymer electrolyte fuel cell, *Sensors and Actuators A: Physical*, 2006, 125, pp.170-177.
- [5] Liang, C.-H., Tsai, C.C., Evaluation of a novel PTC thermistor for telecom overcurrent protection, *Sensors and Actuators A: Physical*, 2005, 121(2), pp.443-449.
- [6] Akbar, S.A. & Madou, M.J., 1998. Ceramic Based Resistive Sensors. *Journal of Electroceramics*, 2(4), pp.273-282.
- [7] Banerjee, A. & Akbar, S.A., 2000. A new method for fabrication of stable and reproducible yttria-based thermistors. *Sensors and Actuators A: Physical*, 87(1-2), pp.60-66.
- [8] Wang, C. et al., 1997. High-temperature thermistors based on yttria and calcium zirconate. *Sensors and Actuators A: Physical*, 58, pp.237-243.
- [9] Wang, C.C. et al., 1995. Review Electrical properties of high-temperature oxides, borides, carbides, and nitrides. *Journal of Materials Science*, 30, pp.1627-1641.
- [10] Norby, T. & Kofstad, P.E.R., 1986. Electrical Conductivity of Y2O3 as a Function of Oxygen Partial Pressure in Wet and Dry Atmospheres. *Journal of American Ceramic Society*, 89(11), pp.784-789.
- [11] Rossini, D.F., Report on International Practical Temperature Scale of 1968, *Journal of Chemical Thermodynamics*, 1970, 2, pp.447-459.
- [12] Abdelaziz, Y., Megahed, F.M., and Halawa, M.M., Stability and calibration of platinum/palladium thermocouples following heat treatment, *Measurement*, 2004, 35(4), pp.413-420.
- [13] Tong, A., Improving the accuracy of temperature measurements, *Sensor Review*, 2001, 21(3), pp.193-198.
- [14] Chu, D., Bilirl, D.T., Pease, R.F., and Goodson, K.E., Thin Film Nano Thermocouple Sensors for Applications in Laser and Electron Beam Irradiation, In: *12th International Conference on Solid State Sensors, Actuators and Microsystems*. 2003, pp.1112-1115.
- [15] Liu, H., Sun, W., Chen, Q. and Xu, S., Thin-Film Thermocouple Array for Time-Resolved Local Temperature Mapping. *IEEE Electron Device Letters*, 2011, 32(11), pp.1606-1608.
- [16] Kreider, G.K and DiMeo, F., Platinum/ Palladium thin-film thermocouples for temperature measurement on silicon wafers, *Sensors and Actuators A: Physical*, 1998, 69(1), pp. 46.
- [17] Basti, A., Obikawa, T., and Shinozuka, J., Tools with built-in thin film thermocouple sensors for monitoring cutting temperature, *International Journal of Machine Tools and Manufacture*, 2007, 47(5), pp.793-798.

-
- [18] Werschmoeller, D. and Li, X., Measurement of tool internal temperatures in the tool-chip contact region by embedded micro thin film thermocouples, *Journal of Manufacturing Processes*, 2011, 13(2), pp. 147
 - [19] Choi, H. and Li, X., Fabrication and application of micro thin film thermocouples for transient temperature measurement in nanoseconds pulsed laser micromachining of nickel, *Sensors and Actuators A: Physical*, 2007, 136(1), pp.118
 - [20] Kennedy, F.R., Frusescu, D., and Li, J. Thin film thermocouple array for sliding surface temperature measurements, *Wear*, 2007, 207(1-2), pp. 46
 - [21] Ho, J.-R., Chen, C.-C., and Wang, C.-H., Thin film thermal sensor for real time measurement of contact temperature during ultrasonic wire bonding process, *Sensors and Actuators A: Physical*, 2004, 111(2-3), pp.188-195.
 - [22] Zhao, J., Li, H., Choi, H., Cai, W., Abell, J.A., and Li, X., Insertable thin film thermocouples for in situ transient temperature monitoring in ultrasonic metal welding of battery tabs, *Journal of manufacturing Process*, 2013, 15(1), pp. 136
 - [23] Shaw, A., Pay, N.M, Perston, R.C, and Bond, A.D., A proposed standard thermal test object for medical ultrasound, *Ultrasound in Medicine & Biology*, 1999, 25(1), pp. 121
 - [24] Lei, J.-F. and Will, H.A., Thin-film thermocouples and strain-gauge technologies for engine applications, *Sensors and Actuators A: Physical*, 1998, 65(2-3), pp.
 - [25] Aniolek, G.E. and Gregory, O.J, Thin film thermocouples for advanced ceramic gas turbine engines, *Surface and Coatings Technology*, 1994, 68, pp. 70
 - [26] Mutyala, M.S.K, Zhao, J., Li, J., Pan, H., Yuan, C., and Li, X., In-situ temperature measurement in lithium ion battery by transferrable flexible thin film thermocouples, *Journal of Power Sources*, 2014, 260, pp. 43
 - [27] Ali, S.T., Lebak, J., Nielsen, L.P, Mathiasen, C., Møller, P., and Kær, S.K., Thin film thermocouples for in situ membrane electrode assembly temperature measurements in a polybenzimidazole-based high temperature proton exchange membrane unit cell, 2010, *Journal of Power Sources*, 195(15), pp.4835-4841.
 - [28] Heichal, Y., Candra, S., and Bordatchev, E., A fast-response thin film thermocouple to measure rapid surface temperature change, *Experimental Thermal and Fluid Science*, 2005, 33(2), pp. 153
 - [29] Wrbanek, J.D., Fralick, G.C., and Zhu, D., Ceramic thin film thermocouples for SiC-based ceramic matrix composites, *Thin Solid Films*, 2012, 520(17), pp.5801-5806.
 - [30] Gregory, O.J. Busch, E., and Fralick, G.C., Preparation and characterization of ceramic thin film thermocouples, *Thin Solid Films*, 2010, 518(21), pp.6093-6098.
 - [31] Gregory, O.J. and You, T., Ceramic temperature sensors for harsh environments. *IEEE Sensors Journal*, 2005, 5(5), pp.833-838.
 - [32] Gregory, O.J. and You, T., Integrated Ceramic Temperature Sensors For Harsh Environments, In *IEEE – Sensors*, 2004, pp. 1165-1168.
 - [33] Yang, L., Zhao, Y., and Zhou, H., The Influence of Size Effect on Sensitivity of Cu/CuNi Thin- film Thermocouple, *Physics Procedia*, 2011, 22, pp.95-100.
 - [34] Chopra, K., Bahl, S., and Randlett, M., Thermopower in Thin Film Copper—Constantan Couples, *Journal of Applied Physics*, 1968, 39, pp.1525-1528.
-

-
- [35] Schepis, R.S., Matienzo, L.J., and Unertl, W., Influence of deposition rates and thickness on the electrical resistivity and thermoelectric power of thin iron films, *Thin Solid Films*, 1994, 251, pp.99-102.
- [36] Pollock, D.D, *Thermoelectricity: Theory, Thermometry, tools*, ASTM Special Technical Publications, 1985.
- [37] Robin E. Bentley, *Handbook of temperature measurements Vol 03 : Theory and Practice of thermoelectric thermometry*, Springer, 1998
- [38] Fujita, S. and Suzuki, A., *Quantum Theory of Thermoelectric Power (Seebeck Coefficient)*, Kara, S., ed, Electromotive Force and Measurement in Several Systems, ISBN: 978-953-307-728-4, InTech, Available from: <http://www.intechopen.com/books/electromotive-force-and-measurement-in-several-systems/quantum-theory-of-thermoelectric-power-seebeck-coefficient->
- [39] Mcglashan, M.L., The International Temperature Scale of 1990 (ITS-90), *Journal of Chemical Thermodynamics*, 1990, 22, pp.653-663.
- [40] Tew, W.L. and Strouse, G., *Guidelines for Realizing the ITS-90*, NIST Technical Note, 1990
- [41] Hehn, H., High temperature behaviour of platinum group metals in oxidizing atmospheres, *Journal of Less-Common Metals*, 1984, 100, pp.321-339.
- [42] Chung, G.-S. and Kim, C.-H., RTD characteristics for micro-thermal sensors. *Microelectronics Journal*, 2008, 39(12), pp.1560-1563.
- [43] Kim, J., Kim, J., Shin, Y., and Yoon, Y., A Study on the Fabrication of an RTD (Resistance Temperature Detector) by Using Pt Thin Film, *Korean Journal of Chemical Engineering*, 2001, 18(1), pp.61-66.
- [44] Gregory, O.J. and You, T., Integrated Ceramic Temperature Sensors For Harsh Environments. In *IEEE – Sensors*. 2004, pp. 1165-1168.
- [45] Kulikovsky, A.A., A simple equation for temperature gradient in a planar SOFC stack , *International Journal of Hydrogen Energy*, 2010, 35(1), pp.308-312
- [46] Vander Steen, J.D.J., and Pharoah, J.G., Modelling Radiation Heat Transfer With Participating Media in Solid Oxide Fuel Cells, *Journal of Fuel Cell Science and Technology*, 2006, 3(1), pp.62.
- [47] Yakabe, H., T. Ogiwara, M. Hishinuma, and I. Yasuda, 3-D model calculation for planar SOFC, *Journal of Power Sources*, 2001, 102, pp.144-154
- [48] Nagata, S., Momma, A., Kato, T., and Kasuga, Y., Numerical analysis of output characteristics of tubular SOFC with internal reformer, *Journal of Power Sources*, 2001, vol.101(1), pp60-71
- [49] Fischer, K. and Seume, J.R., Thermo-mechanical stress in tubular solid oxide fuel cells: Part II – Operating strategy for reduced probability of fracture failure, *IET Renewable Power Generation*, 2012, 6, pp194.
- [50] Lockett, M., Simmons, M.J.H., and Kendall, K., CFD to predict temperature profile for scale up of micro-tubular SOFC stacks, *Journal of Power Sources*, 2004, 131(1-2), pp.243-246
- [51] Kakac, S., Pramuanjaroenkij, A., and Zhou, X.Y., A review of numerical modelling of solid oxide fuel cells, *International Journal of Hydrogen Energy*, 2007, 32(7), pp.761-786
-

-
- [52] Marra, D., Sorrentino, M., Pianese, C., and Iwanschitz, B., A neural network estimator of Solid Oxide Fuel cell performance for on-field diagnostics and prognostics applications, *Journal of Power Sources*, 2013, 241, pp.320-329
- [53] Razbani, O. and Assadi, M., Artificial neural network model of a short stack solid oxide fuel cell based on experimental data, *Journal of Power Sources*, 2014, 246, pp. 581-586
- [54] Milewski, J. and Swirski, K., Modelling the SOFC behaviour by artificial neural network, *International journal of hydrogen energy*, 2009, 34(13), pp.5546-5553
- [55] Arriagada, J., Olausson, P., and Selimovic, A., Artificial neural network simulator for SOFC performance prediction, *Journal of Power Sources*, 2002, 112(1), pp 54-60
- [56] Inoue, T., Eguchi, K., Setoguchi, T., and Arai, H., Cathode and anode materials and the reaction kinetics for the solid oxide fuel cell, 1990, 40/41(1), pp.407-410.
- [57] Kamata, H., Hosaka, A., Mizusaki, J., and Tagawa, H., High temperature electrocatalytic properties of the SOFC air electrode, *Solid State Ionics*, 1998, 106(3-4), pp.237-245.
- [58] Hammouche, A., Siebert, E., Hammou, A., Kleitz, M., and Caneiro, A., Electrocatalytic Properties and Nonstoichiometry of the High Temperature Air Electrode $\text{La}_{1-x}\text{Sr}_x\text{MnO}_3$, *Journal of the Electrochemical Society*, 1991, 138(5), pp.1212-1216.
- [59] Iwata, M., Hikosaka, T., Morita, M., Iwanari, T., Ito, K., Onda, K., Esaki, Y., Sakaki, Y., and Nagata, S., Performance analysis of planar-type unit SOFC considering current and temperature distribution, *Solid State Ionics*, 2000, vol.132(3-4), pp.297-308
- [60] Achenbach, E., Three-dimensional and time-dependent simulation of a planar solid oxide fuel cell stack, *Journal of Power Sources*, 1994, 49(1-3), pp.333-348
- [61] Saunders, J.E.A. and Davy, M.H., In-situ studies of gas phase composition and anode surface temperature through a model DIR-SOFC steam-methane reformer at 973.15K, *International Journal of Hydrogen Energy*, 2013, vol. 38(31), pp.13762-13773
- [62] Saunders, J.E.A. and Davy, M.H., High-temperature vibrational Raman spectroscopy of gaseous species for solid-oxide fuel cell research, *International Journal of Hydrogen Energy*, 2012, 37(4), pp.3403-3414.
- [63] Razbani, O., Waernhus, I., and Assadi, M., Experimental investigation of temperature distribution over a planar solid oxide fuel cell, *Applied Energy*, 2013, 105, pp.155-160
- [64] Razbani, O. and Assadi, M., Artificial neural network model of a short stack solid oxide fuel cell based on experimental data, *Journal of Power Sources*, 2014, 246(15), pp. 581-586
- [65] Celise, S., Timurkuthluk, B., and Mat, M.D. Measurement of the temperature distribution in large solid oxide fuel cell short stack, *International Journal of Hydrogen Energy*, 2013, 38, pp10534-10541.
-

**Chapter 4 : Design and Numerical Calculations of
Multi-Junction Thermocouples**

Chapter Summary

This chapter presents two multi-junction thermocouple architectures, namely, the array and the grid architecture for multi-point temperature measurements from SOFC with fewer thermoelements. The thermoelectric performances of these architectures in temperature measurement are numerically calculated based on Seebeck theory.

Section 4.1 introduces the rationale for the proposed architectures. Sections 4.1.1 and 4.1.2 describe the underlying science. The array and the grid architectures are described in Sections 4.1.3 and 4.1.4, respectively. Section 4.2 is dedicated to describe the detailed procedure of numerical calculations where, Section 4.2.1 describes the method of Seebeck coefficient calculation at different temperature and Section 4.2.2 describes the method employed to calculate the temperature using numerical data. Section 4.2.3 describes how the thermocouple materials were chosen for rest of the calculations in this chapter. The performance of the array architecture under different operating conditions is presented and discussed in Section 4.3, while the performance of the grid architecture is presented and discussed in Section 4.4. Chapter concludes with some conclusions made based on the results of the numerical calculations, in Section 4.5.

4.1 Introduction

In Chapter 2, a conclusion was systematically drawn that the thermocouple thermometry is the most convincing form of thermometry for *in situ* temperature sensing from solid oxide fuel cells (SOFCs). However, the design constraint of thermocouples requiring two thermoelements⁴ per each independent sensing point was identified as a barrier to increasing the spatial resolution of temperature measurements from SOFC without causing significant adverse effects on fuel cell performance. Difficulty in passing a large number of wires through the gas-tight sealing is one of the significant technical challenges in increasing the spatial resolution of measurement when using conventional thermocouples. Further, the potential disturbance that these wires may cause to a stack's operation might divert the stack from its normal operation. Therefore, the measured temperature may not be accurate enough to represent a cell's temperature under normal operation. To measure the cell surface temperature distribution with sufficiently higher spatial resolution (approximately 10 mm × 10 mm as stated in Chapter 3) while reducing the aforementioned disadvantages of using thermocouples, this chapter proposes two thermocouple architectures based on the same concept of sharing thermoelements between sensing points to measure temperatures from multiple points with fewer number of thermoelements than sets of thermocouples would require for the same number of temperature measuring points. The underlying science of operation of these multi-junction thermocouples is the same Seebeck effect that thermocouple thermometry is based on. In addition, the law of intermediate conductors in thermocouple thermometry is also used to introduce intermediate junctions along thermoelements to reduce the number of thermoelement requirement by sharing thermoelements between sensing points.

4.1.1 Seebeck Effect

When two dissimilar conductors (for example, wires) are joined at their ends forming a closed loop, and when the two joints are at two different temperatures; a very small electric current can be observed to flow through the closed loop. This temperature-driven flow of current is due to the Seebeck effect. The name Seebeck is given to this phenomenon as an honour to Sir Thomas Seebeck, who first observed this phenomenon. In other words, when the two ends of an open-ended conductor are kept at two different temperatures, thus, subjecting the conductor to a temperature gradient along its length, an electromotive force (EMF) is induced along the length of the conductor. This is depicted in Figure 4.1 where, T_1 and T_2 are the temperatures at the ends and, ΔV is the induced

⁴ Each of the two conductors that form a thermocouple by joining together is called a thermoelement.

voltage due to Seebeck effect. (A detailed description of the Seebeck effect is presented in Chapter 3)

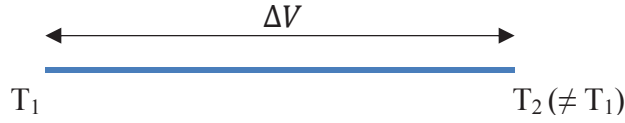


Figure 4.1 A schematic representation of the Seebeck voltage

The magnitude of the induced voltage per unit temperature gradient is mainly a material specific, temperature-dependent property called “Seebeck coefficient”. The Seebeck coefficient (S) is defined in Equation (4.1). The equation is written in differential form because, the Seebeck coefficient, so as the Seebeck effect, varies with temperature. However, if the Seebeck coefficient does not change very sharply with temperature for any material, then, the Seebeck coefficient of such material at any temperature can be expressed as Equation (4.2) without introducing significant errors into calculations.

$$S = \frac{dV}{dT} \quad (4.1)$$

Where;

dV – the potential difference across the conductor at a given temperature

dT – the temperature gradient across the conductor

$$S = \frac{\Delta V}{\Delta T} \quad (4.2)$$

Where;

ΔV – the potential difference across the conductor at a given temperature

ΔT – the temperature gradient across the conductor

4.1.2 The Law of Intermediate Conductors

The underlying science of multi-junction thermocouples, proposed for SOFC temperature sensing in this thesis, is the law of intermediate conductors for thermocouples. Therefore, before explaining the mathematical calculations, the law is described below.

The law of intermediate conductors states that ‘the sum of the absolute thermoelectric powers of dissimilar conductors is zero when their ends are at the same

uniform temperature' ([36], p.122). This law has been used as the basis to develop multi-junction thermocouples that share thermoelements between sensing points to reduce the number of thermoelements required in multi-point temperature sensing.

This law can be proven mathematically using Seebeck theory described previously. Figure 4.2 shows a schematic diagram of a thermocouple having an intermediate conductor in one of its thermoelements (the section $b-c$ on the thermoelement $a-d$). Thermoelements $a-b$ and $c-d$ are made of the same material having Seebeck coefficient S_A . Thermoelement $e-d$ is made of a different material having Seebeck coefficient S_B (essentially, $S_A \neq S_B$ for the functioning of the thermocouple). The Seebeck coefficient of the intermediate conductor, $b-c$, is S_C , which must be different than S_A , but it can be similar to or different than S_B . The distal ends of the thermocouple leads are at temperature T_0 , and the hot junction is at T_J . The temperatures at b and c are T_B and T_C , respectively. V_{emf} is the electromotive force (EMF) induced across the distal ends of the thermoelements due to the temperature gradient between the junction and distal ends of the thermoelements. This voltage can be calculated by rearranging Equation (4.1) and performing cyclic-integration over the entire temperature cycle (from T_0 to T_0 via T_B , T_C , and T_J) along thermoelements as given in Equation (4.3). The result of the cyclic integration is given in Equation (4.4).

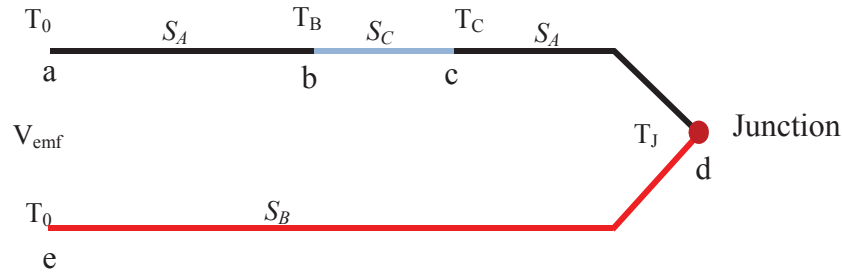


Figure 4.2 Schematic diagram of a thermocouple with an intermediate conductor

$$V_{emf} = \oint S dT \quad (4.3)$$

Where,

S – Seebeck Coefficient of the thermoelement concerned at its temperature

$$V_{emf} = \int_{T_0}^{T_J} S_B dT + \int_{T_J}^{T_C} S_A dT + \int_{T_C}^{T_B} S_C dT + \int_{T_B}^{T_0} S_A dT \quad (4.4)$$

Where,

V_{emf} – electromotive force (EMF) across the distal ends of thermocouple

S_A – Seebeck coefficient of thermoelements a-b and c-d

S_B – Seebeck coefficient of thermoelements e-d

S_C – Seebeck coefficient of the intermediate conductor b-c

T_0 – Temperature at the distal ends of thermoelements

T_J – Temperature at the junction

T_B / T_C – Temperatures at the two ends of the intermediate conductor b-c

If there is no temperature gradient present across the intermediate thermoelement (b-c) thus; $T_B = T_C$, the integration term associated with S_C in Equation (4.4) yields zero. Therefore, mathematically, Equation (4.4) simplifies to Equation (4.5) where Equation (4.5) is equivalent to the voltage induced across a thermocouple made of two thermoelements having Seebeck coefficients S_A and S_B and the junction at temperature T_J while the distal ends are at temperature T_0 . Therefore, the presence of an intermediate conductor does not influence the temperature measurements when there is no temperature gradient across the intermediate conductor. This shows the potential of making intermediated junctions on thermoelements to produce multi-junction thermocouples to make multi-point temperature measurements with a reduced number of thermoelements.

$$V_{emf} = \int_{T_0}^{T_J} S_B dT + \int_{T_J}^{T_0} S_A dT \quad (4.5)$$

Based on this scientific foundation, two multi-junction thermocouple architectures, namely the array architecture and the grid architecture, were investigated. The array architecture is the foundation design of the multi-junction thermocouples while; the grid architecture is a derivative of it. Although the concept of multi-junction thermocouples is scientifically sound, practical implementation requires extensive investigations to understand the factors influencing the performance. Thus, some numerical calculations to understand the performance under different fabrication and operating conditions were performed.

4.1.3 Array Architecture

The recursive unit of the array architecture is schematically shown in Figure 4.3. Thermoelement c must be made of a material different from that of both thermoelements a and b . The thermoelement material of a and b can either be the same or distinct from each other. The intersection of thermoelements c and b forms the first temperature measuring junction (J_1), and the intersection of thermoelements c and a forms the second temperature measuring junction (J_2). Any external circuitry (such as a data logger) interfaces with the thermocouple array at the connection-pads denoted by p1, p2, and p3 to measure the electromotive forces (EMFs) generated as a result of the temperature at junctions. The EMF v_1 is a measure of the temperature gradient between J_1 and the connection-pads. The EMF v_2 is a measure of the temperature gradient between J_2 and the connection-pads. Therefore, in general, the temperature at the connection-pads must be known in order to compute a junction's temperature (refer Chapter 2 for the operational principle of thermocouples). If connection-pads maintain the same constant temperature, a single temperature measurement of a pad is sufficient, making the process simpler. Thus, the enclosed region denoted by k is considered an isothermal region, whose temperature may be measured separately with a commercial temperature sensor. In a special case where the connection-pads are at the same temperature as the data logger, the cold junction compensation feature of a data logger (e.g., NI 9213^[2]) can directly compute the junctions' temperatures without requiring the connection-pads' temperatures to be measured separately (refer Chapter 2 for a description on cold junction compensation).

Three different designs of the array architecture, based on the above recursive unit, are shown in Figure 4.4; each colour represents a unique material. The designs are different in the number of isotherms. All designs have nine independent temperature sensing points, numbered from 1 to 9. The design in Figure 4.4(a) requires the lowest number of thermoelements among all: it requires $\{N+1\}$ number of thermoelements for

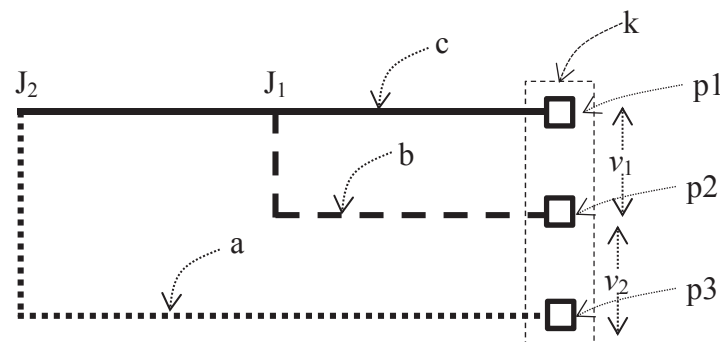
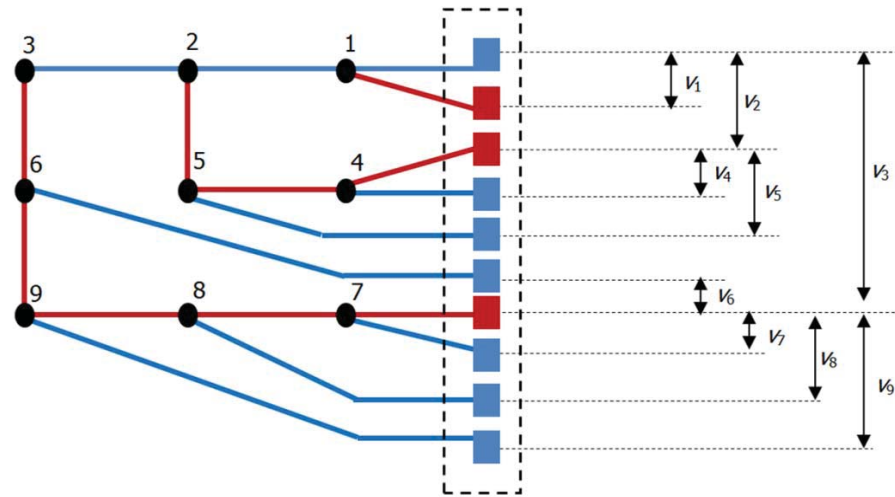


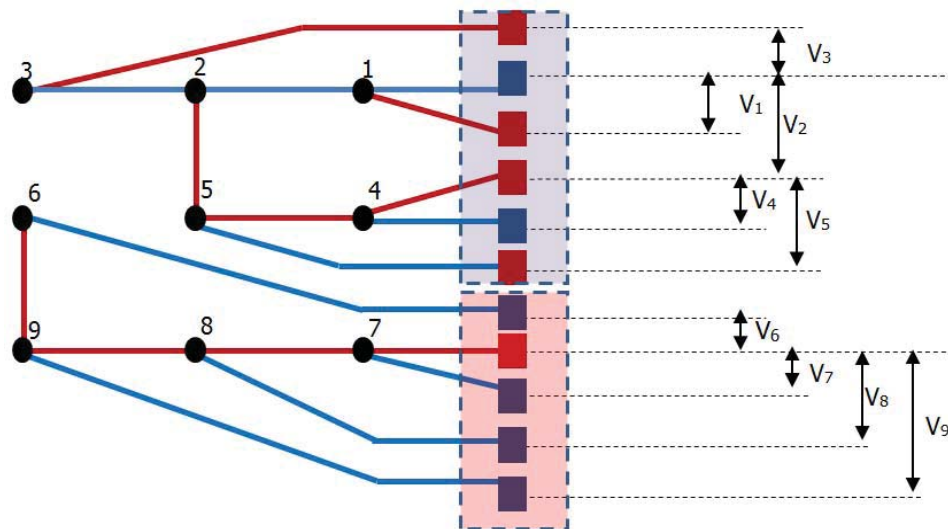
Figure 4.3 Recursive unit of the array architecture

$\{N\}$ number of temperature sensing points. However, this arrangement has only one isotherm covering all the connection-pads (the rectangle drawn in dashed line encompassing all the connection-pads). Unless the connection-pads are at room temperature, maintaining a large isotherm is a challenging task, particularly with a large number of junctions. The second design, shown in Figure 4.4(b), has two isotherms. Therefore, one set of connection-pads can stay at one temperature while the others remain at another temperature. Although this arrangement reduces the size of the isotherm, the number of thermoelements has increased to 11. Therefore, this arrangement requires $\{N+2\}$ number of thermoelements for $\{N\}$ number of temperature measuring points. The third design, shown in Figure 4.4(c), further increases the number of isotherms to three, and consequently, it requires $\{N+3\}$ number of thermoelements for $\{N\}$ temperature measuring points. Since reducing the number of isotherms increases the number of thermoelements, an appropriate balance must be reached considering application-specific constraints and requirements.

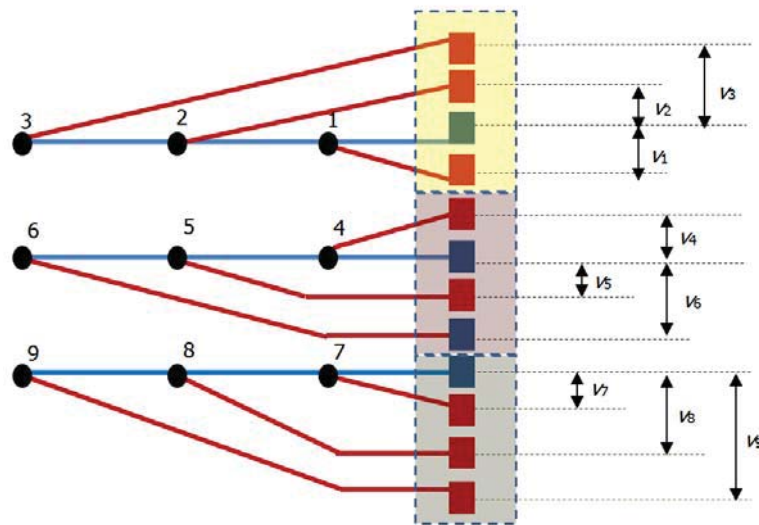
If multi-junction thermocouples are made of wires, sufficiently long wires can be used to ensure that thermoelements are directly connected to the data logger at data logger's temperature. However, if thermoelements are made integral to cells as thin-films, the external wire connection must be made at the cell's temperature. Nevertheless, if the external wires are chosen from the same thermoelement material, the functional connection can still be brought to the data logger's temperature although the physical connection is made at the cell's temperature. Under these conditions, the need of maintaining isotherms can be avoided. This is, in fact, a widely adopted method to extend thermocouples' lead wires. A detailed discussion of this approach is presented in Chapter 5.



(a) N+1 architecture



(b) N+2 architecture



(c) N+3 architecture

Figure 4.4 Three iterations of the array architecture

4.1.4 Grid Architecture

The grid architecture requires even fewer thermoelements than the array architecture requires. While the array architecture requires at least one thermoelement in excess to the number of temperature measuring points, the grid architecture measures temperatures at $\{N^2\}$ number of points with only $\{2N\}$ number of thermoelements. Therefore, the grid delivers the greatest reduction in the number of thermoelements required for multi-point temperature sensing. The reduction of thermoelements becomes more prominent when the number of temperature sensing points increases. For example, a grid of 100 temperature sensing points (junctions) can be made with only 20 thermoelements. This is a significant advantage in enhancing the spatial resolution of measurements.

The recursive unit of the grid architecture is schematically shown in Figure 4.5. Thermoelements a and b are made of one material, and thermoelements c and d are made of a second material. The intersection of thermoelements a and c forms junction J_1 , and that of a and d forms junction J_2 . Similarly, the intersection of thermoelements c and b forms junction J_3 , and that of b and d forms junction J_4 . The primary criterion in selecting thermoelements is: any two thermoelements that form a junction by intersection must be made of different materials. (In fact, the “difference” is the difference in their Seebeck coefficients, not necessarily the chemical composition). Connection-pads, p_1 to p_4 , are where the external circuitry, such a data logger, interfaces with the thermocouple grid to measure the thermoelectric EMF generated along thermoelements. For example, the EMF measured between connection-pads p_1 and p_3 is a measure of the temperature gradient

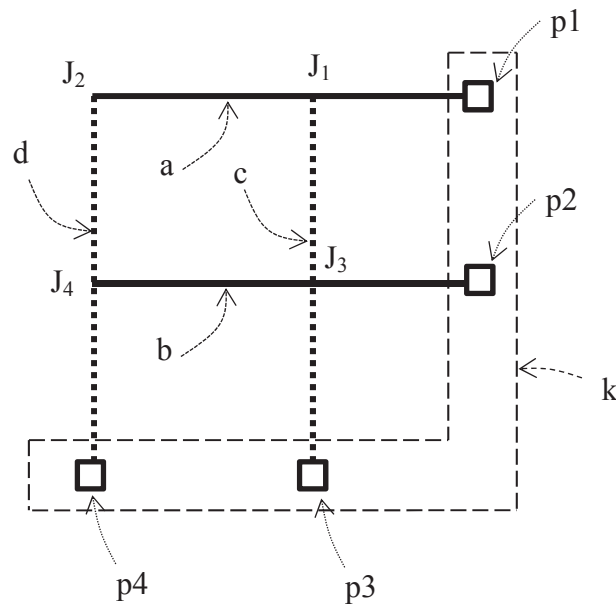


Figure 4.5 The recursive unit of the grid architecture

between J_1 and the connection-pads. Similarly, the EMF measured between p_2 and p_4 is a measure of the temperature gradient between J_4 and the connection-pads. The requirement of maintaining isotherms (the dotted enclosure denoted by k) and the arrangement to avoid that requirement are the same with the array architecture presented previously.

A multi-junction thermocouple grid having nine temperature measuring points is schematically shown in Figure 4.6. Hence, it is equivalent to the array architecture presented previously concerning the number of temperature measuring points. As the sketch depicts, this design requires only six thermoelements for nine independent temperature sensing points (equivalent to $\{N\} = 3$). The dotted enclosure is the isotherm as described previously.

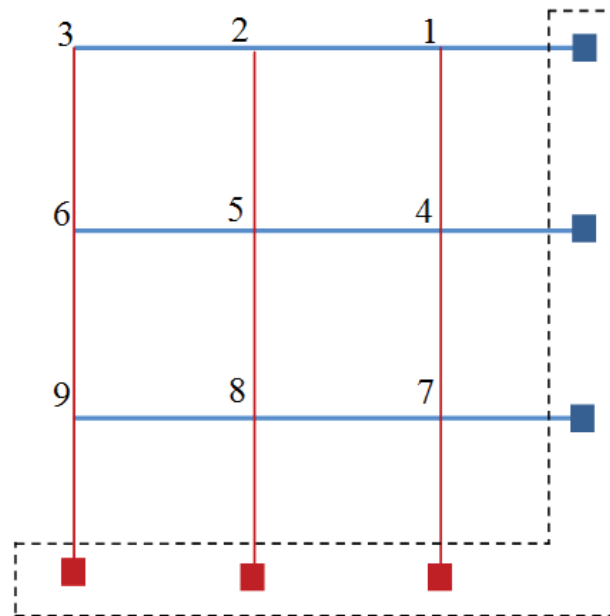


Figure 4.6 A grid architecture with nine temperature sensing points

Although the $\{N^2\}$ to $\{2N\}$ arrangement restricts the number of temperature measuring points to a second order pattern of an integer (e.g., 4, 9, 16, etc.), a different plurality of the recursive unit can easily break this restriction; however, this occurs at the expense of increasing the number of thermoelements. For example, appending more recursive units to the sketch in Figure 4.6 will yield 11 temperature measuring points with seven thermoelements. Although the $\{N^2\}$ to $\{2N\}$ relationship is broken in this instance, the number of thermoelements is still less than what would be required with thermocouples or array architecture for 11 temperature measuring points.

4.2 Numerical Calculation of Performance

Although both architectures have a scientific basis supported by the Seebeck theory and the law of intermediate conductors for thermocouples, it is advantageous to evaluate the performance numerically to investigate operational restrictions and effectiveness prior to laboratory testing. Therefore, a set of numerical calculations were performed using purposely written MATLAB codes to assess the performance of the array and the grid architectures under different fabrication and operational conditions. The calculations were carried out over a temperature range from 700 °C to 900 °C to adequately cover the typical operating temperature range of an operating SOFC.

Since NIST⁵ stipulated performance data are available for commercial thermocouple materials, those materials were the material choice for the calculations. Among them, K type (alumel and chromel), S type (Pt / Rh 87% / 13% and Pt), R type (Pt/Rh 90%/10% and Pt), and N type (nicrosil and nisil) were specifically chosen considering their high-temperature applicability.

4.2.1 Method of Seebeck Coefficient Calculation

Seebeck coefficients of the chosen materials from 0 °C to 1,000 °C with 200 °C intervals were taken from published data (Table 4.1). The Seebeck coefficients at other temperatures, at 1 °C interval, were obtained using polynomial regression. The criterion for selecting the degree of polynomial was to ensure the estimation error, defined in Equation (4.6) to be a minimum within the temperature range from 700 °C to 900 °C; this is the temperature range within which the thermocouple network (array or grid) is expected to be most accurate during its operation. Fifth order polynomial regression was found to minimise the estimation error. The polynomial regression equation is given in

Table 4.1 Seebeck coefficient^[37]

Temperature (°C)	Seebeck Coefficient ($\mu V/^{\circ}C$)						
	<i>Alumel</i>	<i>Chromel</i>	<i>Pt</i>	<i>Pt/Rh</i>	<i>Pt/Rh</i>	<i>Nicrosil</i>	<i>Nisil</i>
0	-17.7	21.8	-4.0	1.3	1.4	11.4	-14.5
200	-16.2	23.7	-9.0	-0.2	-0.6	14.0	-19.0
400	-20.0	22.2	-12.3	-2.0	-2.8	14.0	-23.1
600	-24.0	18.5	-15.2	-3.9	-5.1	12.8	-26.2
800	-27.2	13.8	-18.3	-6.0	-7.5	10.9	-28.4
1000	-29.6	9.4	-21.4	-8.2	-9.9	8.8	-29.8

⁵ National Institute of Standards and Technology

Equation (4.7) and the polynomial coefficients are listed in Appendix I. Further improvement in estimation accuracy with K-type materials could be achieved by changing the Seebeck coefficient of alumel at 200 °C to $-17.35 \mu V/^{\circ}C$ from its measured value of $-16.2 \mu V/^{\circ}C$. Although this change was not experimentally or otherwise supported, the change was adapted to increase the accuracy of calculations because the accuracy of temperature estimation is more important than the accuracy of the Seebeck coefficient at one temperature. These interpolated Seebeck coefficients were used for all the calculations presented in this chapter.

$$\text{estimation error} = |T_{\text{true}} - T_{\text{estimate}}| \quad (4.6)$$

Where,

T_{true} – true temperature (i.e. the set temperature in calculations)

T_{estimate} – estimated temperature based on the numerically generated EMFs

$$S_t = \sum_{i=0}^n (a_{n-i})t^i$$

Where,

S_t – Seebeck coefficient at temperature t °C (4.7)

a_{n-i} – The polynomial coefficient of the $(n-i)^{\text{th}}$ element

t – temperature in °C

n – degree of the polynomial

4.2.2 Method of Temperature Calculation

In order to calculate the temperature at a junction, the electromotive force (EMF) induced at the junction must be calculated first. Once the EMF is known, the corresponding temperature can be calculated using standardised conversion functions, generally known as inverse temperature functions. (The inverse temperature functions for all commercial thermocouple materials are available in NIST database).

Since the Seebeck coefficient is a function of temperature, if that function is known correctly, the EMF for a given temperature gradient can be calculated by evaluating the integral given in Equation (4.8). However, there are no standardised functions for Seebeck coefficient in terms of temperature; only standardised EMF values for each

commercial thermocouple type at different temperatures are available in NIST database. Therefore, it is impossible to use integration to calculate EMFs. Thus, a simple numerical technique, which can make sufficiently accurate temperature estimations, was adapted to estimate the EMF generated under all temperature gradients considered in the calculations as described below.

$$EMF = \int_{T_1}^{T_2} SdT \quad (4.8)$$

Where;

S – Seebeck coefficient

T_1/T_2 – End values of the temperature gradient concerned

As described previously, for small temperature gradients, the Seebeck coefficient can be considered as a constant without introducing significant errors into calculations for materials whose Seebeck coefficient does not change very sharply with temperature. Thus, Equation (4.8) can be re-written as Equation (4.9) for small temperature gradients ΔT at each temperature. When the temperature gradient (ΔT) is taken as 1 °C, the induced EMF is equal to the sum of the Seebeck coefficients in the temperature range considered as given in Equation (4.10). Since 1 °C is a sufficiently small temperature gradient across which the Seebeck coefficient can be regarded as constant, Equation (4.10) was used to estimate the EMF induced at different temperatures. Since the Seebeck coefficients were interpolated with 1 °C intervals as described previously, adding the Seebeck coefficients between a given temperature range yields the EMF induced in that temperature range.

$$EMF = (\Delta T)_{T_1}S_1 + (\Delta T)_{T_2}S_2 + (\Delta T)_{T_3}S_3 + \dots + (\Delta T)_{T_n}S_n \quad (4.9)$$

Where;

$(\Delta T)_{Ti}$ – A temperature difference of ΔT at temperature T_i

S_i – Seebeck coefficient of the material at temperature T_i

$$EMF = S_1 + S_2 + S_3 + \dots + S_n \quad (4.10)$$

Once the EMF generated for a given temperature gradient is calculated as described above, the temperature corresponding to the EMF can be back-calculated by NIST approved inverse temperature function given in Equation (4.11). The inverse coefficients were taken from NIST database, whose values for K-type thermocouples are given in Table 4.2.

$$t_{90} = \sum_{i=0}^n d_i (V_{emf})^i \quad (4.11)$$

Where,

t_{90} – temperature in °C according to ITS-90 standards

V_{emf} – Induced EMF

d_i – inverse coefficients

$n = 9$ for K, N, and S-type; $n = 10$ for R-type

Table 4.2 Inverse coefficients for K-type thermocouples

Coefficient symbol	Value of inverse coefficients	
	Between 0 – 500 °C	Between 500 – 1372 °C
d0	0.000000E+00	-1.318058E+02
d1	2.508355E+01	4.830222E+01
d2	7.860106E-02	-1.646031E+00
d3	-2.503131E-01	5.464731E-02
d4	8.315270E-02	-9.650715E-04
d5	-1.228034E-02	8.802193E-06
d6	9.804036E-04	-3.110810E-08
d7	-4.413030E-05	0.000000E+00
d8	1.057734E-06	0.000000E+00
d9	-1.052755E-08	0.000000E+00

4.2.3 Material Selection for Calculations

Since the aim of the numerical calculations is to assess qualitatively the factors affecting the accuracy of multi-junction thermocouples, these calculations are independent of the material type. Thus, the thermocouple type that gives the minimum error in calculations is to be chosen.

The electromotive forces (EMFs) produced by K, S, R, and N-type thermocouples at temperatures from 0 °C to 1,000 °C were calculated and the temperatures corresponding to these EMFs were calculated following the method described in Section 4.3.2. Taking the set temperatures (0 °C to 1,000 °C) as the true temperature, the estimation error was calculated by subtracting the estimated temperature from the true temperature. The estimation error was plotted against the true temperature as shown in Figure 4.7. K-type thermocouple produced the least error in temperature estimation in the range from 700 °C to 900 °C. Thus, K-type materials were chosen for rest of the calculations presented in this chapter. The errors associated with the other types are not characteristic errors of those thermocouple types; instead, they should have been caused by errors in the Seebeck coefficients chosen. However, when K-type thermocouples already provide sufficiently accurate estimations, no further investigations were carried out to improve the estimation accuracy of other materials.

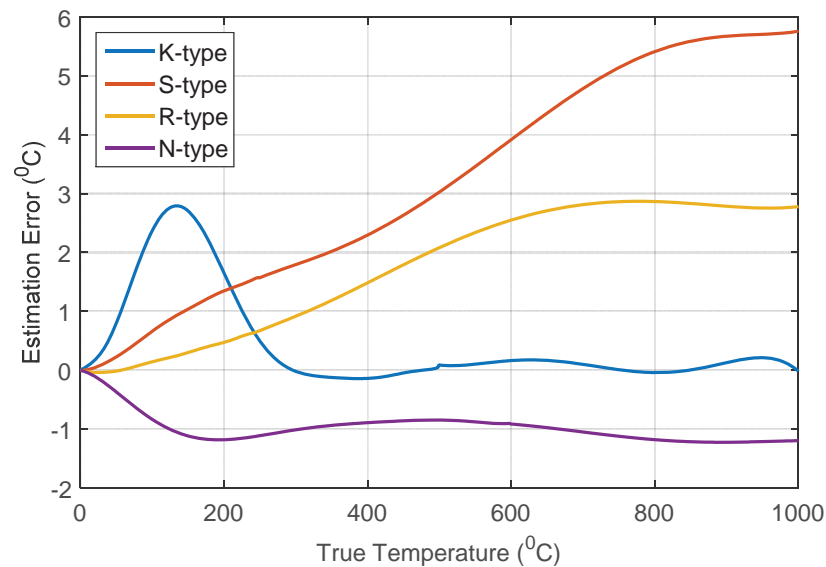


Figure 4.7 The estimation errors resulted by K, S, R, and N type thermocouples at different temperatures during temperature calculations

4.3 Calculations 1: Array Architecture ~ $\{N+1\}$

The multi-junction thermocouple array, schematically shown in Figure 4.8 is considered for the calculations. The four temperature measuring junctions are denoted by J_1 to J_4 . Thermoelement $a-b$ is considered made of chromel and thermoelements $c-d$, $e-f$, $g-h$, and $i-j$ are considered made of alumel. Therefore, each junction is equivalent to a K-type thermocouple with the exception that there is an intermediate material, alumel, on the shared thermoelement because of the intermediate junctions.

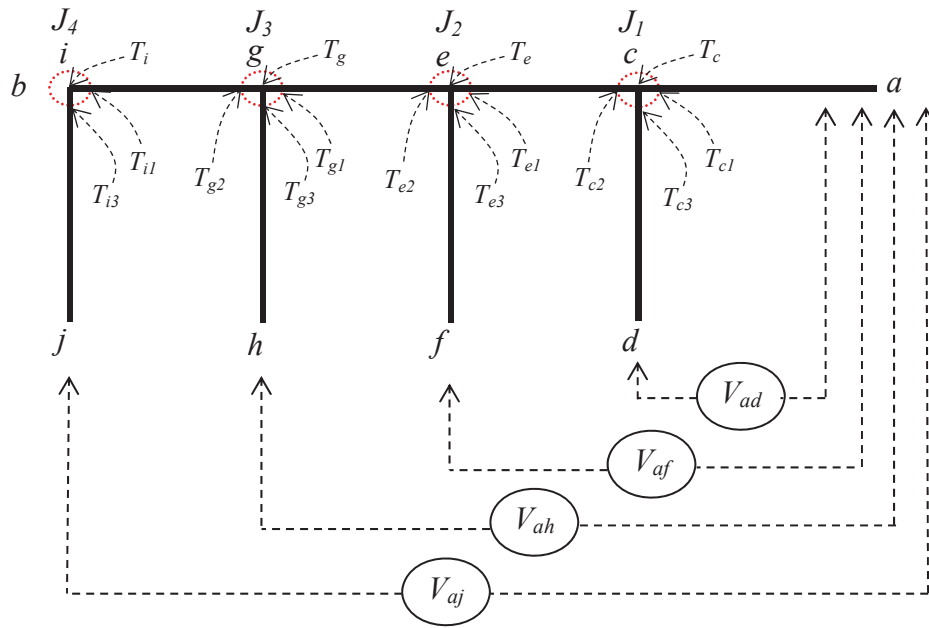


Figure 4.8 N+1 Architecture of multi-junction thermocouple array

The junction fabrication process might alter the structural integrity of thermoelements at junctions. Therefore, the Seebeck coefficient of thermoelements at each junction is considered to be different than their corresponding base material's Seebeck coefficient. The region where the Seebeck coefficient is considered to be different is referred to as the “dissimilar zone” in the remaining sections of this chapter. The dissimilar zones are the locations where two solid lines meet, and marked as dotted circles in the diagram (Figure 4.8). The point of intersection of the circle and a thermoelement defines the zonal boundary on the corresponding thermoelement. The exact properties within dissimilar zones are not known. Therefore, the Seebeck coefficient of the segment of thermoelement that lies within the dissimilar zone is expressed as a percentage of the corresponding thermoelement's base material Seebeck coefficient. For example, the Seebeck coefficient of the segments of thermoelement $a-b$ within the dissimilar zone at J_1 to J_4 is expressed as a percentage (e.g. 5% higher or lower) of the

Seebeck coefficient of chromel. This percentage can be altered in the computer code to investigate the effects of Seebeck coefficient changes.

Temperatures at junctions J_1 to J_4 are denoted by T_c , T_e , T_g , and T_i , respectively. The temperatures denoted by a numbered subscript represent the temperature at the boundary of a dissimilar zone on the corresponding thermoelement; for example, T_{c1} , T_{c3} , T_{e3} are the temperatures at the dissimilar zone boundary of thermoelement $a-c$, $c-d$, and the $e-f$, respectively. (As previously defined, a dissimilar zone boundary is the point of intersection of a dotted circle and a thermoelement.) Each thermoelement, $c-e$, $e-g$, and $i-g$, has two dissimilar zone boundaries at both of their ends. The junction temperatures were allowed to change randomly within a pre-defined temperature range, and the temperature at zonal boundaries can also vary as a percentage of the corresponding junction's temperature; the range of the percentage change can also be defined in the code.

Thermoelectric voltages V_{ad} , V_{af} , V_{ah} , and V_{aj} are a measure of the temperature at junction J_1 to J_4 , respectively. The induced thermoelectric voltage can be calculated from Equation (4.12), which is based on the definition of the Seebeck coefficient (see Section 4.1.1). All the distal ends (a , d , f , h , j in Figure 4.8) of the multi-junction thermocouples are considered to stay at a constant temperature of T_0 . Performing the cyclic integration along the two thermoelements of sensing points J_1 , J_2 , J_3 , and J_4 , the induced EMF across their distal ends (V_{ad} , V_{af} , V_{ah} , and V_{aj} , respectively) can be commonly expressed as Equation (4.13). However, the actual EMF values and the corresponding temperatures based on the numerical values of Seebeck coefficients were calculated following the method described Section 4.2.2. This is because no standardised expression of the Seebeck coefficient as a function of the temperature available to perform integrations to estimate the EMFs.

$$V_{emf} = \oint S dT \quad (4.12)$$

Where,

S – Seebeck coefficient of the thermoelement concerned

$$V_{xy} = \int_{t_1}^{t_2} S dT \quad (4.13)$$

Where;

V_{xy} – Thermoelectric voltage induced across the distal ends of a junction (for example, V_{ad} for junction J1)

t_1 and t_2 – temperatures at the ends of a thermoelement segment of a junction where a segment is the part of a thermoelement whose Seebeck coefficient is constant throughout.

S – Seebeck coefficient of the thermoelement concerned

Although the mean error in temperature estimation over a number of iterations is a reliable statistical tool to compare accuracies under different operating conditions, the estimation error can either be positive or negative thus, likely to cancel some effects when the mean is taken. Therefore, root-mean-square value of the measurement error, calculated according to Equation (4.14), is used to compare accuracy in temperature estimation. To enhance the unbiasedness of the error, RMS value over 50,000 iterations were considered in each of the calculations presented in this chapter. The use of over 30,000 iterations eliminated the biasedness of error. However, 50,000 iterations were chosen to further enhance the unbiasedness of the error as increasing the number of iterations does not consume too much of the computing power for these types of simple calculations.

$$RMS\ error = \sqrt{\frac{\sum (T_{true} - T_{est})^2}{number\ of\ iterations}} \quad (4.14)$$

Where;

T_{true} - set temperature for a given junction (represents the true temperature)

T_{est} – the estimated temperature using EMF values generated at the junction

4.3.1 Performance without Dissimilar Zones

In these calculations, the dissimilar zones were considered non-existent. Thus, there is no change of the Seebeck coefficient along any thermoelement. These calculations were performed as the baseline to assess the effects of dissimilar zones. In each of the iterations, four random numbers, in the range from 700 to 900, were generated to represent the temperatures at four junctions. Since there is no dissimilar zone exists, there is no zonal boundary. Temperatures at the distal ends of all thermoelements were set to 0 °C. Thus, the estimated temperature gradient between a junction and its distal ends represents the true temperature at the junction. The EMF induced under each random temperature and the temperatures corresponding to the EMFs were calculated by following the method described previously. The estimation error for each of the four junctions was calculated by subtracting the estimated temperature from the set temperature of the corresponding junction. The RMS values of the temperature estimation error at each of the four junctions were calculated over 50,000 iterations using Equation (4.14).

4.3.2 Influence of Dissimilar Zones

Investigating the influence of dissimilar zones to the measurement accuracy of the array is crucial. A simple fabrication technique like spot-welding can be expected to form junctions with very small heat-affected zones. Thus, there can be hardly any temperature gradient across such a short length. However, it is still worthwhile to understand the effects of the dissimilar zone on accuracy, especially when the multi-junction thermocouple is applied in an unknown environment within a fuel cell. Two sets of calculations were carried out: 1) the effect on accuracy by Seebeck coefficient change at a dissimilar zone, and 2) the influence of the boundary temperature on the accuracy for a given change in the Seebeck coefficient at a dissimilar zone.

4.3.2.1 The Effect of Seebeck Coefficient Change

The Seebeck coefficient of alumel was increased by 5%, and that of chromel was decreased by 5% within the dissimilar zones. Temperatures at the zonal boundaries were set to change randomly within a range of ± 2 °C from the corresponding junction's temperature. Four random numbers in the range from 700 to 900 were generated to represent the temperatures at four junctions in each of the iterations. The EMF generated and the temperature corresponding to that EMF were calculated following the method described previously. Calculations were performed over 50,000 iterations, and the RMS error in temperature estimation for each junction was calculated based on Equation (4.14).

4.3.2.2 Influence of the Boundary Temperature on Accuracy

As the Equation (4.13) suggests, the zonal boundary temperature affects the induced voltage across a dissimilar zone adversely affecting the measurement accuracy. Therefore, it is important to gain a brief idea about how the boundary temperature will affect the measurement accuracy.

The change of the Seebeck coefficient within dissimilar zones was kept unchanged from previous calculation as 5% increase for alumel and 5% decrease for chromel to ensure the effect from Seebeck coefficient change remains unchanged from the previous estimates. The range over which a boundary temperature could randomly vary was increased from its previous value of ± 2 °C to ± 5 °C. The junction temperatures were randomly chosen between 700 °C to 900 °C. The method of temperature estimation, and the RMS error calculation was unchanged. The RMS errors produced by each of the four junctions were recorded over the same 50,000 iterations.

4.3.3 Results and Discussion

The RMS errors generated in temperature-estimation by the four junctions without the presence of any dissimilar zone are given in Table 4.3 where, J_1 , J_2 , J_3 , and J_4 are the four junctions as shown in Figure 4.8. The error values are rounded to two decimal places. Accuracy to two decimal places of a degree Celsius is sufficient to compare the estimation error under the different conditions tested. Since the temperatures corresponding to EMFs were calculated based on the standard equations, the estimation errors should be due to errors in Seebeck coefficient calculations and the errors in the method of temperature estimation. Although the Seebeck coefficient was considered to remain constant over 1 °C temperature gradient, that assumption is not perfectly accurate as the Seebeck coefficient is a continuous function of temperature. Therefore, that assumption is likely to introduce some errors no matter how trivial that error is. Despite these known error sources, the measurements were accurate to ± 0.07 °C as the results show. This is a level well above the Class 1 accuracy range under BS EN 60584-1:2013 standard specifications (The most accurate thermocouples demonstrate accuracy in class 1 range). Thus, no further actions on accuracy improvements were considered necessary. Most importantly, the estimation error for all four junctions remains identical and has no correlation with the location of the junction. Since junction J_1 has no intermediate junctions on its thermoelements, J_1 is essentially a conventional thermocouple. Other three junctions showing the identical accuracy as J_1 proves that all four junctions could measure temperature (mathematically) as accurately as a set of four conventional thermocouples when there is no dissimilar zone exists.

Table 4.3 RMS errors under no dissimilar zones

Junction	J_1	J_2	J_3	J_4
RMS Error (°C)	0.07	0.07	0.07	0.07

Table 4.4 presents the RMS errors generated at four junctions when the Seebeck coefficient of alumel was increased by 5% and that of chromel was decreased by 5% within the dissimilar zones and when the zonal boundary temperature is ± 2 °C different to the corresponding junction's temperature. The values are rounded to two decimal places as before.

Table 4.4 RMS errors with dissimilar zones and ± 2 °C boundary temperature

Junction	J ₁	J ₂	J ₃	J ₄
RMS Error (°C)	5.28	6.26	7.11	7.15

Comparing with the results with no dissimilar zones (given in Table 4.3), the measurement accuracy can be identified to deteriorate when there are dissimilar zones exist near junctions. A dissimilar zone is, as described previously, a region where the Seebeck coefficient is different from the base metal's Seebeck coefficient. Therefore, the electromotive force induced across these dissimilar zones is different to that would be induced if the Seebeck coefficient was not altered (remain at the value of the base metal). The induced EMF is higher than that would be induced with base metal if the altered Seebeck coefficient is greater than the base metal's Seebeck coefficient and vice versa. When estimating the temperature at a junction, the total EMF induced across the distal ends is counted for each junction. Therefore, all these local changes in EMF affect the EMF across the distal ends. Thus, the generated EMF is different than that would be generated by a K-type thermocouple for the same temperature. However, Equation (4.11) gives the temperature corresponding to the EMF produced by a standard K-type thermocouple. Thus, when the inaccurate EMF values for a given temperature is substituted to Equation (4.11) to calculate the temperature, it generates an incorrect temperature. For example, if the estimated EMF is higher than the standard EMF produced by a K-type thermocouple (due to the influence by dissimilar zones) for the same temperature, Equation (4.11) yields a higher temperature than the true temperature and vice versa. This is the reason for the observed increase in RMS error.

A similar phenomenon happens in practical applications of temperature sensing as well. When the Seebeck coefficients of thermoelements are altered, the induced voltage for a given temperature is different to that would be induced by a K-type thermocouple. However, if the data logging device is set to measure temperature from a K-type thermocouple, it compares the measured EMF with the standard K-type EMF values and returns the temperature corresponding to that EMF value. Thus, the recorded temperature is different to the true temperature at the junction causing measurement errors. Therefore, the presence of dissimilar zones affects practical temperature measurements in a similar fashion to that affected the numerical calculations performed.

Besides to having an overall adverse effect on the accuracy, importantly, there is a clear correlation between the measurement error and the location of the junction where the error increases from J_1 to J_4 . Since J_1 has only one dissimilar zone (near its junction), it has one section that possibly generate a different EMF than the standard K-type thermoelement would generate. Thus, the estimation error is less. On the other hand, J_2 has two dissimilar zones, one formed at its junction and the other near J_1 junction. Thus, it has two sections that generate inaccurate EMFs. Consequently, the measurement error of J_2 is higher than that of J_1 . The same reason explains why the measurement error of J_3 is greater than that of J_2 and the measurement error of J_4 is the highest. The results of this calculation suggest that if it is not possible to prevent the formation of dissimilar zones during junction forming process, location-dependant measurement errors should be expected. Further, an application-dependent agreement needs to be reached on the number of multiple junctions employed and how far the measurement accuracy can be compromised.

The change of the Seebeck coefficients and the change of the zonal boundary temperatures considered in these calculations are purely arbitrary values and have no experimental support. Thus, the results remain only as a qualitative assessment. In order to assess the accuracy in practical applications, it is necessary to calibrate individual junctions separately.

The RMS errors given in Table 4.5 shows the measurement error induced when the zonal boundary was allowed to changed ± 5 °C from the corresponding junction's temperature while the change of the Seebeck coefficient remained unchanged at 5% increase for alumel and 5% decrease for chromel. The results show deterioration of the accuracy with the increase of the boundary temperature. The reason for this error is as same as described previously. The thermoelectric EMF is a product of Seebeck coefficient and the temperature gradient, thus; the higher the temperature gradient, the higher the induced EMF. Therefore, when the zonal boundary temperature increases, the magnitude of the erroneous EMF induced across the dissimilar zones increases. Thus, the EMF across the distal ends diverts further away from the real EMF across the distal ends for a given temperature. This explains the observed increase in RMS error with the increase of the zonal boundary temperature. The explanation for the locational correlation of the junction and the error is the same as before.

Table 4.5 RMS errors with dissimilar zones and ± 5 °C boundary temperature

Junction	J ₁	J ₂	J ₃	J ₄
RMS Error (°C)	11.77	14.02	15.89	16.01

Table 4.6 lists the RMS errors produced when there is no temperature gradient across the dissimilar zone though the dissimilar zones exist. The change of Seebeck coefficients of alumel and chromel remains unchanged from previous calculations at 5% increase for alumel and 5% decrease for chromel. However, the temperature gradient across dissimilar zones was set to zero. The measurements errors are identical to those produced when there is no dissimilar zone exist (see Table 4.3). Thus, as the mathematics already suggested in Equation (4.13), when there is no temperature gradient across dissimilar zones, no adverse effects on the accuracy will occur despite having areas with altered Seebeck coefficients along thermoelement.

Table 4.6 RMS errors with dissimilar zones but no temperature gradient across

Junction	J ₁	J ₂	J ₃	J ₄
RMS Error (°C)	0.07	0.07	0.07	0.07

In all previous calculations, where there exist dissimilar zones, the change of Seebeck coefficients of thermoelement was the same. In order to investigate any biasedness of that to the results, the changes of Seebeck coefficients were swapped: alumel's was decreased and chromel's was increased by a magnitude of 5% for each. The zonal boundary temperature was allowed to vary within a range of ± 5 °C from the corresponding junction's temperature. The RMS values of the estimation errors generated over 50,000 iterations are listed in Table 4.7. These errors are similar to those presented in Table 4.5 where the Seebeck coefficient changes were swapped while boundary temperature range is the same. Thus, the absence of any biasedness in results is sufficiently proven.

Table 4.7 RMS errors with different changes to Seebeck coefficient

Junction	J ₁	J ₂	J ₃	J ₄
RMS Error (°C)	11.86	14.02	15.88	15.95

4.4 Calculations 2: Grid Architecture $\sim \{N^2 \text{ to } 2N\}$

The grid architecture and the array architecture share the same scientific reasoning: the theory of intermediate conductors described in Section 4.1.2. However, these two designs are structurally different from one another. All thermoelements in the grid architecture consist of intermediate materials, while only one thermoelement in the array architecture has intermediate materials. These structural differences may influence the array and the grid architectures to perform differently from each other. Therefore, a set of calculations focused on assessing the grid architecture's performance under varying operating conditions was carried out. The multi-junction thermocouple grid having nine junctions (denoted by J_1 to J_9), shown in Figure 4.9, was considered for the calculations. Each junction is formed by intersecting an alumel and a chromel thermoelement. The horizontal thermoelements ($o-c$, $n-f$, and $m-i$) are considered to be made of chromel, and the three vertical thermoelements are considered to be made of alumel. The dissimilar zones are marked with dotted circles, and the temperatures at zonal boundaries are marked in the diagram with a numbered subscript (ex: T_{a1} , T_{b2}). The voltage across distal ends of thermoelements is a measure of the corresponding junction's temperature. For

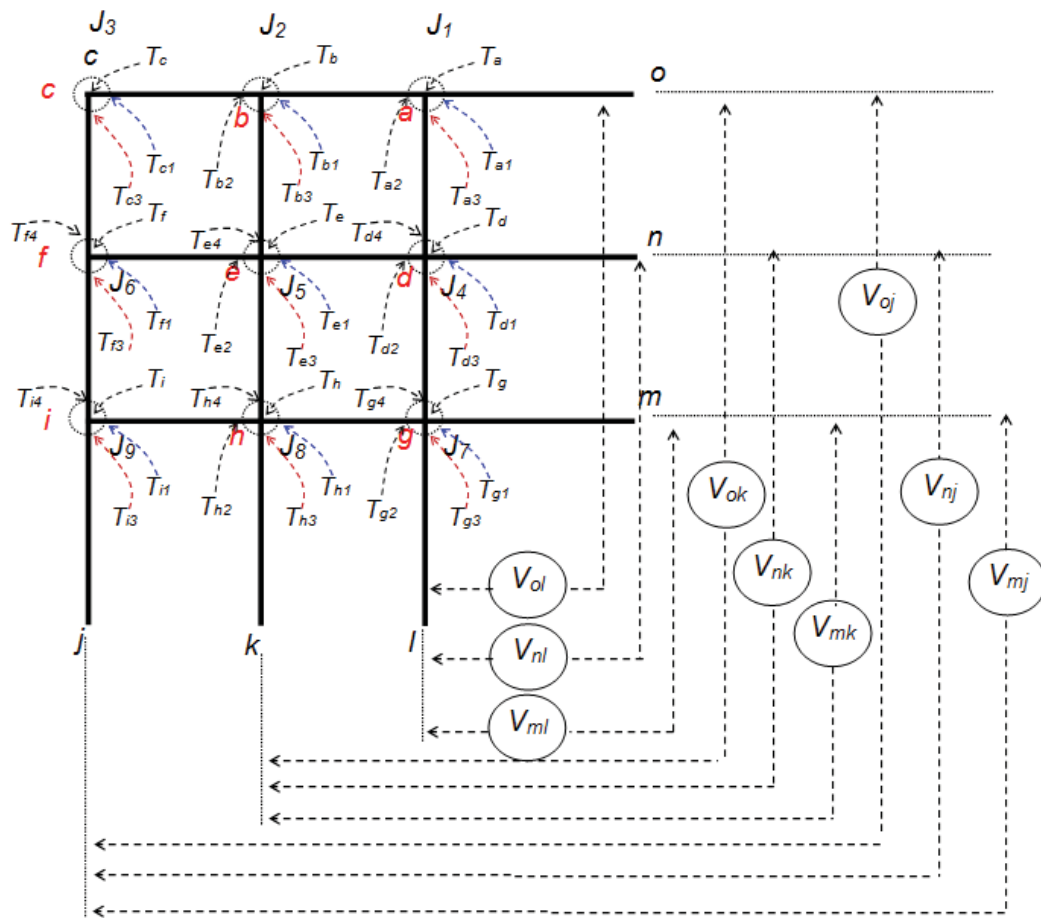


Figure 4.9 A schematic diagram of a 9-point thermocouple grid

example, V_{ok} , V_{oj} , V_{nj} and V_{ml} represent the temperature at junctions J_2 , J_3 , J_6 , and J_7 , respectively.

The thermoelectric voltages induced across the distal ends of thermoelements can be commonly expressed as Equation (4.15). However, calculation of these voltages based on available Seebeck coefficient values and corresponding temperatures were performed by following the same method used for previous calculations due to lack of proper expressions for Seebeck coefficient in terms of temperature to perform integrations. Calculation of the RMS error is also same as that of the array calculations. The number of iterations done in calculating the RMS errors remained unchanged from previous estimates at 50,000 iterations due to the same reason.

$$V_{xy} = \int_{t_1}^{t_2} S dT \quad (4.15)$$

Where;

V_{xy} – Thermoelectric voltage induced across the distal ends of a junction (for example, V_{ol} for junction J1)

t_1 and t_2 – temperatures at the ends of a thermoelement segment of a junction where a segment is the part of a thermoelement whose Seebeck coefficient is constant throughout.

S – Seebeck coefficient of the thermoelement concerned

4.4.1 Performance without Dissimilar Zones

These calculations were performed to set the baseline for accuracy comparison under the effect of dissimilar zones. The methodology is similar to that followed by the array architecture under no dissimilar zones. Nine random numbers were generated in each of the 50,000 iterations, in the range from 700 to 900, to represent the temperatures at nine junctions. The induced EMF and the corresponding temperatures were calculated following the method described in Section 4.2.2. The RMS values of the temperature estimation error at each of the nine junctions were calculated over the entire set of iterations using Equation (4.14).

4.4.2 Influence of Dissimilar Zones

As with the array architecture, two sets of calculations were carried out to investigate the effects of 1) Seebeck coefficient change and, 2) zonal boundary temperature on the measurement accuracy as described below.

4.4.2.1 The effect of Seebeck coefficient change

The Seebeck coefficient of alumel was increased by 5%, and that of chromel was decreased by 5% within the dissimilar zones. The boundary temperatures of dissimilar zones were also allowed to change randomly within a range of ± 2 °C from the corresponding junction's temperature. A set of nine random numbers were generated, within the range from 700 to 900, in each of the iterations to represent junction temperatures. The EMF produced, and the corresponding temperatures were calculated as described before. The RMS error at each junction over the entire set of iterations was calculated and recorded.

4.4.2.2 Influence of the Boundary Temperature on Accuracy

The calculations performed with the array architecture showed an increase of the error with the increase of the boundary temperature due to the increased of the erroneous voltage induced. However, since the grid architecture has intermediate junctions on all thermoelements while the array had intermediate junctions only on one thermoelement, the influence of the boundary temperature is likely to be different in the grid architecture.

Changes of Seebeck coefficients were left unchanged at 5% increase for alumel and 5% decrease for chromel. The range at which the zonal boundary can vary was increased to ± 5 °C from the corresponding junction's temperature. The RMS errors in estimation were recorded over 50,000 iterations.

4.4.3 Results and Discussion

The RMS estimation error produced at nine junctions when there are no dissimilar zones exist is listed in Table 4.8. The values are rounded to two decimal places. The errors are identical for each junction and they are the same produced with the array with the absence of a dissimilar zone (see Table 4.3). The explanations for the observed error with the array, presented in Section 4.3.3, describes the error observed with the grid as well. Since there are no intermediate junctions on the thermoelements that form junction J_7 , it is essentially a conventional thermocouple in its function. (Although there are intermediate junctions on its thermoelements beyond the junction, they are not affecting the junction's temperature measurements). Since all the other junctions also demonstrate the same accuracy; that implies all the nine junctions have functioned as accurately as a set of conventional thermocouples when there are no dissimilar zones.

Table 4.8 RMS error under no dissimilar zone for the grid architecture

Junction	J_1	J_2	J_3	J_4	J_5	J_6	J_7	J_8	J_9
RMS Error (°C)	0.07	0.07	0.07	0.07	0.07	0.07	0.07	0.07	0.07

Table 4.9 shows the RMS estimation error for the nine junctions when the Seebeck coefficient of alumel was increased by 5% and that of chromel was decreased by 5% while allowing the boundary temperature to vary within a range of ± 2 °C from corresponding junction's temperature. Junction J_7 , which has no intermediate junctions along its thermoelements, shows the least error. In fact, junctions J_7 , J_8 , and J_9 are architecturally similar to junctions J_1 , J_2 , and J_3 on the array, respectively because both these set of junctions have only one thermoelement shared among junctions. The errors produced by the array architecture at junctions J_1 , J_2 , and J_3 are 5.28, 6.26, and 7.11 °C, respectively (see Table 4.4). These errors are almost identical with the errors produced by J_7 , J_8 , and J_9 junctions of the grid architecture. Thus, the two sets of junctions are not only architecturally similar but also functionally similar.

Table 4.9 RMS error under dissimilar zone and ± 2 °C boundary temperature range

Junction	J_1	J_2	J_3	J_4	J_5	J_6	J_7	J_8	J_9
RMS Error (°C)	9.74	10.29	10.87	7.82	8.54	9.17	5.28	6.25	7.11

The middle row of junctions (J_4 , J_5 , J_6), each of which has one intermediate junction along their alumel thermoelement (because of junctions J_7 , J_8 , and J_9) has a higher error than the bottom row of junctions. This is because of having an intermediate junction on their respective alumel thermoelement. The measurement error has already shown to increase proportionally with the number of intermediate junctions on thermoelements. Further, the error can be identified to increase from J_4 to J_6 . This is because of the addition of intermediate junctions along the chromel thermoelement as junctions progressed from J_4 to J_6 . A similar pattern can be observed with the top row of junctions having J_3 as the least accurate junction out of all nine junctions. This is because; it has the highest number of intermediate junctions on both of its thermoelements: two junctions on each thermoelement. These results, once again, shows that the presence of intermediate junctions along thermoelements adversely affects the measurement accuracy when the Seebeck coefficients are altered. Also, the locational correlation between junction and the magnitude of the error is, once again, demonstrated. The reason for the error has already been described with the array architecture and the same reason applies to the grid architecture as well.

The RMS measurement error recorded for the same level of Seebeck coefficient change but for ± 5 °C boundary temperature ranges is listed in Table 4.10. These results also show a similar correlation between the magnitude of the error and the position of the junction as observed and described previously. The magnitude of the error appears to have increased with the increase of the zonal boundary temperature. The reason for this increase has already been described in Section 4.3.3 as an increase of the erroneous EMF with the increase of temperature gradient across dissimilar zones.

Table 4.10 RMS error under dissimilar zone and ± 5 °C boundary temperature range

Junction	J_1	J_2	J_3	J_4	J_5	J_6	J_7	J_8	J_9
RMS Error (°C)	21.69	23.04	24.07	17.56	19.07	20.55	11.80	14.04	15.98

The above presented RMS errors generated when the dissimilar zones are subjected to ± 2 °C and ± 5 °C temperature gradients are graphically shown in Figure 4.10. These graphs show that the error at a given junction increases with the increase of zonal boundary temperature. Further, locational correlation of the error is also clearly visible where S_1 showing the greatest error while S_7 showing the least error.

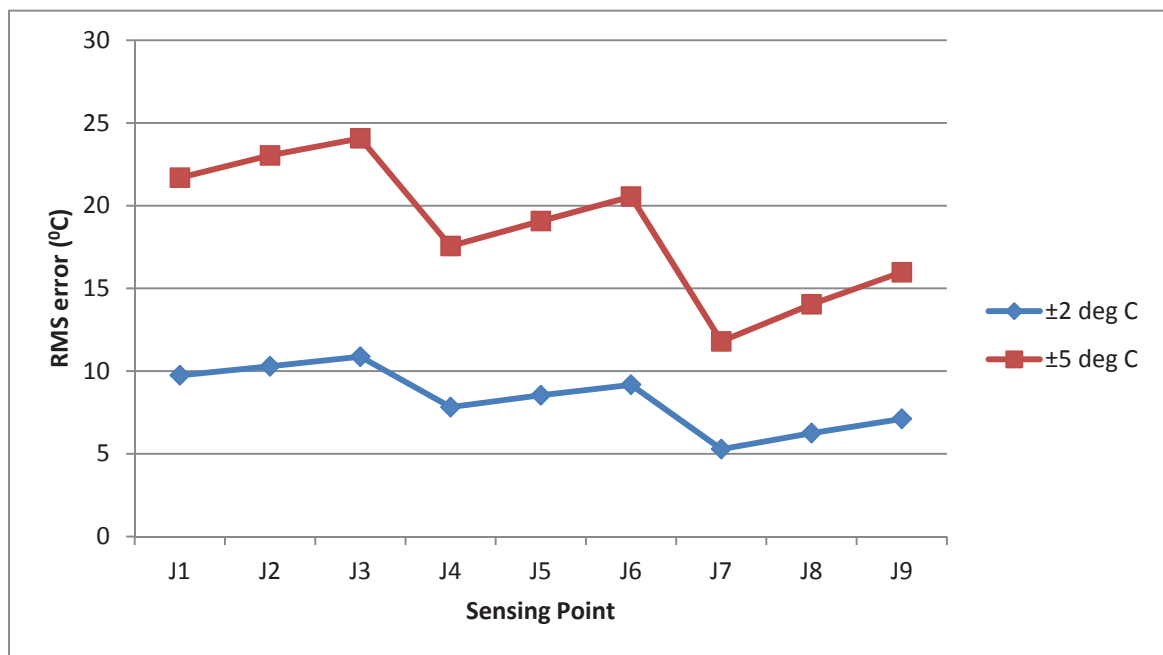


Figure 4.10 Change of error with the increase of boundary temperature range

4.5 Conclusions

Multi-junction thermocouples that share thermoelements across different sensing points to reduce the total number of thermoelement required in multi-point temperature sensing from SOFC are proposed. The concept is built based on the theory of intermediate conductors for thermocouples. Based on this science, two multi-junction thermocouple architectures, namely, the array and the grid architecture were designed. The array architecture can measure temperatures at $\{N\}$ number of points with only $\{N + 1\}$ number of thermoelements. The grid architecture, on the other hand, requires only $\{2N\}$ number of thermoelements for $\{N^2\}$ number of sensing points.

A set of numerical calculations were performed based on Seebeck theory to qualitatively assess the thermoelectric influences of multiple junctions on the temperature measurement accuracy of the two architectures. These calculations showed that the array architecture and the grid architecture could function equally accurately as thermocouples when the junction forming method does not alter the Seebeck coefficient at junctions. Thus, the multi-junction thermocouple architectures can, fundamentally, be used for multi-point temperature sensing with a reduced number of thermoelements.

When the junction forming method alters the Seebeck coefficient at junctions, the measurement accuracy was found to be significantly affected. Further, the measurement error was found to have a proportionality with the number of intermediate junctions on thermoelements: the higher the number of intermediate junctions, the greater the error. However, if there is no temperature gradient across the dissimilar zones, the measurement accuracy is left intact despite having dissimilar zones.

The level of influence on the accuracy depends not only on the change of the Seebeck coefficient at the junctions but also on the temperature at the dissimilar zone's boundary. The larger the temperature gradient across a dissimilar zone the greater the measurement error for a given change in the Seebeck coefficient. Therefore, if it is impossible to prevent changes to the Seebeck coefficient during junction forming, care must be taken to minimise the dimensions of the affected areas such that the temperature gradient across the boundary of such an affected area is negligibly small. If that can be assured, temperature measurements with multi-junction thermocouples can still be performed with only a minimal sacrifice on the accuracy.

All the calculations considered only the thermoelectric effects only. Since the aim of the calculations was to ensure the conceptual verity of the multi-junction thermocouple

concept, potential error sources, such as heat transfer along thermoelements, were not considered in above assessment. Such investigations need to be performed when developing data logging systems to eliminate errors.

4.6 References

- [1] Pollock, D.D, *Thermoelectricity: Theory, Thermometry, tools*, ASTM Special Technical Publications, 1985.
- [2] *NI 9213 16- Channel Thermocouple Module* [online], National Instruments, 2014.
[viewed 03/03/2015]. Available from: <http://www.ni.com/datasheet/pdf/en/ds-69>
- [3] Robin E. Bentley, *Handbook of temperature measurements Vol 03 : Theory and Practice of thermoelectric thermometry*, Springer, 1998

**Chapter 5 : Experimental Investigation of Performance of
Multi-Junction Thermocouples**

Chapter Summary

Experimental investigations of the effects of using multiple thermocouple-junctions on thermoelements to produce multi-junction thermocouples are presented and discussed in this chapter. Section 5.1 presents the material selection for thermoelements. Section 5.2 describes the criteria behind external wire selection. The effect of having multiple junctions on a thermoelement on measurement accuracy is examined and discussed in Section 5.3. Whether multi-junction thermocouples can measure temperature independently without any thermoelectric interference from their adjacent sensing points is investigated in Section 5.4. A multi-junction thermocouple grid was employed to detect temperature changes on a surface; the methodology and the results are presented and discussed in Section 5.5. Finally, the chapter describes conclusions drawn from the experimental investigations in Section 5.6.

5.1 Introduction

The mathematical calculations presented and discussed in Chapter 4 suggested that if the junction-forming process does not alter the Seebeck coefficient of thermoelements, the presence of multiple junctions along a thermoelement does not introduce errors into temperature measurements of multi-junction thermocouples. Thus, a multi-junction thermocouple can function as accurately as sets of conventional thermocouples. Furthermore, the same calculation suggested that if there are any measurement inaccuracies due to multiple junctions, the magnitude of the error has a relationship with the location of the sensing point: the higher the number of intermediate junctions along the thermoelement of a junction, the greater the measurement error of that sensing point (junction). Thus, this locational correlation can be used to identify measurement errors caused by multiple junctions. Based on that, this chapter focuses on investigating whether spot-welded multi-junction thermocouples can function as a set of conventional thermocouples and the ability of multi-junction thermocouples to measure spatial temperature variations in a given space.

The choice of materials determines the balance between the quality and the economy of experiments. Devoting considerable attention to both aspects, K-type thermocouple materials (alumel-Ni:Al:Mn:Si 95:2:2:1 by wt. and chromel-Ni:Cr 90:10 by wt.) were chosen for thermoelement materials. K-type materials can operate well above the expected operating temperature range of a typical SOFC, and they have NIST⁶ standardised performance up to 1,372 °C^[1]. Furthermore, they have a very linear temperature-EMF relationship that makes it easier to identify and calibrate any measurement errors. The widespread use of K-type thermocouples in several industrial applications is also a strong, although non-scientific, reason to rationalise the choice. In terms of the economic point of view, K-type materials are more economical than other high-temperature materials such as platinum and platinum alloys for S-type or R-type thermocouples. Despite the aforementioned merits of K-type materials that make them suitable under the experimental conditions encountered in this research project, the adverse effects on the quality of measurements must be noted, particularly under prolonged application in SOFC.

The adverse effects of using K-type materials, particularly chromel, in an SOFC environment for prolonged operation are dual-faceted: (a) Thermoelements deteriorates the performance of the cell, and (b) SOFC environment deteriorates the thermoelements,

⁶ National Institute of Standards and Technology

causing time-dependant measurement inaccuracies. One of the two constituents of chromel is chromium (Cr), 10% by weight. If chromium is liberated from chromel and migrates into the cathode (made of LSM⁷), it interferes with the oxygen reduction process at the cathode and causes significant cell performance deterioration. This phenomenon is known as “chromium poisoning”, and it is one of the major degradation mechanisms of SOFC. Although an in-depth discussion on chromium poisoning is beyond the scope of this research, a comprehensive discussion is presented elsewhere^[1]. On the other hand, the reducing environment within an SOFC can deteriorate the performance of K-type thermocouple materials by a commonly known process called “green rot attack” on chromium (chromium oxidation). This results in rapid deterioration of the EMF produced and thus the accuracy of measurements^[3]. Although these facts suggest that K-type materials are not suitable for long-term application within SOFCs, there is no evidence for refraining from using them for short-term testing aimed at concept verification and temperature distribution measurement from an operating SOFC.

The domain for material selection was confined only to standard thermocouple materials because of the availability of their standardised performance data. Having such data makes performance evaluation of the proposed multi-junction thermocouple architectures much simpler and more accurate. However, ideally, only two constraints apply in selecting thermoelements materials: (1) Each thermoelement should have its unique Seebeck coefficient at any given temperature, and (2) the temperature-EMF relationship must be characterised by one-to-one mapping (i.e., it must not generate the same EMF at two or more temperatures).

The data logging systems that the author developed (briefly described in Appendices III and IV) were used for data recording in experiments described throughout this chapter. However, there are a number of different ways to record data depending on the application requirements.

The term “sensor” is used in this text to commonly represent either/both the array or/and grid architectures of multi-junction thermocouples. Unless otherwise stated, the terms “array” and “grid” are used in isolation to represent the multi-junction thermocouple array architecture and the multi-junction thermocouple grid architecture, respectively.

⁷ Lanthanum Strontium Manganite

5.2 External Wire Selection

The sensor is generally located inside the SOFC stack during the operation, while the data logging device (NI-9213 for temperature data, in this research) is outside. Unless the sensor is made with sufficiently long lead wires, enabling it to connect directly to the data logger, external wires are needed to couple the data logger to the sensor. This method becomes essential when the sensor is fabricated integral to the cell as a thin-film sensor. It is highly unlikely that the connection points between the sensor and the external wires will remain at the data logger's terminal temperature (of course, it is impossible with thin-film sensors because thermoelements end, at most, at the edge of the cell, which is at the operating temperature of the SOFC). Therefore, unless the external wire is made of a material similar to the corresponding thermoelements, it forms an intermediate junction at the connection point. This intermediate junction produces a voltage in relationship to its temperature, and that influences the temperature measurements. This influence was simulated developing MATLAB code with the aid of the thermocouple schematically shown in Figure 5.1. Since each sensing point of a multi-junction thermocouple is essentially a thermocouple, the simulation with conventional thermocouple architecture sufficiently reflects the effect on multi-junction architectures.

Thermoelements 1 and 2, which form junction J , are made of two materials having Seebeck coefficients S_b and S_c , respectively. The external lead wires (3 and 4) connect with the thermoelements at connection points denoted by p_1 and p_2 . These connection points are at a common temperature of T_c . Both external wires are made of the same material and hence have the same Seebeck coefficient of S_a . Junction J is at temperature T_j , whereas the data logger terminals are at temperature T_0 . V_{emf} is the thermoelectric voltage induced across the data logger's terminals as a result of the temperature gradient between the junction and the data logger's terminal. This voltage is a measure of the

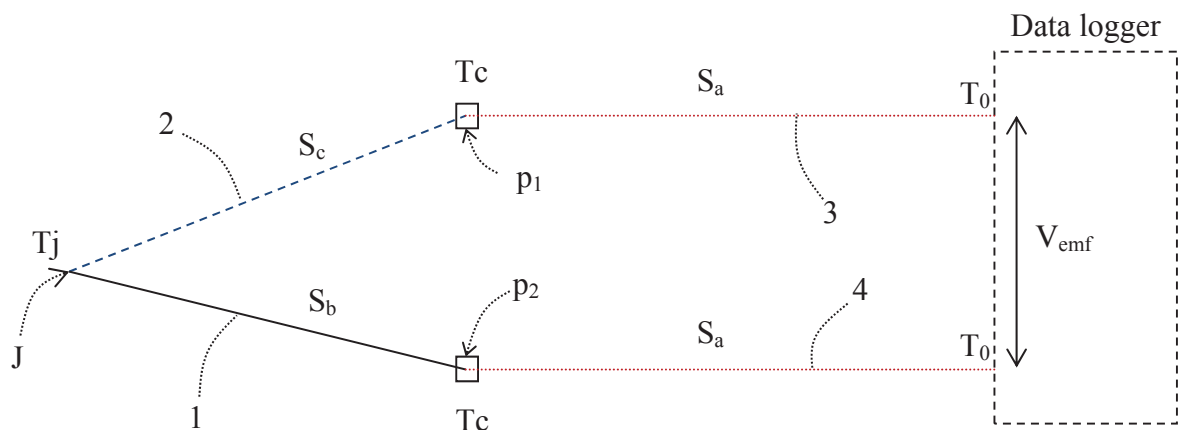


Figure 5.1 Schematic diagram of a thermocouple attached to a data logger

temperature at the junction. The induced thermoelectric voltage, V_{emf} , can ideally be calculated from Equation (5.1) when the Seebeck coefficients are known as functions of temperature.

$$V_{emf} = \int_{T_0}^{T_c} S_a dT + \int_{T_c}^{T_j} S_b dT + \int_{T_j}^{T_c} S_c dT + \int_{T_c}^{T_0} S_a dT \quad (5.1)$$

where:

S_a —Seebeck coefficient of external wires 3 and 4

S_b —Seebeck coefficient of thermoelement 1

S_c —Seebeck coefficient of thermoelement 2

T_j —Temperature at hot-junction (J)

T_c —Temperature at external wire connection points (p_1 and p_2)

T_0 —Temperature at the data logger's terminals

V_{emf} —Induced thermoelectric EMF

The selected materials for thermoelements and external wires for the simulation are given in Table 5.1. Seebeck coefficients of the materials at certain temperatures were taken from a reference as given in Table 5.2. The values for the other temperatures were estimated using polynomial curve fitting. A detailed discussion of the selection criterion of the degree of the polynomial is presented in Chapter 4.

Table 5.1 Thermoelement and external wire materials

Thermoelement	Material
1	Chromel
2	Alumel
3 and 4	Nicrosil

Table 5.2 Seebeck coefficients of the selected materials^[37]

Temperature (°C)	Seebeck Coefficient (μV/K)		
	Alumel	Chromel	Nicrosil
0	-17.7	21.8	11.4
200	-16.2	23.7	14.0
400	-20.0	22.2	14.0
600	-24.0	18.5	12.8
800	-27.2	13.8	10.9
1000	-29.6	9.4	8.8

The temperature at the junction was incremented from 0 °C to 1,000 °C with 1 °C steps. The temperature at connection points (T_c) was set as a percentage of the junction's temperature (from 45% to 95% with 10% increments). The objective of the simulation is to visualise the effect of the external wires' material on the measurements, rather than estimating it. Thus, the range of percentages was chosen in a way that the actual temperature at the connection point can plausibly fall within the selected range. The lower limit of the percentage was restricted to 45% because if the connection point is at an even lower temperature, it is highly likely that the connection occurs at a distal point from the hot region of the stack. If the connection could be taken to a place having less than 45% of the stack's temperature, there should not be much difficulty in taking it directly to the data logger's terminal, eliminating the need for external wires. The temperature at the data logger's terminal, T_0 , was taken as 0 °C. Although this is not true under experimental conditions in which it remains at room temperature, the cold junction compensation artificially enforces 0 °C at the terminal either computationally or electronically. Thus, this setting does not divert the simulation from reality.

Figure 5.2 shows the induced voltages (V_{emf}) at different junction temperatures and under different connection point temperatures. The thermoelements of the simulation are presumed to be made from K-type materials. The graph with legend "K-type" is the thermoelectric voltage induced when external wires are made from the same thermoelements materials (or when the thermoelements are directly connected to the data logger without any intermediate connection wires). Therefore, this is the voltage induced when there is no influence from external wires on the measurements. Thus, in this simulation, the graph "K-type" represents the voltage that a conventional K-type thermocouple should produce at the given temperatures. The graphs show that the

magnitude of measurement error increases with the increase of the connection points' temperature. Since the source of error is the connection points' temperature, which may vary over time, it is essential to measure it to estimate the true temperature at the junction based on the measured temperature. However, measuring the connection points' temperature is not simple, particularly when they are located inside the fuel cell stack. Furthermore, as seen from the graphs, the sensitivity of measurements significantly decreases with increases of the connection points' temperature. The reduction of sensitivity is prone to cause measurement errors that may be difficult to filter out. Therefore, it was decided to use external wires made of the same material as the corresponding thermoelements to eliminate the aforementioned problems encountered when using different materials. Hence, in all experiments that use alumel and chromel thermoelements, an alumel wire is connected to an alumel thermoelement, and a chromel wire is connected to a chromel thermoelement throughout this chapter and the thesis.

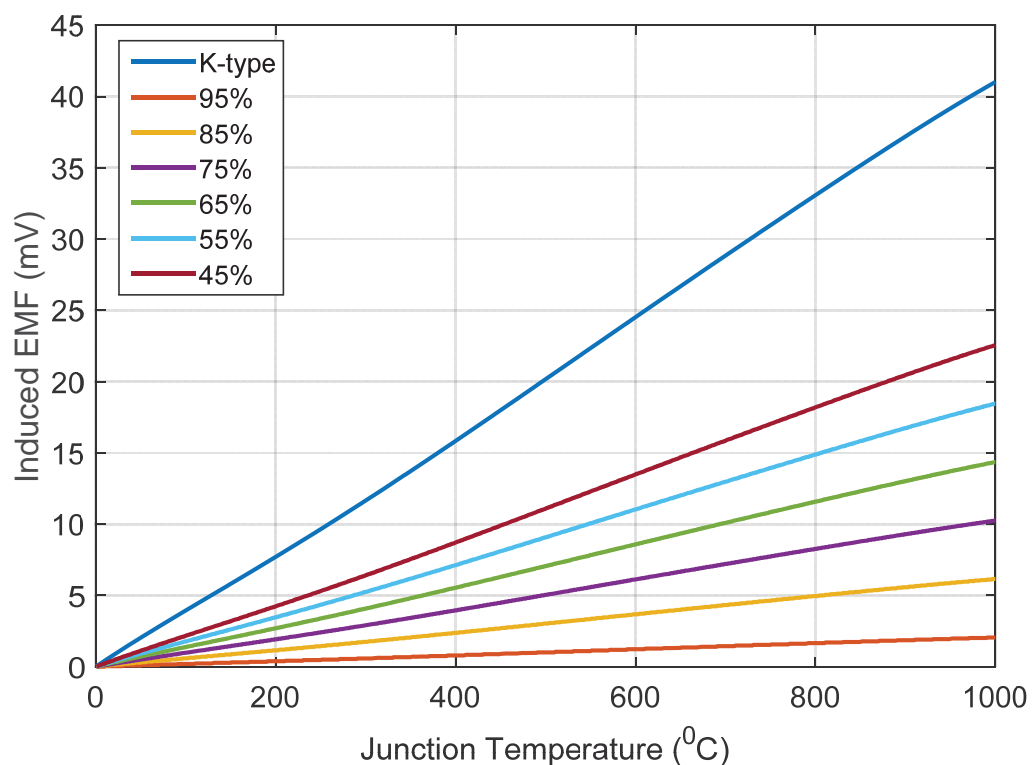


Figure 5.2 Variation of EMF at different connection point temperatures when the external wires are made of nicrosil

5.3 Effects of Multiple Junctions on Measurement Accuracy

The effects of having multiple junctions on a thermoelement on the measurement accuracy of multi-junction thermocouples were numerically investigated in Chapter 4. It was found that if the junction-forming method alters the Seebeck coefficient of thermoelements at the junction and if there exists a temperature gradient across such Seebeck coefficient altered zones (called dissimilar zones in Chapter 4), the accuracy of measurements is adversely affected (this can also be predicted from the law of intermediate conductors). Thus, whether spot-welded multi-junction thermocouples experience such adverse effects on measurement accuracy was investigated prior to applying this technology for SOFC temperature measurements.

A multi-junction thermocouple array of four sensing points, hence, having five thermoelements, was fabricated by spot-welding Ø0.5 mm alumel and chromel wires. Figure 5.3 shows a schematic diagram of the array. Thermoelements 1 is made of alumel, and all the others (2-5) are made of chromel. *S1-S4* are the four sensing points of the array. The distance between two adjacent sensing points is approximately 10 mm.

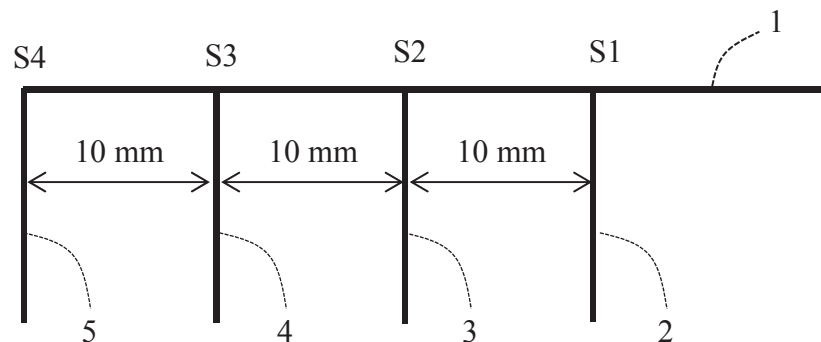


Figure 5.3 Schematic diagram of the architecture (the array)

Four K-type thermocouples (1.5 mm probe diameter) were fixed with the array such that there is one thermocouple at each sensing point (see Figure 5.4). The thermocouples were calibrated according to UKAS⁸ calibration standards. Thermocouples did not touch the array, and the distances between the array's sensing point and the corresponding thermocouple were approximately 1 mm for *S2*, *S3*, and *S4*, while that for *S1* was approximately 2 mm. The setup (array and thermocouples) was placed in a furnace and heated from room temperature to 700 °C at 400 °C/hour. Although this methodology ideally keeps the entire thermocouple array at the same temperature, in practice, there are temperature gradients inside the furnace. Temperature measured by the calibrated

⁸ United Kingdom Accreditation Service

thermocouples confirms this. Thus, this experimental methodology can subject the array to different temperatures across its sensing points. The sensor was placed towards the middle of the furnace where the two heating elements were approximately 10 cm and 20 cm from *S4* and *S1*, respectively. Temperatures from the four sensing points of the array and from the four thermocouples were recorded at 1Hz.

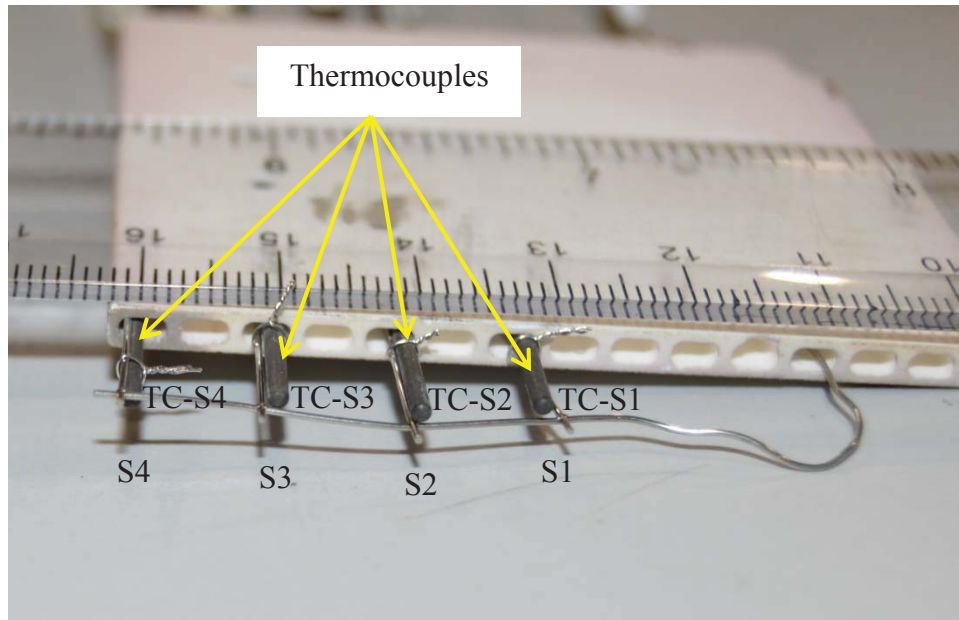


Figure 5.4 Multi-junction thermocouple with four commercial thermocouples (S1-S4: four sensing points of array; TC-S1 to TC-S4: four thermocouples at S1 to S4)

5.3.1 Results and Discussion

Table 5.3 shows the calibration data of the four thermocouples at 650 °C and 700 °C. *TC-S1*, *TC-S2*, *TC-S3*, and *TC-S4* are the thermocouples placed adjacent to *S1*, *S2*, *S3*, and *S4*, respectively. The upper temperature limit of the experiment was limited to 700 °C because heating beyond that caused the temperature at the insulated cable connection to thermocouples to reach unsafe levels due to heat transfer from the furnace. However, since 700 °C already covered two calibrated points of thermocouples, this limitation has no adverse impact on achieving the objective of the experiment.

Table 5.3 Thermocouple calibration data

	TC-S1	TC-S2	TC-S3	TC-S4
Error at 650 °C	2.07 °C	1.45 °C	2.30 °C	1.89 °C
Error at 700 °C	2.00 °C	1.51 °C	2.30 °C	1.86 °C
Uncertainty at each temperature	0.0	0.0	2.8	0.0

Table 5.4 shows temperatures measured by the four sensing points and their corresponding thermocouples at 650 °C and 700 °C nominal temperatures. The results show that *S2* was the most accurate sensing point of the array at 650 °C and *S4* and *S1* were the second and third accurate sensing points, respectively. *S3* appears to be the least accurate sensing point of the array, having a significantly greater temperature gap with its thermocouple. This temperature difference of *S3* must be compared with the accuracy of its thermocouple (*TC-S3*). The calibration data shows that *TC-S3* is the least accurate thermocouple among the four at 650 °C. Furthermore, it has 2.8 °C uncertainty in error. Therefore, it can be speculated that the calculated temperature difference between *S3* and *TC-S3* might largely be influenced by the measurement error and the uncertainty of *TC-S3*. This abnormality of *S3* can be observed at 700 °C as well. The measurement error and the uncertainty of the thermocouple *TC-S3* remains unchanged at its 650 °C values. Thus, the same explanation applies to the discrepancy observed at 700 °C.

Table 5.4 Temperatures measured by thermocouples and the array at calibration temperatures

At 650 °C nominal temperature		At 700 °C nominal temperature	
TC-S1	= 650.024 °C	TC-S1	= 700.040 °C
S1	= 648.691 °C	S1	= 700.176 °C
Difference	= 1.333 °C	Difference	= - 0.136 °C
TC-S2	= 650.061 °C	TC-S2	= 700.142 °C
S2	= 649.824 °C	S2	= 700.376 °C
Difference	= 0.237 °C	Difference	= - 0.334 °C
TC-S3	= 649.986 °C	TC-S3	= 699.999 °C
S3	= 645.165 °C	S3	= 696.561 °C
Difference	= 4.821 °C	Difference	= 3.438 °C
TC-S4	= 650.061 °C	TC-S4	= 700.004 °C
S4	= 649.104 °C	S4	= 700.813 °C
Difference	= 0.957 °C	Difference	= - 0.809 °C

According to the numerical calculations on performance presented in Chapter 4, if the intermediate junctions have contributed the measurement error, the sensing point having the largest number of intermediate junctions should have the greatest measurement error while that having the least number of intermediate junctions on its thermoelements should have the least error. Therefore, *S4* should be the least accurate sensing point, and *S1* should be most accurate sensing point if multiple junctions contribute the observed measurement error. However, *S4* was the most accurate sensing point, while *S1* was the third most accurate sensing point at 650 °C.

However, at 700 °C, *S1* was the most accurate sensing point, while *S2* and *S4* were the second and third most accurate sensing points, respectively. If *S3* is eliminated from the investigation due to its thermocouple's large uncertainty, the measurement error of the remaining three sensing points is well aligned with what can be explained by the effect of multiple junctions on accuracy.

There is one possibility that the effect of multiple junctions on the accuracy will not affect the measurement accuracy at one temperature while it is affected at another temperature. As the numerical calculations in Chapter 4 suggested, if there is no temperature gradient across a dissimilar zone, the presence of dissimilar zones does not affect the accuracy. However, the temperature gradient across the array at 650 °C and 700 °C were 6.619 °C and 6.319 °C, respectively. These values are reasonably close enough that the aforementioned phenomenon is extremely unlikely. Therefore, the locational correlation of the error at 700 °C can be considered purely random. Since Seebeck coefficient changes with temperature, that change caused this random behaviour.

Table 5.5 lists the temperatures measured by the four thermocouples at two instances of time around 650 °C and 700 °C. The data show the presence of a temperature gradient across the multi-junction array at each of the tested temperatures. Therefore, the temperature difference between a sensing point of the array and its corresponding thermocouple, calculated to three decimal places, should not entirely be due to measurement error of the array. There can be at least a fraction of a degree Celsius temperature gradient across the gap between a sensing point and its corresponding thermocouple. On the other hand, considering the length of that gap (2 mm for *S1* and 1 mm for the others) and the temperature gradient across the array, the total difference cannot be due to the temperature gradient. Therefore, it is evident that the array has some measurement errors, as the thermocouples have. However, the measurement error is not due to any effect from the multiple junctions on thermoelements.

Table 5.5 Temperature measured by thermocouples at two instances

The instance of time	TC-S1	TC-S2	TC-S3	TC-S4
near 650 °C	650.034 °C	653.304 °C	656.653 °C	655.399 °C
near 700 °C	695.044 °C	698.225 °C	701.363 °C	700.003 °C

5.3.1.1 Measurement of Spatial Temperature Variations

Although the experiment was primarily designed to investigate any influence of multiple junctions on measurement accuracy, the presence of a temperature gradient within the furnace additionally revealed the ability of multi-junction thermocouples in measuring spatial temperature variations. Table 5.6 shows the temperature measured by the array and by the four thermocouples at a random instance of time. The data show that thermocouple arrays could measure the temperature, having been subjected to previously established accuracy levels (or differences), while the array was subjected to a temperature gradient of approximately 6.57 °C (measured by commercial thermocouples). Thus, the results confirm that the multi-junction thermocouple array could detect spatial temperature variations across it. The Bespoke experiments to investigate the ability of multi-junction thermocouples in detecting spatial temperature variations are discussed in the next section.

Table 5.6 Temperature at a random instance of time near 650 °C

Temperature by thermocouple	Temperature by the array
TC-S1 = 654.125 °C	S1 = 652.815 °C
TC-S2 = 657.384 °C	S2 = 657.161 °C
TC-S3 = 660.699 °C	S3 = 655.852 °C
TC-S4 = 659.436 °C	S4 = 658.480 °C

5.4 Multi-Junction Thermocouples: Concept Validation

Although the previous experiment inadvertently demonstrated that different junctions could measure different temperatures at the same time, a more focused investigation was carried out to study whether sharing thermoelements between sensing points will cause the multi-junction thermocouples to measure an average temperature due to shared thermoelectric effects between sensing points or whether they can independently measure different temperatures without thermoelectric influences from adjacent junctions.

A multi-junction thermocouple having three sensing points, as schematically shown in Figure 5.5, was fabricated by spot welding Ø0.5 mm alumel and chromel wires. The chromel thermoelement is shared between three sensing points (junctions) denoted by *S1* to *S3*. The distance between two adjacent sensing points is approximately 10 mm. Three K-type thermocouples (1.5 mm probe diameter) were fixed with the array so there is one thermocouple at each sensing point of the multi-junction array. The two thermocouples adjacent to *S1* and *S2* had been calibrated according to UKAS calibration standards, while the one next to *S3* was not calibrated. Although initially a calibrated thermocouple was used at that point as well, the thermocouple failed halfway during the experiment. Therefore, the experiment had to be repeated with a non-calibrated thermocouple having identical manufacturer's specifications to the other two thermocouples (RS Pro, product code 397-1236). The distances between sensing points of the array and its corresponding thermocouple were approximately 1 mm for *S1* and *S2* and approximately 3 mm for *S3*. The setup (the array and the three commercial thermocouples) were fixed in atmospheric air inside the lab with all the thermoelements lying almost horizontally. The sensing points and their corresponding thermocouples were subjected to different temperatures by pouring water of different temperatures. The horizontal arrangement of the array

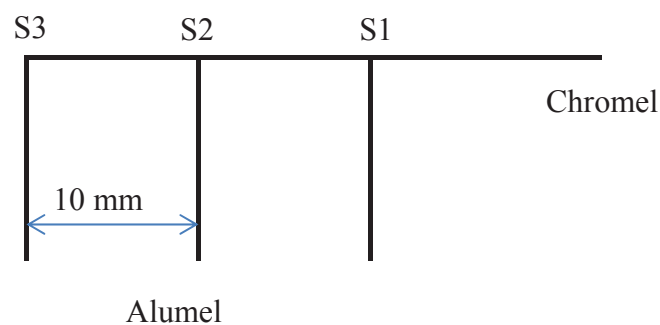


Figure 5.5 A schematic diagram of the three-point multi-junction thermocouple

facilitated pouring water only at the intended point without flowing into other junctions. Temperatures from the multi-junction thermocouple and the commercial thermocouples were recorded while the sensing points were subjected to different temperatures. The data logging system described in Appendix IV was used to record temperatures.

5.4.1 Results and Discussion

Figure 5.6 show the temperatures recorded by the three sensing points of the multi-junction array and their corresponding thermocouples at four random instances of time. The absolute values of the temperature differences between a sensing point and its corresponding thermocouple are also marked on the graph.

The maximum difference between a sensing point's temperature and a thermocouple's temperature is 1.5 °C. Thus, it is reasonable to consider that the multi-junction thermocouple measured temperature with very close accuracy to the commercial thermocouples. However, since the two calibrated thermocouples were also not calibrated at the experiment's operating temperature, a reliable assessment of accuracy cannot be made based on these measurements. In fact, since the accuracy assessment has already

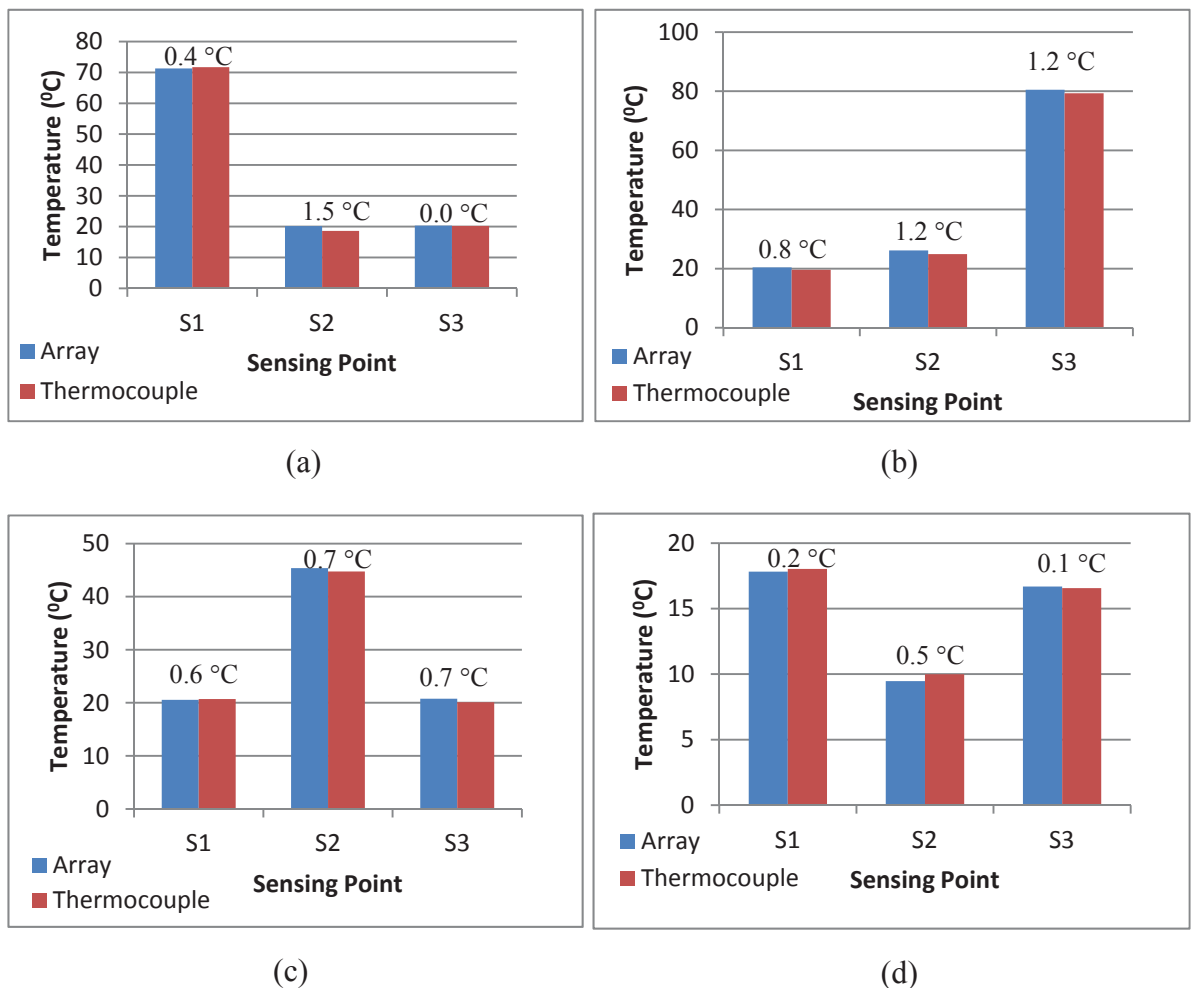


Figure 5.6 Spatial temperatures measured by the multi-junction thermocouple and conventional thermocouples. (a) to (d) are four random instances of time.

been performed previously, this investigation did not intend to re-assess accuracy. The purpose of having commercial thermocouples adjacent to sensing points of the array was only to make a rough comparison of accuracy.

There are two plausible reasons for the measurements of the array not fully complying with those of the commercial thermocouples. Firstly, there can be intrinsic measurement inaccuracies in the thermocouples as well as in the array. Secondly, a sensing point and its adjacent thermocouple may not have been heated uniformly while manually pouring hot water using a jar. If the rate of mass flow touching the sensing point and thermocouple is different or if water is not uniformly heated (perhaps due to air bubbles formed during pouring), a sensing point and its corresponding thermocouple can be subjected to different temperatures. Thus, measurement discrepancies between the array and the commercial thermocouples can be expected.

Despite the observed minor measurement discrepancies, the results show that the multi-junction thermocouple could measure different temperatures from its sensing points despite sharing a thermoelement between sensing points. Thus, sharing thermoelements between sensing points does not contribute any thermoelectric interferences that prevent different sensing points from measuring temperature independently from one another.

The core temperature sensing methodology proposed in this thesis for SOFC temperature sensing is the method of sharing thermoelements between sensing points to reduce the total number of thermoelements required for multi-point temperature sensing. The array and grid are two different architectures based on this concept, while different architectures may be derived using the same concept. However, all these architectures are thermoelectrically similar to one another because they are built on the concept of sharing thermoelements. Therefore, all other architectures built by sharing thermoelements should be free from thermoelectric interferences between adjacent sensing points.

An explicit validation of the temperature measured by a multi-junction thermocouple grid on working and non-working SOFCs was performed (see Chapter 6). Therefore, that investigation is not repeated in this chapter.

Despite the results showing that multi-junction thermocouples can measure spatial temperature variations independent from any thermoelectric interference from adjacent sensing points, there can still be implications depending on the application. Since metals are highly thermal conductors, heat from a hot point to a cold point can flow along a thermoelement, causing the temperature at a cold point to increase while the temperature at the hot point decreases. Thus, the measured temperature can change without much effect on the temperature of the object being measured. However, the time it takes to raise

the temperature of a nearby sensing point through heat transfer along thermoelements depends on the temperature gradient across the two sensing points: the higher the temperature gradient, the shorter the time due to the high rate of heat transfer. When the array or grid is in good thermal contact with the SOFC, part of the heat transfer along thermoelements transfers back to the cell at the cold point. Thus, only part of the heat transferred along the thermoelement actually contributes to raising the temperature at the cold sensing point. Furthermore, the electrical noses may also affect multiple sensing points at the same time because the thermoelements are shared between sensing points. This problem is rather acute in the grid architecture because of relatively highly dense sensing points compared to the array.

Because of these effects, there is a possibility that multi-junction thermocouples can show overall temperature increases across a cell while only one point has actually increased in temperature. If such a problem becomes serious, that may possibly be solved by advancing the data logging system appropriately (see Chapter 8). Since the SOFC temperature sensing experiments presented in this thesis did not show such a problem, no such efforts were made. However, the author would like to alert users who attempt to use this technology in other applications to be vigilant about these potential implications. Since the concept of multi-junction thermocouple was proven independent of the application domain and the theory of intermediate conductors is independent of the application domain, multi-junction thermocouples should be usable in any application other than SOFC. However, application-specific data logging systems may be needed to overcome the aforementioned issues, if they exist.

5.5 Surface Temperature Measurements

Having confirmed the necessary performance parameters of the multi-junction thermocouples required to qualify for SOFC temperature sensing, the other important investigation was to see how well a multi-junction thermocouple can detect temperature changes on a surface. The grid architecture was specifically chosen for this experiment because it is more useful than the array architecture in detecting two-dimensional temperature variations on a surface. This investigation is important because temperature evolutions in the cell of an operating SOFC are driven by chemical reactions. Thus, air/gas temperatures might be slightly different than surface temperature, and the sensor should measure the surface temperature accurately irrespective of the gas temperature. The experiment was designed to provide a controlled slight cooling to a substrate, from which temperature is measured by the grid while the surrounding remains at a different temperature. If the grid could detect any cooling of the substrate, that indicates it can detect surface temperature independent of surrounding gas/air temperature.

The multi-junction thermocouple concept validation presented in Section 5.4 showed that the presence of multiple junctions on a thermoelement does not thermoelectrically affect the adjacent sensing point, thus causing the entire array to measure a single temperature. Instead, the experiment confirmed that different sensing points could measure different temperatures that they are subjected to. This is, in fact, a re-validation of the theory of intermediate conductors. When operating as a thermocouple network, the functional difference between the array and the grid is that the array has multiple junctions on one thermoelement of a junction, while the grid has multiple junctions on both the thermoelements of a junction (an exception to this applies to junctions at some corners/ends that are identical to conventional thermocouples—no junctions on any of their functional parts of the thermoelements; the functional part is the segment of a thermoelement up to the junction from the data logging device). Since having intermediate junctions on one thermoelement did not cause thermoelectric interference to adjacent junctions, in principle, having multiple junctions on both thermoelements should also not cause any thermoelectric interference. Furthermore, the theory of intermediate conductors that the concept of multi-junction thermocouples is based on is not restricted to one thermoelement. Thus, the principle of operation of the multi-junction thermocouples as validated in Section 5.4 is equally valid for the grid as well (possibly, to any other architecture as well that shares thermoelements between junctions). Nonetheless, a middle sensing point of the array is connected to three conductors (for example, *S2* of Figure 5.5), while the middle sensing point of the grid is

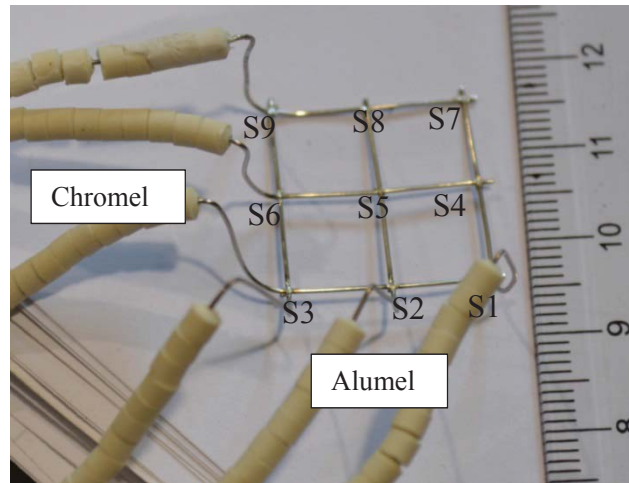
generally connected to four conductors (for example, *S5* of Figure 5.7 (a)). Thus, the paths of heat transfer to some junctions in the grid are higher than those of the array. Consequently, the measurement accuracy of some points of the grid may be inferior to the accuracy of the array in applications in which heat transfer along thermoelements is significant. Therefore, not only application specific data logging systems will be needed in such applications, but as suggested previously, the data logging system may also need to consider the architecture of the multi-junction thermocouple (whether array or grid) when rectifying measurement errors caused by heat transfer along thermoelements. However, since the grid's measurements reasonably agreed with the calibrated thermocouples when applied to SOFC temperature sensing in this research (see Chapter 6), no investigation into heat transfer phenomena along thermoelement was carried out. However, the author has briefly presented a conceptual methodology in Chapter 8 that can be used to rectify potential errors caused by heat transfer along thermoelements.

Figure 5.7(a) shows the nine-point multi-junction thermocouple grid used for the experiment. The grid was fabricated by spot-welding alumel and chromel wires of 0.5 mm diameter. An SOFC test cell (5 cm × 5 cm, *NextCell*TM) fitted into the SOFC test rig, shown in Figure 5.7(b), was used as the temperature-controlled substrate. The test cell is an electrolyte-supported cell having an effective electrode area of 4 cm × 4 cm. The cathode is facing up in Figure 5.7(b). The grid was placed on the cell (more specifically, on the cathode) and forced onto the cathode surface by means of a dead weight (approximately 20 g) to maintain good thermal contact between the grid and the cell.

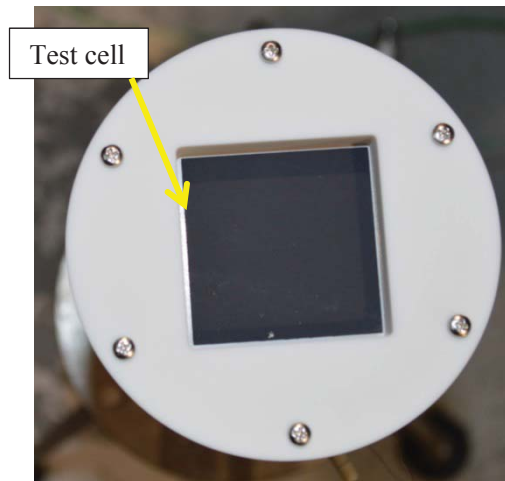
The cathode and the grid were open to air inside the furnace. The other side of the cell, the anode, was in the gas chamber of the test rig. A K-type commercial thermocouple was fixed in the air approximately 5 mm above the *S1* sensing point on the cathode to measure air temperature near the surface. Figure 5.8 shows the setup inside the furnace (Carbolite VST/200). The heated length (the height of the heating element) of the furnace is 20 cm, and the internal diameter is approximately 11 cm. As Figure 5.8 shows, the cell was in the upper half of the heated length. The maximum power of the furnace is 1 kW, and maximum achievable temperature is 1,100 °C. Once the thermocouple grid was placed inside the furnace, the top of the furnace was covered with thermal insulating fibre (Superwool 607, RS Components) to reduce convective cooling and maintain the inside temperature close to the set point.

The furnace was heated at a rate of 400 °C/hour. Some temperature interruptions were intentionally introduced during the heating process by changing the heating rate to investigate the response of the grid. Temperature measurements from the grid as well as

from the thermocouple were recorded at 3 second intervals. While the temperature was being recorded under normal heating conditions, a flow of nitrogen ($500 \text{ cm}^3/\text{min}$) was supplied to the anode chamber around 520°C to force-cool the cell. Pressure of nitrogen before entering the mass flow controller was set to 3.5 bar. As per the setup of the test rig, the nitrogen impinges on the cell perpendicularly to it approximately from its centre..



(a)



(b)

Figure 5.7 (a) nine-point thermocouple grid; (b) SOFC test cell fitted onto the cell holder having its $4 \text{ cm} \times 4 \text{ cm}$ cathode facing up

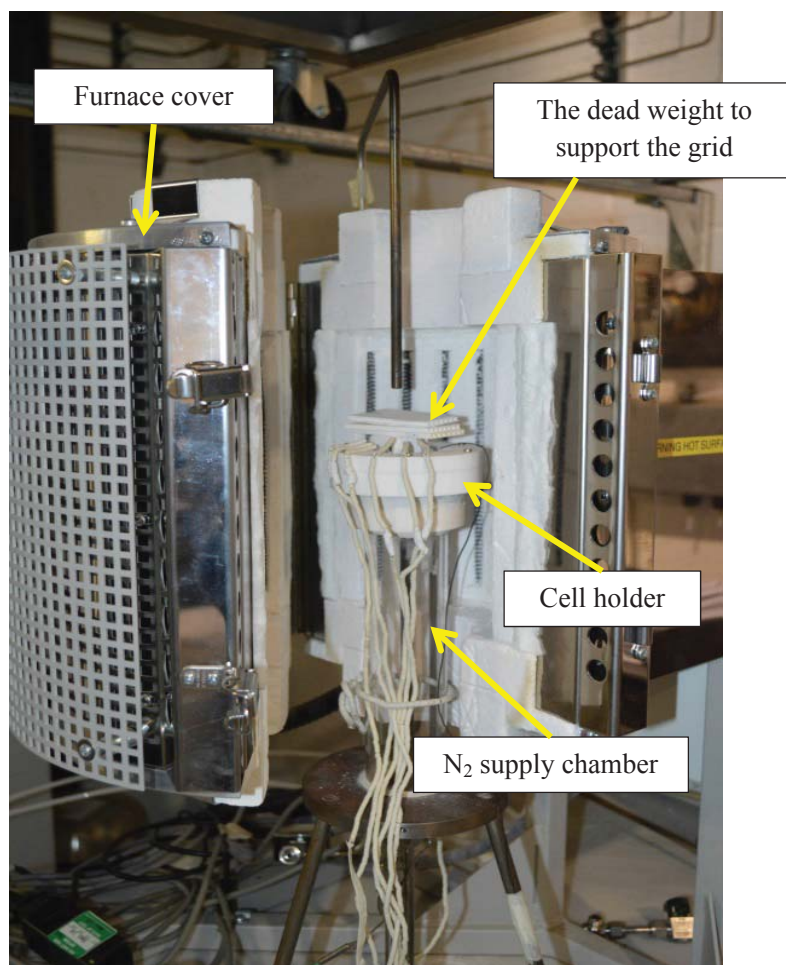


Figure 5.8 SOFC test rig with the cell in place. The dead weight was used to force the grid onto the cathode

5.5.1 Results and Discussion

Figure 5.9 shows the temperature recorded from the grid and the thermocouple. The region where nitrogen was fed into the anode chamber is marked on the figure. The non-uniform heating pattern is a result of the intentional interruption introduced to heating. As evident from the graph, introduction of nitrogen around 520 °C caused the cell to cool as expected. However, no cooling effect can be noticed by inspecting only the cell's temperature measured by the grid because the furnace was in a rapid heating cycle while nitrogen was introduced. Thus, temperature continued to increase. However, it can clearly be seen that the cell, which was at a higher temperature than the air, suddenly starts demonstrating a lower temperature than the air, and this continues throughout the rest of the experiment. This implies that the air temperature has increased more rapidly than the cell temperature. This is because cooling from nitrogen has suppressed the heating rate of the cell.

The average cell temperature variation with time shown in Figure 5.10 shows more clearly how the cell heating was suppressed by cold nitrogen flow. Prior to introducing nitrogen, the cell temperature was higher than the thermocouple temperature. For example, the cell temperature at the 80th minute was 34 °C higher than the thermocouple. However,

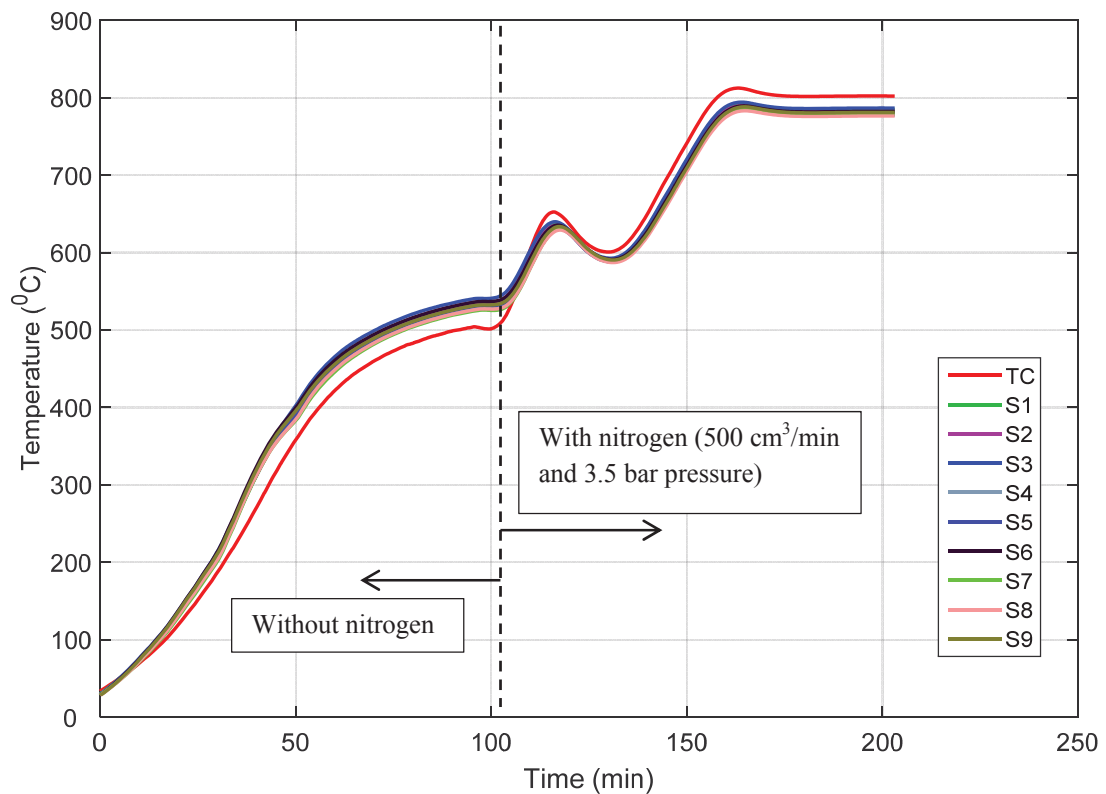


Figure 5.9 Temperature from the grid and the thermocouple (Heating rate 400 °C/hour—set value) S1 to S9: nine sensing points of the grid, TC: commercial thermocouple

after introducing nitrogen, the cell temperature dropped below the thermocouple's measurement of the cathode air temperature. For example, the cell temperature at the 140th and 180th minutes was lower than the thermocouple by 25 °C and 21 °C, respectively. The drop of cell temperature after introducing nitrogen was due to cell cooling. Therefore, the cooling effect on the cell due to the flow of nitrogen is evident. Importantly, the grid could well detect the temperature change on the cell surface.

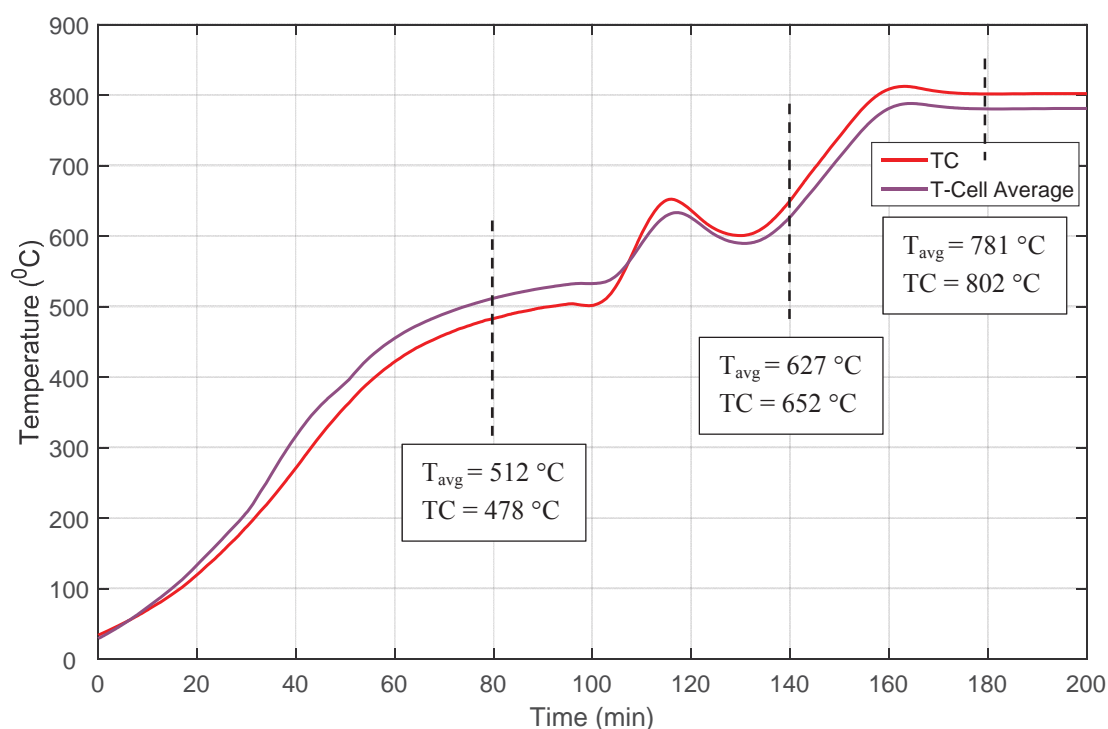


Figure 5.10 Change of average cell temperature and the cathode air temperature (T_{avg} represents average cell temperature and TC represents thermocouple temperature)

Table 5.7 shows temperatures measured by the grid from its nine sensing points. These values show that the grid has recorded different temperatures from its different sensing points. The reason for the presence of a temperature gradient across the grid should be due to differences in the cooling effects on the cell caused by different gas distribution across the cell. Importantly, these results inadvertently show that the grid measured different temperatures from its different sensing points despite sharing thermoelements.

Table 5.7 Different temperatures measured by different sensing points

Sensing point	S1	S2	S3	S4	S5	S6	S7	S8	S9
Temperature at 75 th minute (°C)	504	506	512	498	500	506	493	495	502

5.6 Conclusions

The thermoelectric influences of having multiple junctions on a thermoelement on measurement accuracy, as suggested by the numerical calculations presented in Chapter 4, were experimentally investigated with a spot-welded multi-junction thermocouple array with four sensing points. The experimental results revealed that the junctions formed by spot-welding did not influence measurement accuracy. Although there were measurement inaccuracies (established by the calibrated thermocouples), they were purely random in nature and had no correlation to the location of the sensing point on the array. Therefore, it was experimentally confirmed that the use of multiple junctions on a thermoelement is a plausible technique to reduce the number of thermoelements/external wires required in multi-point temperature sensing.

The ability of multi-junction thermocouples to measure spatial temperatures without any thermoelectric interference caused by shared thermoelement is experimentally confirmed. Thus, despite sharing thermoelements between sensing points, a multi-junction thermocouple does not show an average temperature that it is subjected to. Therefore, they can be used for spatial temperature measurements.

A multi-junction thermocouple grid was employed to measure the surface temperature changes of an SOFC test cell while it was being heated. The results showed that the grid could successfully detect temperature changes on the surface while the air near the surface had a different temperature. Thus, the ability to employ multi-junction thermocouples for surface temperature measurement from SOFC was confirmed.

The use of spot-welding for junction fabrication is proven successful, although the spot-welding of very thin wires (less than $\varnothing 0.5$ mm) is somewhat difficult. Furthermore, inconsistencies in the junction-forming method are likely to cause batch-wise inconsistencies in accuracy. Hence, controlling quality in the fabrication process is essential for better reliability of the sensor.

5.7 References

- [1] National Institute of Standards and Technology, *NIST standard reference database 60—Version 2.0 (Web version)*, [viewed 15/ 08 / 2015]. Available from: <http://srdata.nist.gov/its90/main/>
- [2] Jiang, S.P. and Chen, X., Chromium deposition and poisoning of cathodes of solid oxide fuel cells—review, *International Journal of Hydrogen Energy*, 2014 , 39(1), pp. 505-531
- [3] Davis, J.R., Heat resistant materials, USA, ASM International, 1997, pp. 77
- [4] Robin E. Bentley, *Handbook of temperature measurements Vol 03 : Theory and Practice of thermoelectric thermometry*, Springer, 1998

Chapter 6 : SOFC Temperature Sensing

Chapter Summary

This chapter focuses on applying the proposed multi-junction thermocouple concept to study the influences of temperature on the performance of SOFC and, to investigate how the dynamic operating conditions, such as load changes, affect the cell temperature.

The chapter begins with introducing the experimental setup and the SOFC test cells being used in Section 6.1. Before investigating the SOFC performance, the effects of the thermocouple grid on an operating SOFC is first assessed as presented in Section 6.2. Two case studies on assessing the temperature distribution of non-working SOFCs are presented in Sections 6.3 and 6.4; temperatures from the grid on a non-working cell also validated in these studies. Section 6.5 is dedicated to investigating the temperature and performance relationships of working SOFC under different operating conditions. Further, the temperature measurements from the grid are validated on a working fuel cell as well. Finally, the chapter concludes with some conclusions drawn based on the findings in Section 6.6.

6.1 Introduction

Out of the two multi-junction thermocouple architectures proposed, the grid was chosen for SOFC performance investigations because it delivers a better spatial resolution in temperature measurements than the array. Further, it requires fewer thermoelements than the array for the same number of sensing points, which makes handling easy. The ease of placing the grid on the electrode than putting the array was an added advantage. However, the choice of the grid for this experiment is only a case study where any different architecture built on the concept of multi-junction thermocouples may be used for SOFC temperature sensing, for example, the array can also be used.

Typical SOFCs, either planar or tubular, have two accessible surfaces to take temperature measurements: the anode and the cathode. Selecting one of them was a primary choice to make. Although the temperature from a cathode and an anode may divulge different operational characteristics of an SOFC, the selection of the electrode for temperature sensing was primarily governed by the simplicity in application and the safety in operation. The anode chamber requires gas-tight sealing, whereas the cathode of the test rig used in this research is open to atmosphere. Thus, placing the grid on the cathode is simpler than placing it on the anode. Therefore, the cathode was chosen as the temperature sensing electrode. Thus, the cathode temperature is considered as the cell temperature.

Electrolyte-supported $5\text{ cm} \times 5\text{ cm}$ test cells (*NextCell-5*) were used for the experiments throughout. The cathode of these cells is made of lanthanum strontium manganite (LSM) and the anode is made of nickel oxide-yttria stabilised zirconia (NiO-YSZ). Each electrode is approximately $50\text{ }\mu\text{m}$ in thickness and square in shape with side length 4 cm . The electrolyte is made of a confidential, proprietary formulation called HionicTM, whose conductivity and strength are said to be similar to those of 10ScSZ and 6ScSZ, respectively. The thickness of the electrolyte is approximately 0.13 mm to 0.17 mm .

The data logging system that the author developed and briefly described in Appendix IV was used for data recording.

6.2 Effects of Thermocouple Grid on SOFC Performance

Before applying the thermocouple grid for temperature sensing from SOFC, it is important to assess if the thermocouple grid's operation as a sensor causes any influence to the performance of the SOFCs being investigated. This can be accomplished by comparing the performances of a cell with and without the thermocouple grid. Two methods were initially considered to carry out this investigation as described below.

Method I: Physical Isolation

In this method, an SOFC is tested at a known set of operating conditions (temperature, current, flow rate, and flow composition) without fixing the grid on the cathode. Then, the thermocouple grid is attached to the cathode, and the cell is tested under the same operating conditions. Comparing the polarisation curves in the two cases enables to assess any influence from the grid on the performance of the SOFC.

Method II: Electrical Isolation

In this method, the thermocouple grid stays on the cell at all times of the SOFC operation. However, from time to time, the grid is electrically disconnected from the data logging system (by mechanically disconnecting it from the data logger) to stop its operation. Because of the electrical disconnection of the grid from the data logging system, the grid has no electrical activity on it. Thus, the sensor becomes only a piece of metal grid staying on the cathode of an SOFC. Since K-type thermocouples are used for cathode temperature measurements in these experiments, the presence of the grid (made of K-type materials) does not introduce any new material into the cathode chamber. Placing a grid on the cathode does not prevent oxygen from making contact with the cathode (with the absence of any forced air flow on the cathode, no disturbance to flow can happen). Thus, having a non-operating thermocouple grid on the cathode can, reasonably, be expected not to make any influence on the performance of a cell. While running the SOFC at pre-determined operating conditions (temperature, current, flow rates, and flow composition), the performance of the cell is recorded when the sensor is electrically connected to / disconnected from the data logging system. Comparing the performance under the two cases enables to assess any influence from the grid's operation as a sensor to the performance the SOFC.

6.2.1 Method Selection

Method I requires connecting or disconnecting the thermocouple grid between two performance tests, which then needs cooling down the cell to room temperature between the two tests. Therefore, there is a potential risk of cell degradation or failure due to anode re-oxidation^[1]. Consequently, the two cell-operations will not be adequately comparable and may lead to performance disparities that are difficult to distinguish whether caused by the grid or not. Assembly or disassembly of the grid involves a significant level of manual handling. This manual handling may result in movements of the current collector on the cathode causing its contact points with the cathode to be different in the two performance test. Since contact points contribute to overall electrical resistance in the current carrying path, changes in contact points is likely to influence the current and the voltage across the load. Further, the position of the cell inside the furnace may not be identical in the two tests causing disparities in the temperature distribution across the cell. Therefore, because of the aforementioned reasons, the performance of the cell in the two tests will be different from one another even without any influence from the thermocouple grid. In contrast, Method II is free from all the above problems caused by assembly and disassembly of the grid between the two tests. The presence of some excess amount of K-type material, which has chromium, on the cathode is the key plausible detrimental impact that can be expected on the SOFC performance when Method II is employed. However, if the performance test does not last for any more than a couple of hours (circa, 2-3 hours), degradation due to chromium poisoning cannot expect to be noticeable/exist^[2]. Thus, Method II was chosen to investigate any effects of having the grid on the cathode on the performance of an SOFC.

6.2.2 Methodology

A thermocouple grid having nine sensing points was fabricated by spot-welding of Ø0.5 mm alumel and chromel wires. A schematic diagram of the grid is shown in Figure 6.1. The grid was placed on the cathode (properties are as described in Section 6.1) towards the middle of it. The cathode current collector (a platinum mesh) was placed towards a corner of the cathode as schematically shown in Figure 6.2. A variable resistor (maximum resistance 10 kΩ) was connected across the cell, as the DC⁹ load of the cell, to alter the current drawn from the cell. The anode was reduced at 800 °C for over 3 hours using a mixture of hydrogen and nitrogen with a volumetric composition of 60 ml/min and 240 ml/min, respectively.

⁹ Direct Current

The cell was operated at 800 °C with a fuel mixture of hydrogen and nitrogen with a volumetric composition of 100 ml/min H₂ and 200 ml/min N₂. The DC load (variable resistor) was adjusted to draw a current of approximately 30 mA from the cell. The current was chosen as 30 mA to bring the cell into a moderately active operation (neither overactive nor underactive). The grid was kept electrically disconnected from NI-9213 temperature data logger for approximately 30 min. Thereafter, it was connected to the data logger for rest of the operation. Current, voltage, and cell temperature were recorded at 2 second intervals. Power output of the cell was calculated by multiplying the current and the voltage (power = voltage × current) as a measure of the cell performance.

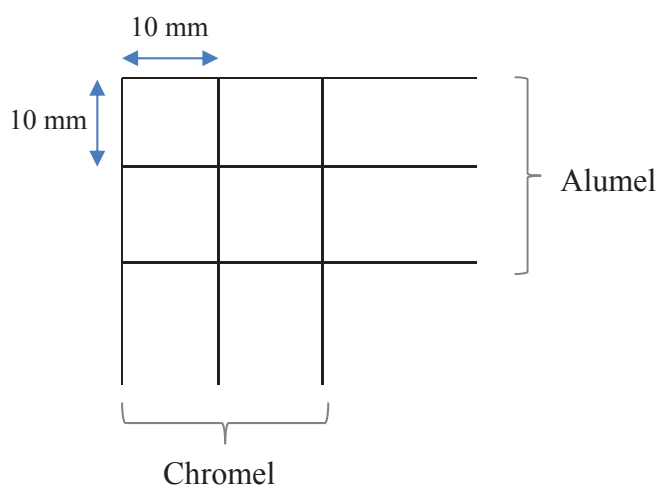


Figure 6.1 A schematic diagram of the nine-point K-type thermocouple grid (each wire is 0.5 mm in diameter)

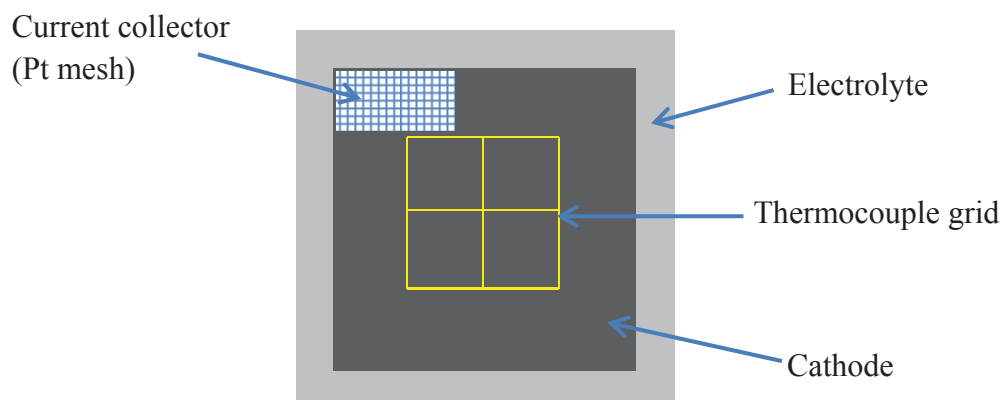


Figure 6.2 A schematic diagram of the locations of the grid and the current collector on the 4 cm × 4 cm cathode of *NextCell-5*

6.2.3 Results and Discussion

Figure 6.3 shows the power output the cell delivered throughout the experiment. The regions where the grid was electrically connected to / disconnected from the data logging circuitry are marked on the graph. The mean power output in each region was 23.8 mW. If the functioning of the grid as a sensor affected the performance of the cell, the power output should be different in the two regions. The absence of any such differences confirmed that the functioning of the grid on the cathode as a sensor does not influence the performance of the cell. (Reasons behind the very low power output are discussed later in this chapter.)

Long-term operation of an SOFC while having K-type thermocouple materials on the cathode may cause premature degradation of the cell due to chromium poisoning. However, this experiment did not focus on such long-term impact assessment; rather, it focused on assessing the effects of having a sensor grid on the performance of a cell. If K-type materials are not suitable for the operating conditions required, changing the material is not a technically tough step (choice of K-type materials for this research and its potential implications were discussed in Chapter 5).

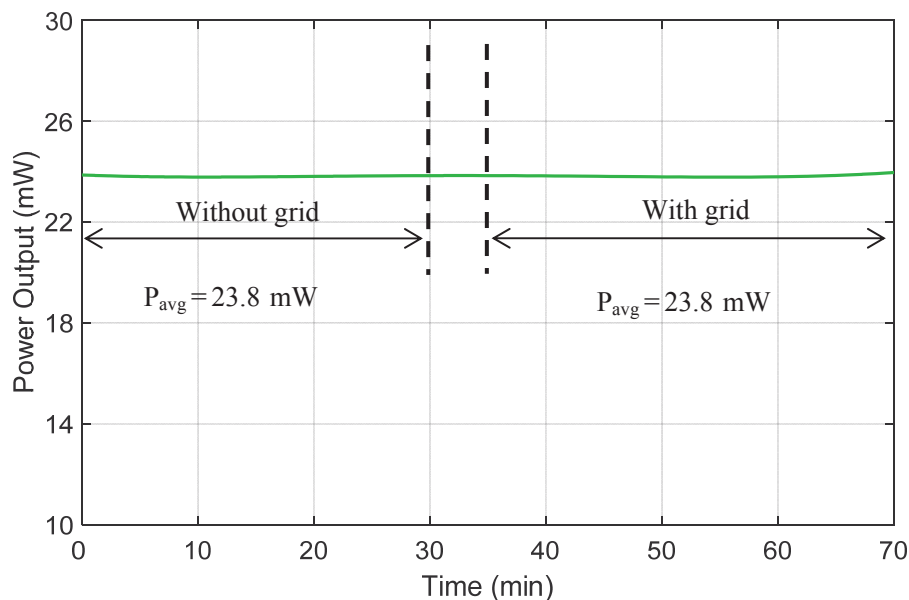


Figure 6.3 Change of the cell current over time with and without the thermocouple grid operating on the cell. (P_{avg} : the average power output)

6.3 Temperature of a Non-Working Cell: Case I – Grid Only

In this section, the cell surface temperature distribution of an SOFC measured during the anode reduction process and when the cell is in open-circuit mode (non-working) are presented and discussed.

A thermocouple grid fabricated by spot-welding of Ø 0.5 mm alumel and chromel wires was used for the experiment (Figure 6.4), which is the same grid used for the surface temperature measurement experiment presented in Chapter 5. The distance along a thermoelement between two adjacent sensing points is approximately 10 mm. Thus, the grid measured temperatures from nine points within an approximate area of 4 cm² from the cathode' active area.

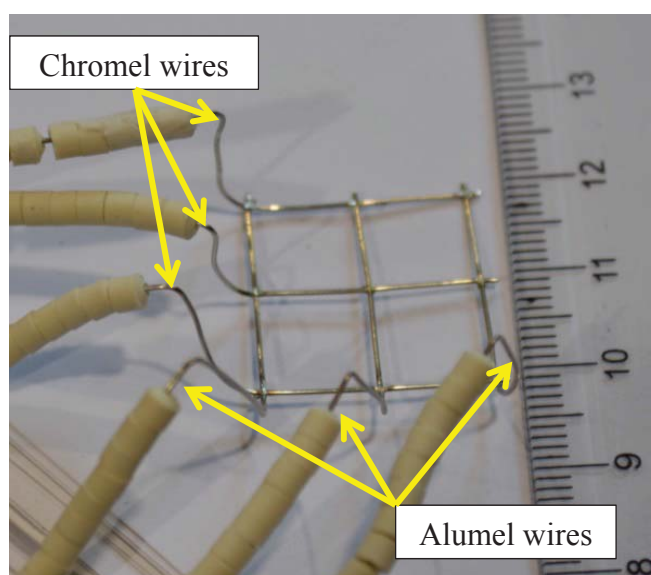


Figure 6.4 The nine-point thermocouple grid

A nickel mesh and a platinum mesh were used as current collectors on the anode and the cathode, respectively. The thermocouple grid was placed on the platinum mesh, and a dead weight as been put on top of the grid, as shown in Figure 6.5, to retain the contact between the grid and the mesh on the cathode. The approximate locations of the temperature sensing points on the cathode are shown in Figure 6.6. A commercial K-type thermocouple was placed in the air-chamber adjacent to *S1* sensing point and approximately 7 mm above the cathode to measure the air temperature near cathode surface. Current collecting wires from the two electrodes were connected to NI-USB-6210 data logger for OCV measurements. The thermocouple grid and the commercial thermocouple were connected to NI-9213 data logger for temperature measurements.

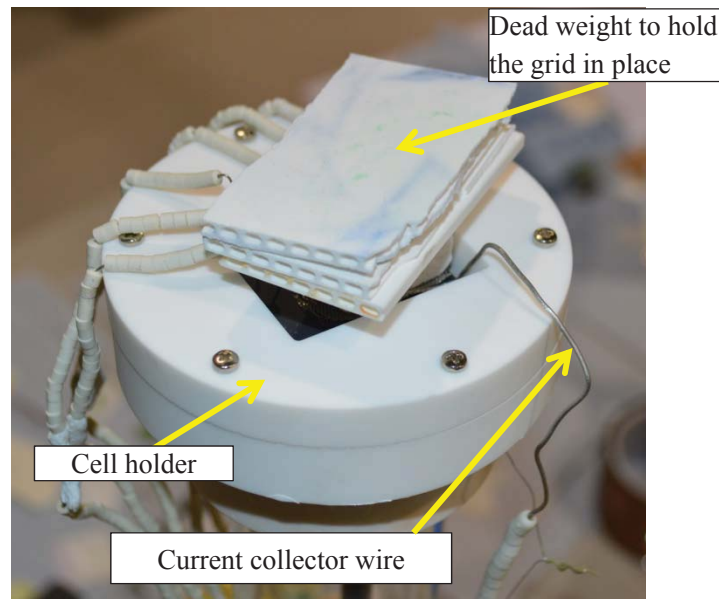


Figure 6.5 The cell with the grid and the current collector in place

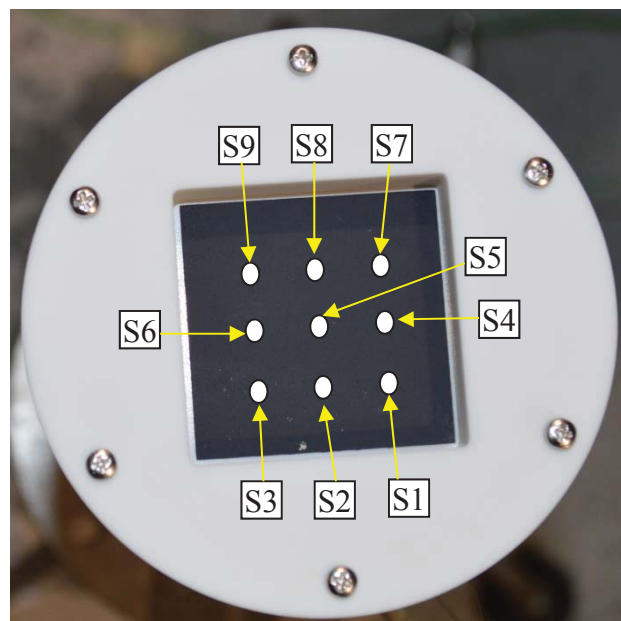


Figure 6.6 Approximate locations of sensing points on the cathode

The test rig with the sensor attached cell in place was heated at an approximate rate of 400 °C/hour up to 800 °C. The complete test rig arrangement is shown in Figure 6.7. Nitrogen was introduced into the anode chamber at a rate of approximately 180 ml/min from the beginning of the heating process to expel any air inside the anode chamber to facilitate anode reduction. Hydrogen was introduced to the anode chamber at around 630 °C with a volumetric flow rate of approximately 15 ml/min to initiate the reduction of NiO into Ni. The volumetric composition of nitrogen and hydrogen was set as approximately 5% H₂ and 95% N₂ out of total volume following published data^[1]. The

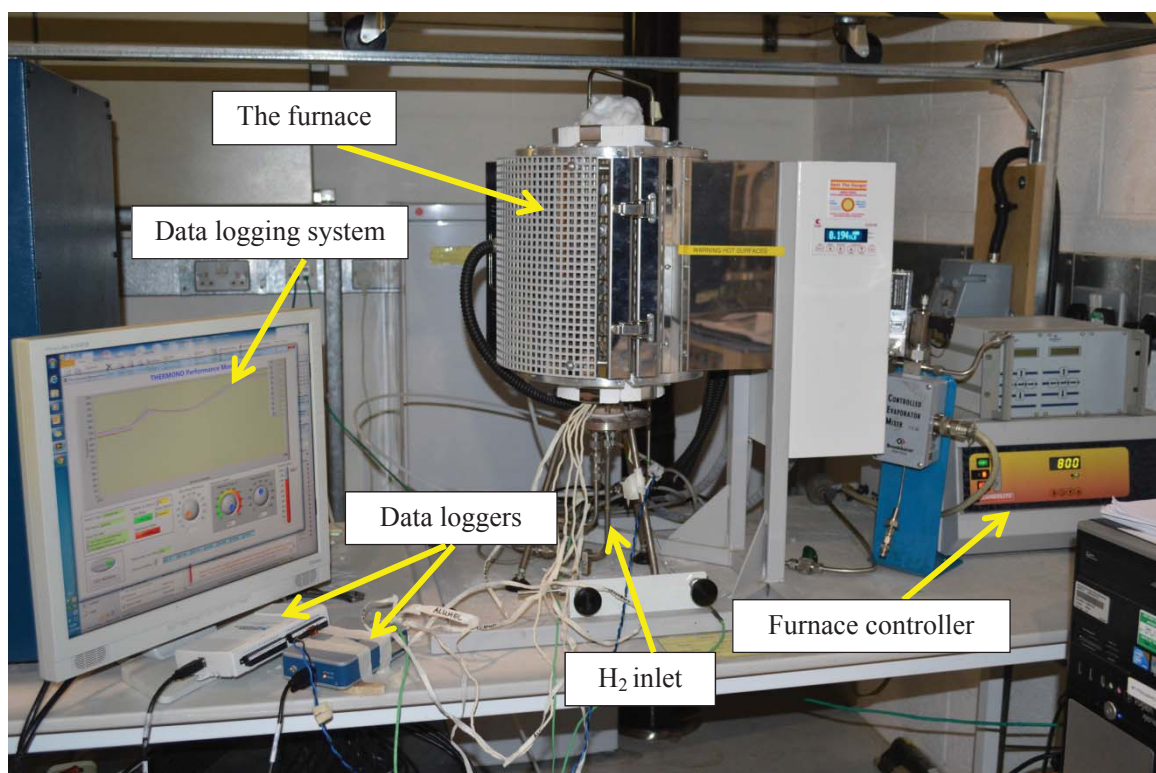


Figure 6.7 SOFC test setup used for OCV measurements

gas supply was continued for approximately 65 minutes to allow a substantial time for the anode reduction process to complete. The furnace remained at 800 °C for roughly 60% of the total reduction time (approximately 40 minutes). The hydrogen supply was disconnected 65 minutes after its introduction to complete the reduction process. However, nitrogen was continued to provide for further 5 minutes to expel any residual hydrogen from the anode chamber. The purpose of removing hydrogen from the anode chamber was to investigate the cell's response to a fresh flow of hydrogen once the cell operation is commenced, which was merely a curiosity-led step to see how quickly the cell voltage changes with the introduction of hydrogen. However, the data recording frequency was not the ideal one to investigate the time response.

Once the nitrogen supply was disconnected, hydrogen was supplied to the anode chamber at variable volumetric flow rates given in Table 6.1. Different flow rates of hydrogen were employed to investigate any corresponding variations in cell temperature due to varying flow rates. The period of existence of each flow rate was determined such that the cell temperature and the OCV become stable at a given flow rate. The flow rates were cycled to investigate the repeatability of measurements. The pressure of hydrogen at the entrance to the mass flow controller was approximately at 3.5 bar; the test rig did not facilitate the anode chamber pressure monitoring. Since the cathode was freely open to atmosphere, the air supply onto the cathode was not controllable. Neither the air nor the

hydrogen was preheated. The furnace's control system maintained the set temperature at 800 °C with an accuracy of ± 1 °C throughout the experiment. Temperatures from the grid and the commercial thermocouple as well as the OCV were monitored and recorded at 3 second intervals.

Table 6.1 Hydrogen flow rates with approximate duration

Region	H ₂ flow rate (cm ³ /min)	Duration (min)
A	500	15
B	250	15
C	150	15
D	100	15
E	50	15
F	100	15
G	150	30
H	250	15
I	500	10

6.3.1 Results and Discussion

Temperatures measured from the grid and the commercial thermocouple during the anode reduction process are shown in Figure 6.8. The temperature sketch drawn on the graph shows the average temperature from nine sensing points of the grid between the 45th and 68th minute of the operation and that of the thermocouple (positioning of the sensing points on the sketch is similar to the actual position of the sensing points – see Figure 6.6). The maximum of the standard deviation of temperature measured by each sensing point in this period is 0.32 °C. Therefore, the calculated values of the average temperature of a sensing point is a reasonably accurate figure to represent the respective sensing point's temperature over the entire period considered.

Since the grid was in thermal contact with the cell, its measurements can represent the cell's surface temperature with a satisfactory degree of verity. The results show that the commercial thermocouple, held approximately 7 mm above the cathode, has recorded slightly a higher temperature than the thermocouple grid recorded (approximately 21 °C greater than the average cell temperature). A similar behaviour was observed previously under forced-cool surface temperature measurement experiment discussed in Section 5.5 of Chapter 5 due to cell cooling. Although the total volumetric flow rate of the gas mixture employed in this study was much lower than that used in the surface temperature measurement experiment, the observed temperature disparity between the thermocouple and the grid may be attributed to a chilling effect enforced by the cold gas mixture. Importantly, *S8* records the lowest temperature of 776.2 °C while *S5* records the second

lowest temperature of 777.4 °C. Although *S5* was positioned almost above the gas pipe in the anode chamber, the pipe was not perfectly vertical. If its slight inclination caused the gas to focus towards *S8*'s position than onto *S5*, the lowest temperature at *S8* could also be explained by the same chilling effect. The maximum temperature gradient across the cell (10.2 °C) is recorded between *S8* and *S3*. This temperature gradient may be a combined effect of the cell-chilling and characteristic temperature gradients present within the furnace.

Importantly, the results show that the introduction of hydrogen (around 630 °C) and the subsequent reduction process has not altered the cell's temperature profile in any noticeable magnitude. The slight overshoot of the temperature as it reached 800 °C set-point was made by the temperature controller's controlling characteristics. The PID¹⁰ controller of the furnace was unable to reach 800 °C smoothly; instead, it slightly overshoot before settling at the set point.

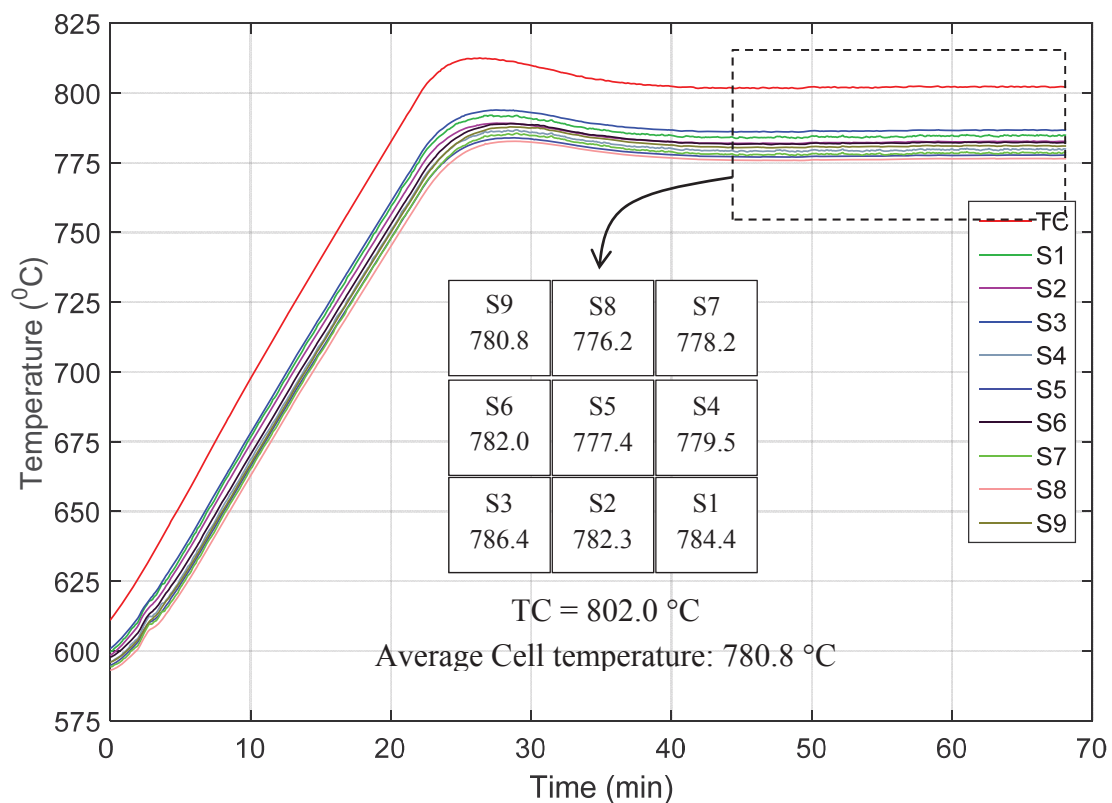


Figure 6.8 Temperature distribution during the anode reduction and the average temperatures over 45th and 70th minute (TC: commercial thermocouple S1-S9: nine sensing points of the grid. Temperature values are in degree Celsius)

¹⁰ Proportional-integral-derivative

Figure 6.9 shows the temperature distribution and the OCV of the cell under different hydrogen flow rates. The marked regions (from *A* to *I*) represent the different hydrogen flow rates given in Table 6.1. The graphs are plotted with raw data (without any processing); hence, the minor fluctuations on measurements might be some noises in the recorded signals. Since these noises do not distract distinguishing the overall trends, they were not eliminated with data filtering. The grid's temperature distribution shows the presence of a relatively significant temperature gradient across the small region ($2\text{ cm} \times 2\text{ cm}$) that the grid occupied. The greatest temperature gradient of $14.1\text{ }^{\circ}\text{C}$ occurred between *S5* and *S9* in the flow region *I*, where *S9* is higher than *S5*. This temperature gradient is slightly greater than the gradient observed during the anode reduction process ($10.2\text{ }^{\circ}\text{C}$). In general, *S8* and *S5* sensing points, which recorded the lowest temperatures during anode reduction, continued to record the lowest temperature during most of the experiment, except under 500 ml/min flow rate regions. This behaviour could be attributed to local cooling caused by cold gasses impinging on the cell as explained previously under the reduction process. The slight abnormality of *S8* during 500 ml/min flow rate regions could be due to flow leakages as described below.

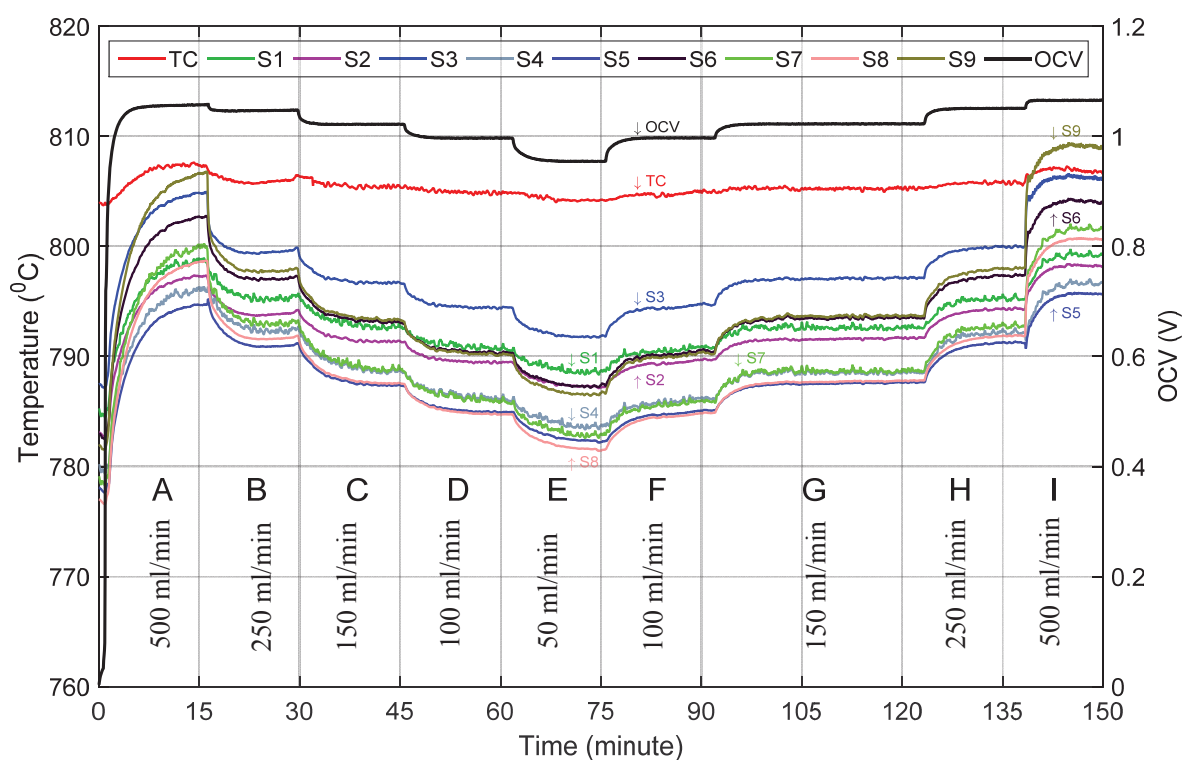


Figure 6.9 Temperature and OCV over cell operation
(TC: thermocouple, S1-S9: sensing points of the grid, OCV: open circuit voltage of the cell)

The average cell temperature shows a proportional variation with the hydrogen flow rate as shown in Figure 6.10 where the lowest cell temperature corresponds to the lowest volumetric flow rate of hydrogen (region *E*) and the highest temperature corresponds to the highest volumetric flow rate (region *A* and *I*). If the observed average cell temperature profile was generated solely by a chilling effect of the cold stream of hydrogen; then, the lowest temperature should correspond to the highest volumetric flow rate and vice versa. However, the observed temperature versus flow relationship is quite opposite to what could ideally be explained with a chilling effect. Thus, the observed cell temperature changes to varying flow rates cannot be wholly ascribed to a chilling effect. (However, the overall cell cooling is possible due to chilling effect causing the average cell temperature to stay below the furnace temperature at certain flow rates.) The higher flow rates of hydrogen appear to have released more heat energy than the lower flow rates making the cathode hotter at higher flow rates. This behaviour could happen due to a gas leakage through the sealing or through a defective electrolyte enabling hydrogen to combust directly on the cathode surface. The higher flow rates of hydrogen may enhance the leakage, and thus, the direct combustion may take place at a higher rate liberating more heat to the cathode. The behaviour of *S8* sensing point can also be explained in terms of a gas leakage. Although *S8* was the coolest sensing point during the anode reduction, its temperature has dramatically increased under 500 ml/min flow rate, as

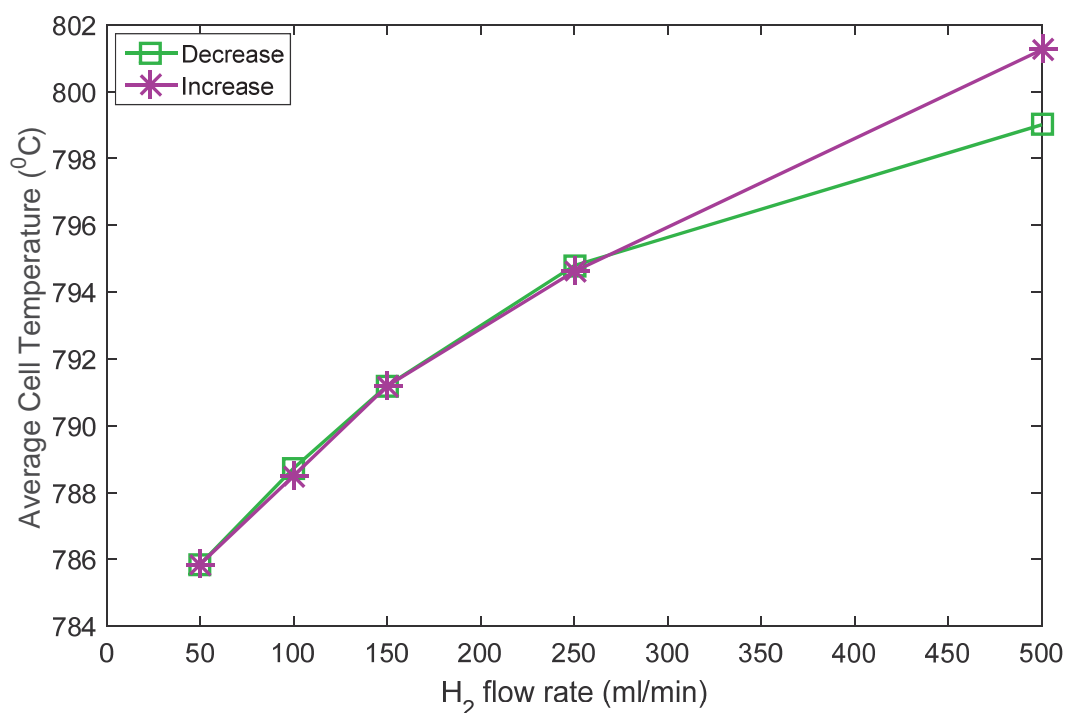


Figure 6.10 Variation of average cell temperature with hydrogen flow rate
 (“Decrease”- Temperature during flow rate was decreased from 500 ml/min to 50 ml/min
 “Increase”- Temperature during flow rate was increased from 50 ml/min to 500 ml/min)

shown in Figure 6.9. Further, it can be seen that its temperature gradually decreases with the reduction of hydrogen flow rate making it, once again, the coolest point under 50 ml/min flow rate. The gas leakage, which is likely to be proportional to the flow rate, has made temperature at *S8* higher at higher flow rates by burning more fuel adjacent to it. This may be why *S8* could not continue to remain as the lowest sensing point while *S5* continued to be in the lowest two positions.

A leakage test carried out later revealed the presence of gas leakages from the anode chamber to outside air in the furnace, which is the cathode chamber. Importantly, diagnosis of the gas leakage was driven by the cell surface temperature profile obtained by surface temperature sensing because the temperature variations the commercial thermocouple demonstrated with varying flow rates was subtle compared to those the variations demonstrated by the grid.

The temperature measured by the commercial thermocouple (labelled as TC in Figure 6.9) was almost non-responsive to the dramatic temperature changes took place in the cell. The thermocouple continued to record nearly a constant temperature, yet slightly higher than the furnace's set temperature, all over the experiment. The disparity between the thermocouple's measurement and the furnace's setting was observed during the anode reduction process as well. Thus, it can be speculated that the temperature within the furnace was slightly higher than what the controller's display shown. In fact, such temperature gradients are possible to take place within a furnace. Importantly, comparing the surface temperatures measured by the thermocouple grid and the near-surface temperature measured by the commercial thermocouple sufficiently convince the significance of surface temperature sensing over near-surface temperature sensing.

The average cell temperature in each flow region plotted against the flow rate, shown in Figure 6.10, shows that the cell temperature was also reproduced adequately when the flow rates were cycled. However, a slightly lower temperature was recorded at 500 ml/min flow rate in the first half of the experiment. This discrepancy can be understood concerning the fuel composition of the anodic gas. Prior to beginning the performance test, nitrogen was continued to supply to expel hydrogen from the anode chamber. As a result, the anode chamber should have been enriched with nitrogen by the commencement of the performance test. Accordingly, a diluted hydrogen mixture could be present at the beginning of the experiment. As fuel leakage from the test rig explained the flow-rate-temperature relationship, when a diluted mixture of hydrogen is leaked out

it produces less heat energy as nitrogen does not burn. Therefore, the resulting cell temperature could be lower at the beginning of the experiment. As the experiment progress, nitrogen may have gradually expelled increasing the composition of hydrogen in the anode chamber. Thus, leaking a mixture with a higher composition of hydrogen can release more heat by direct combustion and thus; the temperature could increase more prominently.

The average OCV produced at each flow rate was calculated and plotted against the flow rate as shown in Figure 6.11. The legend “Decrease” represents the OCV recorded when the flow rate decreased from 500 ml/min to 50 ml/min (during the first half of the experiment). The legend “Increase” represents the OCV recorded when the flow rate increased back to 500 ml/min from 50 ml/min passing through the same flow rates (second half of the experiment). The graph shows that the OCV increased with the increase of flow rate. However, at higher flow rates, the cell temperature was also high (as shown in Figure 6.10). Thus, theoretically, the OCV should be lower at higher temperatures. However, suppressing the effect of increasing temperature, the OCV has increased. Therefore, with the increase of flow rate, the partial pressure of hydrogen should have increased. This can happen in two ways. Although pure hydrogen was used for the experiment, the residual nitrogen within the anode chamber might have mixed with hydrogen making a fuel mixture. Thus, at higher flow rates of hydrogen, the partial pressure of hydrogen increases causing the OCV to increase due to Nernst effect. This

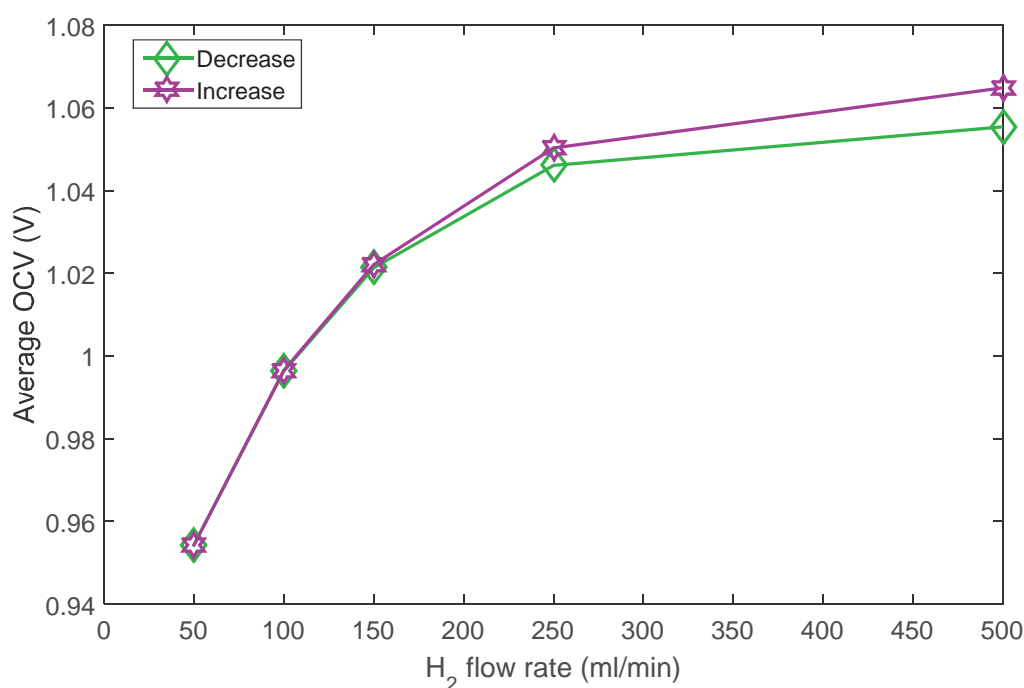


Figure 6.11 Variation of OCV with hydrogen flow rate

hypothesis of residual nitrogen in the anode chamber adequately explains the slightly lower OCV at the first half of the experiment as well. At the first half, hydrogen composition should be low because more nitrogen should be there in the anode chamber at the beginning of the experiment thus, causing a low partial pressure of hydrogen. Since nitrogen was not supplied, over the cause of time, the partial pressure of nitrogen decreases while that of hydrogen increases. Thus, the OCV produced in the second half of the experiment is higher due to the higher partial pressure of hydrogen. The second explanation for the growth of OCV with the increase of the hydrogen flow considers a blockage in the vent pipe system of the test rig causing a slow removal of gasses from the anode chamber. Because of the blockage, the pressure inside the anode chamber could build up with the increase in the flow rate. Thus, even without the presence of nitrogen, the partial pressure of hydrogen increases causing the OCV to increase. However, considering the low flow rates of hydrogen employed, the presence of residual nitrogen causing the OCV increase with the increased flow rate is a more plausible explanation than the second explanation.

The average OCV in each flow region was calculated and plotted against the mean cell temperature in the corresponding flow region as shown in Figure 6.12. The graph manifests a positive correlation between the cell temperature and the OCV. This behaviour is against the well-known understanding of OCV-temperature relationship

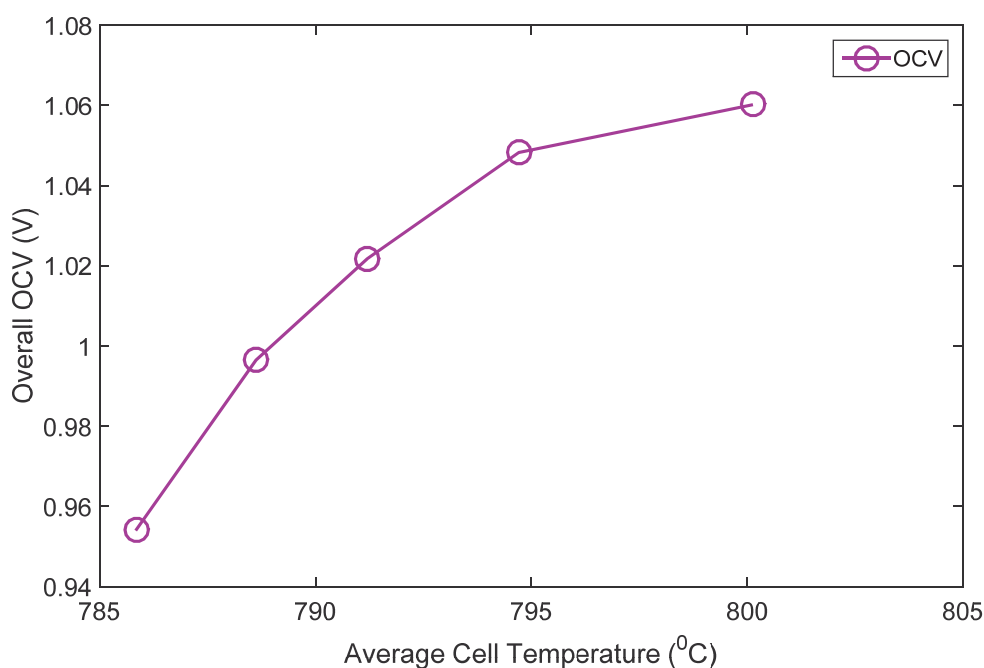


Figure 6.12 Change of OCV with cell temperature

explained by Nernst equation and Gibbs-Helmholtz equation (discussed in Chapter 2) where the OCV should decrease with the increase of temperature due to the decrease in the Gibbs free energy.

The proportionality of OCV to fuel flow rate was previously described as a Nernst effect. Proportionality of the cell temperature to flow rate was also explained as caused by leakages. Above mutually exclusive influences of the flow rate on the OCV and on the cell temperature may have appeared as a bogus positive correlation between the OCV and the cell temperature; this is why Figure 6.12 shows a result that is against the established science: increasing OCV with increasing temperature.

6.4 Temperature of a Non-Working: Case II – Grid with Thermocouples

The cell temperature measurements in the previous experiment were made only by the thermocouple grid. Therefore, although the accuracy level of multi-junction thermocouples had been established previously (Chapter 5), an in-situ validation was deemed to be more relevant because of potential batch-wise inconsistencies in fabrication. This section describes the experimental validation of the grid's measurements using three commercial thermocouples.

The same thermocouple grid used for the previous experiment was used for this validation test as well. The platinum mesh (cathode current collector) was firmly flattened and placed on the cathode. An edge of the mesh was wrapped around the current collector wire to ensure substantial electrical connectivity between the mesh and the wire. The grid was placed on the platinum mesh as shown in Figure 6.13 where *S1* to *S9* are the nine sensing points of the grid. Instead of putting a dead weight to keep the grid in touch with the cell, the grid's lead wires themselves and the current collector wire was used to fix the grid firmly in contact with the current collector and the cell. The cathode chamber air temperature sensing thermocouple was placed in adjacent to *S5* sensing point and approximately 2-3 mm above the cell. This thermocouple was deliberately placed more closely to the cell than in the previous experiment to investigate any improvements in its

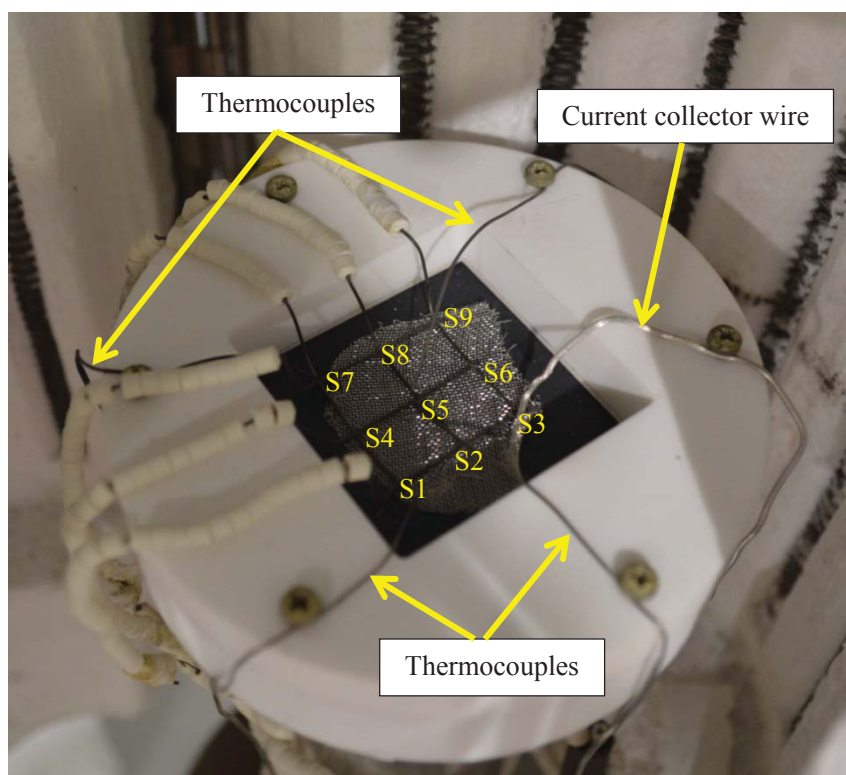


Figure 6.13 SOFC test cell with the thermocouple grid in place

ability to follow the cell temperature once it is placed closer to the cell. Three more commercial thermocouples were attached approximately 2-3 mm adjacent to *S1*, *S5*, and *S7* having their tips in touch with the cell. These three thermocouples were expected to establish the level of validity of the grid's measurements. Another thermocouple was inserted from the bottom of the anode chamber to measure the anodic gas exhaust temperature. Figure 6.14 shows the whereabouts of this thermocouple.

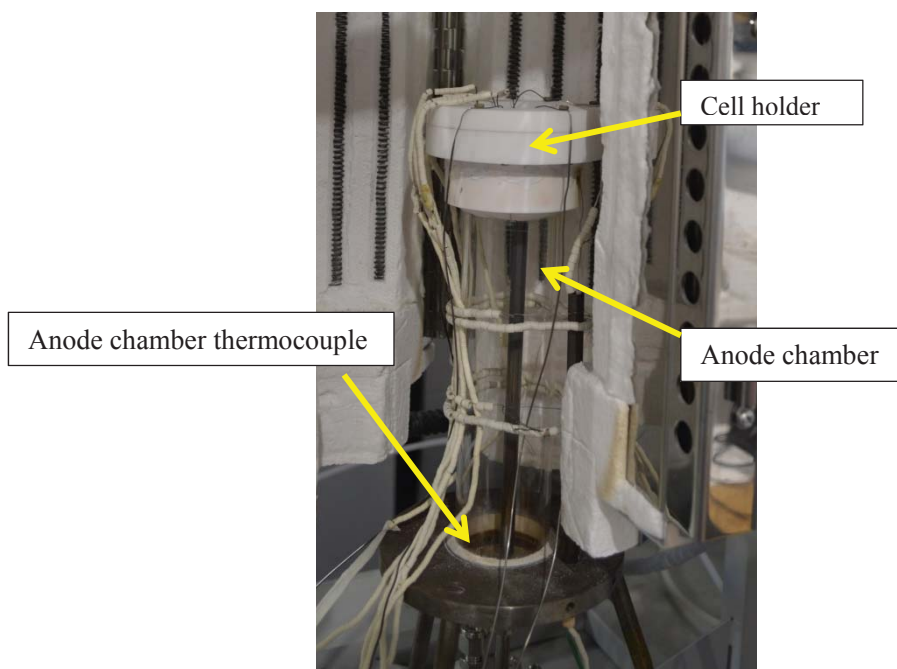


Figure 6.14 Location of the anode's thermocouple

The cell was first reduced in the presence of nitrogen and hydrogen with a volumetric composition of 300 ml/min and 15 ml/min, respectively. The furnace was heated at a rate of approximately 500 °C/hour up to 800 °C. While the furnace was at its early stage of heating, the anode chamber was fed with nitrogen to purge any residual air inside (the anode chamber fills with air when the piping is disconnected from it). Hydrogen was introduced as the furnace temperature reached approximately 650 °C. Temperatures from the grid, as well as that from thermocouples, were recorded at 1 Hz. The cell's OCV was also recorded as an indicator for the anode reduction. Once the cell continued to produce an OCV close to 1 V, the hydrogen supply was disconnected to end the reduction process. The reduction process took place approximately 25 min at a temperature above 750 °C. Nitrogen was continued to provide for further 5 min to remove hydrogen for the same purpose as before.

The hydrogen supply was restarted with variable volumetric flow rates given in Table 6.2 to commence the cell operation. The experiment was run at each flow rate for approximately 8 minutes except for the first flow rate, which was maintained for approximately 15 minutes because of the long settling time. Flow rates were cycled to investigate the repeatability of measurements. The hydrogen supply was cut off once a complete cycle was performed. The OCV and temperatures from the grid as well as from thermocouples were recorded at 1 Hz.

Table 6.2 Hydrogen flow rates

Region	H ₂ flow rate (cm ³ /min)
A	25
B	50
C	100
D	150
E	200
F	250
G	200
H	150
I	100
J	50
K	25
L	0

6.4.1 Results and Discussion

Temperatures of the cell during the anode reduction process are shown in Figure 6.15. The legends *S1* to *S9* represent the temperatures from the grid; *TC-S1*, *TC-S5*, and *TC-S7* represent the temperatures from the commercial thermocouples kept in touch with the cathode in adjacency to *S1*, *S5*, and *S7*, respectively. *TC-Cathode* is the temperature measured by the commercial thermocouple in the cathode chamber. Temperatures at the 80th, 90th and the 100th minutes are given in Table 6.3. The maximum temperature gradients across the cell, measured by the grid, at above three time intervals are 5 °C, 5.9 °C, and 4.9 °C, respectively. Further, the differences between the average cell temperature and the cathode chamber temperature at the 80th, 90th and the 100th minute are 6.2 °C, 3.0 °C and, 4.8 °C, respectively. This is a relatively small difference compared to the temperature difference observed previously during the anode reduction process (see Figure 6.8). Placing the cathode chamber's thermocouple more closely (approx. 2 mm) to the cathode than in the previous placement (approx. 7 mm) could have enabled the thermocouple to follow the cell's temperature more closely. Thus, the difference may have been reduced.

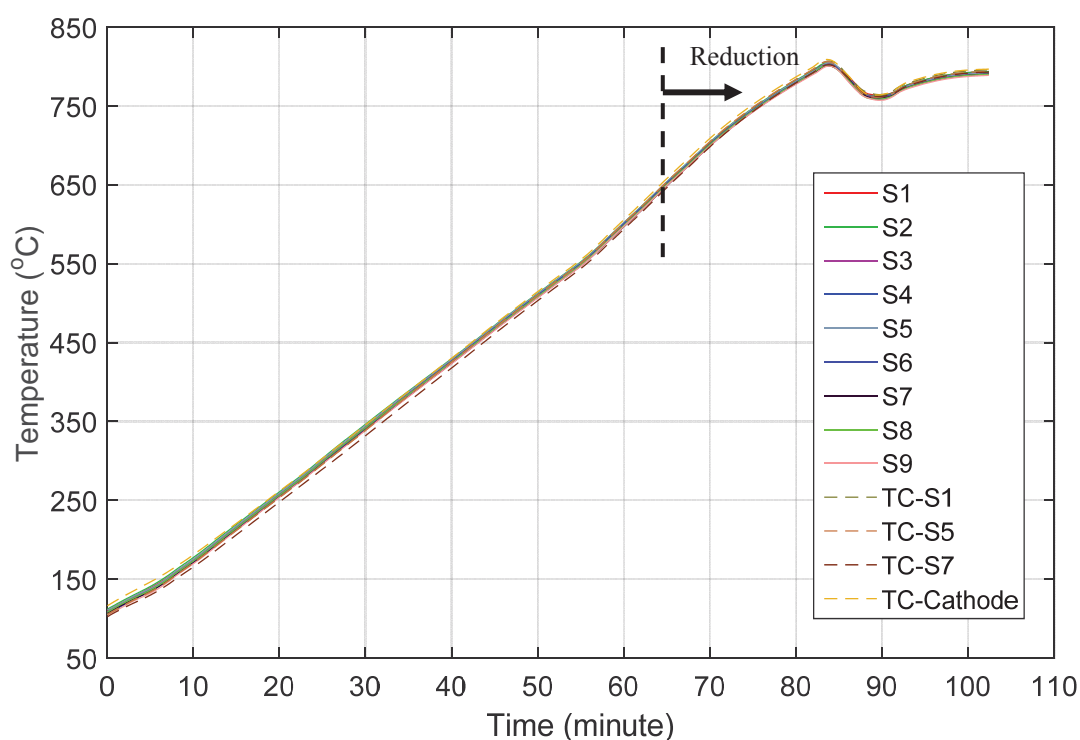


Figure 6.15 Temperature during the anode reduction
(S1 to S9: temperatures from the grid, TC-S1, TC-S5, TC-S7: thermocouples near S1, S5, and S5, respectively. TC-Cathode: Cathode thermocouple)

Table 6.3 Temperatures at 80th, 90th, and 100th minutes

Sensing point	Temperature (°C)		
	at 80 th minute	at 90 th minute	at 100 th minute
S1	781.4	760.8	792.3
S2	782.5	759.9	792.4
S3	780.8	759.0	790.9
S4	780.6	758.1	790.5
S5	781.5	756.8	790.5
S6	779.8	756.0	789.1
S7	778.3	757.1	788.9
S8	779.1	755.8	788.8
S9	777.5	755.0	787.4
TC-S1	783.4	762.2	794.4
TC-S5	783.8	758.5	792.6
TC-S7	779.3	759.4	791.6
TC-Cathode	786.8	761.3	795.6

A rapid growth of OCV was observed with the introduction of hydrogen around 650 °C while, the average OCV produced during the anode reduction process was 0.98 V. This is a good indication that the anode had been reduced by this time. In fact, the cell had previously been used for testing thus; it should have remained reduced despite being cooled down to room temperature. The temperature drop seen in Figure 6.15 between 80th and 90th minutes was a deliberate change imposed to briefly visualise the temperature effect on the OCV. However, this was not a comprehensive investigation. An extensive study on the OCV-temperature relationship is presented and discussed later in this chapter.

The method of using OCV as an indication of the level anode reduction was sufficient for this experiment as the cell performance was not investigated in this study. However, when the cell performance is assessed, the OCV should not be taken as an indication to the level of anode reduction because a cell can produce OCV even if only the anode is partly reduced.

Figure 6.16 shows how the OCV and the cell temperature varied with varying volumetric flow rates of hydrogen. Average temperatures measured by the nine sensing points of the grid at each flow rate are given in Figure 6.17. The locations of the sensing points indicated in this sketch are similar to the actual locations as depicted in Figure 6.13. Analogous to the previous experiment, an increase of the cell temperature and the OCV could be observed when the flow rate was increased. However, the changes were subtle compared with the previous experiment where high volumetric flow rates of hydrogen were involved. Since the leakages in the test rig were not eliminated in this experiment, the OCV-temperature relationship can be explained as before considering gas leakages. The less prominent temperature changes with the flow rate in this study could be due to low fuel leakages at the low flow rates used in this experiment. The previous explanation on the growth of OCV with the increase of flow rate is applicable for these results as well.

Temperature measurements from the cathode chamber thermocouple (*TC-Cathode*) show that reducing the gap between the cell and the thermocouple has enabled it to follow the cell temperature more closely.

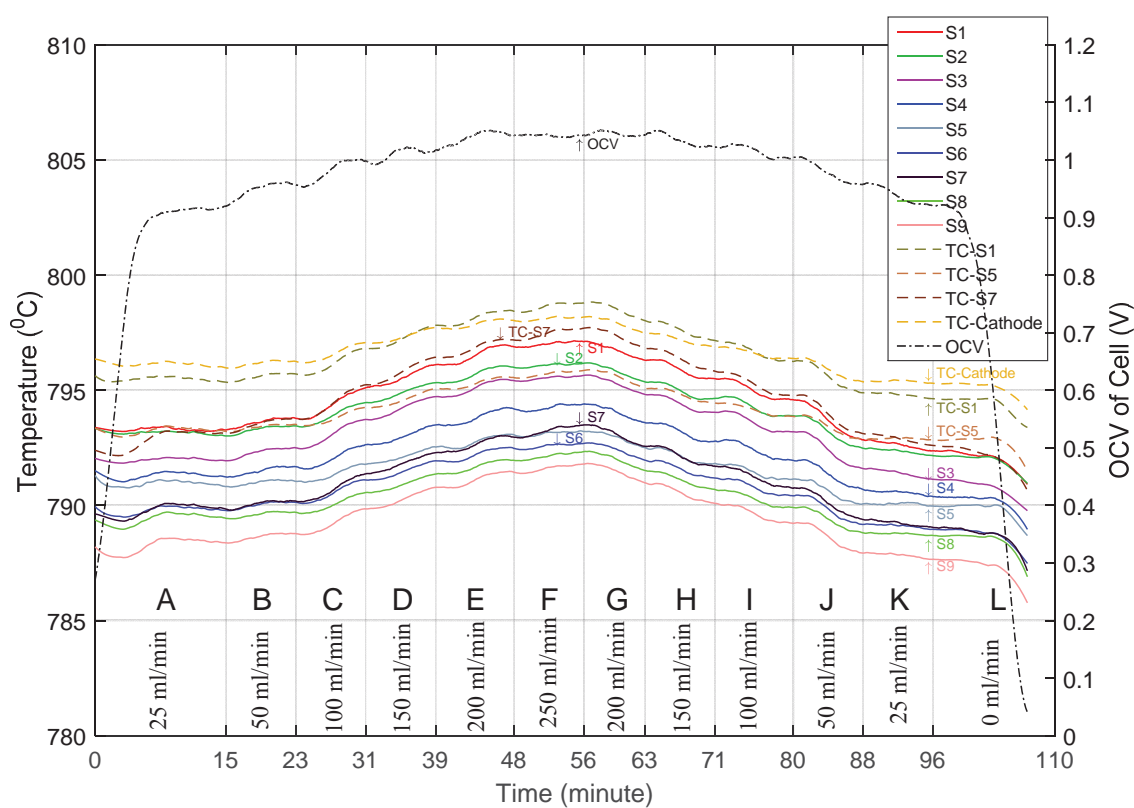


Figure 6.16 OCV and temperature response during cell operation

<p>S7</p> <p>$T_{25} = 789.6\text{ }^{\circ}\text{C}$ $T_{50} = 790.0\text{ }^{\circ}\text{C}$ $T_{100} = 791.2\text{ }^{\circ}\text{C}$ $T_{150} = 792.0\text{ }^{\circ}\text{C}$ $T_{200} = 793.1\text{ }^{\circ}\text{C}$ $T_{250} = 793.1\text{ }^{\circ}\text{C}$</p>	<p>S8</p> <p>$T_{25} = 789.2\text{ }^{\circ}\text{C}$ $T_{50} = 789.4\text{ }^{\circ}\text{C}$ $T_{100} = 790.3\text{ }^{\circ}\text{C}$ $T_{150} = 791.0\text{ }^{\circ}\text{C}$ $T_{200} = 792.0\text{ }^{\circ}\text{C}$ $T_{250} = 792.1\text{ }^{\circ}\text{C}$</p>	<p>S9</p> <p>$T_{25} = 788.1\text{ }^{\circ}\text{C}$ $T_{50} = 788.5\text{ }^{\circ}\text{C}$ $T_{100} = 789.6\text{ }^{\circ}\text{C}$ $T_{150} = 790.4\text{ }^{\circ}\text{C}$ $T_{200} = 791.5\text{ }^{\circ}\text{C}$ $T_{250} = 791.5\text{ }^{\circ}\text{C}$</p>
<p>S4</p> <p>$T_{25} = 791.0\text{ }^{\circ}\text{C}$ $T_{50} = 791.3\text{ }^{\circ}\text{C}$ $T_{100} = 792.4\text{ }^{\circ}\text{C}$ $T_{150} = 793.1\text{ }^{\circ}\text{C}$ $T_{200} = 794.1\text{ }^{\circ}\text{C}$ $T_{250} = 794.2\text{ }^{\circ}\text{C}$</p>	<p>S5</p> <p>$T_{25} = 790.6\text{ }^{\circ}\text{C}$ $T_{50} = 790.7\text{ }^{\circ}\text{C}$ $T_{100} = 792.4\text{ }^{\circ}\text{C}$ $T_{150} = 793.1\text{ }^{\circ}\text{C}$ $T_{200} = 794.1\text{ }^{\circ}\text{C}$ $T_{250} = 794.2\text{ }^{\circ}\text{C}$</p>	<p>S6</p> <p>$T_{25} = 789.5\text{ }^{\circ}\text{C}$ $T_{50} = 789.8\text{ }^{\circ}\text{C}$ $T_{100} = 790.8\text{ }^{\circ}\text{C}$ $T_{150} = 791.5\text{ }^{\circ}\text{C}$ $T_{200} = 792.5\text{ }^{\circ}\text{C}$ $T_{250} = 792.5\text{ }^{\circ}\text{C}$</p>
<p>S1</p> <p>$T_{25} = 793.0\text{ }^{\circ}\text{C}$ $T_{50} = 793.5\text{ }^{\circ}\text{C}$ $T_{100} = 795.0\text{ }^{\circ}\text{C}$ $T_{150} = 795.7\text{ }^{\circ}\text{C}$ $T_{200} = 796.8\text{ }^{\circ}\text{C}$ $T_{250} = 797.0\text{ }^{\circ}\text{C}$</p>	<p>S2</p> <p>$T_{25} = 792.8\text{ }^{\circ}\text{C}$ $T_{50} = 793.1\text{ }^{\circ}\text{C}$ $T_{100} = 793.4\text{ }^{\circ}\text{C}$ $T_{150} = 795.0\text{ }^{\circ}\text{C}$ $T_{200} = 796.0\text{ }^{\circ}\text{C}$ $T_{250} = 796.1\text{ }^{\circ}\text{C}$</p>	<p>S3</p> <p>$T_{25} = 791.8\text{ }^{\circ}\text{C}$ $T_{50} = 792.2\text{ }^{\circ}\text{C}$ $T_{100} = 793.6\text{ }^{\circ}\text{C}$ $T_{150} = 794.3\text{ }^{\circ}\text{C}$ $T_{200} = 795.4\text{ }^{\circ}\text{C}$ $T_{250} = 795.5\text{ }^{\circ}\text{C}$</p>

Figure 6.17 Average cell temperature sketch at each flow rate
 $(T_x = \text{average temperature at } x \text{ ml /min flow rate})$

The anode chamber's exhaust temperature variation with time is shown in Figure 6.18. The continuous increase of the anode chamber temperature shows that it has not reached steady state condition. The low anode gas temperature, as discussed previously, may have contributed to the overall cell temperature to remain lower than the furnace temperature. However, it has not contributed to any noticeable level to the dramatic temperature changes took place on the cell. Thus, the effect of cold anodic gasses is more likely to move down the average cell temperature.

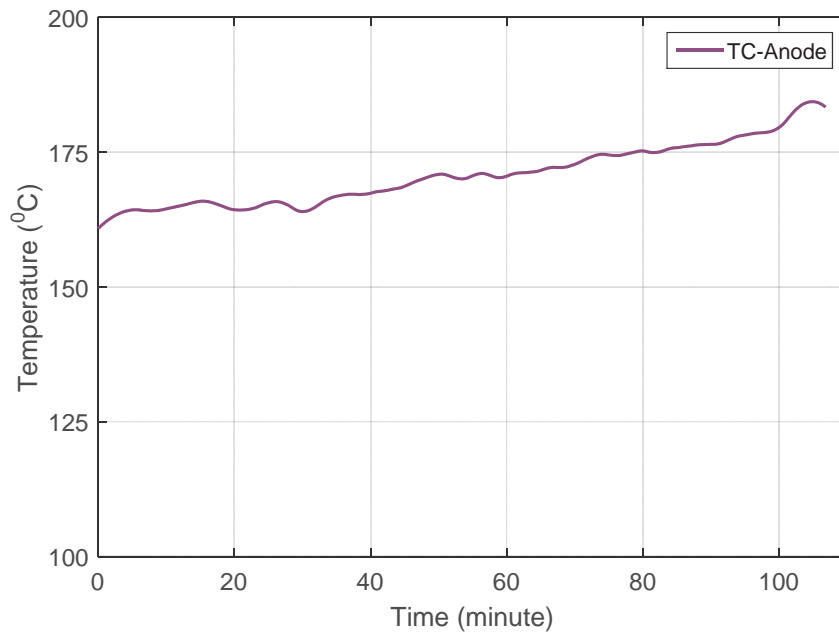


Figure 6.18 Anode chamber exhaust gas temperature

6.4.1.1 The Grid Validation on a Non-Working Cell

The temperatures measured by *SI*, *S5*, *S7* and their corresponding adjacent thermocouples (*TC-SI*, *TC-S5*, and *TC-S7*) are given in Figure 6.19 (a), (b), and (c), respectively. These graphs show that the grid's temperature and corresponding thermocouple's temperature maintained almost identical profiles with only slight differences in magnitudes. The temperature difference between each of the three sensing points and their corresponding thermocouples is given in Figure 6.19(d). This shows that the maximum difference is less than 4.5 °C. These differences in measurement may partly be ascribed to inaccuracies associated with in-house fabricated multi-junction thermocouples as discussed in Chapter 5. On the other hand, the grid's sensing points might not have maintained a good thermal contact with the cell as their corresponding thermocouples did maintain. Since the commercial thermocouples were much thinner than the thermoelements of the grid, the flexibility of the thermocouples enabled them to maintain a very good contact with the cell. Although heat transfer along thermoelements could result in measurement errors in multi-junction thermocouples, as discussed in Chapter 5, the comparison made with the commercial thermocouples does not show the presence of such errors in this setup. However, a different test setup may generate such errors. Thus, an in-depth investigation on the heat transfer characteristics of multi-junction thermocouples may need to be carried out and, an advanced data logging system may need to be developed to eliminate the errors due to heat transfer as discussed in Chapter 8 under further research.

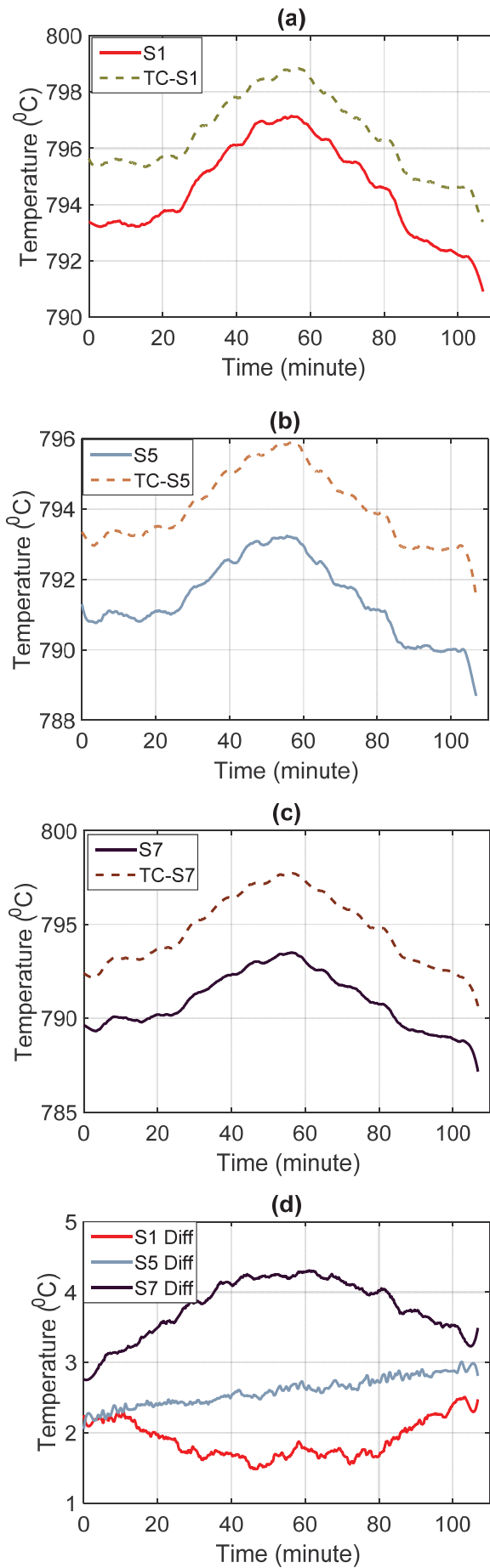


Figure 6.19 Temperature from the grid and adjacent thermocouples
 (a) S1 and TC-S1 (b) S5 and TC-S5 (c) S7 and TC-S7 (d) difference between grid points and their corresponding thermocouples

Placing the grid on the current collector leading to potential short-circuiting of thermoelements was an overwhelming scientific criticism raised against the arrangement. This argument has already been invalidated with the experimental validation discussed above as the grid could accurately follow the temperature profile recorded by commercial thermocouples. However, following discussion explains how the problem of short-circuiting could affect temperature measurements and how to overcome it.

A junction's temperature of a thermocouple is a measure of the thermoelectric voltage induced across the entire length of each thermoelements. Short-circuiting the two thermoelements is electrically equivalent to two thermocouples connected in parallel. Thus, the measured temperature is an average temperature of the two junctions. When these multiple junctions remain at almost the same temperature, the measurement inaccuracy becomes negligibly small. Apart from this general explanation, the particular arrangement of the grid on the cell in preceding experiments had little chance for short-circuiting. When the thermocouple grid was fabricated by spot-welding, one thermoelement always remained above the others; the image of the grid shown in Figure 6.4 elaborates this. Thus, when the grid was placed on the well-flattened current collector, only one set of thermoelements were actually in touch with the current collector. The other thermoelement might come into contact with the grid, only at locations where the current collector had lost its flatness and formed an uneven surface, i.e. warps. However, the formation of such sharp warps at many places was less probable as the grid firmly pressed the mesh against the cell. Thus, the number of short-circuiting paths, if there any, is not significant. The grid being able to measure temperature independently in previously described experiments justifies the argument on non-short-circuiting. Therefore, the criticism on short-circuiting does not hold a significant value, though it may be a potential risk on certain cells and stack. In circumstances where, short-circuiting is a genuine problem, that may be overcome by coating thermoelement with a dielectric material such as alumina.

6.5 Temperature Measurements from a Working Cell

The preceding sections presented and discussed the temperature distribution over a cell during anode reduction and while the cell was in open circuit. In this section, the performance of an operating SOFC measured along with the cell temperature distribution under different operating conditions is presented and discussed. Further, validation of the temperature measurements by the grid with calibrated commercial thermocouples is discussed.

A thermocouple grid having nine sensing points was fabricated by spot-welding of Ø0.5 mm alumel and chromel wires. The grid was fixed onto the cathode of *NextCell-5* cell. A platinum mesh and a nickel mesh were connected to the cathode and the anode, respectively to collect current from the two electrodes. Silver paste was used as the bonding agent to attach the meshes. Curing silver at 100 °C for 2 hours solidified the paste attaching the two meshes onto their respective electrodes. Once silver was solidified, the cell was firmly fixed to the test rig. Two gaskets (Thermiculite 866) were used at either side of the electrolyte surface to prevent gas leakages through the cell-seating on the test rig. A 0.2 mm thick gasket was used at the anode side, and 0.5 mm thick one was used at the cathode side (the difference in thickness is to fit it better into the shape of the cell holder). Therefore, the exposed section of the electrolyte, which is used to support the cell, was sandwiched between two gaskets. A variable resistor (maximum resistance 10 kΩ) was connected to the cell as the load.

The grid was firmly placed onto the cathode. Three K-type thermocouples, calibrated in line with UKAS¹¹ calibration standards, were also attached to the test rig having their tips touching the cathode to validate the temperature measurements from the grid. The approximate positioning of the nine sensing points of the grid and three thermocouples are as depicted in Figure 6.20 where *S1* to *S9* are the nine sensing points of the grid. The positioning of the three thermocouples, with respect to the grid, is as depicted in Figure 6.21, where *TC-S1*, *TC-S5*, and *TC-S9* are the three thermocouples placed adjacent to *S1*, *S5*, and *S9* sensing points of the grid, respectively.

Cell was heated from room temperature to 800 °C at a rate of 5 °C/ min. Nitrogen was continuously supplied to the anode chamber at a rate of 300 ml/min throughout the heating process to expel air inside the anode chamber. Once the furnace reached 800 °C, a

¹¹ United Kingdom Accreditation Service

mixture of hydrogen and nitrogen with a volumetric composition of 60 ml/min H_2 and 240 ml/min N_2 was supplied over 3 hours for the anode reduction to take place.

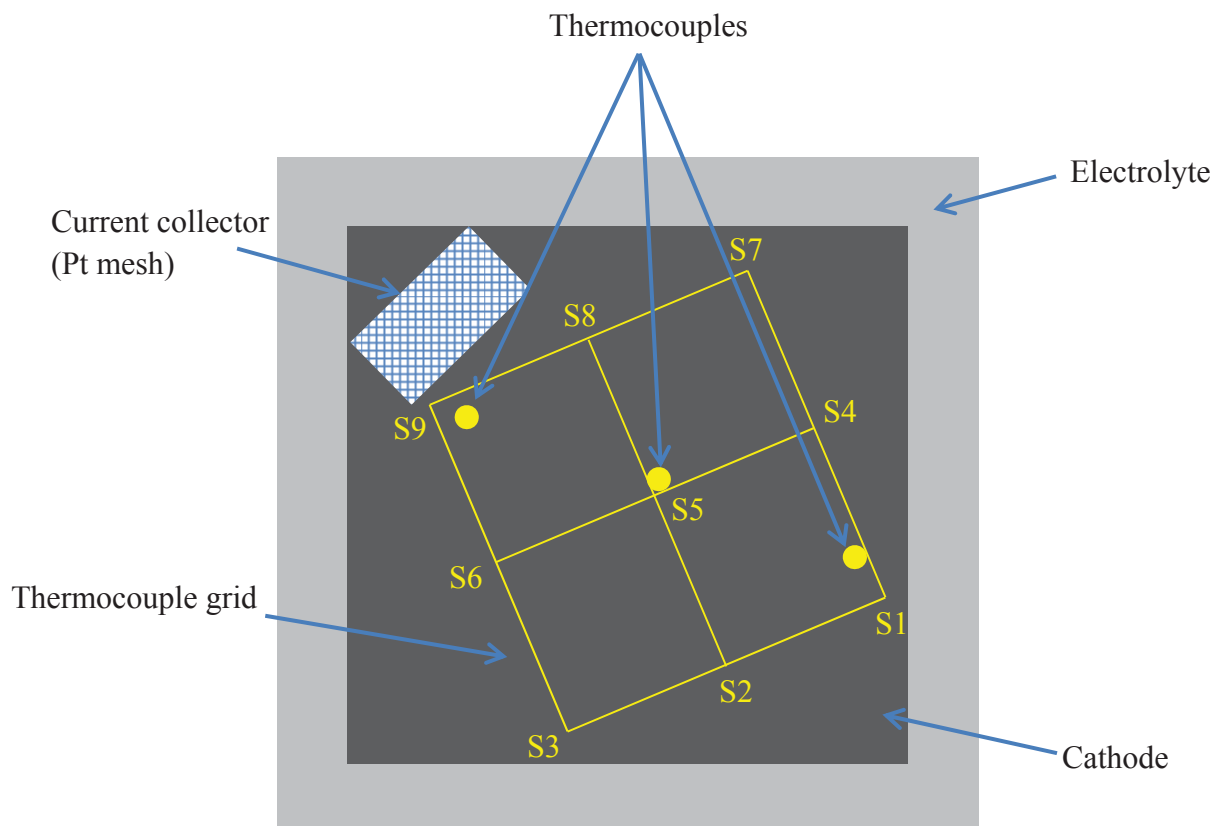


Figure 6.20 A schematic diagram of the location of the grid, thermocouples, and the current collector on the 4 cm \times 4 cm cathode

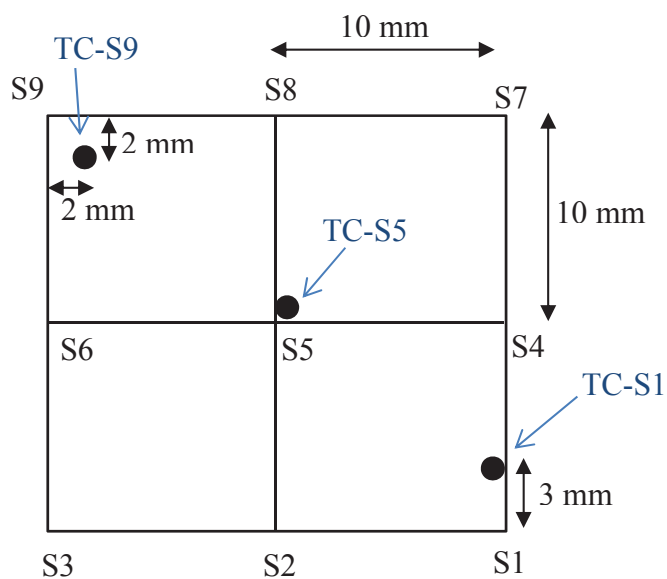


Figure 6.21 Dimensions of the grid and the positioning of thermocouples

After the anode reduction process, the cell was operated at 700 °C, 750 °C, 800 °C, and 850 °C with a mixture of hydrogen and nitrogen of volumetric composition 250 ml/min H₂ and 50 ml/min N₂. At each operation, different currents were drawn from the cell by changing the variable resistor to investigate the temperature response to changing loads. OCVs at each operating temperature were also recorded to study the OCV-temperature relationship.

While the cell was operating at 850 °C and 70.8 mA current, the volumetric composition of fuel mixture was altered to investigate the cell's temperature response to fuel composition and flow rates. For the first 10 minutes, a fuel composition of 275 ml/min H₂ and 25 ml/min N₂ was supplied while rest of the parameters were kept unchanged. In the second 10 minutes, the fuel composition was changed to 295 ml/min H₂ and 20 ml/min N₂.

Data were recorded at 1 Hz using the data logging system described in Appendix IV. When the cell testing was not performed, the cell was set to remain at 700 °C while nitrogen being fed into the anode chamber at 300 ml/min to prevent any chance of anode re-oxidation.

6.5.1 Results and Discussion

The anode reduction temperature was chosen as 800 °C differently to previous experiments, in which the reduction was allowed from around 650 °C. High-temperature anode reduction has been selected because it delivers better performance over low-temperature reduction for hydrogen^[3]. Reducing the anode at high temperature produces nickel particles that are well connected to each other. Since nickel is an excellent electrical conductor, well-connected nickel particles make a good passage for electrons to reach the current collector reducing the ohmic polarization on the anode.

Since the cell temperature was lower than the furnace temperature at all times, the term “nominal operating temperature” is used in the following discussion to represent the temperatures at which the cell was expected to operate at (700 °C, 750 °C, 800 °C, and 850 °C).

The average cell temperature (measured by the grid and thermocouples) over the course of operation at each nominal operating temperature was less than the furnace’s operating temperature by approximately 20 – 24 °C. Meanwhile, the average anode exhaust gas temperature was approximately 440 °C lower than the furnace temperature at each nominal operating temperature. Therefore, the temperature difference between the cell and the furnace can be ascribed to overall cell cooling due to heat transfer to cold gasses from the cell. However, the temperature difference between the cell and the furnace’s set temperature was generally smaller than the above-recorded difference in the open-circuit experiments presented in Sections 6.3 and 6.4. This higher difference is possibly due to no (or low) gas leakage obtained in the current experimental settings by using gaskets. When the fuel leaked out in the previous experiment, the heat liberated by direct combustion of hydrogen and oxygen contributed to raising the overall cell temperature. Thus, the cooling effect is suppressed to some extent. Therefore, the temperature gap between the cell and the furnace’s set temperature might have been decreased. With the absence of leakages, the cell cooling is more pronounced; consequently, the difference between cell temperature and the furnace temperature increases.

6.5.1.1 Voltage and Cell Temperature Relationship

The average OCV produced at each nominal operating temperature was calculated by taking approximately 150 OCV values per each temperature; the results are listed in Table 6.4. The average cell temperature (computed from the measurements of the

thermocouple grid and the three commercial thermocouples) at each nominal operating temperature is also listed in the same table. A decrease in the OCV can be observed with the increase of temperature. Although this decline is subtle, this is well-aligned with the theoretical explanation of OCV- temperature relationship where OCV decreases with the increase of temperature due to the decrease in the Gibbs free energy.

Table 6.4 Change of OCV with temperature

Furnace Temperature (°C)	700	750	800	850
OCV (V)	1.1256	1.1055	1.0963	1.0853
Average cell temperature (°C)	680.67	729.20	779.27	827.61

Table 6.5 shows the cell temperature recorded for approximately 60 mA current over the four nominal operating temperatures. To minimize the effects of any measurement inaccuracies, the values were averaged for over 100 measurements at each nominal operating temperature. The data shows a marginal increase of the cell voltage with the increase of the operating temperature. Although the OCV decreases with the increase of operating temperature, the operating cell voltage has increased with the increase of temperature. This increase of cell voltage is due to the decrease of resistance in the electrolyte to ionic conduction at higher temperatures. When the resistance decreases, the ohmic polarisation decreases enabling a cell to provide a higher voltage for a given current density (thus, higher power output).

The magnitude of temperature increase between each operating temperatures is relatively a constant (approximately 50 °C). However, the voltage increase resulted from the increase of operating temperature does not show any linearity with the temperature. This is because; the change of resistance (decrease of electrolyte's resistance and the increase of rest of the conductors' resistance) with temperature is not a linear function. Thus, voltage change also does not show linearity with the temperature

Table 6.5 Change of cell voltage different temperature under 60 mA current

Furnace Temperature (°C)	700	750	800	850
Cell voltage (I = 60 mA)	0.426	0.455	0.463	0.494

6.5.1.2 Load-Temperature Relationship

The polarisation curve and the temperature at each current at the 850 °C nominal operating temperature are shown in Figure 6.22. The polarisation curve does not show any activation polarisation. However, very clear ohmic polarisation can be observed. It is accepted that the activation polarisation of SOFC is not very prominent because the high operating temperature makes the reaction species to remain sufficiently energised to overcome the activation barrier. A slight increase of the steepness of the polarisation curve can be identified from approximately 72 mA. This is an indication of concentration polarisation becomes active due to high current drawn from the cell. The cell temperature, measured by the grid as well as by the three commercial thermocouples, increased with the increase of current. When current is drawn from a cell, the cell becomes electrochemically active producing heat. As the current increases, the level of electrochemical activity of the cell increases to provide a higher flow of electrons. Thus, at higher currents, more heat is liberated causing the cell temperature to increase. Table 6.6 lists the cell temperature when the cell was delivering no current (open-circuit) and when it was producing approximately 71 mA current. The mean of cell temperature

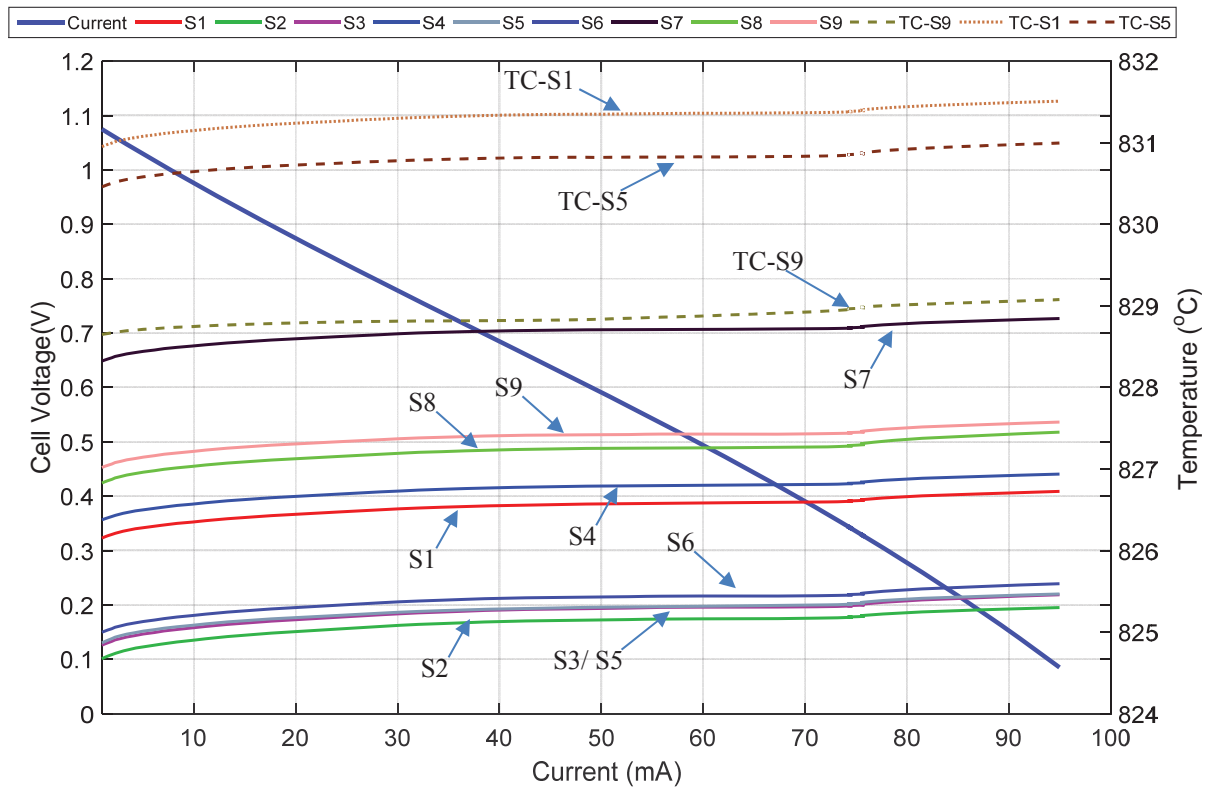


Figure 6.22 Polarisation curve at 850 °C operations along with cell temperature (S1-S9: nine sensing points of the grid, TC-S1, TC-S5, TC-S9 are the thermocouples near S1, S5, and S9, respectively)

increase between the two currents is 0.53 °C. The low increase of temperature is due to the low increase of electrochemical activity of the cell. Although the cell current was increased, the magnitude of the increase was less than 100 mA. This current increase should only have marginally increased the electrochemical activity of the cell causing only a little extra heat to release. Thus, the magnitude of the temperature increase is small. Despite the magnitude, cell temperature measurements clearly show an increase of the cell temperature with increase of the load (current). Thus, cell temperature changes due to load changes are clearly demonstrated. When a cell produces larger current density, the resulting temperature increase should also be large causing relatively large temperature gradients to present across a cell. (The reason for low current density is discussed later).

Table 6.6 Cell temperature at open circuit and 71 mA current

Sensing point	Temperature (°C)		
	I = 0 mA	I = 71 mA	Increase
S1	826.06	826.60	0.54
S2	824.60	825.18	0.58
S3	824.74	825.32	0.58
S4	826.30	826.82	0.52
S5	824.71	825.34	0.63
S6	824.91	825.46	0.55
S7	828.25	828.73	0.48
S8	826.69	827.28	0.59
S9	826.93	827.44	0.51
TC-S1	830.87	831.38	0.51
TC-S5	830.36	830.85	0.49
TC-S9	828.59	828.94	0.35

In a similar manner to detecting the increase of cell temperature with the increase of current, formation of hot-spots could also be identified by observing the temperature distribution. A hot-spot is, generally, an electrochemically highly active region where high level of heat is generated. Thus, the temperature in these regions abruptly increases. Detecting such abruptly high-temperature zones is a way to detect hot-spots. However, with the absence of such abrupt temperature changes in above results, it can be suggested

that there were no hot-spots formed during the operation, at least, in the vicinity of sensing points.

The cell temperature shows a relatively steep increase as the cell entered into concentration polarisation region (beyond approx. 72 mA). Concentration polarisation is an irreversibility, which causes entropy generation. With the increase of entropy, the portion of enthalpy being converted to heat increases where part of this heat contributes to increase the cell temperature. Thus, relatively steep increase of cell temperature can be expected under concentration polarisation in parallel with the steep decrease of cell voltage. Since concentration polarisation occurs due to reactant starvation (fuel / oxidant), cell temperature measurements may be used to identify the regions in a stack which don't get sufficient gas supply.

Figure 6.22 further shows another steep temperature increase at the beginning of the cell operation. However, the steepness of the increase gradually flattens as the current increases. An increase of the cell temperature with the start of cell operation can be expected because of the start of an imbalanced electrochemical activity. However, the vague fact is the sharp increase in temperature and then gradual flattening of the growth. This could be explained concerning entropy generation in activation polarisation, if there was any activation polarisation. However, the cell does not show any sign of activation polarisation from its polarisation curve. Therefore, this sharp increase and then gradual flattening of temperature could, perhaps, be due to the changes in heat loss from the cell. As the cell temperature increases, the rate of heat loss from the cell also increases. Thus, the increase of cell temperature could be suppressed with time making it be less steep with time (current was increased with time).

Figure 6.23 shows the average cell temperature change with respect to cell current change at 850 °C nominal operating temperature. Although cell temperature increased with the increase of current, the temperature response to current increase lags behind the current change. This delay could be due to delays in heat transfer. The electrochemical reactions generate heat at triple phase boundaries, which are more close to the electrolyte than to the electrode surface. However, temperature measurements are done on the cathode surface. Thus, for the temperature to be detected by the grid/ thermocouples, the generated heat must transfer to the cathode surface. The delayed response of temperature to current may be due to the time taken for heat transfer to take place. However, above two explanations (flattening of temperature change with time and delayed response of

temperature to current) can only be confirmed after an in-depth heat transfer analysis of the phenomena.

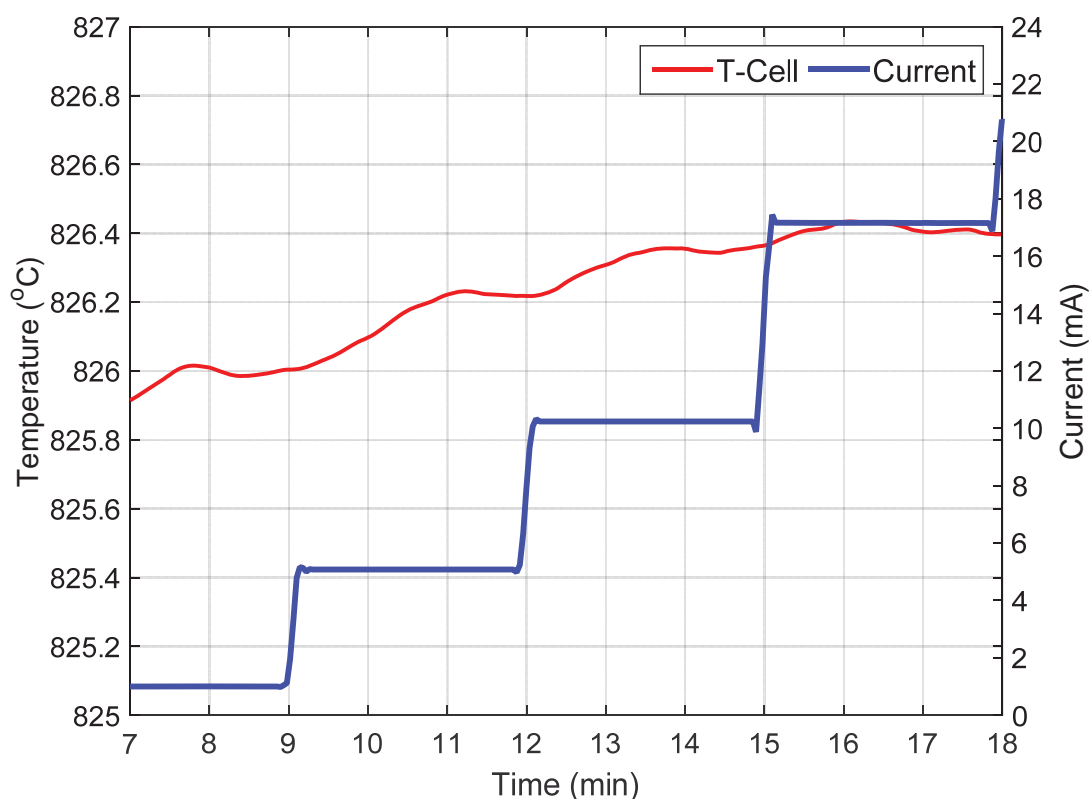


Figure 6.23 Change of average cell temperature with current (Cell operation at 850 °C)

Temperature measurements from the grid revealed the presence of approximately 3.5 °C gradient between *S7* and *SI*, which are approximately 2 cm apart from each other. This temperature gradient could either be due to a temperature gradient present within the furnace or due to a difference in the electrochemical activity of the cell at those regions. However, since local current densities were not measured, any relationship between the temperature gradient and the electrochemical activity of the cell cannot be established with these results.

The polarisation curves and the corresponding temperature distribution at 700 °C, 750 °C, and 800 °C are shown in Figure 6.24, Figure 6.25, and Figure 6.26, respectively. Due to malfunction of the variable resistor whose resistance refused to reach sufficiently higher values to get low current outputs, obtaining low current outputs were restricted in these operations. The average cell temperature increase from 35 mA to 75 mA under all three operating temperature is 0.1 °C (to one significant figure). This temperature increase is due to the increased electrochemical activity of the cell and the reason for very small

temperature increase is the low electrochemical activity of the cell, as described previously.

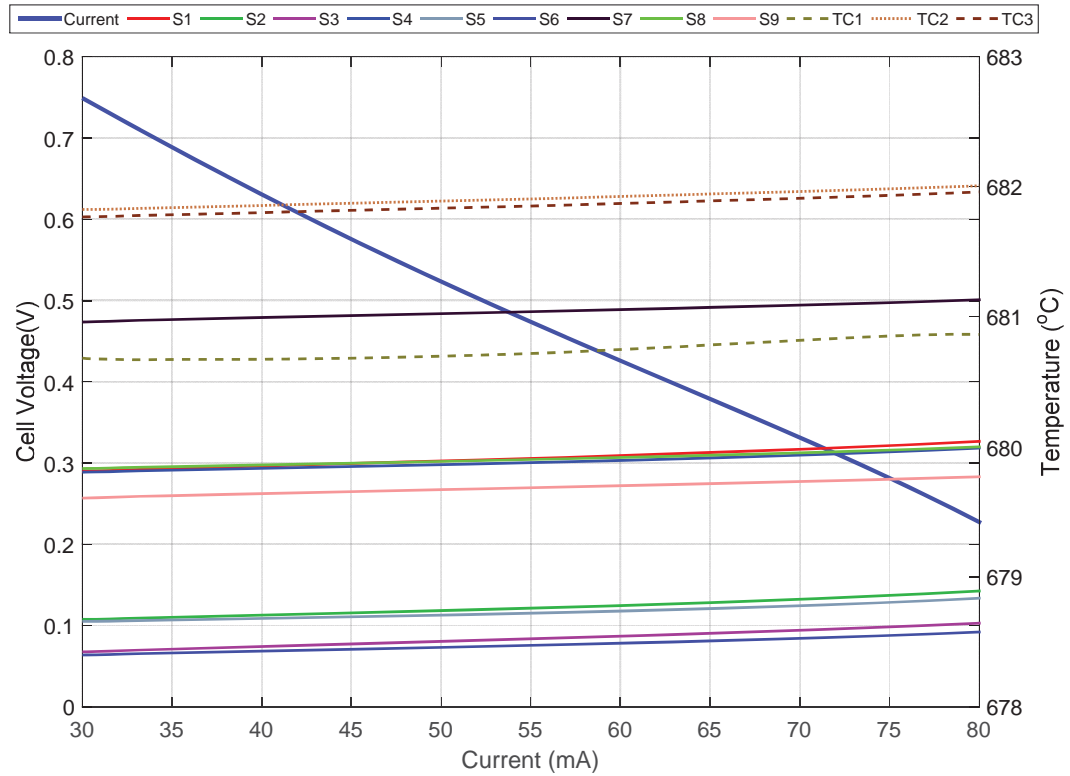


Figure 6.24 Polarisation curve at 700 °C operations along with cell temperature (S1-S9: nine sensing points of the grid, TC-S1, TC-S5, TC-S9 are the thermocouples near S1, S5, and S9, respectively)

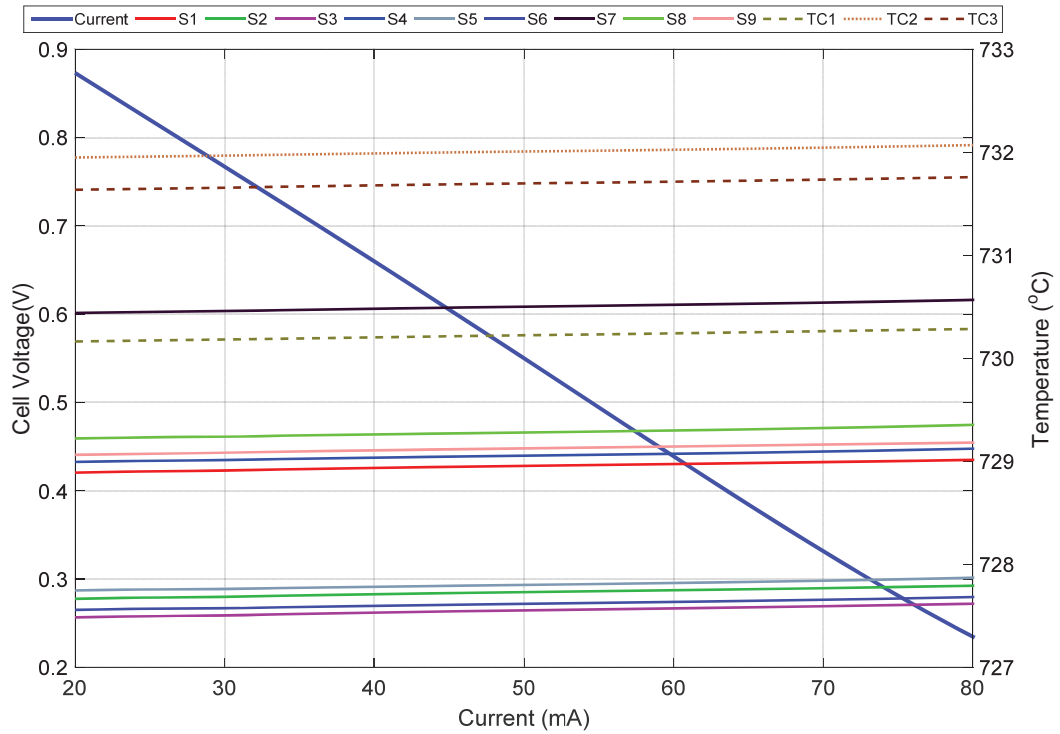


Figure 6.25 Polarisation curve at 750 °C operations along with cell temperature (S1-S9: nine sensing points of the grid, TC-S1, TC-S5, TC-S9 are the thermocouples near S1, S5, and S9, respectively)

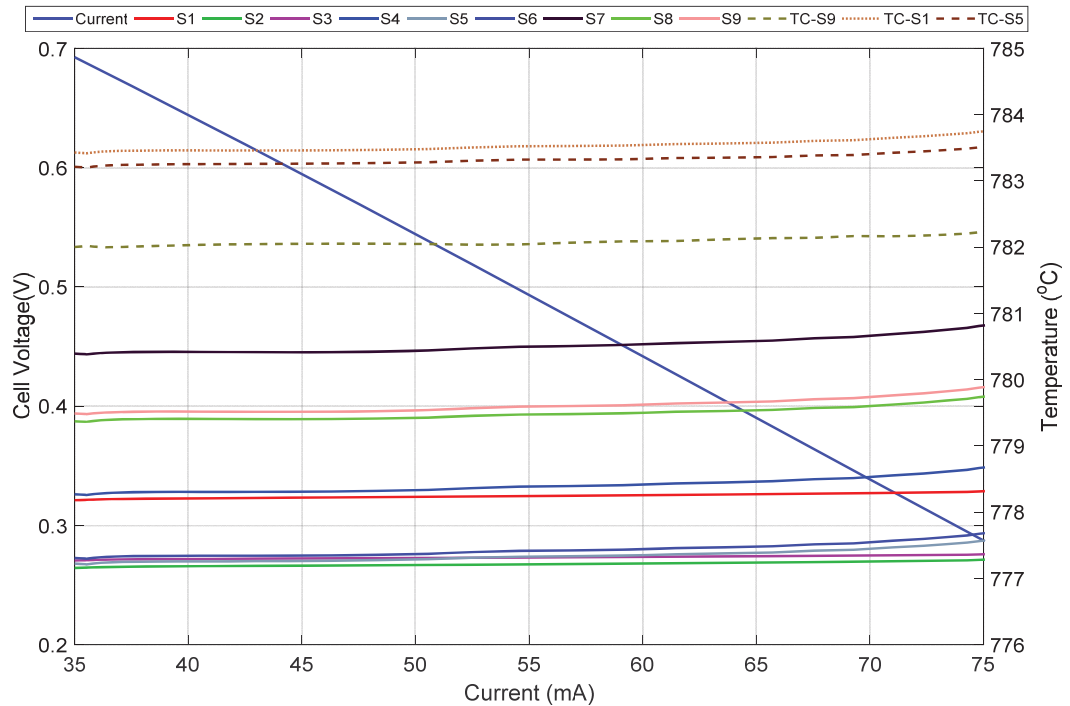


Figure 6.26 Polarisation curve at 800 °C operations along with cell temperature (S1-S9: nine sensing points of the grid, TC-S1, TC-S5, TC-S9 are the thermocouples near S1, S5, and S9, respectively)

6.5.1.3 Temperature Response to Flow Changes at Constant Current

The voltage and temperature distribution of the cell at 850 °C nominal operating temperature and 70.8 mA current under volumetric compositions of 275 ml/min H₂ with 25 ml/min N₂ and 295 ml/min H₂ with 20 ml/min N₂ are shown in Figure 6.27. The graph does not demonstrate any correlation the fuel composition maintained with the cell temperature. In previous experiments, described in Section 6.3.1, a clear correlation between the cell temperature and hydrogen flow rate could be observed. The leakages in the test rig were identified to cause those temperature increases. The absence of a similar temperature response to flow rate with this experiment suggests that the test-rig was free from significant fuel leakages. A marginal drop of cell temperature could be observed in the second half of the experiment where the total volumetric flow rate is 15 ml/min higher than the first half of the experiment. This could, perhaps, be due to increased cell cooling with the increased flow rate or, just due to a random increase in heat loss from the furnace. However, in either case, it was not considered important enough to further investigate.

Although the voltage fluctuates over the entire duration of the experiment, no pattern could be identified that can be related to the change in fuel composition and rates. The mean cell voltage over the entire experiment is 0.3857 V with the standard deviation of 0.0069 V. The measurement accuracy of NI-9215 voltage data logger, which recorded

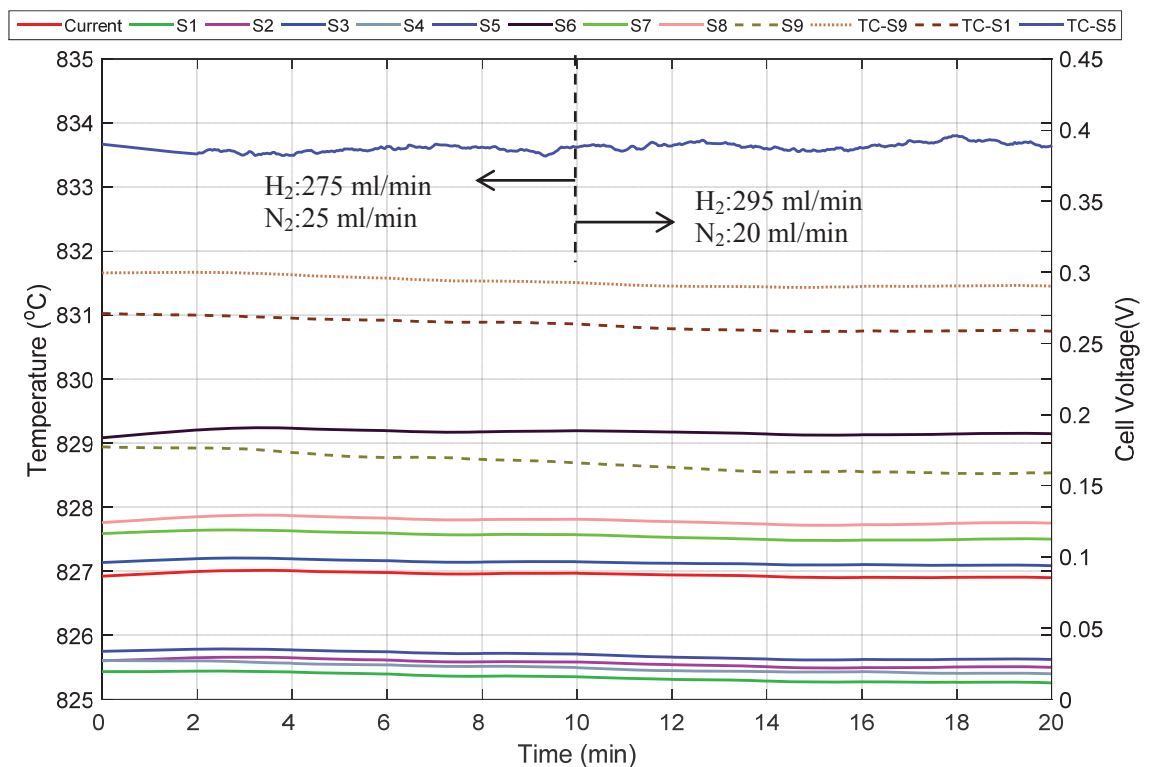


Figure 6.27 Temperature and voltage response to different flow compositions / rates at 70.8 mA and 850 °C

voltages, is 0.003456V. Thus, these minor fluctuations in cell voltage could likely be due to inherent errors in voltage measurements. Further, it is possible to have electrical noises induced on the current collector wires due to the magnetic field inside the furnace created by current-carrying heating elements. Thus, minor fluctuations are plausible.

The increase of hydrogen composition in the fuel mixture increases hydrogen partial pressure. Thus, according to the Nernst effect, the cell voltage should increase, at least slightly. The OCV measurements discussed earlier in this chapter evidenced this fact showing a slight increase of the cell voltage (approximately by 0.05 V) when the flow rate increased from 50 ml/min to 100 ml/m (see Figure 6.11.). Since the same data logger, which detected that voltage increase, was used with these experiments, the hardware capability can be confirmed to detect such voltage increases. The reason for the data logger not to detect the increased voltage in an operating cell and to detect that in an open-circuit cell should be due to the voltage losses along the connection wires (current collector wires).

When OCV is measured, the data logger is connected in series with the cell. Thus, no current passes through the circuit due to very high internal impedance of the data logger. Thus, there is no voltage drop along the connecting wires (that connect the cell to data logger). Therefore, the data logger can measure the exact magnitude of the voltage increment. However, when the cell is in operation, the DC load is connected in series with the cell while the voltage data logger is connected in parallel with the DC load. Therefore, any increase in the cell voltage contributes to increase the voltage drop along connecting wires as well as the voltage drop across the load. What the data logger can measure is the voltage change across the load, which is only a part of the actual voltage increase. The portion of the voltage increment across the load depends on the resistance in connection wires; the higher the wire resistance the lower the voltage increment across the load.

Consider the schematic diagram of a cell shown in Figure 6.28. For a given cell voltage V_{cell} , the voltage across the load can be expressed as Equation (2) by Ohm's law and Kirchhoff's voltage law. If the cell voltage is increased by ΔV , the new load voltage can be expressed as Equation (3). Thus, the voltage increment across the load is the algebraic difference of the two equations, given in Equation (4). This shows that the voltage increase across the load, which is measured by the data logger, is only a fraction of the actual cell voltage increment due to the resistance of connection wires and rest of

the conducting components. For small values of cell voltage increases (such as 0.05 V); the voltage increment across the load could be too small for the data logger to distinguish amidst its measurement errors. The resulting increase of the current may also disappear among the measurement errors. Therefore, even if the actual cell voltage has increased due to the increase of fuel concentration (Nernst effect) the increased voltage likely to have disappeared among measurement errors.

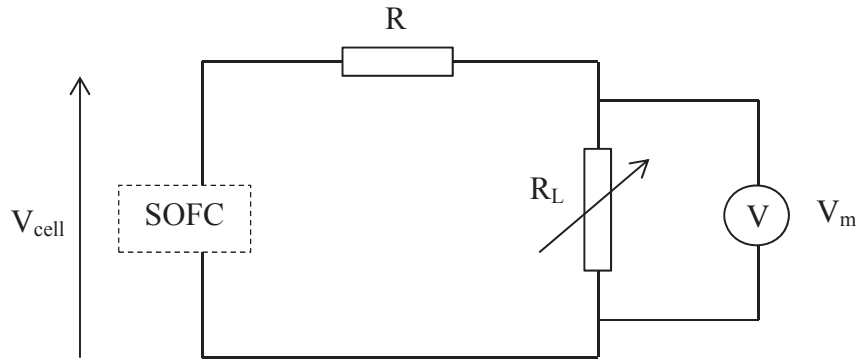


Figure 6.28 Schematic diagram of the SOFC in operation

$$V_L = \left(\frac{R_L}{R + R_L} \right) V_{cell} \quad (2)$$

$$V_L' = \left(\frac{R_L}{R + R_L} \right) (V_{cell} + \Delta V) \quad (3)$$

$$\Delta V_L = V_L' - V_L = \left(\frac{R_L}{R + R_L} \right) \Delta V \quad (4)$$

Where;

V_L – Initial voltage across the load

V_L' - Voltage across the load after cell voltage increment

V_{cell} – Cell voltage

ΔV – Cell voltage increment due to Nernst effect

ΔV_L – Voltage increment across the load

R_L – Load resistance

R – Total resistance along the entire circuit, except R_L

6.5.1.4 Low Power Density of the Cell

The electrode area of the cell used in above experiments was 16 cm^2 . Therefore, considering the cell operation at $850 \text{ }^\circ\text{C}$ nominal temperature, the maximum current density of the cell before concentration polarisation is as small as 0.005 A/cm^2 . Consequently, the maximum power density of the cell is 1.5 mW/cm^2 . This is a far too low power density for a planar SOFC. One possibility for this is the anode had not been fully reduced and consequently, the active electrode area is far too smaller than the physical size of the electrode. However, the literature suggests that cells reduced for much shorter durations (approx. 20 min) with almost similar reduction conditions could produce over 0.5 W/cm^2 power density^[3]. Thus, the probability of insufficient anode reduction is relatively low. A more plausible explanation for the low power density is the improper gas distribution across the cell. In the test rig, the fuel is fed perpendicularly to the cell from the middle of it, approximately 2 cm below the anode surface. Thus, there is a real possibility that only the area above the fuel pipe gets sufficient fuel and thus, remains active. A computation investigation by Chiang *et al*^[4] shows that the current density is highest near the fuel inlet of 5 cm diameter cell, which is fed perpendicularly at the centre similar to the experimental setup in this thesis. The current density in their simulation decreased along the radial direction due to the low fuel supply. A similar condition is likely to present in the test rig used for the experiments throughout this chapter. However; the exact flow pattern of fuel within the anode chamber could only be confirmed with a comprehensive flow investigation/ simulation. Nevertheless, the relatively low power density did not hinder the investigation of temperature response of the cell to different operating conditions. In fact, the temperature response to operating conditions depends primarily on flow configuration, internal reforming, fuel type, stack configuration, etc., which needs investigations as separate case studies. Thus, the experimental setup used in this experiment is one case study to investigate the temperature distribution under different operating conditions.

6.5.1.5 The Grid Validation on a Working Cell

Temperatures measured by *S1*, *S5*, and *S9* sensing points of the grid and their corresponding thermocouples, *TC-S1*, *TC-S5*, and *TC-S9*, respectively are shown in Figure 6.29 (a), (b), and (d), while the cell was operating at 800 °C nominal temperature and under a constant current of 30 mA. Figure 6.29 (d) shows the measurement difference calculated by subtracting the temperature measured by the grid's sensing point and its corresponding thermocouple. The mean and standard deviation of the difference between thermocouple reading and the grid's reading are listed in Table 6.7 **Error! Reference source not found.** along with the error and uncertainty of corresponding thermocouples at 800 °C according to the calibration data.

Cell temperature appears to slowly drop, approximately by 1 °C, during 4.5 hours of operation while the furnace's set temperature maintained at 800 °C. This is possible if this temperature drop is a local temperature drop where the area near the furnace's temperature sensor remains at 800 °C. However, since both the grid as well as

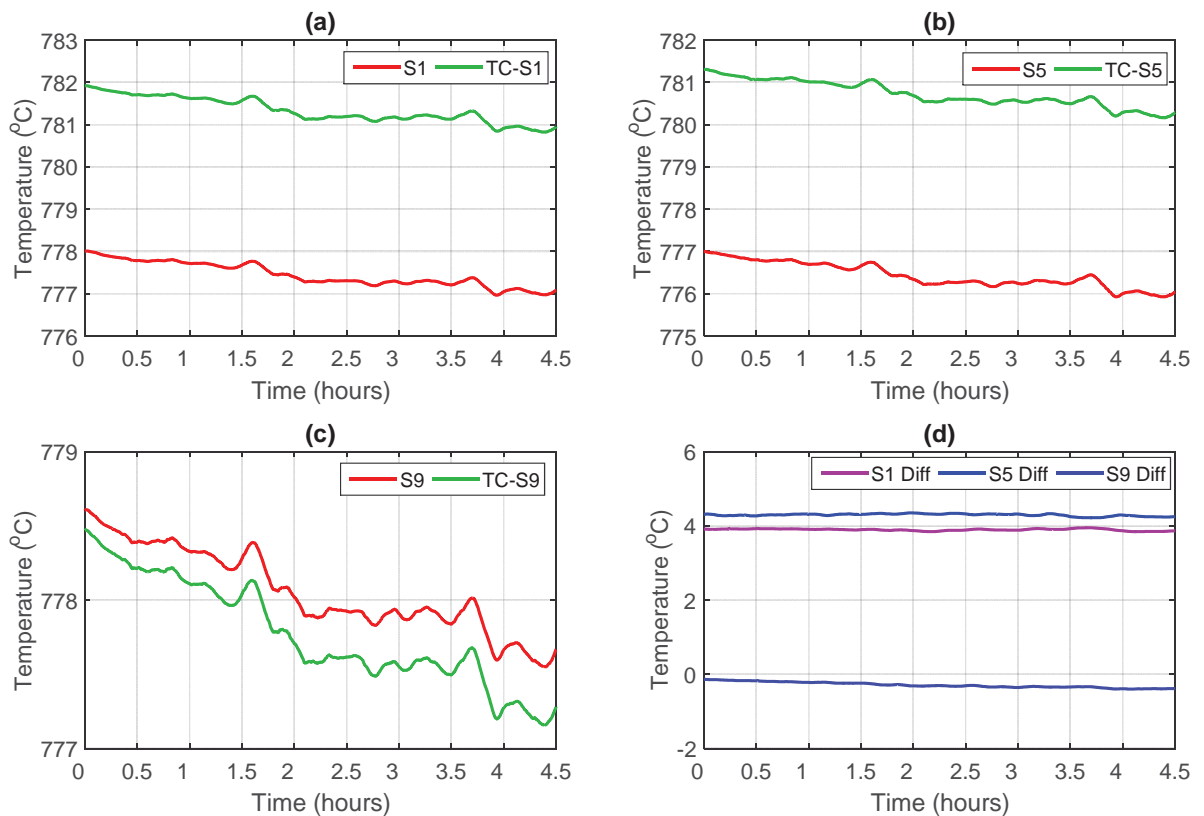


Figure 6.29 Temperature measured by the grid and thermocouples at 800 °C nominal temperature operation under a constant current of 30 mA. (a) Temperature from S1 and TC-S1, (b) temperature from S5 and TC-S5, (c) temperature from S9 and TC-S9, and (d) difference of measurements; where S1, S5, and S9 are three sensing point of the grid and TC-S1, TC-S5, and TC-S9 are the corresponding thermocouples, respectively.

thermocouples equally detect this temperature drop, the cause of the drop is less significant to validate the grid's measurements. In fact, this inadvertently supported to make the validation under transient temperature conditions.

Table 6.7 Mean and standard deviation of temperature difference and calibration data of commercial thermocouples

Sensing points	Mean difference	Standard deviation of the difference	Thermocouple error at 800 °C	Uncertainty
S1 (and TC-S1)	3.8970 °C	0.0304 °C	1.50 °C	0.0 °C
S5 (and TC-S5)	4.2949 °C	0.0459 °C	1.72 °C	0.0 °C
S9 (and TC-S9)	- 0.2892 °C	0.0785 °C	2.30 °C	2.8 °C

Temperatures measured by the grid and their corresponding thermocouple are showing adequately identical variations throughout the entire duration of the experiment, though they are offset from one another. Since the error of thermocouples is a positive value and the thermocouple reading is higher than the grid's reading for *S1* and *S5*, the difference between the true-temperature and the grid's temperature is smaller than the difference between the grid and the thermocouple. However, *S9* appears to measure a temperature higher than the corresponding thermocouple while the thermocouple has a positive error. Thus, ideally, the difference between the true-temperature and that from the grid is larger than the difference between the grid and the thermocouple. However, *TC-S9* thermocouple has 2.8 °C uncertainty while having 2.30 °C error. Therefore, the actual difference between the true-temperature and the *S9*'s measurement could still be in the same range as the other two sensing points.

The observed differences in measurement by the grid and its corresponding thermocouples could be either due to actual measurement discrepancies or, perhaps, there could be actual temperature gradient present within the short gap between a grid's sensing point and its thermocouple. Despite these minor uncertainties, the experimental results comprehensive show that the grid's sensing points measured temperatures that are different from one another. Thus, the fact that the grid did not measure an average temperature is evident. Grid has measured the local cell temperature. Further, it shows that the grid can respond to temperature variations as efftely as commercial thermocouples do. The measurement accuracy of the grid can be different from one

sensing point to the other sensing point so as the measurement accuracy of commercial thermocouples differ from one to another. While commercial thermocouples are fabricated using bespoke technology, the in-house fabricated thermocouple grid was manually fabricated by a general purpose spot-welding machine. Therefore, there is a greater possibility for the condition of each junction to differ from one another thus; yielding differences in measurement accuracy. Notwithstanding aforementioned minor discrepancies, the thermocouple grid was adequately validated on the operating SOFC.

Since the temperature at a grid's sensing point does not change independently from its corresponding thermocouple's measurement with time, the presence of errors due to heat transfer can be considered negligible in this test setup. However, if such problems become significant, an advanced data logging system needs to be developed to correct such errors as discussed in Chapter 8 under further research.

6.6 Conclusions

Multi-junction thermocouple grids along with commercial thermocouples were used to measure the cell surface temperature distribution under different operating conditions of SOFC. A deeper insight into the role of cell temperature on the performance of SOFC could be made, and the effects of different operating conditions on the cell temperature could also be discovered.

The experimental investigation to see if a multi-junction thermocouple grid operating on the cathode causes any influence on the performance of SOFC confirmed that a grid placed on the cathode does not affect the SOFC performance.

The performance of the grid was validated under two conditions; firstly on a non-working cell with thermocouples and then, on a working-cell with calibrated thermocouples. In both cases, the thermocouple grid demonstrated that it could respond to cell temperature variations as comprehensively as thermocouples. Although there were some measurement discrepancies between the grid and its corresponding thermocouples, they were due combined effects of actual measurement errors that can present in any thermocouple and the actual temperature gradients across different sensing locations.

A thermocouple held approximately 7 mm above the cathode showed a very dull response to dramatic variations in cell temperature. However, as the gap between the thermocouple and the cathode was decreased to approximately 3 mm, the thermocouple could follow the cell temperature more closely. This confirms that near-surface temperature is not an adequate representation of the cell temperature.

The OCV measured at different cell temperatures confirmed the decrease of OCV with the increase of cell temperature. However, the operating voltage measured under a constant current of 60 mA at 700 °C, 750 °C, 800 °C, and 850 °C nominal operating temperatures showed a slight increase of voltage with the increase of operating temperature. Thus, a decrease of ohmic polarisation with the increase of temperature could be observed.

A positive correlation between cell temperature and cell current could be discovered. A noticeable, yet small, cell temperature increase could be observed even for less than 100 mA current increase. Therefore, cell temperature fluctuations caused by load fluctuations could be well-understood. A slight out-of-phase response of cell temperature to load changes could be noticed, where the cell temperature response lags the current

change. Although this was speculated as being caused by heat transfer characteristics of the cell, a confirmation may only be reached upon a comprehensive theoretical investigation into heat transfer phenomenon in further research.

The polarisation curve obtained at 850 °C did not show any sign of activation polarisation. However, very prominent ohmic polarisation and slight concentration polarisation could be observed. Even at the very small concentration polarisation, the entropy generation due to increased irreversibilities appears to cause a noticeable increase of the cell temperature. Since concentration polarisation is caused by lack of fuel supply to reaction sites, the local cell temperature can be used as a tool to identify areas with low fuel supply.

A temperature gradient of approximately 10 – 15 °C could be identified to present across approximately 2 cm × 2 cm area of the cell even during the anode reduction process. Further, cell temperature measurements revealed the evolution of dramatic temperature changes on cell due to fuel leakages, while the thermocouple placed approximately 7 mm above the cathode could not comprehensively detect such temperature changes. Thus, the cell surface temperature sensing sufficiently demonstrated its potential in identifying hot-spots formed due to fuel leakages. However, when the fuel leakages were prevented, no hot-spots were detected.

Throughout the experiments, the thermocouple grid's measurements were in good agreement with the measurements from the standard thermocouples confirming the plausibility of using multi-junction thermocouples for SOFC temperature sensing with increased spatial resolution.

6.7 References

- [1] Drescher, I., Lehnert, W., and Meusinger, J., Structural properties of SOFC anodes and reactivity, *Electrochimica Acta*, 1998, vol.43(19-20), pp. 3059-3069.
- [2] Paulson, S.C., and Birss, V.I., Chromium poisoning of LSM-YSC SOFC cathodes, *Journal of the electrochemical society*, 2004, vol. 151(11), pp.A1961-A1968.
- [3] Mallon, C., and Kendall, K., Sensitivity of nickel cermet anodes to reduction conditions, *Journal of Power Sources*, 2005, vol.145, pp.154-160.
- [4] Chiang, L-K., Liu, H-C., Shiu, Y-H., Lee, C-H., and Lee, R-Y., Thermo-electrochemical and thermal stress analysis for an anode-supported SOFC cell, *Renewable Energy*, 2008, vol.33, pp.2580-2588.

**Chapter 7 : Feasibility Investigation on Cell Integration of
Multi-Junction Thermocouples**

Chapter Summary

Some attempts made to fabricate thin-film multi-junction thermocouples integrated to the cathode of an SOFC to monitor cell temperature is presented and discussed in this section.

Section 7.1 provides an overview of the study along with some important parameters to consider. Fabrication and testing of a cell integrated multi-junction thermocouple array is presented in Section 7.2. Some failures experienced in carrying out this experiment were further investigated and results are presented and discussed in Sections 7.3 and 7.4. Two case studies on using cell-integrated thin-film thermocouple array into SOFC temperature sensing are presented and discussed in Sections 7.5 and 7.6. Finally, conclusions are drawn in Section 7.7 based on the overall findings of the investigation.

7.1 Introduction

Multi-junction thermocouples made from thin wires could adequately reveal the surface temperature distribution of operating SOFCs as presented and discussed in Chapter 6. Integrating this sensor into cells as a thin-film sensor is a significant step in advancing the proposed methodology. Cell integrated sensors are, particularly, beneficial in stacks where there is hardly any gap between adjacent cells to accommodate external sensors. Furthermore, since cell integrated sensors share the same thermal body with the cell, the sensors may record a cell's temperature variations more accurately than external sensors. The fast response of thin-films to temperature changes is also an added advantage. These multifaceted advantages justify any efforts into developing cell integrated multi-junction thermocouples.

Fabricating thin-films directly on the electrodes of SOFC requires in-depth investigations on how these films affect the performance and durability of SOFC and how the SOFC operation will affect the sensor in return. Reducing the film dimensions to reduce active cell area coverage, effects of thermal stresses on the durability of cell and the sensor, etc. are some critical aspects to investigate further. However, the research presented in this chapter is limited to investigate the operational feasibility of multi-junction thermocouples fabricated directly on a porous electrode.

The choice of materials for thermoelements is an important parameter that influences the safety and operational health of the sensor. Thermal expansion compatibility of thermoelements with the cell is important to alleviate detrimental effects of thermal stresses on thermoelements as well as on the cell. Ceramic thermoelements might be an excellent choice to curtail thermal expansion mismatch between thermoelements and the cell. However, development of ceramic multi-junction thermocouples is a too broad scope to fit into the current scope of this thesis. Therefore, alumel and chromel were chosen as thermoelement materials with their previously proven success.

There are a number of thin-film deposition techniques available. However, rather than investigating into each of the those to identify their pros and cons to decide the absolute best technique, the main focus of the selection was laid on three factors: (a) readily access to the facility, (b) ability of the technique in meeting the required film characteristics, and (c) economy and efficiency of fabrication. Sputter deposition sufficiently met these criteria and a literature on the successful application of sputter

deposition to fabricate thin-film metallic thermocouples^[1] confirmed the verity of the choice.

Film thickness and junction size are two important parameters that influence the sensitivity of thin-film thermocouples^{[2][3]}. However, the effect of junction size on performance diminishes when it exceeds a few micrometres, for example, $9\ \mu\text{m}^2$ ^[15]. Since the designed width of thermoelements was much larger than that critical range, the junction size was not considered as a critical parameter. Therefore, published literature was consulted only to determine a safe film thickness that ensures the performance is independent of the thickness. Marshall *et al.*, as cited by Chopra *et al.*^[5], state that maximum thermal EMF of thermocouples constructed from nickel, iron, copper, constantan, chromel, and alumel can be obtained when the film thickness is greater than 250 nm. However, Chopra *et al.*^[5] negated this argument by showing that the EMF of copper-constantan thermocouples is independent of the film thickness when copper and constantan films are thicker than 120 nm and 100 nm respectively. In addition, Zhang *et al.*^[6] also have shown that the thickness's influence on performance diminishes in K-type thin-film thermocouples when film thickness exceeds approximately 140 nm. Figure 7.1 shows the induced EMF of a K-type thermocouple having 100 nm thick chromel thermoelement and Figure 7.2 show the standard EMF that a K-type thermocouple should produce at respective temperatures. Visual comparison of these two graphs confirms that the thin-film thermocouple operated almost identical to a standard thermocouple. Therefore, despite the discrepancies found in literature on the minimum safe thickness, a minimum film thickness of approximately 140 nm was initially considered sufficient for the experiments in this research.

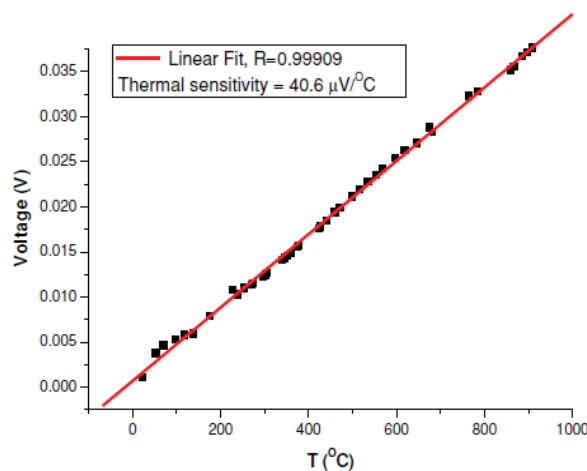


Figure 7.1 Variation of EMF with temperature for 100 nm thick chromel film^[6]

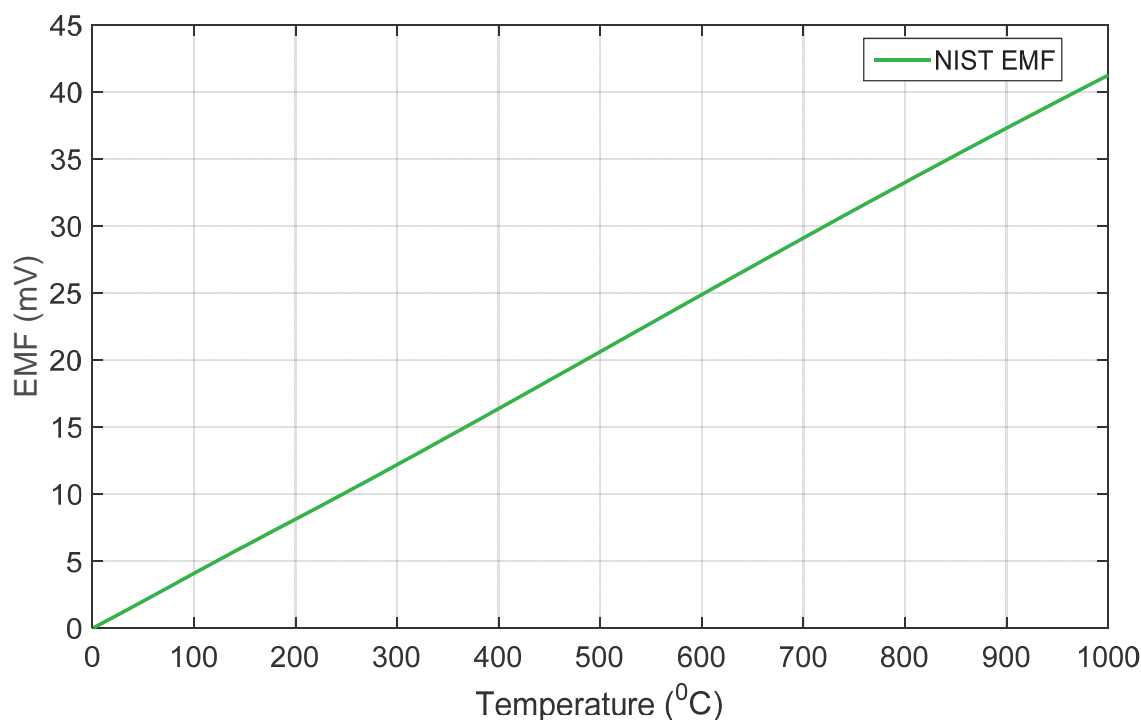


Figure 7.2 NIST standard EMF of a K-type thermocouple (Graph plotted based on NIST thermocouple data)

The cathode was chosen as the substrate to deposit a multi-junction thermocouple array to avoid any potential detrimental interactions between fuel and thermoelement materials. Since the anode is exposed to fuel while the cathode is exposed only to air, the cathode is chemically less harmful than the anode for thermoelements. The presence of hydrogen is detrimental to K-type materials causing time-dependent voltage losses^[3]. Although film oxidation is a problem on the cathode, K-type thermocouples have been in use in many oxidising environments without short-term calibration errors. Further, the cathode has greater porosity than an un-reduced anode. That helps to investigate how successfully the array can survive on a porous substrate.

Temperature and voltage measurements made in experiments outlined in this chapter were made by NI-9213 and NI-USB 6210 data loggers, respectively. Computerised data recording were done using the LabVIEW-based computerised data logging systems described in Appendix III and Appendix IV.

7.2 Fabrication and Testing of Array Architecture

A multi-junction thermocouple array having four sensing points hence, five thermoelements, was sputter deposited on the cathode of Ø52 mm commercial test cell (KERAFOIL®) as shown in Figure 7.3 (Quorum QT150ES sputter coater was used). The substrate was prepared by first cleaning with acetone and then with deionised water followed by drying in a furnace at 150 °C for 10 minutes. This cleansing process was expected to remove any dirt or grease on the substrate, which is likely to disturb the film's adhesion to the substrate. The pattern was obtained by using two masks hand-cut from transparent binding sheets. The alumel thermoelement (*E*) was first deposited and then the chromel thermoelements (*A* to *D*). The width of each thermoelement is approximately 1 mm. Labels *A* to *E* represent the connection pads (3 mm × 3 mm) where external wires connect to films to take the singles. Labels *S*₁ to *S*₄ represent the four sensing points. The potential differences measured across *E*-*D*, *E*-*C*, *E*-*B*, and *E*-*A* represent the temperature at *S*₄, *S*₃, *S*₂, and *S*₁ respectively.

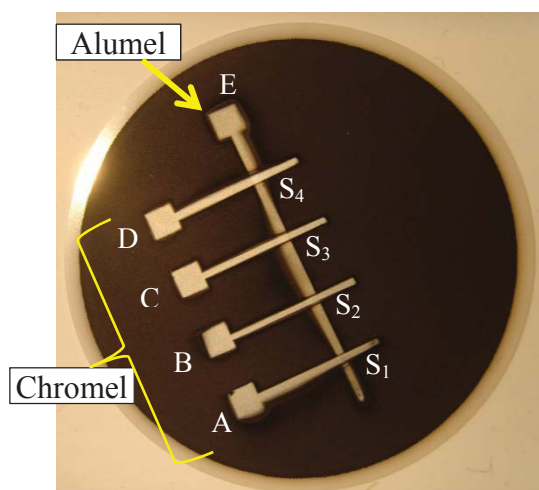


Figure 7.3 The sensor fabricated on the cathode of Ø52 mm SOFC

An alumel wire (Ø0.25 mm) was connected to pad *E* and four chromel wires (Ø0.25 mm) were connected to pads *A* to *D*. Silver paste (from Sigma-Aldrich) was applied to each connection pad to ensure uninterrupted electrical connectivity between the wire and the film (Figure 7.4). In the case where the physical connection between a wire and the film is broken, the electrical connection was expected to maintain through silver. Although the addition of silver introduces a third material, the effect of this introduction on temperature measurements is negligible as there cannot be a significant temperature gradient across a very tiny amount of silver (see Chapter 4 for a similar scientific

derivation). Silver paste was cured at 130 °C for 40 minutes as per the manufacturer's instructions^[8] to obtain a pure and robust silver layer by evaporating binding agent. High pure alumina adhesive (EQ-CAA-2-LD, MTI Corporation, USA) was then applied to the connection pads to provide sufficient mechanical strength for the joints to ease handling. Since alumel and chromel form oxide layers at temperatures beyond 800 °C^[9], the same alumina layer was continued over the films covering the entire set of films as to prevent oxidation of metallic patterns (Figure 7.5). Curing alumina at 250 °C for 30 minutes yielded a sufficiently strong layer of alumina that facilitated ease of handling. The lead wires were sent through ceramic beads to prevent any short-circuiting during handling. The resistances across the distal ends of the wires were measured before the experiment begins and the values are given in Table 7.1.

Table 7.1 Resistance across external wires of the array

External wire connection	Resistance (Ω)
A-E	20
B-E	16
C-E	13
D-E	11

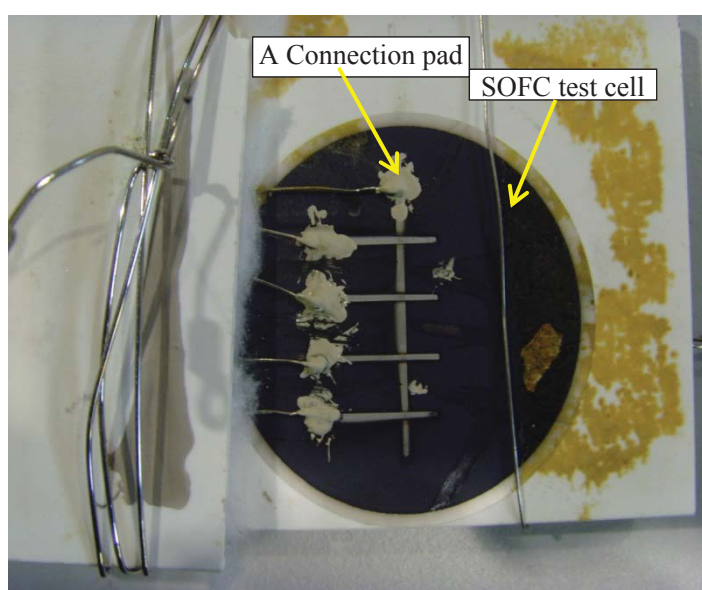


Figure 7.4 External wires connected with Silver paste

The thermocouple array was placed in a box furnace while having fixed a commercial thermocouple within approximately 10 mm adjacency to the cell for comparison purpose. The furnace was heated at a rate of 400 °C/ hour up to 1,050 °C. Once the set temperature was reached, the sensor array was purposely cooled rapidly to introduce a high level of disturbance to temperature. Temperatures from both

thermocouple array and the commercial thermocouple were recorded at 3 seconds intervals.

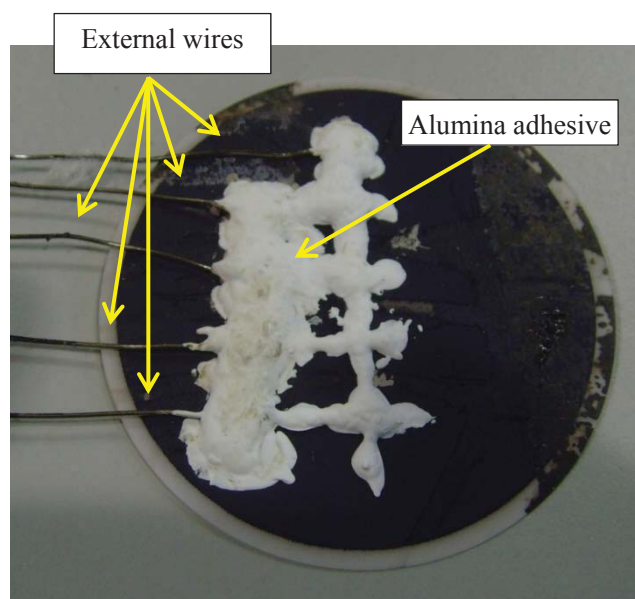


Figure 7.5 Sensor pattern protected by alumina

7.2.1 Results and Discussion

Warping the edges of the plastic mask due to heat inside the sputter chamber has caused poor edge definition on the deposited films. However, this shouldn't have caused any influence to the performance as the film width was already larger than the threshold width.

Figure 7.6 shows the temperature measured from four sensing points of the array (*S1* to *S4*) and from the commercial thermocouple (*TC*). The two abrupt temperature interruptions around 680 °C and 900 °C were introduced by momentarily changing the heating power and by allowing cold air to get into the furnace chamber to investigate the nearly constant discrepancy between thermocouple's reading and the array's reading. The enlarged view of the first temperature interruption shown in Figure 7.7 reveals that the temperature offset between the thermocouple and the array has decreased during sudden temperature drop. Overall, the results show that the cell's temperature measured by the array is in a good agreement with the air temperature measured by the commercial thermocouple. However, *S2* demonstrated an unusual sudden rise in temperature beyond 1,000 °C in heating and then joined back to the others' pattern when cooling down nearly at the same temperature that it had started the diversion. The experimental setup does not provide such a localised high temperature on the cell. Therefore, it should be a result of a

momentary failure occurred somewhere between the data logger and *S2* sensing point along thermoelement *B* causing the electrical resistance to increase; then, the data logger shows higher temperatures as described later.

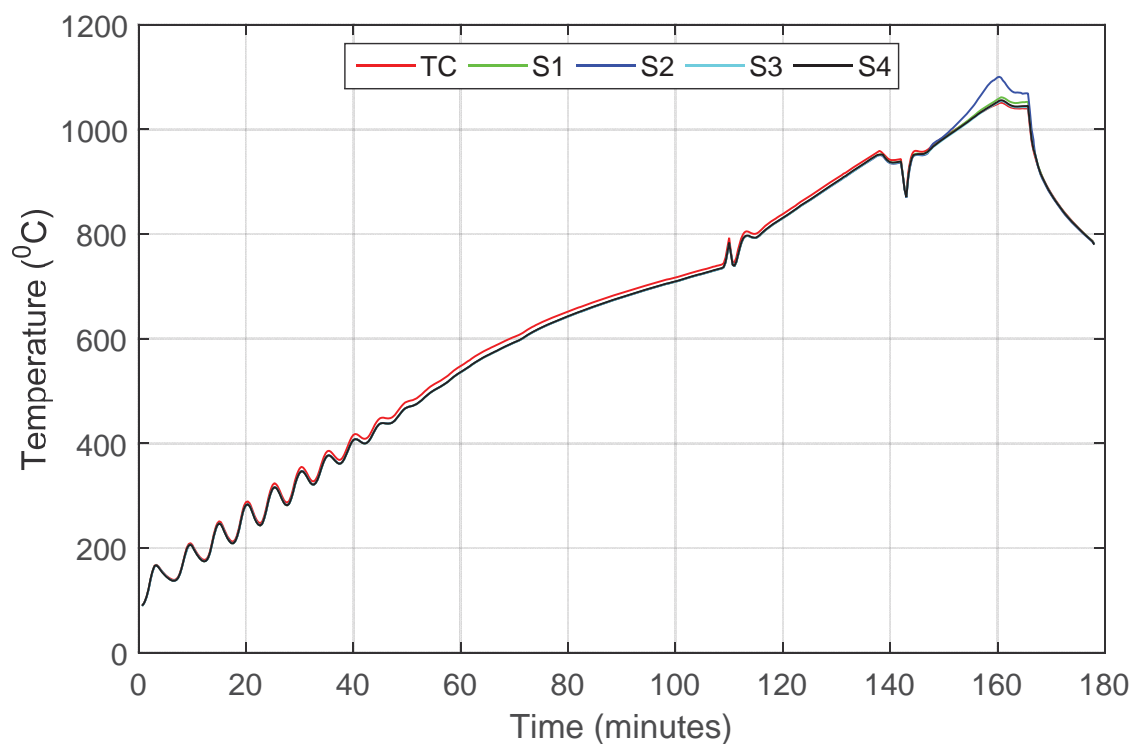


Figure 7.6 Temperature measurements from the array and the thermocouple (S1 –S4: four sensing points of the array, TC – commercial thermocouple)

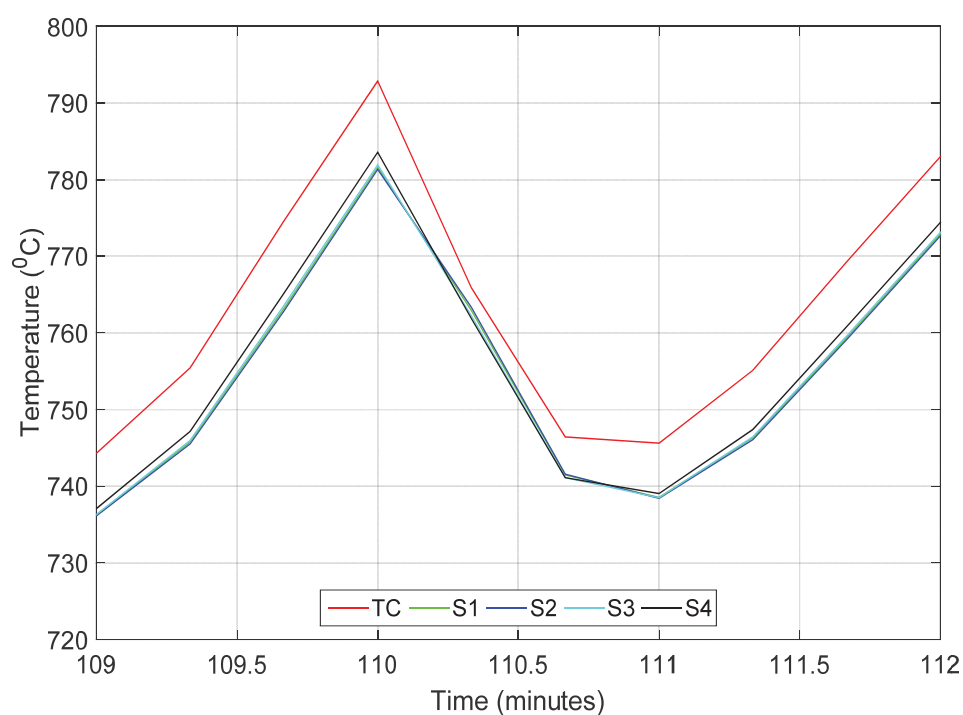


Figure 7.7 Enlarged view of the first temperature interruption

Despite having a good conformity among four sensing points in their temperature measurements, the offset between the commercial thermocouple's reading and that from the array's reading, particularly, during the steady heating period (from about 500 °C to 950 °C) is an important behaviour to investigate further. The author would like to consider two hypotheses to explain this inconsistency.

1) Characteristic differences between thin-films and bulk materials

The sensor material's Seebeck coefficient can be different between thin film and bulk material^[10]. The data logger is calibrated to work on commercial thermocouples, which use bulk material properties. Therefore, there can be intrinsic differences between the temperature measured by a commercial thermocouple and thin-film thermocouples, whether it is a multi-junction or conventional type.

2) The effect of thermal inertia

Since thermal inertia of SOFC test cells is higher than that of surrounding air, temperature response of the cell is much slower than that of air. Therefore, in temperature ramping, the cell heats up slower than the surrounding air. Since thermocouple measures air temperature while the array measures cell's temperature, this makes temperature readings of the array to lag the thermocouple's reading during heating. The same situation may be reversed during fast cooling. In that case, surrounding air cools rapidly than the cell causing the thermocouple's reading to lag the array's reading. However, this lead/lag behaviour should diminish under isothermal conditions.

To investigate the validity of the first hypothesis, the difference between thermocouple's temperature and the array's temperatures was calculated as per equation (7.1) and plotted against the thermocouple's temperature as shown in Figure 7.8. A much clear correlation generated using 5th order curve fitting is presented in Figure 7.9. The abnormal behaviour of *S2* was eliminated from these graphs as it has already been understood as an error. If the 1st hypothesis is valid, the offset should be linear with temperature. However, the graphs show that it has a highly non-linear relationship with the temperature. Also, the magnitude of the offset is different from one sensing point to the other. Therefore, the cause of temperature discrepancy between the array and the thermocouple is not well explained by the 1st hypothesis. However, this experiment lacks isothermal temperature measurements and a sufficiently clear temperature measurement made during cooling. Therefore, even if the 1st hypothesis is confidently nullified, the

experimental evidences are insufficient to validate the 2nd hypothesis comprehensively.

$$\text{Temperature Difference} = TC - S_i \quad (7.1)$$

where $i = 1, 2, 3, 4$

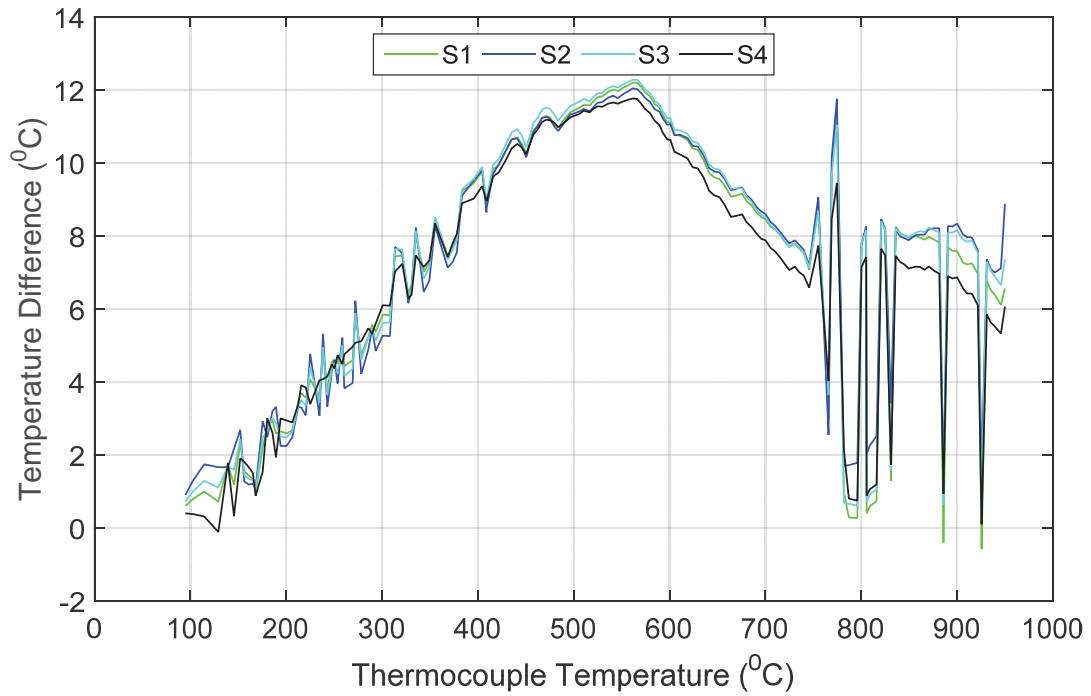


Figure 7.8 Actual temperature difference (raw data)

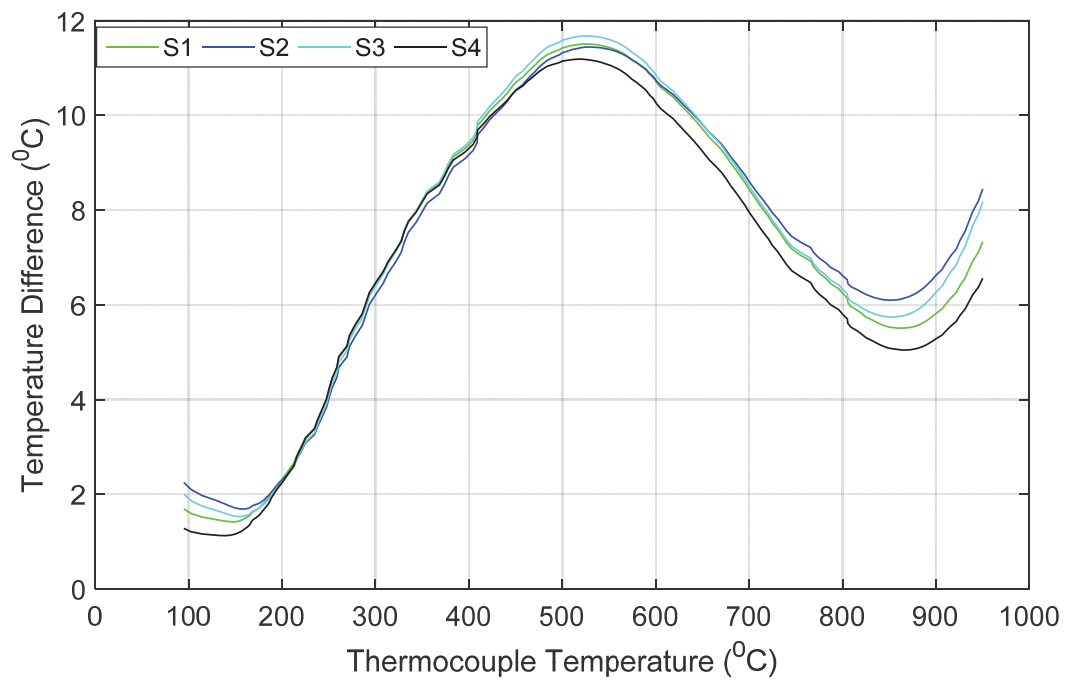


Figure 7.9 Polynomial fitted temperature difference (5th order)

The resistances across the distal ends of the external wires were measured after the experiment, and all of them were in open circuit. However, the cathode remained conductive having only approximately 120 Ω/cm resistance across any two points on the surface. Two plausible speculations behind this complete electrical disconnection between external wires and thin films are 1) failure of thin-films and 2) failure at the connection point. However, the tested sensor design did not facilitate credible investigation into these two speculations.

7.3 Failure Mode Investigation and Hypothesis Testing

A new sensor layout was developed by combining two arrays, primarily, to investigate the two failure modes derived in the previous discussion. In addition, the experiment was designed to further investigate the thermal inertia hypothesis derived in the previous discussion. The new layout, hereafter called as dual-array, was fabricated on the cathode of a 5 cm \times 5 cm commercial SOFC test cell (NextCell-5), as shown in Figure 7.10. The substrate was prepared following the same procedure described in Section 7.2. The same number of sputter depositions cycles and the same sputtering parameters were used as with previous array fabrication to achieve comparably similar film thickness. The pattern was obtained by using two stainless steel masks which were not bespoke preparations for this application; hence, the widths of the two sets of thermoelements are different. The widths of thermoelements *A* and *B* on the mask is 1 mm and that of *C* to *F* is 0.2 mm on the mask. However, the strong magnetic field inside the sputter chamber slightly lifted the mask from its unsupported area causing the deposited films to be wider than their corresponding dimensions on the mask.

Thermoelements *A* and *B* are made of chromel and *C-F* are made of alumel. External wires ($\varnothing 0.25$ mm) of the same thermoelement materials were connected as before by first using silver paste and then alumina adhesive. The entire film was covered with alumina adhesive as before for the same purpose. The resistance across the distal ends of external wires were measured before the experiment and the values are given in Table 7.2

The dual array was placed in the same box furnace which, the previous array was tested while having fixed a commercial thermocouple approximately 10 mm adjacent to the cathode in the middle of it. The commercial thermocouple served the same purposes as before. The furnace was heated to 975 $^{\circ}\text{C}$ at a rate of 400 $^{\circ}\text{C}$ /hour for four heating-cooling cycles. Temperatures from the dual-array as well as from the commercial thermocouple were recorded at 3-second intervals. Although the array had eight sensing

points (S_1 to S_8), temperatures from only the first seven points have been recorded due to a limited capacity of the data logging system present at that time.

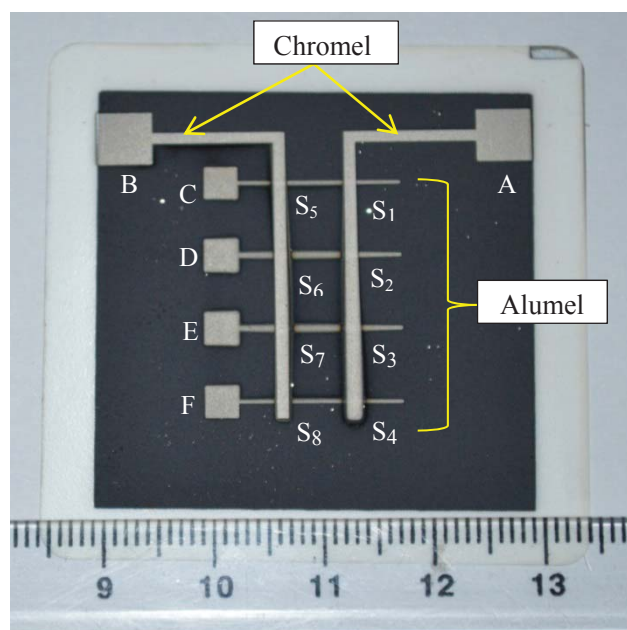


Figure 7.10 dual-array fabricated on cathode

Table 7.2 Resistances across thermoelements

<i>Connection pads</i>	<i>Corresponding sensing point</i>	<i>Resistance (Ω)</i>
<i>A-C</i>	S_1	62
<i>A-D</i>	S_2	59
<i>A-E</i>	S_3	82
<i>A-F</i>	S_4	113
<i>B-C</i>	S_5	19
<i>B-D</i>	S_6	34
<i>B-E</i>	S_7	60
<i>B-F</i>	S_8	95

7.3.1 Results and Discussion

Temperatures measured by the commercial thermocouple and the dual-array throughout the entire experiment are shown in Figure 7.11. Although the actual temperature inside the furnace (indicated by TC) never goes beyond 1,000 °C, the temperature measured from the dual-array goes well beyond 2,000 °C. Since there is no possibility for the internal temperature of the cell to reach this high value, this must be a measurement error. In fact, characteristically, the NI-9213 data logger forces full-scale

voltage across its terminals when it detects an open circuit across its terminals^[11] as illustrated in Figure 7.12. Thus, the data logger shows the maximum temperature that it measures. This characteristic of the data logger explains the unusually high temperature recording from the dual-array as an electrical disconnection between the dual-array and the data logger. Further, it can be seen that this disconnection happens only when the system cools below a certain threshold temperature – approximately 650 °C. Thus, the failure is temperature dependent. The connections at the data logger's terminals are very robust, and they were very well maintained throughout the experiment and even after. Further, the data logger was at room temperature and hence, the temperature dependent nature of the failure cannot be attributed to a failure at the data logger's connection. Therefore, the electrical disconnection must have originated at the high-temperature side of the experiment. It can be a failure at the external wire connection to thin-films or the thin-films themselves. Further, similar to the experiment described before with a thin-film array, the dual-array also showed complete electrical disconnection across its lead wires once it was cooled down to room temperature. Therefore, it can be speculated with a high level of confidence that the root of the failure comes from the same origin.

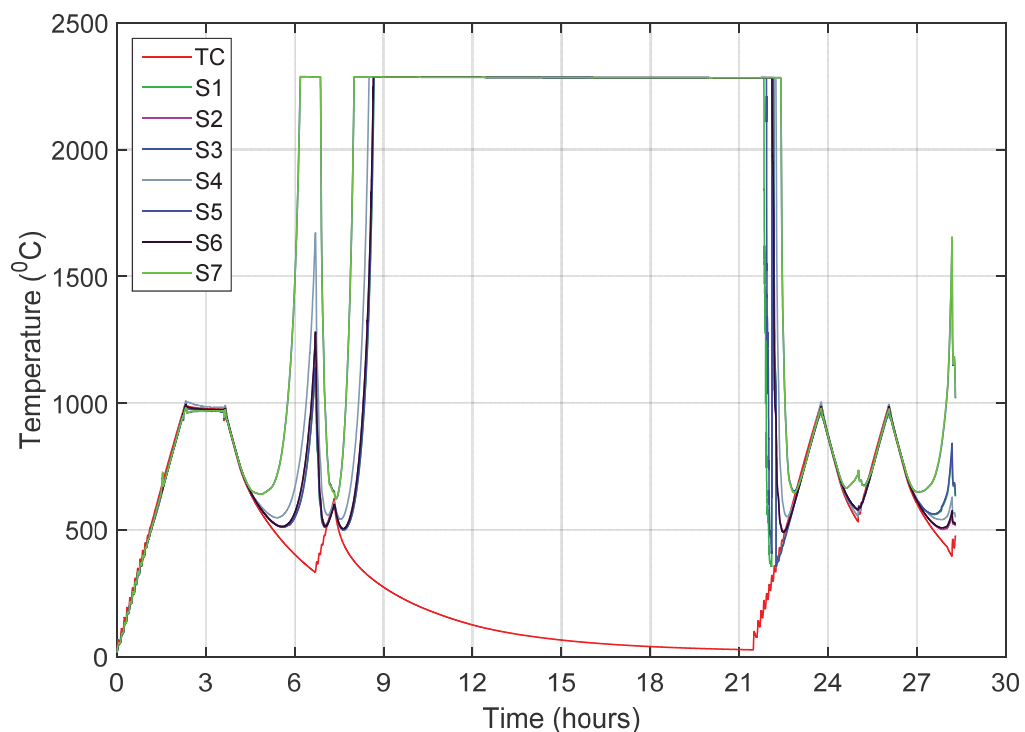


Figure 7.11 Temperature from the dual array and thermocouple (TC: thermocouple, S1-S7: seven sensing points from the dual array)

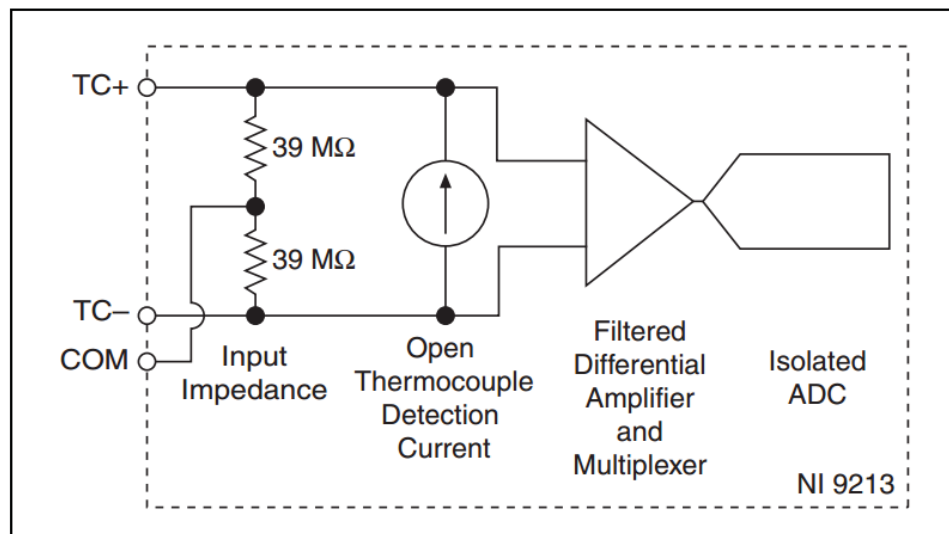


Figure 7.12 Input circuitry for one channel of NI9213^[11]

Figure 7.13(a) shows a momentary diversion of $S3$ and $S7$ from regular heating pattern encountered during the first heating cycle. The enlarged view of the encircled section shown in Figure 7.13 (b) clearly shows a paired-like behaviour of $S3$ and $S7$ during its diversion while showing an independent response before the incident. This signifies that the cause of failure was common to $S3$ and $S7$. Figure 7.14(a) shows the failure of dual-array during the first cooling cycle. $S3$ and $S7$, which showed momentary diversion during heating, were the first to start failing. An enlarged view of the encircled

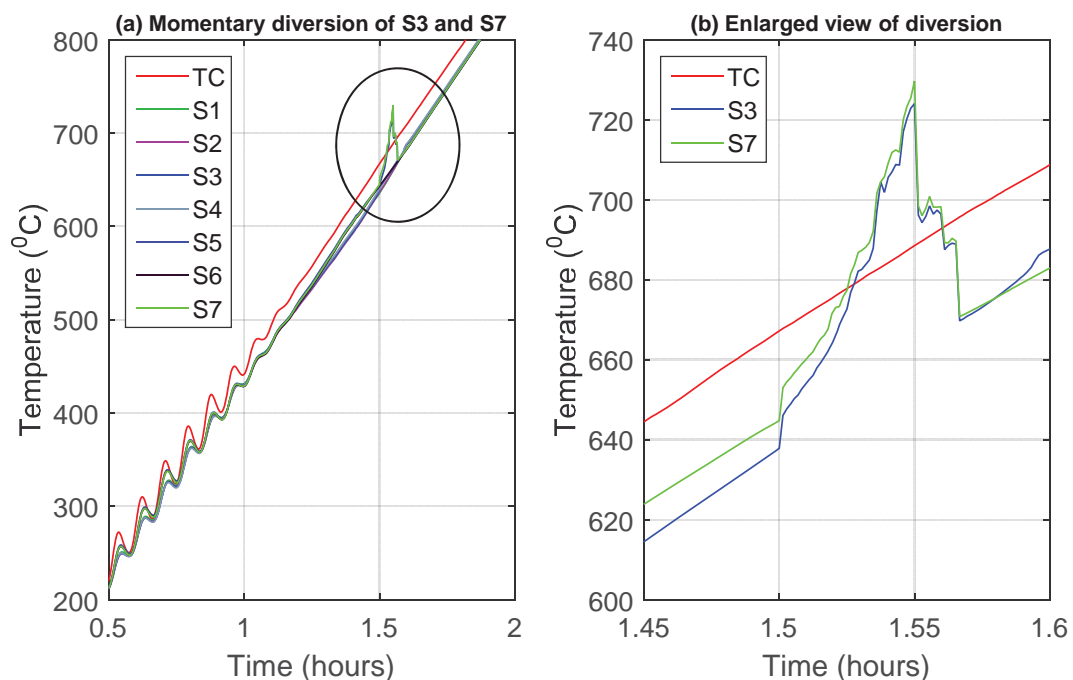


Figure 7.13 (a) momentary diversion during first heating (b), an enlarged view of the encircled section in (a)

section in Figure 7.14(a) is shown in Figure 7.14(b). This shows that $S1-S5$ and $S2-S6$ also failed in pairs. Furthermore, as the drift from true temperature increases, each pair converges onto a single line giving the same reading. This implies that when the cause of

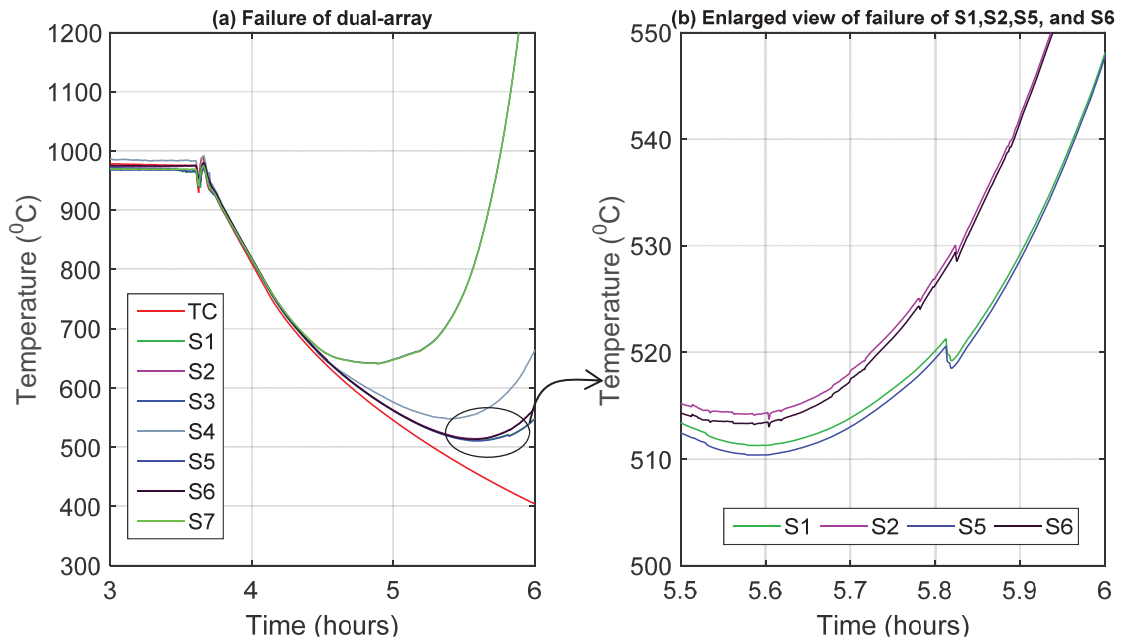


Figure 7.14 (a) first failure of dual-array during cooling (b) enlarged view of diversion encircled in (a)
failure becomes more prominent, it affects the sensing points in each pair similarly.

Each pair of sensing points that failed together shared one thermoelement in common: $S1-S5$ pair shares thermoelement C , $S2-S6$ pair shares D , and $S3-S7$ pair shared thermoelement E (Figure 7.10). The cause of the failure has already been identified as an electrical disconnection between thermoelements and the data logger. As previously explained, the electrical disconnection can happen either at the thin-film connection pads or on thin-film thermoelements themselves. If the films failed, all failures must have occurred between the connection pad and the first sensing point on all thermoelements. Then only the failure becomes common to both sensing points on a given thermoelement, and the paired-like behaviour is justifiable. However, there is no reason for that part of the thin-film to become significantly weaker than the rest in all three common thermoelements. Therefore, the probability of random failure to occur within that region in all three thermoelements is very little. Thus, it can be speculated with a high level of confidence that the failures have occurred at the connection pads at C , D , and E where external wires connect to thin-films. When a failure occurs at those connection pads, the corresponding two sensing points are affected alike making the paired-like failure

explainable. An in-depth investigation into the failure mechanisms and developing an effective miniature connection mechanism are a separate research which needs to be carried out separately. However, the curiosity lead rudimentary level investigation was conducted to understand the failure as presented in Section 7.4.

Once the source of failure is narrowed down to external wire connection, the remaining partly-solved problem is the measurement discrepancy between the thermocouple and the array in the previous experiment. The same discrepancy appears with the dual-array as well. Figure 7.15 shows a part of the first heating, dwelling, and cooling cycle. The graphs show that the thermocouple's reading leads the dual-array during heating and it lags during cooling. The lead/lag behaviour diminishes within the isothermal region. This behaviour is well explained by the thermal inertia hypothesis. Therefore, it can be sufficiently justified that the temperature offset between thermocouple and thin-film multi-junction thermocouples is a result of the difference in thermal inertia.

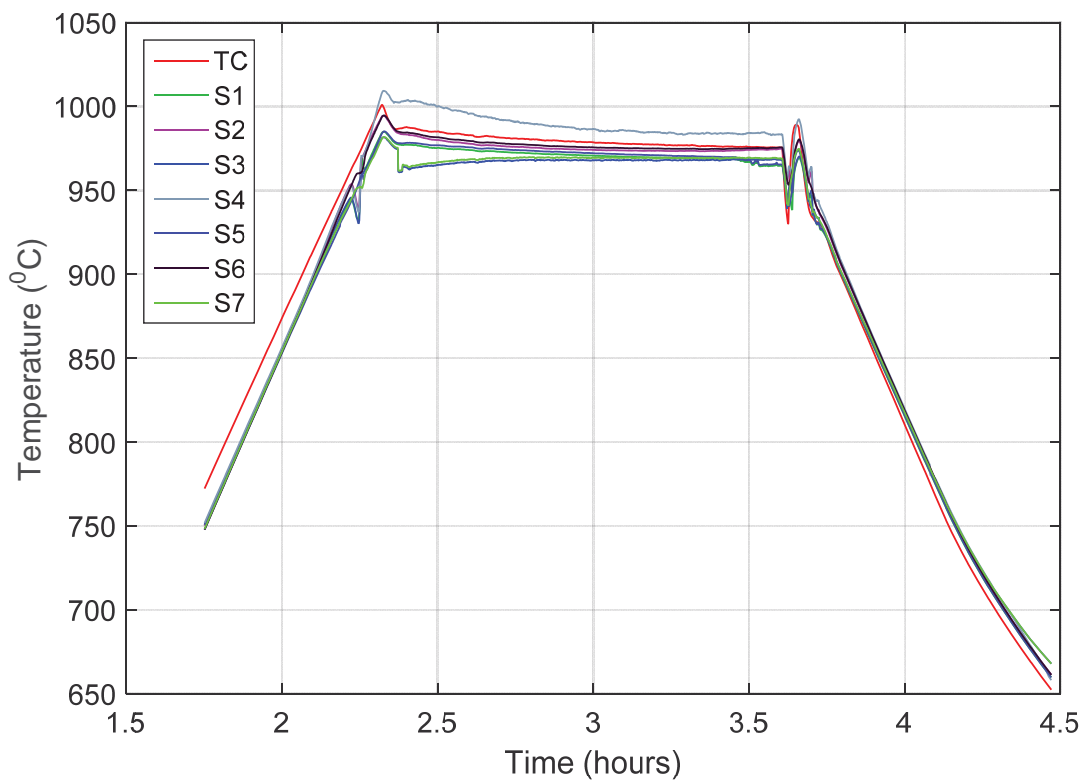


Figure 7.15 First heating and cooling cycle of grid architecture

7.4 Failure Mode Analysis of External Wire Connection

Visual inspections of the connection points did not show any evidence to confirm that silver has escaped from the alumina protective sheath. Therefore, the electrical disconnection is confirmed to have happened while silver remained at junctions to maintain the electrical connectivity. Therefore, some unusual behaviour of silver within the alumina enclosure was speculated to cause electrical disconnection. However, this was only a speculation and any influences from thin-films on the failure were not identified to be trivial. Therefore, to investigate the behaviour of silver while eliminating any influences from thin-films, thin-wire thermocouples were used instead of thin-film thermocouples as described in following sections.

Two thermocouple junctions were fabricated by twisting alumel and chromel wires ($\varnothing 0.25\text{mm}$) together. The length of each thermoelement was approximately 30 mm. Both thermocouples were placed on an alumina substrate ($5\text{ cm} \times 5\text{ cm}$) while having connected the external wires (of same thermoelement materials) to one thermocouple directly by twisting them to thermoelements. External wires to the other thermocouple were connected through silver. Figure 7.16 illustrates the arrangement. Although the external wires of thermocouple “A” are directly connected, the silver paste was added on top of the connection to ensure both thermocouples have silver at their connection points. After curing silver at $125\text{ }^{\circ}\text{C}$ for 20 minutes, a layer of alumina was applied over all four connections to reproduce identical operating conditions as with thin-films’ connection. Alumina was cured at $230\text{ }^{\circ}\text{C}$ for 20 minutes. Figure 7.17 show the two thermocouples once alumina was hardened.

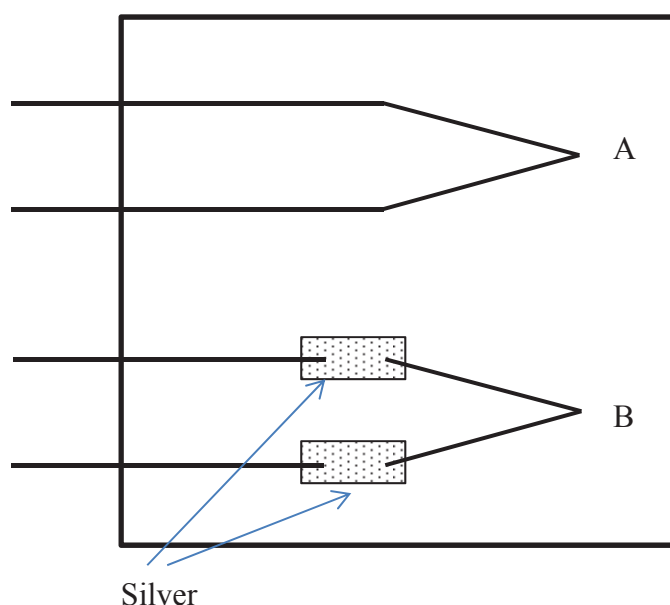


Figure 7.16 wire thermocouple arrangement

The in-house fabricated thermocouples were placed in a box furnace while fixing a commercial K-type thermocouple adjacent to them as shown in Figure 7.18. The furnace was heated at a rate of 400 °C/hour up to 950 °C. Temperatures from the commercial thermocouple as well as from the in-house fabricated two thermocouples were recorded at 5-second intervals.

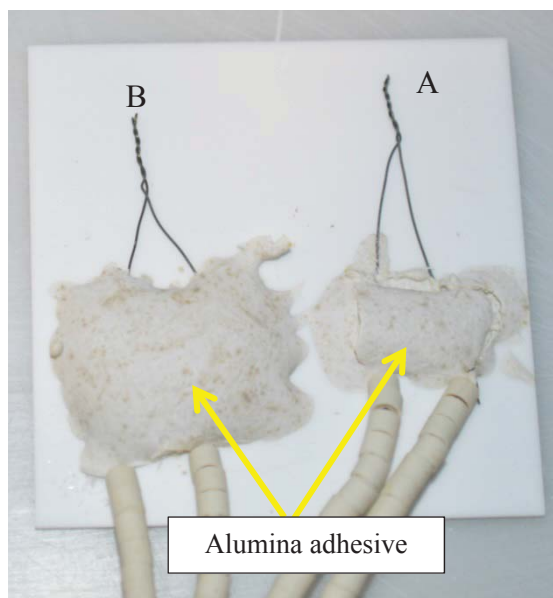


Figure 7.17 thermocouples with alumina protected connection points

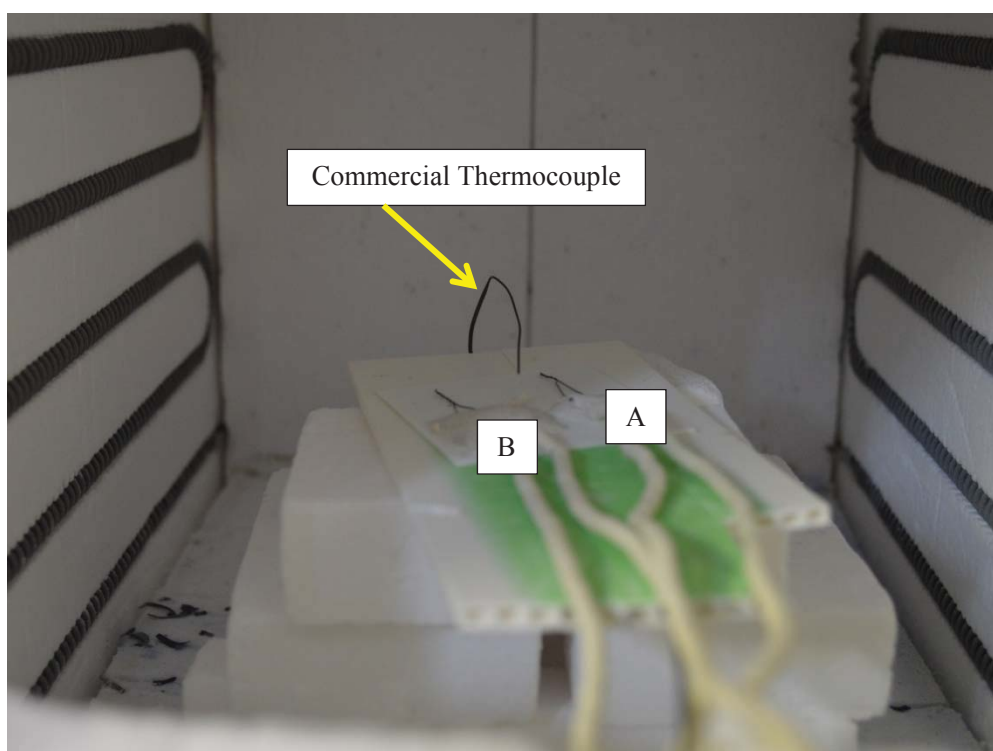


Figure 7.18 thermocouple setup in the box furnace

7.4.1 Results and Discussion

Figure 7.19 shows the temperature measured by the three thermocouples throughout the experiment. Neither of in-house fabricated thermocouples follows the same temperature profile that the commercial thermocouple produces. Twisted wire thermocouples have several touching points at their junctions because of twisting. Thus, the measured temperature should be an average of all the points. On the other hand, quality of a twisted junction is far inferior to that of a commercial thermocouple. Furthermore, in-house fabricated thermocouples were a lot closer to the ceramic substrate than the commercial thermocouple in the experimental setup. Thus, the temperature of the substrate may have influenced the temperature measurements from in-house fabricated thermocouples. A combination of all these facts sufficiently explains the measurement discrepancy between in-house made thermocouples and the commercial thermocouple.

The most important feature of the results is the diversion of thermocouple *B* during cooling below 450 °C (approx.). Thermocouple *A*, whose external wires were directly connected to thermoelements, followed the cooling pattern well, and it remained conductive even after the sensor set cooled down to room temperature. However, thermocouple *B*, whose external wire connections made through silver showed a complete electrical disconnection between the distal ends of its external wires. Post-experimental visual inspections on the connection point did not show any evidence to confirm that silver has escaped from the connection through the encased alumina layer. Therefore, the

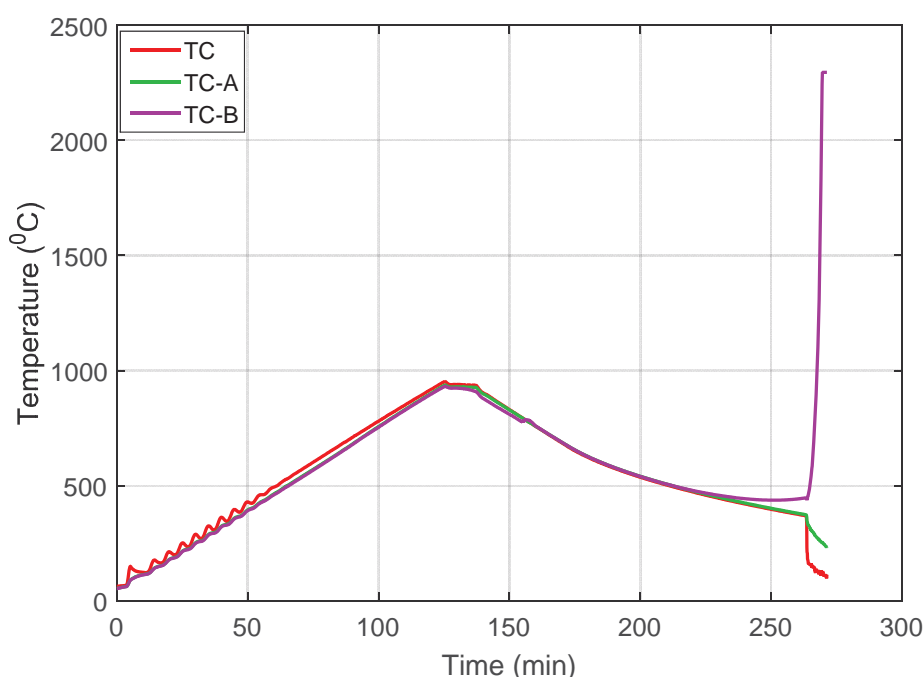


Figure 7.19 Temperature measurements
(TC – commercial thermocouple, TC-A: thermocouple A, TC-B: thermocouple B)

failure mode is well established as a failure of silver at the connection point. However, the design of the experiment did not facilitate any insight into exact failure mechanism.

7.4.2 Failure Mechanism Investigation

A further investigation was carried out with a purposely designed experiment to get an idea of the failure mechanism that caused silver to fail in maintaining electrical connection. Two thermocouples were made by twisting alumle and chromel wires together ($\varnothing 0.25$ mm). The external wires were connected in a manner similar to before: direct attachment to one thermocouple and through silver for the other as shown in Figure 7.20. However, unlike before, silver was not encased with ceramic; this was to aid visual inspection of the silver layer after heating cycles. The two thermocouples were attached to alumina substrate using alumina adhesive. There were some minor cracks on silver, as shown in Figure 7.21, after hardening silver and alumina at 150 °C for approximately 30 min. However, the electrical resistance across distal ends of external wires of the both thermocouples was approximately 20 Ω .

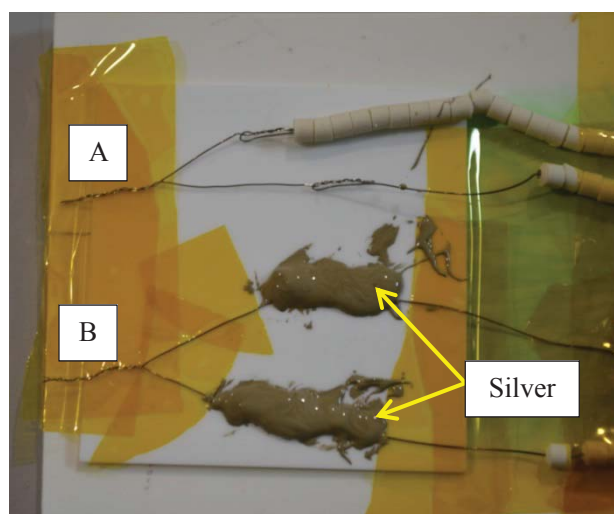


Figure 7.20 External wire connection to thermocouples

The sensor sample was placed in the same box furnace as before and heated at a rate of 400 °C/hour up to 950 °C while having fixed a commercial thermocouple adjacent to the sample. Temperatures from all three thermocouples were recorded at 5-second interval while real-time monitoring the temperature profiles on the computer screen. After thermocouple *B* had started showing clear diversion from the true temperature during cooling, at approximately 300 °C, data collection was stopped and allowed the furnace to cool down to room temperature. The experiment was restarted on the following day with the same furnace settings and with the same data recording intervals. The experiment was

stopped once the diversion of thermocouple *B* was apparent during cooling below approx. 450 °C.

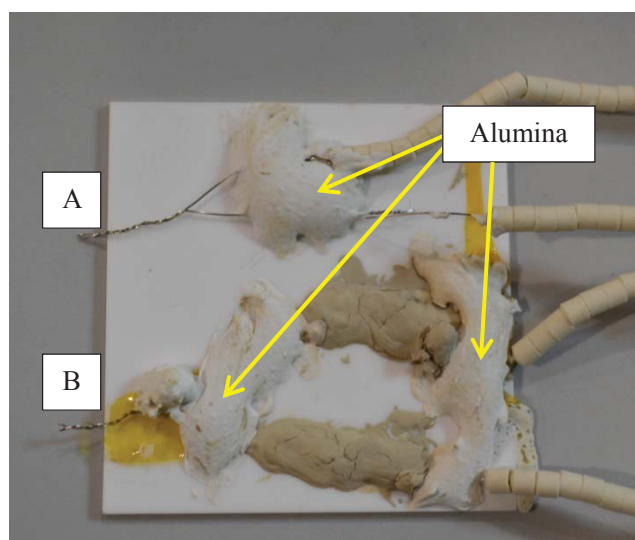


Figure 7.21 Thermocouples as alumina and silver hardened

7.4.2.1 Results and Discussion

Figure 7.22 shows the temperature recorded from the two in-house fabricated thermocouples (*A* and *B*) and the commercial thermocouple during the first part of the experiment. Thermal inertia may have continued to separate the measurements from the commercial thermocouple and the in-house fabricated thermocouples. In addition to thermal inertia, the measurement offset in the isothermal region suggests there might have been inherent measurement inaccuracies associated with in-house fabricated thermocouples and/or significant temperature gradients within the furnace. However, this does not obstruct the intended investigation. Thermocouple *B* starts diverting from the rest of the measurements around 450 °C during cooling. When the furnace was slightly re-heated at that moment when the initial diversion was monitored, it started agreeing with the true temperature above 450 °C. However, when the furnace cools down below 450 °C the diversion re-started, and the reading went further away from the rest two.

Figure 7.23 shows the temperature profile recorded in the second heating-cooling cycle. Thermocouple *B* appears to have electrically disconnected from the data logger during the initial part of the heating cycle. However, it rapidly regained its connectivity and continues to indicate true temperature when heating continues beyond approximately 450 °C. However, when the system cools down below the same threshold temperature,

thermocouple *B* starts diverting from the normal response. This is the same behaviour observed with dual-array thin-film multi-junction thermocouples. Therefore, it's re-confirmed that silver has caused the problem of electrical disconnection during cooling.

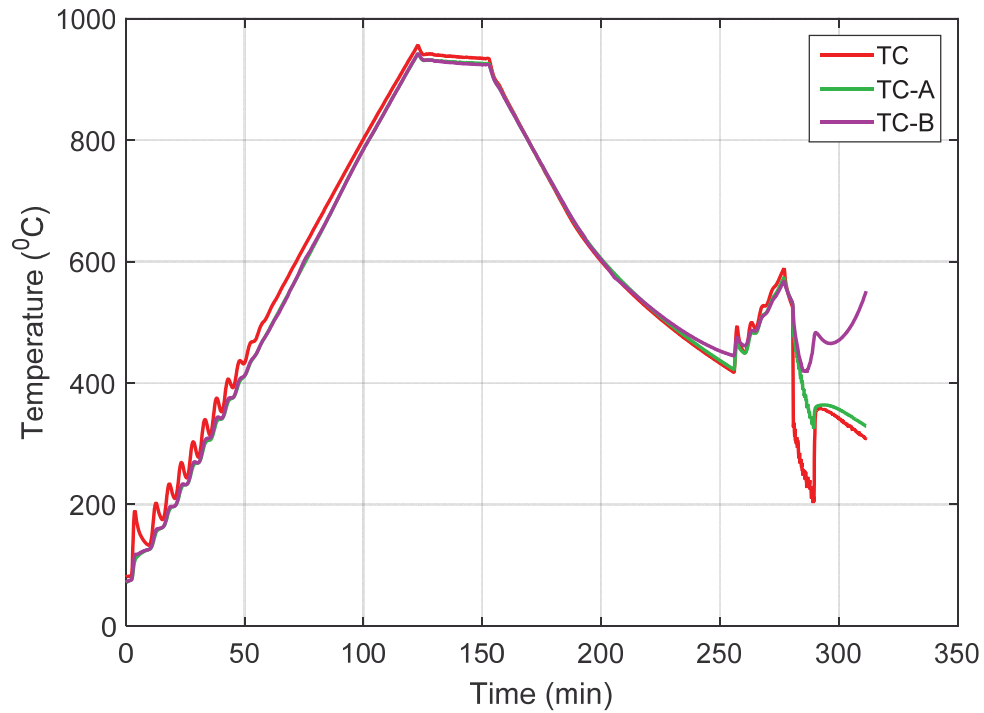


Figure 7.22 Temperature profile during first cycle

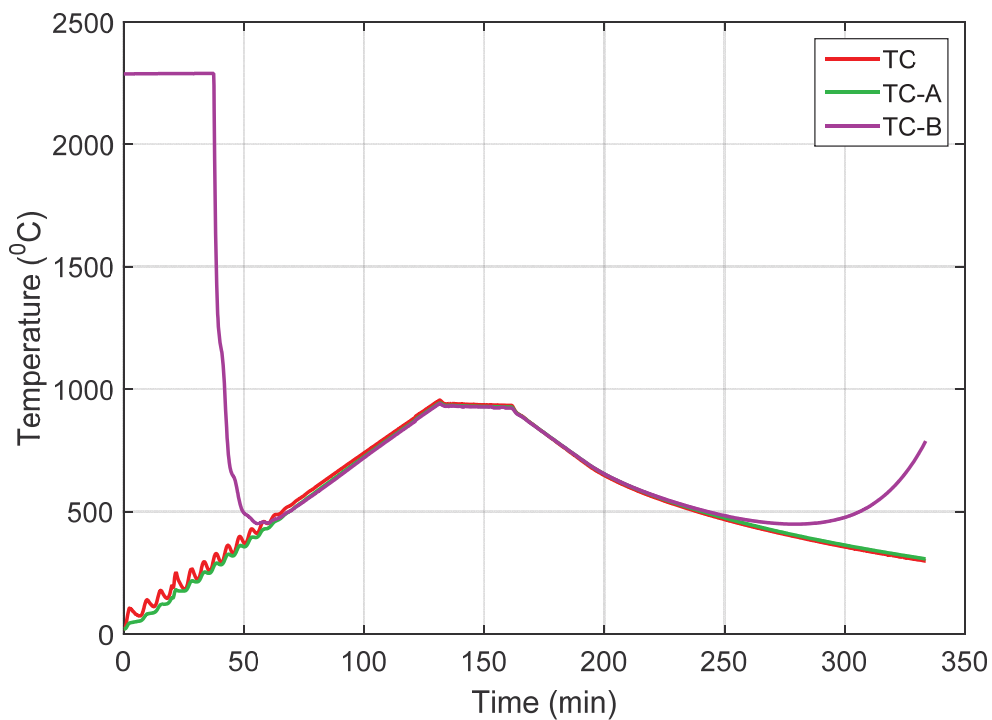


Figure 7.23 Temperature profile during second cycle

Resistance measurements made once the setup was cooled down to room temperature showed that the two external wires of thermocouple *B* were electrically disconnected from each other. It is evident in Figure 7.24(a) that the cause of the electrical disconnection as the formation of excessively large cracks on the silver layer making electrical connection discontinued. Comparison of Figure 7.24(a) and (b) reveals that the small cracks formed during curing of alumina have enlarged significantly during testing at elevated temperature. The threshold temperature, which the silver-assisted thermocouple diverted from normal operation, may be the temperature at which, thermal expansion of silver links scattered segments together re-building the electrical connection during heating.

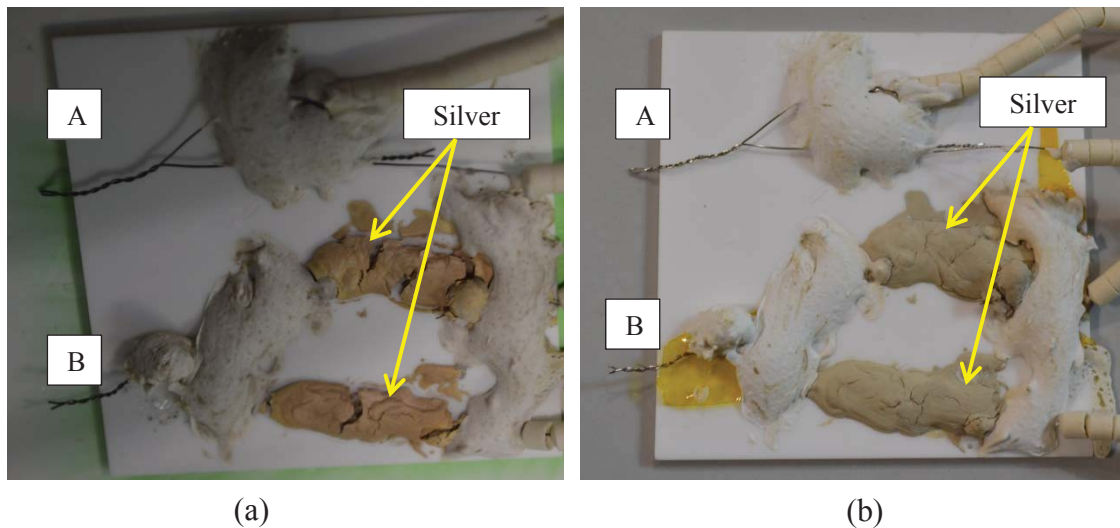


Figure 7.24 appearance of the silver (a) after experiment (b) before experiment

7.5 Application into SOFC Temperature Sensing: Case I

Cell integrated thin-film multi-junction thermocouples could survive on porous cathode throughout the entire operating temperature range of a typical SOFC though; the external wire connection was unsuccessful. Despite having the known problems at the connection, cell integrated sensors were employed to measure temperature distribution of an operating SOFC. However, this experiment was not aimed at learning cell temperature distribution instead; the objective was to learn to at what accuracy level the sensor can represent cell's temperature distribution.

A multi-junction thermocouple array having four sensing points was sputter deposited on the cathode of Ø52 mm SOFC test cell (KERAFO[®]L). The same fabrication process and substrate preparation process explained in Section 7.2 was adopted. The external wires were connected first with silver and then encasing the complete sensor pattern with alumina. The only exception to the array was the four chromel thermoelements were made shorter to get a larger surface area on the cathode available to place current collecting platinum mesh. The sensor attached cell is shown in Figure 7.25.

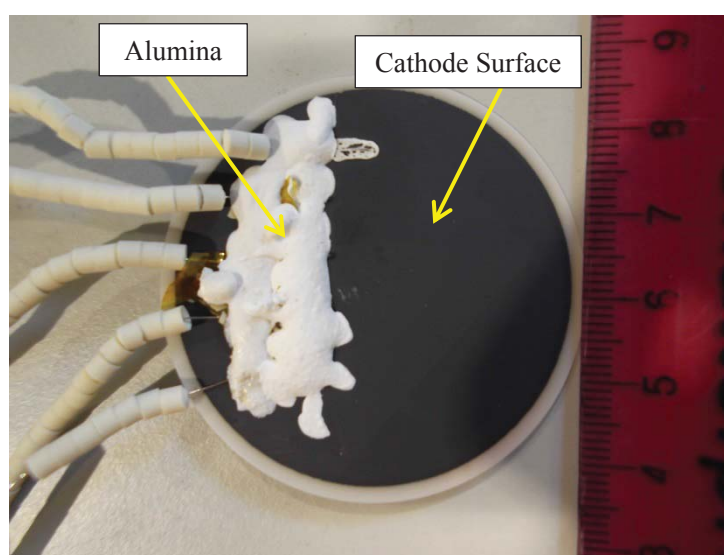


Figure 7.25 thermocouple array fabricated on cathode and covered with alumina

The sensor attached cell was fixed in the SOFC test rig as shown in Figure 7.26. A commercial thermocouple was also attached approximately 5-10 mm adjacent to the cathode to measure air temperature near the cathode surface. Nitrogen was provided to the anode chamber at a rate of 300 ml/min while the furnace temperature was between 480 °C and 800 °C. The temperature was recorded at 5 second intervals. Hydrogen was

introduced (at a rate of 15 ml/min) for a reduction process approximately 15 minutes after the cell has reached 800 °C. After allowing approximately 30 minutes for reduction process to take place, nitrogen supply was cut off, and hydrogen and air were provided in volumetric ratios given in Table 7.3. Furnace's set temperature was maintained at 800 °C during the cell operation. The open circuit voltage (OCV) and temperatures from the array as well as from the thermocouple were recorded at 5 second intervals.

Table 7.3 fuel and air flow rates

Region	Hydrogen flow rate (ml/min)	Air flow rate (ml/min)
A	0.5	0.5
B	1.0	0.5
C	0.25	0.5
D	0.5	0.5

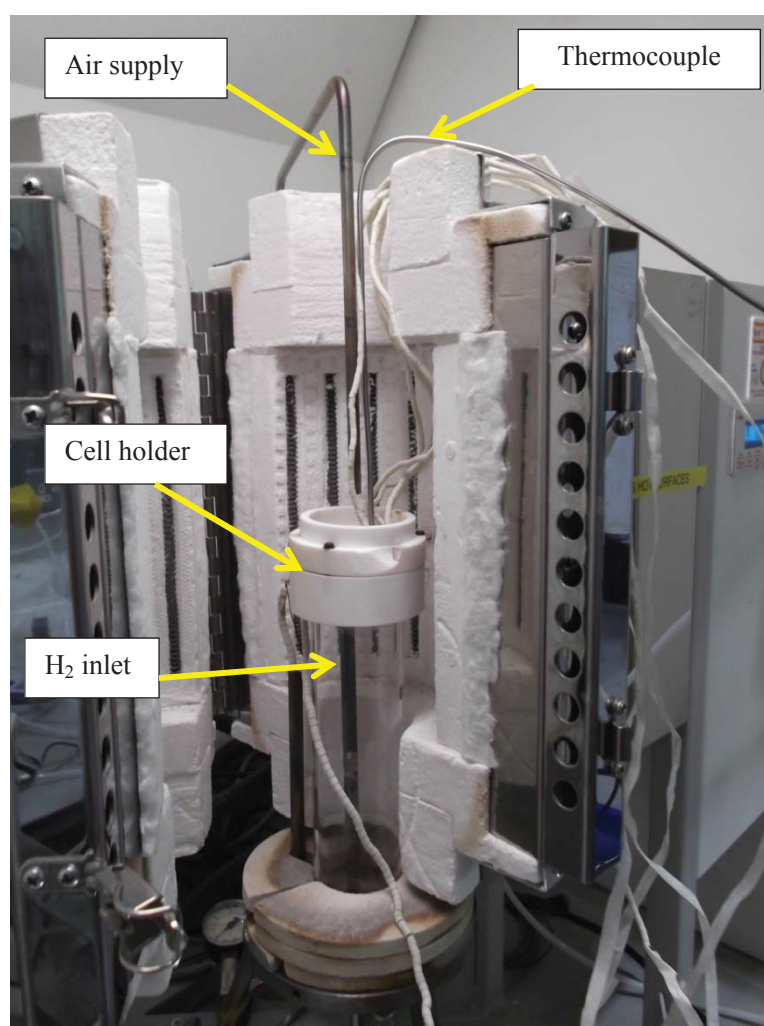


Figure 7.26 Test rig with sensor attached cell in place

7.5.1 Results and Discussion

Figure 7.27 shows the temperature distribution before and after hydrogen was introduced to the anode chamber for anode reduction. An abrupt temperature drop on the cell can be noticed immediately after hydrogen was introduced around the 15th minute. The cell temperature recovers approximately 4 minutes after though a temperature gradient between sensing points continued. Noticeably, the air chamber temperature measured from commercial thermocouple (denoted by *TC*) remains approximately 30 °C higher than the cell temperature recorded from thin-film multi-junction thermocouple array (*S1–S4*). Since thin-wire multi-junction thermocouples did not measure this kind of temperature changes during the reduction process (discussed in chapter 6) and the thin-wire thermocouples were proven to be accurate, these temperature gradients are likely to be caused by some errors. Sources of such errors need to be further investigated.

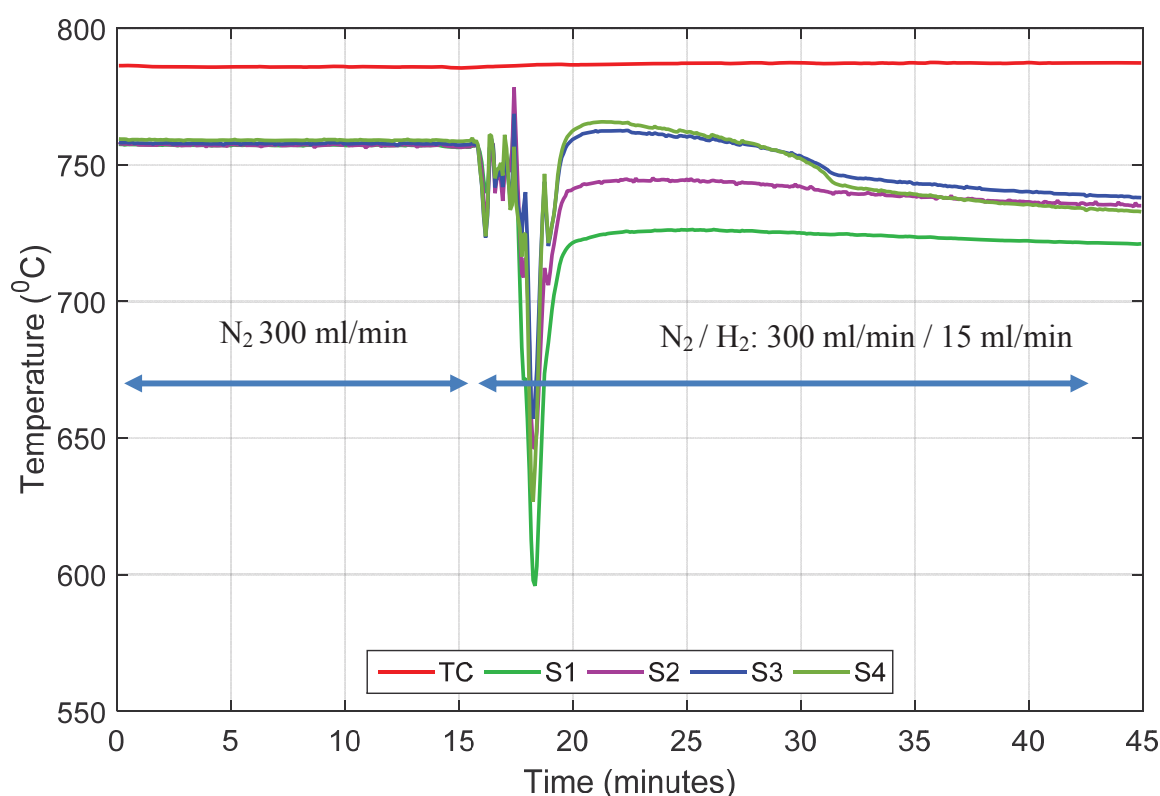


Figure 7.27 Temperature distribution during anode reduction

Figure 7.28 shows how the temperature and OCV distribution under different flow conditions given in Table 7.3. A positive correlation between OCV and the cell temperature can be observed though it is not very consistent throughout. The correlation between average cell temperature (average of four measurements) and the OCV can be clearly seen from Figure 7.29. This behaving has already been discussed in Chapter 6 as a

combined effect of OCV increase with flow rate and gas leakages in the test rig. The thermocouple in air chamber was almost non-responsive to temperature changes on the cell. The cold air supplied to cathode chamber may have brought in a chilling effect as discussed in Chapter 6. The temperature gradient between sensing points of the array is measured to be over 200 °C. Realistically; there is no possibility for such a large temperature gradient to exist across the sensing points, as such gradient should fail the cell by causing cracks on them, due to thermal stress development. Therefore, although thin-film sensors could detect spatial temperature variations on the cell, their magnitudes are not very reliable. Importantly, like the multi-junction thermocouples made from wires, thin-film sensors measure temperature independently from each sensing points despite being fabricated on a conductive cathode. Thus, the concept of cell integration confirmed possible though it needs a significant level of further research to ensure the reliability of measurements, and the durability of sensors.

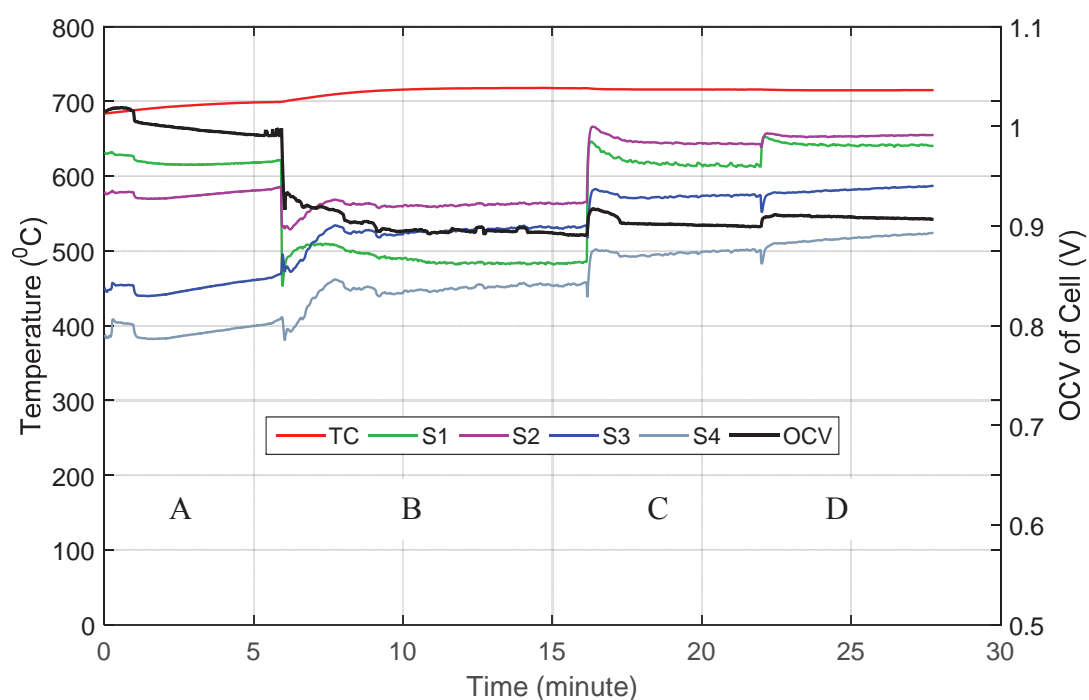


Figure 7.28 Temperature and OCV during cell operation
(TC: commercial thermocouple, S1-S4: four sensing points, OCV – Cell's OCV)

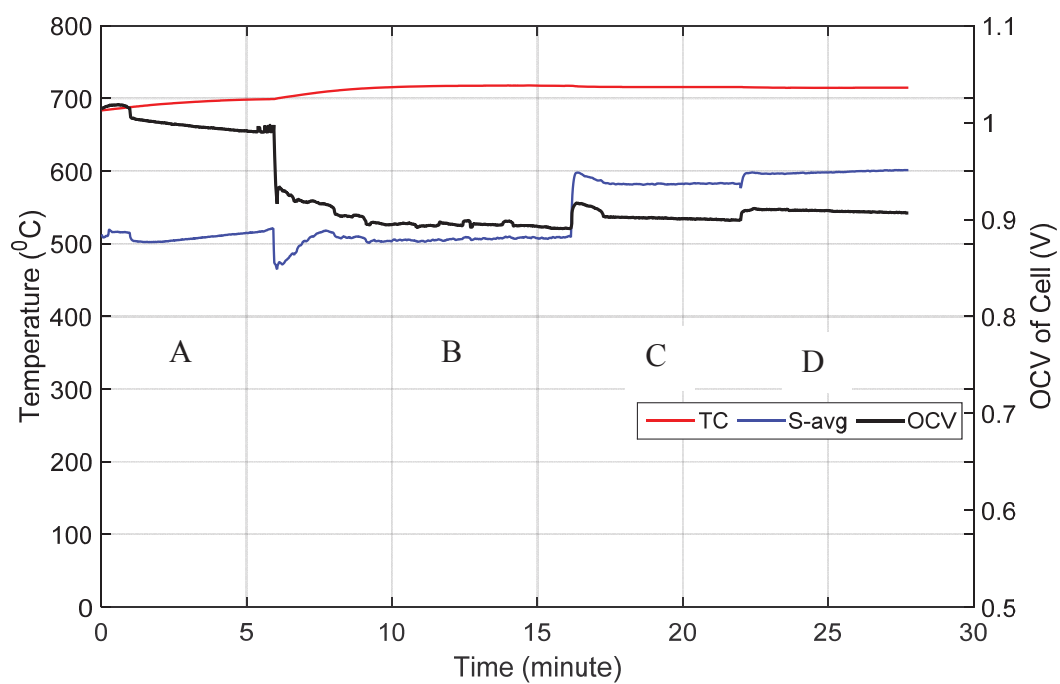


Figure 7.29 Correlation between average cell temperature and OCV

7.6 Application into SOFC Temperature Sensing: Case II

The previous attempt at using thin-film sensors for SOFC temperature sensing did not deliver any reliable temperature measurements. Although failures were too complicated in nature to make a simple root-cause analysis, the prior experience with connection failures provided sufficient reasons to speculate any abnormal behaviour at the external wire connection points. Therefore, the study was repeated making changes, mainly to, the connection. The general purpose silver paste used before was replaced with a purposely developed silver paste with an inorganic binding agent for sensor applications (Aremco-bond 597). Further, the connection points were left open to the atmosphere without covering them with alumina. This was to eliminate any effects from the thermal stresses generated by alumina on silver. Further, thin-films were also left open to the atmosphere without covering them by alumina to see if they can survive. Although above changes were not scientifically supported, those speculation-driven changes were made to discover a way that would work.

A multi-junction thermocouple array having four sensing points hence, five thermoelements, was sputter deposited on the cathode of 5 cm × 5 cm commercial SOFC (NextCell-5) using Quorum QT 150TS sputter coater. The SOFC test cell is similar to the ones used for experiments described in Chapter 6. Sputter current of 140 mA and deposition rate of between 12 -15 nm/min were employed to obtain a film thickness of approximately 500 nm. The film thickness was not measured but, prior experience with similar deposition parameters produced films with approximately 500 nm with the same material. Higher thickness was chosen differently to previous depositions because the film was not protected by alumina. Thus, thicker films were expected not penetrate their oxide layer into the film (another assumption made). Before the deposition, the cathode was prepared by first cleaning with acetone and then with deionised water followed by drying in a furnace at 150 °C for 10 minutes to remove any dirt or grease that may disturb the proper film adhesion to the cathode. The alumel thermoelements were deposited prior to the chromel thermoelement. The pattern was obtained by using two stainless steel masks of thickness 0.075 mm: one for alumel thermoelements and the other for chromel thermoelement. To prevent stainless steel masks being lifted due to the magnetic field inside the sputter chamber, the masks were forced onto the cathode by means of two thin wood strips (spatula). The width of each thermoelement is approximately 0.2 mm. Each open end of a thermoelement has 3 mm × 3 mm connection pad to facilitate external wire connection. External wires (Ø 0.25 mm) of the same material as the thermoelements were

connected to thin-film thermoelements at the connection pads. The edge of all the wires, which were in touch with the connection pads, was gold plated using sputter deposition to prevent possible oxidation of the connection interface at high temperature. Approximately half the perimeter of the wire was expected to have a gold layer as they were fixed horizontally during sputter deposition. Silver paste (Aremco-bond 597) was applied to the connection points, as shown in Figure 7.30(a), to increase the electrical connectivity between the film and the wire. The electrolyte supported test cell used for the experiment is shown in Figure 7.30(b) having its cathode facing up. The wires were sent through ceramic beads to prevent short circuiting during handling. The wire connected cell was placed in a furnace for 2 hours at 90 °C for silver solidification. Since silver does not provide sufficient mechanical strength to hold the wires in place during handling, two thin strips of alumina sheets were glued to the cell using alumina adhesive to hold the wires in place. This arrangement is different to previous arrangement where the connection pads were fully covered with alumina along with thin-films. Thin films and the connection pads were purposely made free from alumina to eliminate any influence from alumina on the performance of the sensor array. Curing alumina for 2 hours in the furnace at 100 °C made strong alumina bond firmly holding the wires in place and giving enough freedom to handle the wires.

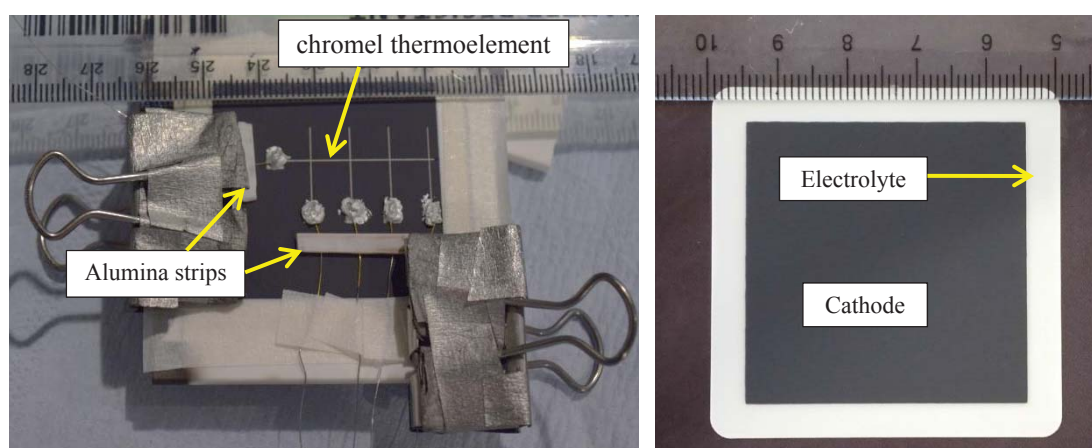


Figure 7.30 Wire connected cell (a) connecting external wires to the cell (b) the SOFC test cell (NextCell-5) with the cathode facing up before connecting wires

The thin-film thermocouple array integrated cell was fixed to the SOFC test rig as shown in Figure 7.31. *S1* to *S4* are the four sensing points of the array. The cell was placed between two gaskets to prevent any gas leakages through the interface between the cell and the ceramic cell holder. The current collector meshes made of nickel and platinum were attached to the anode and the cathode, respectively using the same silver paste. Two commercial thermocouples (K-type) were also fixed in adjacency to the cathode for comparison purposes. The tip of one thermocouple was at *S1*, approximately 2 mm above the cathode, while the other's tip was between *S1* and *S2* sensing points having its tip approximately 5 mm above the cathode. Based on this arrangement, the fuel supply pipe was approximately underneath *S2* sensing point. Oxygen for cathodic reactions was taken from the ambient air inside the furnace. No external air supply was employed to prevent excessive cooling as gas pre-heating was not employed.

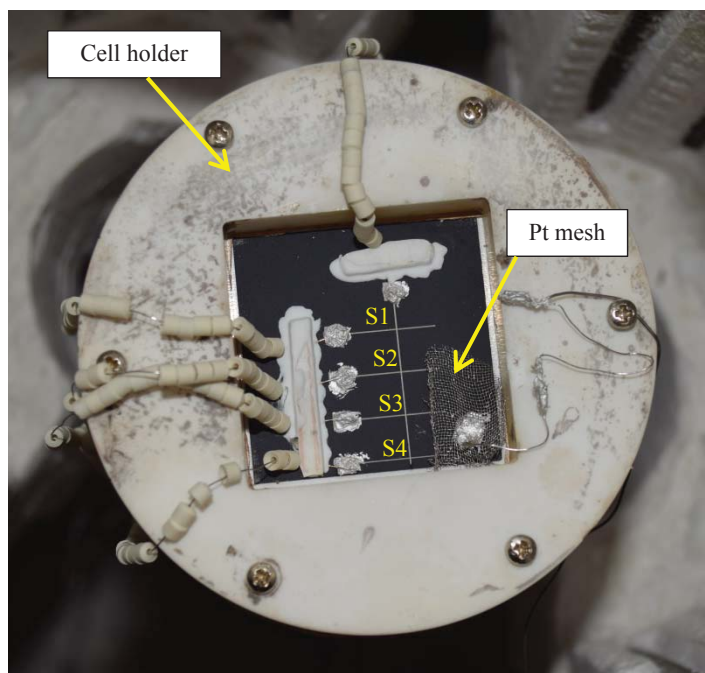


Figure 7.31 The cell fixed to the cathode with sensing locations shown

The furnace was heated at 500 °C per hour up to 750 °C. Nitrogen was supplied to the anode chamber at a rate of 300 ml/min since the beginning of the heating process to expel air inside the anode chamber to facilitate anode reduction. Hydrogen was introduced at a volumetric rate of 15 ml/min from approximately 650 °C to start the reduction process and continued to supply for approximately 30 min (at 750 °C cell temperature) for the anode reduction to complete.

After the reduction process, a mixture of hydrogen and nitrogen, having the total volumetric flow rate of 250 ml/min, was supplied at varying volumetric compositions as listed in Table 7.4. The hydrogen flow rate was controlled via BronkhorstTM FlowView software while; the nitrogen flow was manually controlled. Because of the manual control of nitrogen, it took nearly 30 seconds to settle the flow rate at 250 ml/min at each flow change. The flow rates were cycled to assess the repeatability of measurements to enhance the reliability. The testing duration at each flow rate was set to approximately 10 min to enable the cell to stabilise its temperature and OCV. The furnace temperature was maintained at 750 °C with an accuracy of ± 1 °C. After experiment, the cell was brought back to room temperature under natural cooling. Nitrogen was continued to supply at a constant rate of 250 ml/min throughout the cell cooling to prevent anode re-oxidation.

Table 7.4 Volumetric flow rates

Flow Region	Flow rates (ml /min) H ₂ / N ₂	Time (min) (Approx.)
A	100 / 150	10
B	150 / 100	10
C	200 / 50	10
D	250 / 0	10
E	200 / 50	10
F	150 / 100	10
G	100 / 150	10

7.6.1 Results & Discussion

Since the film thickness and junction size were larger than the critical dimensions for K-type thermocouples, discussed in Section 7.1, the performance of thin-film multi-junction thermocouple array can be considered independent of its size. Unlike in the previous experiment, the array continued to measure temperature even after it cooled down near to room temperature. Thus, the new silver paste is likely to have contributed to making successful connections between thin-films and the external wires. The effects of gold plating the wires at its connection area could not be distinguished from the results. However, the new connection methodology has worked well bringing the cell down to room temperature and not generating any errors as observed in the experiments presented previously in this chapter.

Figure 7.32 shows the temperature measured by the thin-film multi-junction thermocouple array and the two commercial thermocouples under varying fuel compositions. Regions marked by letters from *A* to *G* are the flow configurations given in Table 7.4. The temperature measured by two thermocouples (RS – Pro), which has faceplate accuracy of $\pm 0.004T$, recorded approximately 10 °C lower temperature than the furnace's set temperature. This is different to what observed in the previous experiment, presented in Section 6.3 (of Chapter 6), where the temperature recorded by the thermocouple kept approximately 7 mm above the cathode was higher than the furnace's set temperature. Although no exact reason for this lower temperature could be identified, the presence of a temperature gradient between *TC1* and *TC2* themselves suggests there had been a temperature gradient within the furnace. The cell temperature continued to stay below the furnace temperature. This was explained in Chapter 6 as due to overall cell cooling imposed by cold anodic gases. The sensing point *S2*, which was the closest sensing point to the gas supply (almost right above it), shows the lowest cell temperature throughout the experiment. *S4*, which was located furthest away from the gas inlet, showed the highest overall cell temperature throughout the experiment. Since *S4* is furthest away from the gas inlet, the cooling effect near *S4* should be lower due to low cooling resulted by uneven gas distribution at the anode surface. Since the cell was not active, no net heat generation could have taken place on the cell due to electrochemical reactions. Thus, cooling effect predominantly determines the cell temperature distribution. However, although *S1* and *S3* are on the either side of *S2* having equal distances from *S2*, it is impossible to make any comment on the cooling effect at those locations without

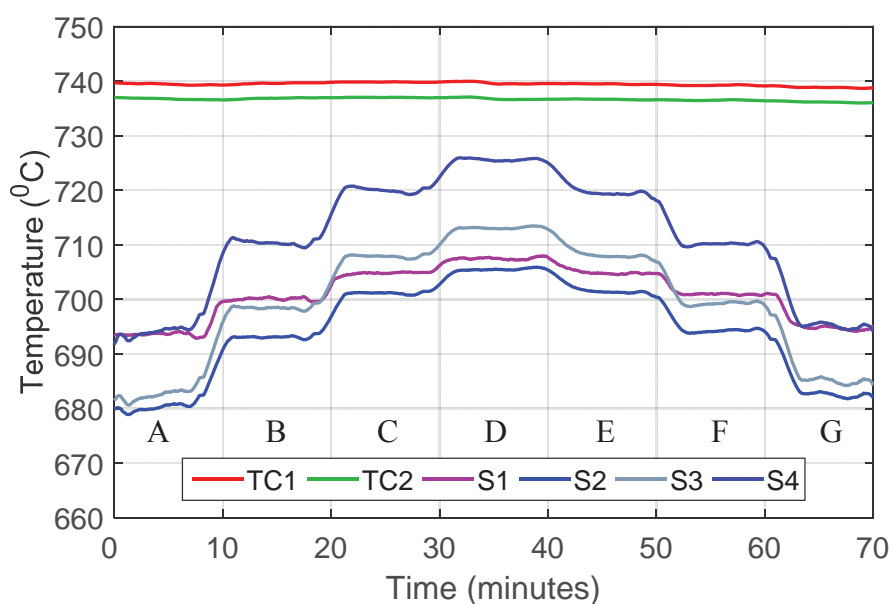


Figure 7.32 Temperature response to varying flow rates

having comprehensively investigated the flow pattern across the cell; such a study was not conducted. More importantly, the two thermocouples have, once again, failed to follow the dramatic temperature changes taken place in the cell, which the thin-film array could detect.

Figure 7.32 further shows that the overall cell temperature has maintained a positive correlation with the hydrogen composition of the fuel: the higher the hydrogen composition, the higher the cell temperature. This correlation repeated as the volumetric composition was cycled confirming the verity of the observed correlation. A similar correlation between cell temperature and OCV was confirmed to have resulted by gas leakages (see Chapter 6). Although the gasket could prevent leakages that took through the cell and the cell holder, the test rig was diagnosed to have some significant leakage through a hole used to pass the anode current collector wire into the anode chamber (this was later solved by properly covering it with alumina).

The average OCV under each flow composition was plotted against the volumetric hydrogen composition as shown in Figure 7.33. This behaviour is well-explained by the Nernst effect. As the composition of hydrogen increases, the partial pressure of hydrogen increases thus; the OCV also increases due to Nernst effect. However, since the cell temperature also increased with the flow rate, this led to a positive correlation between OCV and the cell temperature. This relationship was explained as a bogus relationship in Chapter 6. However, to re-confirm the OCV temperature relationship, OCV was recorded by varying the furnace temperature (from 700 °C to 800 °C with 25 °C increments) while having set the volumetric compositions of hydrogen and nitrogen at 200 ml/min and 50

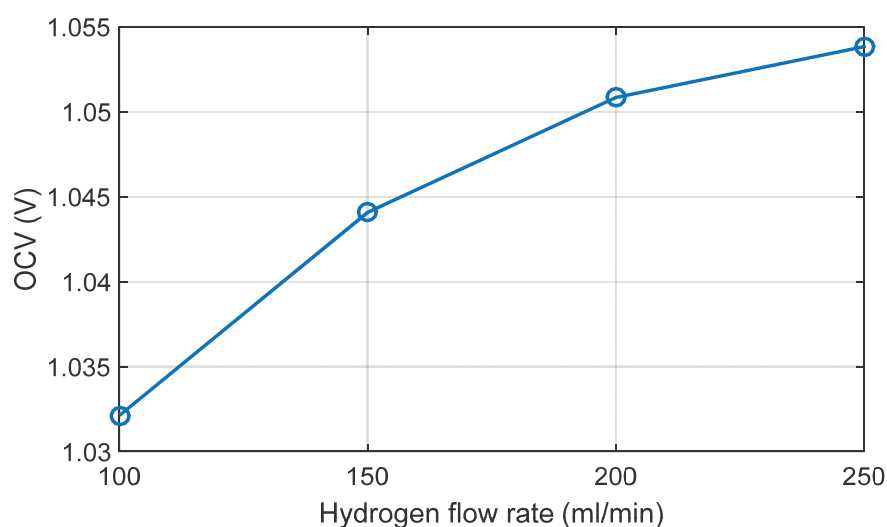


Figure 7.33 Change of OCV with hydrogen composition

ml/min, respectively. The OCV was plotted against the mean cell temperature (calculated from the array's measurements) as shown in Figure 7.34. This shows that the increase of cell temperature has decreased the OCV. This negative correlation between OCV and cell temperature agrees with the Nernst relationship where, increasing operating temperature decreases the Gibbs free energy, thus; the OCV decreases with the increase of temperature.

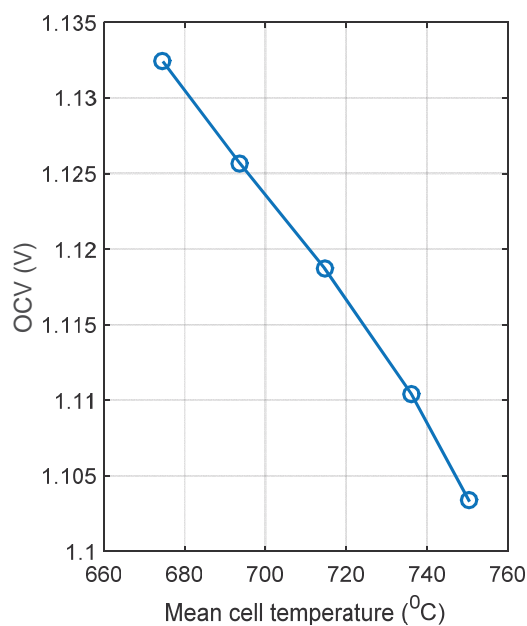


Figure 7.34 Change of OCV with cell temperature

7.7 Conclusions

Thin-film multi-junction thermocouple arrays were directly fabricated on the cathodes of commercial SOFC test cells using sputter deposition. External wires to collect the signals from the sensor were used from the same material as the individual thermoelements. Use of silver as an electrical connection agent to connect external wires onto thin films failed in initial attempts making the sensor unable to measure temperature during cooling down thus; measurements were not repeatable below a certain threshold temperature (approximately 500 °C). However, an inorganic solvent based silver paste along with gold plated wires could adequately (in electrical perspective) improve the connection enabling the sensor to function during both heating as well as in cooling down to room temperature.

The first application of the thin-film array into SOFC temperature sensing could not reveal much meaningful temperature distribution at cell level. However, the second application with modified connection mechanism could reveal the presence of notably high temperature gradients across the cell under different flow configurations. The commercial thermocouples placed approximately 5 mm adjacency to the cathode were completely non-responsive to temperature variations on the cell. This confirms the importance of cell surface temperature measurements compared to the near-cell temperature sensing. Flow composition dependent cell temperature variations, led by gas leakages through the cell holder, were observed. Although gaskets could satisfactorily eliminate gas leakage through the cell support, leakage through other holes leaked hydrogen into cathode chamber directly burning hydrogen inside the furnace.

A positive correlation between OCV and hydrogen composition could be observed agreeing to Nernst effect. Further, the increase of cell temperature observed to cause a decrease in the OCV as expected due to low Gibbs free energy at higher temperatures.

Application of cell integrated thermocouple array into SOFC temperature sensing showed similar temperature variations, which were observed by thin-wire thermocouple grid placed on the cathode, under similar operating conditions. However, unlike thin-wire sensors put on the cathode, direct deposition of thin-films cover active reaction sites. Thus, thin-wire sensors may be applied in application where space permits insertion of thin wires between cells. When there is no sufficient space, thin-film sensors may be used. However, a less bulky connection mechanism is required to fully utilise the size advantage of thin-film sensors.

7.8 References

- [1] Kreider, K.G. and Gillen, G., High temperature materials for thin-film thermocouples on silicon wafers, *Thin Solid Films*, 2000, 376(1-2), pp. 32
- [2] Cattani, M., Salvadori, M.C., Vaz, A.R, Teixeira, F.S, and Brown, I.G., Thermoelectric power in very thin film thermocouples: Quantum size effects, *Journal of Applied Physics*, 2006, 100(11), pp. 114905- 114905-4
- [3] Yanga, L., Zhao, Y., Feng, C., and Zhou, H., The influence of size effect on sensitivity of Cu/CuNi thin-film thermocouples, *Physics Procedia*, 2011, 22, pp. 95
- [4] Liu, H., Sun, W., Chen, Q, and Xu, S., Thin-Film Thermocouple Array for Time-Resolved Local Temperature Mapping. *IEEE Electron Device Letters*, 2011, 32(11), pp.1606-1608.
- [5] Chopra, K.L, Bahl, S.K, and Randlett, M.R., Thermopower in thin-film copper-constantan couples, *Journal of Applied Physics*, 1986, 39(3), pp.1525
- [6] Zhang, X., Choi, H., Datta, A., and Li, X., Design, fabrication and characterization of metal embedded thin film thermocouples with various film thicknesses and junction sizes, *Journal of Micromechanics and Microengineering*, 2006, 16, pp. 900
- [7] Davis, J.R., Heat resistant materials, USA, ASM International, 1997, pp. 77
- [8] Sigma-Aldrich, *Silver Conductive paste properties* [online], [viewed 10/06/2015]. Available from:
<http://www.sigmaaldrich.com/catalog/product/aldrich/735825?lang=en®ion=GB>
- [9] Kriukience, R. and Tamulevicius, S., High temperature oxidation of thin Chromel-Alumel thermocouples, *Materials Science*, 2004, 16 (2), pp. 136
- [10] Wunderlich, W., Shinohara, Y., and Matsumura, Y. Magnetron sputtering of (TiZr)NiSn thin films on different substrates for thermoelectric applications, *Journal of Physics: Conference Series*, 2012, 379, pp.01
- [11] National Instruments, *Operating instructions and specifications NI9213* [online], [viewed 15/06/2015]. Available from: <http://www.ni.com/pdf/manuals/374916a.pdf>

Chapter 8 : Conclusions and Future Works

Since each chapter contains a conclusion of its own, this chapter focuses on drawing the overall conclusion of the research with respect to its aim and objectives. Limitations of the research methodology, possible complications of the results and recommendations for further research are also provided.

8.1 Conclusions

This research focused on exploring the cell level temperature distribution of operating SOFC via attempting to develop a better (concerning the spatial resolution and cell-level temperature measurability) temperature sensing methodology than what currently in practice. The difficulty or inability in measuring the cell-level temperature distribution and the inadequacy of spatial resolution of measurements were identified as the primary weaknesses in the present attempts as discussed in Chapter 3. The following sections draw together the core findings of this research to demonstrate how the aim is accomplished through the progressive achievement of individual objectives. Possible implications of the results and further research needed to bring forward the works of this research are also provided.

Chapter 2 presented the state of the art SOFC technology and its fundamental sciences I operation. The primary heat sources and sinks of SOFC are discussed. Effect of temperature and temperature distribution on the performance and durability of SOFC are discussed.

In Chapter 3, the currently available methods to measure the temperature of operating SOFCs are reviewed, and the necessity to use contact thermometry for SOFC temperature sensing has been adequately explained. From among different contact thermometry types, resistance temperature detector (RTD), thermocouple, and thermistor were initially identified as the candidate technologies. After carefully investigating the strengths and weaknesses of each of the three thermometry types, the thermocouple thermometry was recognised as the best-suited thermometry for this research. Enhancing the spatial resolution of measurement with thermocouple thermometry was identified as the critical technological barrier to effectively measure the cell surface temperature from SOFC with sufficiently higher spatial resolution.

To overcome the problems associated with thermocouple thermometry in enhancing the spatial resolution of measurements in multi-point temperature sensing, the author proposes to use multi-junction thermocouples to measure temperature with a reduced number of thermoelements. The concept is scientifically built on the law of intermediate conductors on thermocouples. Based on the concept of sharing thermoelements between sensing points, two multi-junction architectures are proposed namely, the array and the grid. The array is the fundamental building block of multi-junction thermocouples while; the grid is a derivative having better spatial resolution and better reduction in the number of thermoelements required. The junction forming process was speculated to alter the

homogeneity of thermoelements at junctions and consequently, to introduce measurement errors. The potential influences of such flaws on the measurement accuracy were numerically assessed and the results were qualitatively analysed. If the junction forming process does not significantly alter the Seebeck coefficient of thermoelements or, if the temperature gradient across a junction is negligibly small, then the errors in measurements were found to be negligible. Above investigation is presented and discussed in Chapter 4.

The experimental investigation of the practical plausibility of the proposed architectures was assessed and presented in Chapter 5. It has been demonstrated that the multi-junction thermocouples made by spot-welding of 0.5 mm diameter alumel and chromel wires are free from the above speculated performance anomalies. However, inconsistencies in accuracy between sensing points of the same thermocouple array were observed. Performances were validated with calibrated standard thermocouples. The observed discrepancy in accuracy among different junctions identified to be related to the fabrication method: Spot-welding. The ability of multi-junction architectures in measuring distinct temperature from its various sensing points without a thermoelectric interference from adjacent sensing points was experimentally validated. The grid architecture was selected over the array architecture to progress with the research as thin-wire sensors. The feasibility of a multi-junction grid in detecting surface temperature was also experimentally investigated. Although the grid architecture was used as a thin-wire sensor, the array was also used as a thin-film sensor, fabricated integral to an SOFC, to measure the cell temperature distribution, as presented in Chapter 7.

When employed into SOFC temperature sensing, the grid architecture could successfully measure the cell surface temperature distribution of an operating SOFC under different operating conditions; the methodology is presented and results are discussed in Chapter 6. The grid's measurements adequately complied with the temperature measured by the commercial thermocouples. The cell surface temperature distribution measured from the grid led a system level fault diagnosis to identify a significant gas leakage in the test rig. The significance of the surface temperature measurements against the near-surface temperature measurements is qualitatively analysed. A near-surface temperature measurement made at a distance approximately 7 mm from the cell surface was almost non-responsive to dramatic temperature fluctuations on the cell surface. Polarisation curves under different operating conditions were obtained along with the cell temperature. A positive correlation between the cell temperature and

the current was observed. Concentration polarisation was also appeared to increase the cell temperature. The OCV and the cell temperature were measured at different running temperatures. The results revealed a decrease of OCV with the growth of temperature while an increase of the actual cell voltage with the increase of temperature. Thus, a reduction in the ohmic polarisation with the increase of cell temperature was confirmed.

A further advancement of the proposed methodology was attempted by fabricating a thin-film multi-junction thermocouple array onto the cathode of an SOFC. A sputter deposited sensor could measure the cell surface temperature distribution of an SOFC under different flow rates. These results are discussed in Chapter 7.

Findings of this research have successfully achieved the stated objectives though there still have limitations and possible implications as discussed later in this chapter. Chapter 3 have achieved the objectives 1 and 2, respectively. Chapter 4 and Chapter 5 have collectively achieved the third objective. Chapter 6 has simultaneously achieved objectives 4 and 5. Finally, the progressive achievement of all the objectives has facilitated the successful accomplishment of the research aim.

The impacts and the contributions of the findings towards the advancement in the SOFC knowledge domain are multifaceted in nature. Chapters 4 and 5 have introduced new temperature sensing methodology for SOFC temperature sensing. This method may be used in different other fields as well, possibly, after further research as discussed later in this chapter. Chapters 6 and 7 have brought new insight into the SOFC performance concerning the cell temperature. While already known correlations between OCV and operating cell voltage with operating temperature reconfirmed, a clear positive correlation between current and cell temperature could be observed. A potential way to identify concentration polarisation in running cells, thus; fuel starvation, in terms of cell temperature was evolved. The cell surface temperature distribution of a number of cells/stack architectures under a number of different operating conditions can be used assess the performance and temperature related degradations of such architectures. Further, the cell surface temperature distribution measurements made using the proposed sensing technology can be used for the development of new materials, testing of different fuel types and internal reforming, new stack architectures, testing different operating parameters, different reactant flow configurations, etc. On the other hand, the already developed computational models may be validated with the experimental temperature

measurements. Thus, the findings of this research as well as its methodology have made a potentially notable impact to advance the knowledge and technology of SOFC.

8.2 Limitations and Implications

The research methodology is associated with some limitations. Though they do not curtail delivering the aforementioned impacts, they still require some careful further investigations. The primary limitation is associated with the choice of materials for thermoelements. The K-type materials are not suitable for prolonged application within an SOFC's operating environment as discussed in Chapter 5. Thus, the suitability of alternative materials, such as platinum-based materials, should be investigated as thermoelements when this technology is applied for prolonged operation within operating SOFCs. The second limitation is linked with the fabrication technique. The spot-welding process could not produce identically performing junctions. Consequently, the accuracy of measurements was not consistent across different junctions (Chapter 5 discusses this effect). Further, thermoelements thinner than $\Phi 0.5$ mm could not be used because of weakening of the welded junctions. Since thinner thermoelements demonstrate better temperature response than their thicker counterparts, the thermal response was constrained. Although, fundamentally, spot-welding is capable enough to fabricate multi-junction thermocouples; a spot-welder with better control over welding parameters is necessary.

The temperature measurements from the operating SOFCs presented in Chapters 6 and 7 are likely to have implications due to the operational characteristics of the test rig. Especially, the reactants were not pre-heated. Thus, the cell operation may be impaired and consequently, the measured temperature distribution likely to be different to that with pre-heating employed.

Heat transfer along thermoelements in multi-junction thermocouples can potentially introduce measurement errors though no such were observed in the SOFC experiments carried out. However, different cells sizes and different temperature gradients across cells may lead to such errors. These errors are more prone with the grid architecture as it has a greater number of heat transfer paths than the array. If such errors come into notice with the grid, then, the array architecture may be attempted. If the errors still appear, advanced data logging systems will be needed to filter out such errors as proposed in the following section.

8.3 Recommendations for Future Research

Since the proposed multi-junction thermocouples share thermoelements between sensing points, heat can flow from one sensing point to the other. Therefore, the temperature at particular sensing points may increase without any actual temperature increase of the SOFC or any other object whose temperature being measured. This problem depends on the heat transfer characteristics of thermoelements and the temperature gradient across sensing points. Therefore, a comprehensive heat transfer analysis of the multi-junction thermocouples should be carried out, and the effects of heat transfer on measurement accuracy need to be investigated under all possible conditions within an SOFC. Once the consequences of heat transfer on measurement accuracy are quantified for different operating conditions, various thermoelement materials, and different multi-junction architectures; a data logging system needs to be developed to offset errors caused by heat transfer. Depending on the results of the heat transfer analysis, the task the data logging system has to do to eliminate measurement errors may be complicated in nature. Thus, the author considers the use of artificial intelligence methodologies, particularly multi-agent systems, would be a better approach because of the complexity of the problem. Nonetheless, if slight measurement errors can be tolerated or if the operating conditions are somewhat similar to what being used throughout this thesis, this methodology may be used without requiring aforementioned advanced data logging systems.

Another concept being investigated is the use of the thermocouple grid as a current collector. In which, the thermocouple grid will simultaneously measure temperature and collect current from the cell. Preliminary investigations have been completed with promising results, and further studies are being progressed.

Cell integration of the proposed sensor architecture requires extensive research and developments mainly in two directions. Firstly, the fabrication technique and appropriate thermoelement dimensions that enable safe operation within the harsh environment inside an SOFC should be investigated. An appropriate method to shield the thermoelements may also be incorporated into the same research. The second direction is the development of an efficient external wire connection mechanism that can be implemented in commercial SOFC stacks.

After these advancing steps are successfully carried out, multi-junction thermocouples may be in the right stage to be used as a diagnostic tool to investigate the temperature-related performance/ degradations of an operating SOFC under different

operating conditions. Perhaps, this sensing technology may also be embedded to commercial stacks to remotely monitor the operational health of an installed stack throughout its lifetime.

Appendix I

Polynomial Coefficients

The following are the polynomial coefficients used in regression equations to estimate the Seebeck coefficients at different temperatures.

Alumel:		Chromel	
a ₀	8.1×10^{-14}	a ₀	$-1.3628571428571 \times 10^{-2}$
a ₁	-2.68229×10^{-10}	a ₁	25.047619047619055
a ₂	$3.47395833 \times 10^{-7}$		
a ₃	$-2.09270833333 \times 10^{-4}$		
a ₄	3.7475×10^{-2}		
a ₅	-17.699999999999950		
Platinum		Pt:Rh 90:10 (R-type)	
a ₀	0.0	a ₀	1.3×10^{-14}
a ₁	1.3021×10^{-11}	a ₁	-3.3854×10^{-11}
a ₂	$-4.5312500 \times 10^{-8}$	a ₂	3.1770833×10^{-8}
a ₃	$4.4479166667 \times 10^{-5}$	a ₃	$-1.4895833333 \times 10^{-5}$
a ₄	$-3.2191666666667 \times 10^{-2}$	a ₄	$-5.541666666667 \times 10^{-3}$
a ₅	-3.999999999999989	a ₅	1.3000000000000007
Pt:Rh 87:13 (S-type)		Nicrosil	
a ₀	5.0×10^{-15}	a ₀	2.3×10^{-14}
a ₁	-1.3021×10^{-11}	a ₁	-7.0313×10^{-11}
a ₂	1.2500000×10^{-8}	a ₂	9.0104167×10^{-8}
a ₃	$-6.979166667 \times 10^{-6}$	a ₃	$-6.9687500000 \times 10^{-5}$
a ₄	$-9.008333333333 \times 10^{-3}$	a ₄	$2.385833333333 \times 10^{-2}$
a ₅	1.4000000000000004	a ₅	11.400000000000000
Nisil			
a ₀	1.8×10^{-14}	a ₃	$-1.7812500000 \times 10^{-5}$
a ₁	-5.4687×10^{-4}	a ₄	$-2.0925000000000 \times 10^{-2}$
a ₂	5.9895833×10^{-8}	a ₅	-14.499999999999977

Appendix II

Inverse Coefficients: K-type

Following are the standard inverse coefficients for K-type thermocouples. These values are available at the online NIST databases.

(http://srdata.nist.gov/its90/download/type_k.tab)

Coefficient	Temperature Range (°C)		
	-200 to 0	0 to 500	500 to 1,370
d ₀	0.0000000E+00	0.000000E+00	-1.318058E+02
d ₁	2.5173462E+01	2.508355E+01	4.830222E+01
d ₂	-1.1662878E+00	7.860106E-02	-1.646031E+00
d ₃	-1.0833638E+00	-2.503131E-01	5.464731E-02
d ₄	-8.9773540E-01	8.315270E-02	-9.650715E-04
d ₅	-3.7342377E-01	-1.228034E-02	8.802193E-06
d ₆	-8.6632643E-02	9.804036E-04	-3.110810E-08
d ₇	-1.0450598E-02	-4.413030E-05	0.000000E+00
d ₈	-5.1920577E-04	1.057734E-06	0.000000E+00
d ₉	0.0000000E+00	-1.052755E-08	0.000000E+00

Appendix III

Temperature Data Logging system:

Following is a brief description of the data logging system developed for multi-junction thermocouple testing.

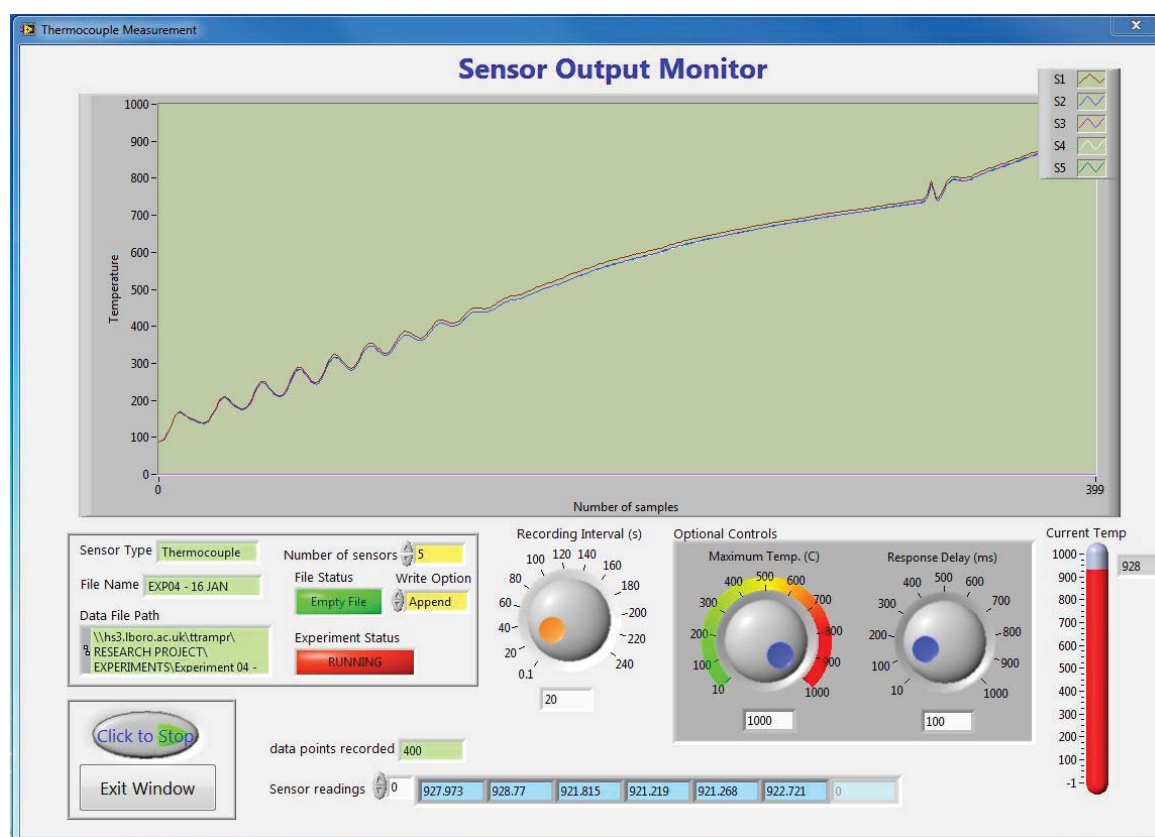
The system's current features are strictly limited to the requirements raised in this research. However, since it has adapted a modular architecture; it is easily scalable to accommodate any new requirements. Figure A3.1 shows a screenshot of the experimental monitor. The visual indicators are for visualisation purposes only; they do not restrict the range of the data being recorded. Data recording can be terminated at any point during an experiment and, data can be appended to the same file once the experiment resumed.

Language: LabVIEW

Thermometry: Thermocouple (upgradable for RTD as well)

Compatible Data logger: NI 9213

Data file format: MS Excel



A3.1 A screenshot of the experimental monitor

Appendix IV

SOFC Performance Monitoring System:

Following is a brief description of the data logging system developed to measure the performance of an operating SOFC. Although the intended use of this software is for SOFC performance monitoring, this can generally be used for other voltage or temperature measurements.

Figure A4.1 shows a screenshot of the experiment monitoring window with the voltage graph visible. This system is currently capable of recording temperature and voltage. The basic coding for recording current is also incorporated though, it may require some modifications. An empty module has been allocated for real-time I-V curve plotting as well. This programme is also developed in modules thus, easily scalable for any future requirements. The visual indicators are for visualisation purposes only; they do not restrict the range of the data being recorded.

Language: LabVIEW

Data types: Temperature and Voltage (basic features for current is added)

Compatible Data logger: NI 9213 / NI-USB 6210 (or any other NI voltage and current data logger)

Data file format: MS Excel

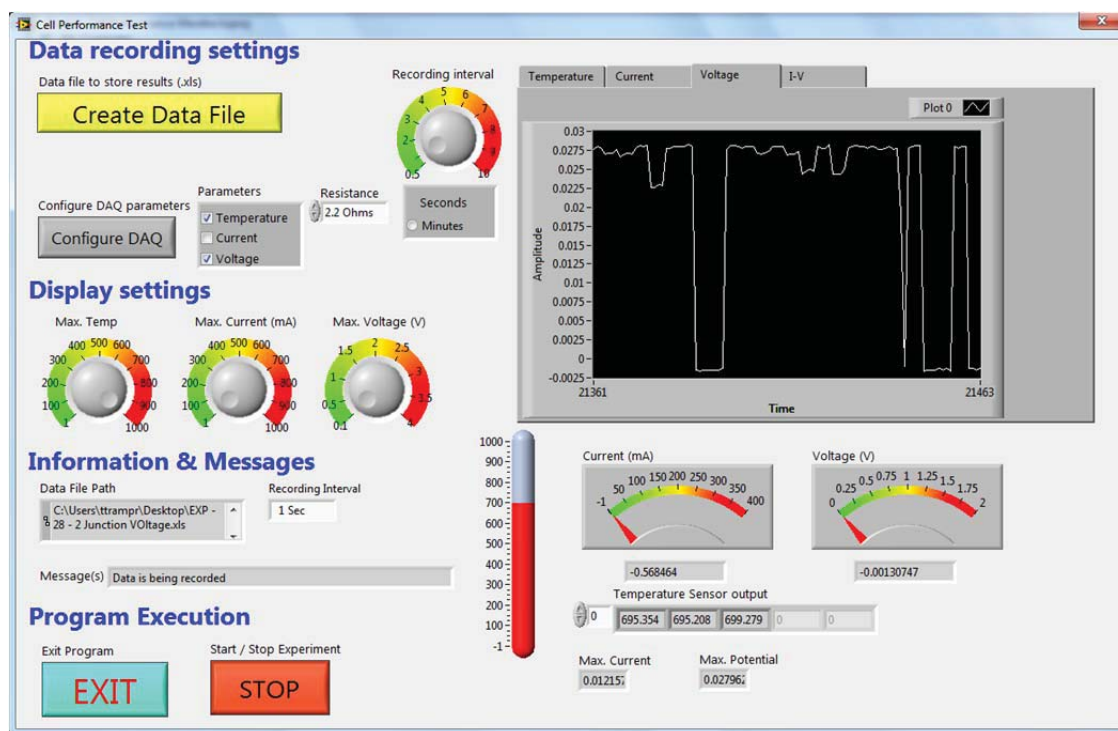


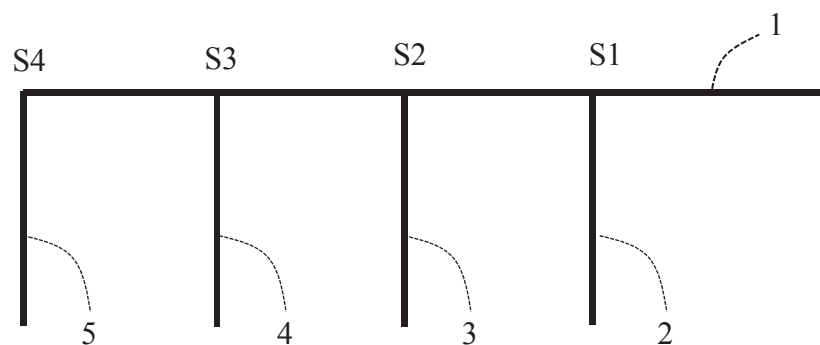
Figure A4.1 The data monitoring window

Appendix V

A5.1 Performance of the Array Over SOFC Temperature Range

The cyclic performance of the array for four heating-cooling cycles was tested covering the operating temperature range of a typical SOFC (from 600 °C – 900 °C). The experiment lasted over 53 hours. This experiment was designed to investigate the robustness of the sensor during high-temperature operation. The experimental procedure is presented, and the results are discussed in this section.

A multi-junction thermocouple array having four sensing points was fabricated by spot-welding of Ø 0.5 mm alumel and chromel wires as schematically shown in Figure A5.1. The array was placed in a furnace while having fixed two thermocouples in close proximity to it: approximately 10 – 20 mm from *S1* and *S2* sensing points. Preliminary experiments revealed that a temperature gradient exists in the furnace even at a steady state condition. Thus, two thermocouples were used to estimate the level of the suspected gradient. The tips of the thermocouples were approximately 10 mm apart from each other. The furnace was heated to 925 °C at a ramping rate of 400 °C/ hour. Temperature measurements from the two commercial thermocouples and from the array were recorded at 3 second intervals. The cyclic performance was recorded over 53 hours of operation while introducing some temperature interruptions between the 45th to 49th hours (approx.) to investigate the dynamic response. The first two cycles were carried out in moderate heating and cooling conditions, and the third cycle had a rapid cooling. The rapid cooling was introduced to investigate the response of the array to a drastic temperature changing condition. This harsh cooling was performed in three ways: 1) opening the furnace's door; 2) taking the sensor set (the array and thermocouples) outside the furnace; and 3) submerging the sensor set in a cold water bath.



A5.1 Schematic diagram of the array

A5.1.1 Results and Discussion

Temperature profiles recorded from thermocouples and the array during the entire course of operation are given in A5.2. Legends *S1* to *S4* are the temperature from four sensing points of the array, and *TC1* and *TC2* are the temperatures from two commercial thermocouples. The temperatures measured by the array and two thermocouples at sections A, B, C, and D are listed in Table A5.1. These data show that there is a temperature difference between the two commercial thermocouples, except at room temperature. Therefore, it can be identified that there was a temperature gradient across the furnace even when at times where the furnace was not ramping. At room temperature, the array appears to measure almost the same temperature that the two commercial thermocouples measured. Therefore, differences between the measurements from the commercial thermocouples and the array are likely to be due to actual temperature differences present across different sensing points. Thus, it can be said that the array has functioned as accurately as the two thermocouples during the test.

Signals from the array agree well with that from the thermocouples throughout the whole operation. Further, it has successfully survived in harsh cooling conditions to which it was exposed. Figure A5.3 confirms that the array was able to respond very favourably to abrupt temperature interruptions that it was subjected to.

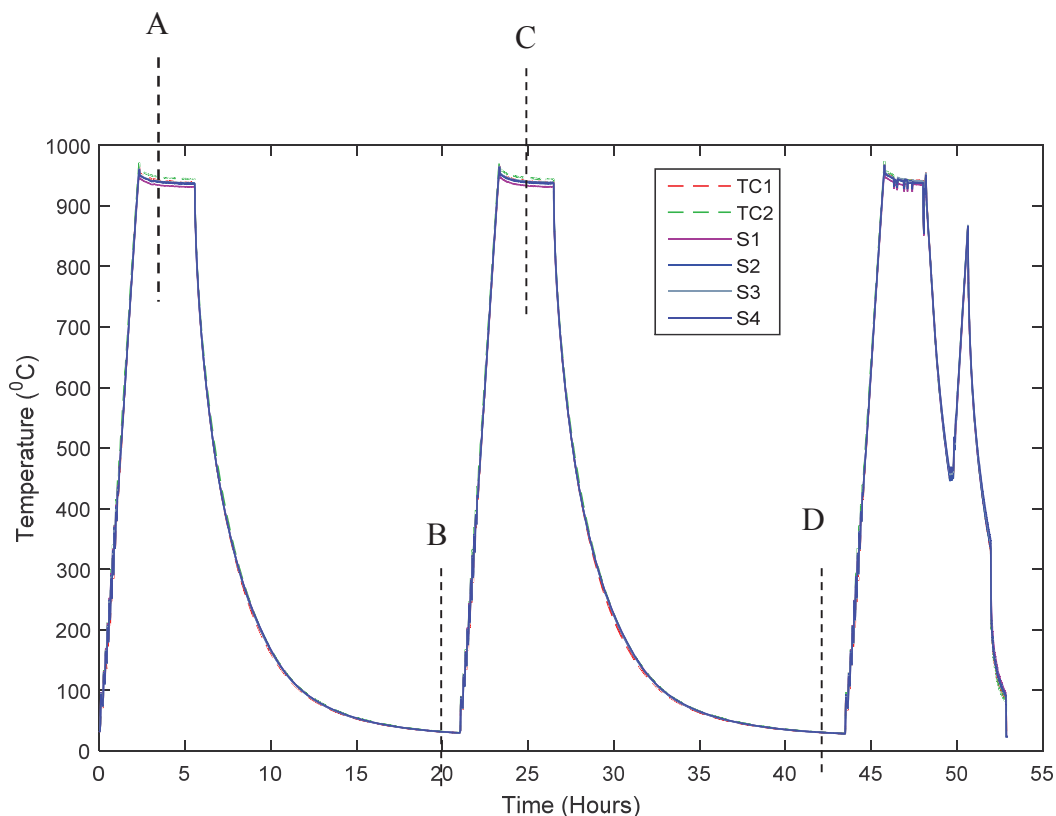


Figure A5.2 Temperature measurements during the entire course of the experiment

Table A5.1 Temperatures at selected sections (measured in °C)

Section	TC1	TC2	S1	S2	S3	S4
A	942.79	948.28	934.77	939.66	941.10	940.46
B	31.27	31.60	31.28	31.28	31.38	31.42
C	941.30	946.05	933.28	938.44	940.45	939.63
D	29.55	29.74	29.53	29.55	29.65	29.67

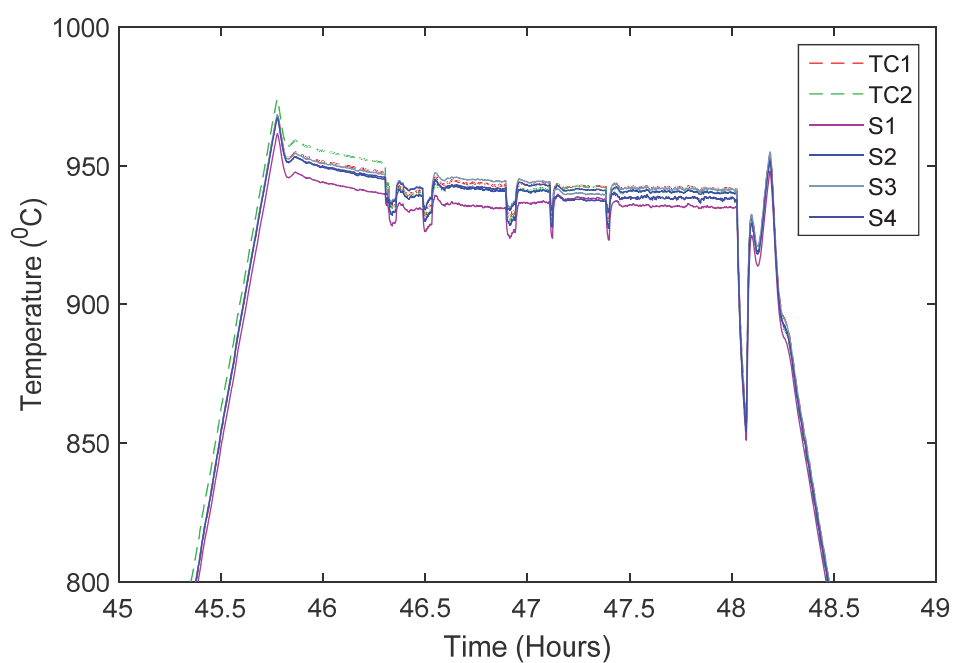


Figure A5.3 Response to temperature interruptions

A5.2 Performance of the Grid Over SOFC Temperature Range

A multi-junction thermocouple grid having 12 sensing points was fabricated by spot-welding of four alumel wires and three chromel wires each of Ø0.25 mm. A schematic diagram of the grid is shown in Figure A5.3. *S1* to *S12* are the 12 sensing points. The grid was placed inside a furnace while having fixed a commercial thermocouple approximately 10 mm adjacent to *S7*. The grid was subjected to three heating-cooling cycles with a heating rate of 450 °C/hour. The maximum set temperature was 925 °C. Temperatures from the grid as well as from the thermocouple were recorded at 5 second intervals. The experiment ran approximately 22 hours.

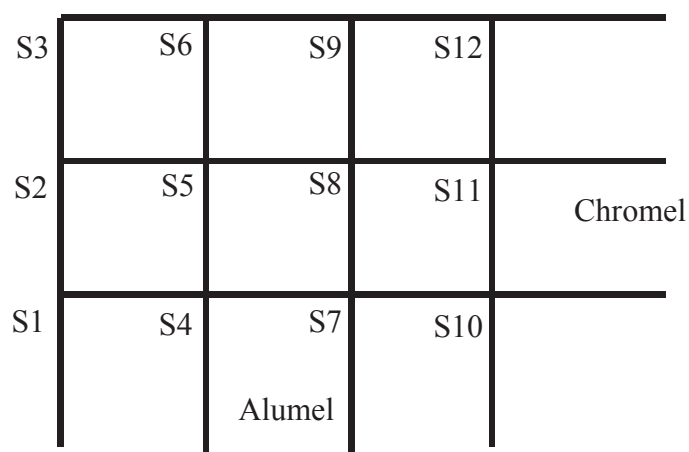


Figure A5.3 Schematic diagram of 12 point grid

A5.2.1 Results and Discussion

Figure A5.4 shows the temperature measured from the grid and from the commercial thermocouple throughout the experiment. Temperatures measured at 2nd, 6th, 8th, and 18th hour are listed in Table A5.2. Temperature measurements show that while the grid measuring different temperatures from its sensing points, the average temperature is very close to the thermocouple's measurement. Particularly, when the furnace temperature is almost steady, the agreement between the grid's measurements and that of the thermocouple is very close. Therefore, the difference between the grid and the thermocouple's measurements should be due to actual temperature gradient present within the furnace. Overall, the grid could measure temperature in a similar manner to the commercial thermocouple.

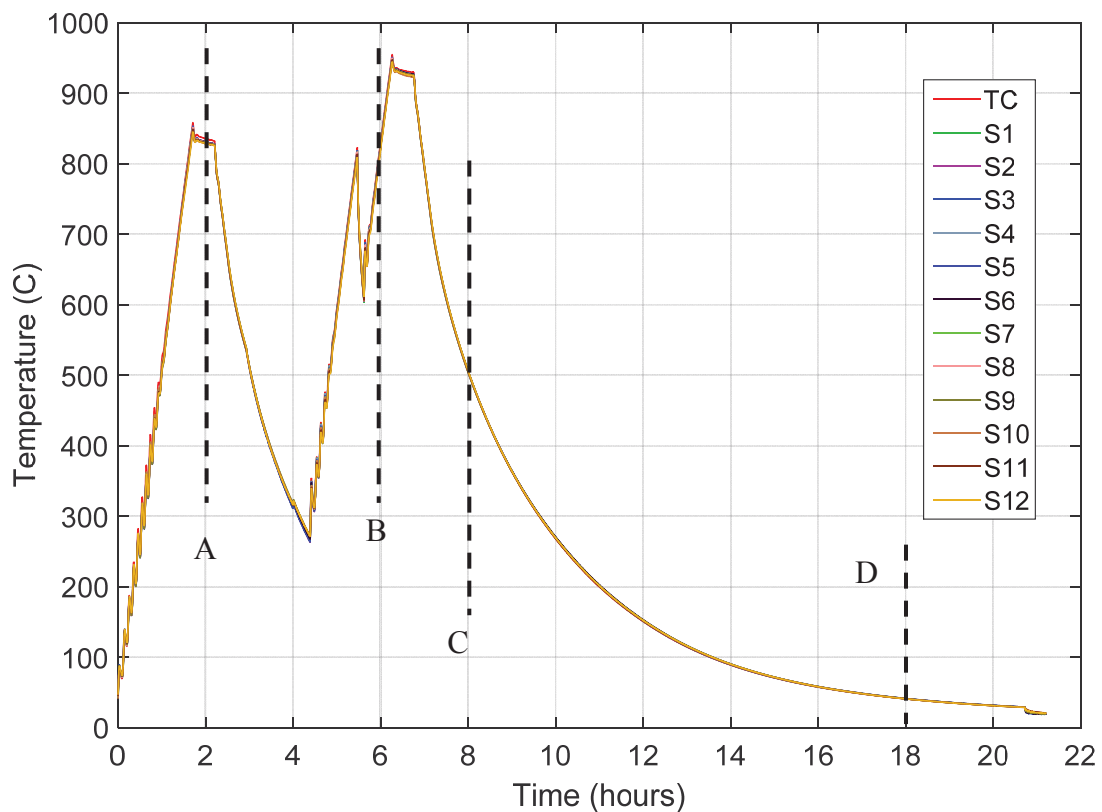


Figure A5.4 Performance of 12-point grid and a thermocouple

Table A5.2 Temperature from the drid and the thermocuple

Sensing point	A	B	C	D
S1	830.2	827.4	504.1	41.1
S2	830.8	827.6	504.8	41.2
S3	830.4	823.5	505.9	41.2
S4	829.9	827.6	504.4	41.3
S5	830.5	827.9	505.1	41.4
S6	830.2	823.9	506.2	41.4
S7	829.3	825.6	504.4	41.1
S8	829.9	825.8	505.0	41.1
S9	829.5	821.7	506.1	41.1
S10	828.1	822.9	504.6	40.9
S11	828.7	823.1	505.3	41.0
S12	828.4	819.0	506.4	41.0
TC	835.1	831.4	505.0	41.0